

**School of
Biosciences**



Chemical sensing at the nanoscale: Local field enhanced
coherent Raman scattering micro-spectroscopy near a
plasmonic nano-antenna

Martina Elisena Recchia

PhD thesis
School of Biosciences
Cardiff University

January 2024

Contents

List of Acronyms	iii
List of Figures	iv
List of Tables	xxvii
Abstract	xxix
Acknowledgements	xxxix
1 Introduction	1
2 Background Theory	9
2.1 Principle of non-linear optics	9
2.1.1 Coherent Raman scattering (CRS)	10
2.1.1.1 Coherent anti-Stokes Raman scattering (CARS)	13
2.1.1.2 Stimulated Raman scattering (SRS)	15
2.1.2 Second harmonic generation (SHG)	16
2.1.3 Two photon fluorescence (TPF)	17
2.2 Optical response of metallic nanoparticles	18
2.3 CARS in the presence of a plasmonic antenna	21
3 Materials and Methods	23
3.1 Silica coated gold nanorods (SiAuNRs) and sample preparation	23
3.2 Gold nanobowties (AuNBs) and samples preparation	28
3.2.1 AuNB design and fabrication	28
3.2.2 Polystyrene (PS) beads	32
3.2.3 HEK293 Cells	34
3.3 Multimodal microscope setup	35
3.3.1 Polarization resolved extinction	35
3.3.2 Heterodyne epi-detected CARS (eH-CARS)	41
3.3.3 Forward-CARS, SRS, SHG, and TPF	44
3.3.4 Setup calibration for eH-CARS measurements in silicone oil	44
3.4 Numerical simulations via COMSOL	47
3.4.1 Extinction	51
3.4.2 LFE eH-CARS	54
4 Optical extinction of nanostructures	62
4.1 SiAuNRs	62
4.1.1 Experimental extinction cross-section	62

4.1.2	Simulated extinction cross-section	65
4.1.3	Optical sizing	68
4.1.3.1	Modification of the gold permittivity	71
4.1.3.2	Error minimisation procedure	74
4.2	AuNBs	78
5	LFE eH-CARS with SiAuNRs	85
5.1	Circular vs Linear excitation polarization	85
5.2	Enhancement quantification (R factor)	91
5.3	Linear Polarization excitation dependence of LFE eH-CARS	94
5.4	NRs stability against the laser exposure	96
5.4.1	Saturation Effect	107
5.5	LFE eH-CARS time traces	109
5.6	Study of third order non linear contributions to the LFE eH-CARS .	111
5.7	CARS local field enhancement	120
5.8	R factor wavenumber dependence behaviour	122
5.9	R factor comparison	129
5.10	Conclusions	132
6	LFE eH-CARS, TPF, SHG with AuNBs	136
6.1	Time trace measurements procedure	138
6.2	Control sample	141
6.3	PS beads	145
6.3.1	Fluctuation correlation analysis: SRS vs SHG, and fluorescence	145
6.3.2	Fluctuation correlation analysis: LFE eH-CARS vs SHG, and fluorescence	153
6.4	Cells	158
6.4.1	Control sample P2X7	158
6.4.2	P2X7-GFP-His	160
6.4.3	Conclusion and Outlook	164
7	Conclusion	167
A	Appendix	173
A.1	Lock-in offset correction	173
A.2	Example of reliability checks with negative outcome	174
A.3	Selection criteria for correlative time traces measurements of Chapter 6.3.2	176
A.4	Correlative time traces measurements performed at bulk-glass cov- erslip interface of a sample prepared with 200nm PS beads in 50% glycerol/water (v/v) solution	179
A.5	Correlative time traces measurements and selection criteria performed on AuNBs sample prepared with the 200nm PS beads in fully DI water solution	181
A.6	Selection criteria for correlative time traces measurements of Chapter 6.4	185
	Bibliography	189

List of Acronyms

AuNB	gold nanobowtie
AR	aspect ratio
BFP	back focal plane
BPD	balanced photodiodes
CARS	Coherent anti-Stokes Raman scattering
CRS	coherent Raman scattering
CCD	charge-coupled device
CMOS	complementary metal-oxide-semiconductor
DIC	differential interference contrast
DBS	dichroic beam splitters
eH-CARS	epi heterodyne detected CARS
EWFD	electromagnetic waves frequency domain
EBL	electron beam lithography
FDTD	finite-difference time-domain
FEM	finite element method
FF	far field
FWHM	full width at half maximum
FWM	four wave mixing
IFD	instantaneous frequency difference
LSPR	localized surface plasmon resonance
LFE	local field enhancement
LFE eH-CARS	local field enhanced eH-CARS
MIR	mid-infrared
NA	numerical aperture

NF near field
NP nanoparticle
NPBS non-polarizing beam splitter
NR nanorod
OPO optical parametric oscillator
PEC perfect electric conductor
PMC perfect magnetic conductor
PML perfectly matched layer
PMT photonmultiplier
PS polystyrene
PSF point spread function
SHG second harmonic generation
SiAuNR silica-coated gold nanorod
S/N signal-to-noise ratio
SR spontaneous Raman
SRS stimulated Raman scattering
TPF two photon fluorescence

List of Figures

1.1	Representative biological Raman spectrum	3
2.1	Schematic of spontaneous Raman scattering. (a) Generic molecule which scatters an incoming light, at ω_P , into Rayleigh (ω_P), Stokes ($\omega_S = \omega_P - \omega_V$) and anti-Stokes ($\omega_{AS} = \omega_P + \omega_V$) components. (b) Energy diagram for Stokes Raman scattering and anti-Stokes Raman scattering. The vibrational state (solid line) are labeled with g and v , while the virtual state (dashed line) is labeled j . The incoming light is represented by solid arrows, while the wiggled ones represent the emitted radiation.	10
2.2	(a) Energy diagram showing the resonant contribution to the CARS signal. Insert: schematic diagram for phase matching in CARS. (b) Energy diagram showing the non-resonant contribution to the CARS signal coming from FWM processes involving the electrons of other molecules different from the target ones. (c) Energy diagram showing an electronic contribution enhanced by a two-photon resonance of the pump beam associated with an excited electronic state. The ground state is labeled with g , while the vibrational states are labeled with v (v') and the electronically excited state with e . Solid lines indicate the real state levels, while dashed lines represent the virtual states.	13
2.3	Energy diagram showing the SRS process. Insert: phase matching automatically satisfied in SRS. The solid line indicates the ground (g) and vibrational (v) state levels, while the virtual states are represented by dashed lines.	15
2.4	Schematic representation of SHG geometry and energy-level diagram, where solid line indicates the ground state level, while the virtual states are represented by dashed lines.	16
2.5	Jablonski diagram for one-photon (left) and two-photon excitation. S_0 and S_1 are the ground electronic state and the first electronic excited state respectively. The solid black lines represent the vibrational states associated with each electronic state.	17
2.6	Complex dielectric function of gold: $\Re(\epsilon_{Au})$ (red lines) and $\Im(\epsilon_{Au})$ (black lines).	21
3.1	TEM images of SiAuNRs. Left: provided by Nanopartz. Middle and right: measured exploiting the electron microscopy facilities at Cardiff University.	23
3.2	Sketch of the sample used for particle characterization: SiAuNR covalently bound to a microscope coverslip in silicone oil bulk	24

3.3	The tosyl reagent is used for reaction with glass hydroxyl groups, forming a reactive tosyl ester. The sulfonyl ester reacts with amines to form secondary amine linkages.	24
3.4	Functionalized coverslip covered by 100 μl of NRs solution in wet atmosphere to prevent particle aggregation.	27
3.5	Sample mounted in the table vise.	27
3.6	AuNB sketch. Left: 3D view; Right: lateral view. α : apex angle; l : length; h : height; c : radius of curvature; g : gap size.	28
3.7	FDTD simulations of gold bowtie nanoantennas. (a-c) Intensity enhancement G (defined in Eq.3.2.1) at the gap center for the CARS ($\lambda_C=660\text{ nm}$), pump ($\lambda_P=820\text{ nm}$), and Stokes ($\lambda_S=1080\text{ nm}$) wavelength for different lengths l and apex angles α . The optimal parameters are chosen to maximize G_C and indicated by the blue star in (a).	29
3.8	SEM images of the gold bowtie nanoantennas. (a) Writefield containing 10×10 nominally equal gold bowtie nanoantennas and labeled with the nominal parameters l and g as well as a unique identifier (here, $(0, 0)$). (b) Zoom-in showing 3×3 exemplary nanoantennas. (c) Zoom-in showing one single nanoantennas with its real antenna length l , gap size g , and apex angle α	30
3.9	Schematic overview of individual steps in the EBL fabrication process of plasmonic structures.	31
3.10	Fluorescence emission/excitation spectrum of YG Fluorescent Microspheres and YG Carboxylate Microspheres.	33
3.11	Wide field images of HEK293 cells (Objective 60x). The optimal cell concentration was determined visually through a wide-field microscope. For that, a $15\ \mu\text{l}$ drop containing cells at $5\times 10^6\ \mu\text{l}^{-1}$, $10\times 10^6\ \mu\text{l}^{-1}$, or $20\times 10^6\ \mu\text{l}^{-1}$ was applied on top of an empty coverslip. After about 30 min the cells settled onto the coverslip and were incubated for 24 h before taking the images.	35
3.12	Widefield transmission images (Objective 100x) of HEK293 cells. The cells were deposited on top of the nanostructures and were imaged before (a) and after (b) the correlative fluorescence-eHCARS measurements with the focus at different z-sections (as indicated) with $z = 0\ \mu\text{m}$ coinciding with the focus of the AuNBs.	36
3.13	Nikon Ti-U inverted microscope with a zoom-in on the sample holder.	37
3.14	Sketch of the geometry of the NP in the measurement reference system. E_{\perp} and $E_{//}$ are in the xy plane. θ represents the angle at which the linear polarizer is set compared to the x axis in the back focal plane of the condenser. Although $E_{//}$ is the predominant field component in the field focus, E_{\perp} and E_z are still present due to the high NA employed.	38
3.15	Simplified ray diagram of the spectroscopy setup. The rays arriving at the input slit are the ones collected by the Objective lens.	39
3.16	Schematic explanation of how the binning for the CCD camera pixels was performed in both horizontal (spectral) and vertical (spatial) direction.	40

3.17	Sketch of laser source and wavelength outputs for multimodal non-linear microscopy. The Ti:Sa laser source provides a laser beam with fundamental wavelength at 820 nm, 80 MHz repetition rate and 150 fs pulse duration. This is used both as Pump beams and also to pump an OPO, after being frequency-doubled via a second harmonic generation crystal, which provides both the Stokes and Reference beam for eH-CARS measurements.	41
3.18	Sketch of the multimodal SRS /SHG/TPF/F-CARS/eH-CARS microscope. Stokes pulses are amplitude-modulated at ν_m and radio-frequency shifted at ν_s using an AOM. Spectral focusing is applied via H-ZF52A glass blocks. The pump travels through a delay line for IFD optimization. Pump and Stokes are coupled via DBSs into an inverted microscope. F-CARS/SHG/MPF are detected in transmission using a bandpass filters (F1, F2, F3) and a PMT. SRS is detected using a bandpass filter F4 and a resonant photodiode (PD) and filtered at ν_m by using a lock-in amplifier. eH-CARS is collected in epi-geometry and combined with a reference pulse (which travels through a delay line for temporal overlap optimization) by using a non-polarizing beam splitter (NBS), polarization split by using a Wollaston prism (WP) and detected by using pairs of balanced photodiodes (BPD).	42
3.19	Dependence of exited vibrational frequency Ω and CARS wavelength λ_{CARS} on the Stokes wavelength (λ_S), keeping the pump wavelength (λ_P) fixed at 820nm.	42
3.20	F-CARS intensity acquired after OPO tuning to have $\text{IFD}_c \sim 2900 \text{ cm}^{-1}$, focusing pump and Stokes laser beams within the non resonant glass coverslip ($P_P=5 \text{ mW}$, $P_S=10 \text{ mW}$), tuning the IFD by varying pump-Stokes delay to tune the IFD over a 400 cm^{-1} range.	46
3.21	Calibration measurements. The sketch illustrates the point of the sample where the laser beams were focused during the two calibration measurements (center, within silicone oil bulk, for the IFD calibration via SRS and red dotted line, at glass-silicone oil interface, for reference delay optimization. (a) Measured SRS spectrum of Silicone oil. (b)eH-CARS amplitude (A) and phase (Φ), for both detected components (horizontal (H) and vertical (V)) of xz scan at glass-oil interface, at $\text{IFD}=2904 \text{ cm}^{-1}$ and with the optimized Reference delay (see text).	48
3.22	Typical geometry and meshing of the COMSOL models adopted within this work. Overview of the simulated volume V_{sim} , a quarter of a sphere encircled by a PML of homogeneous thickness. An NR is placed in the middle of V_{sim} , above the $z = 0$ optical interface and the NR close-up is reported to make visible its Au core and the SiO_2 shell.	50
3.23	Dielectric function of gold, both real (black) and imaginary (red) parts in the visible spectral region measured via spectroscopic ellipsometry measurements on single crystal thick gold surface.	52

3.24	Normalized amplitude of the scattered (top) and total (bottom) electric fields obtained, with a 40 nm×68 nm NR, having a 10 nm SiO ₂ shell, placed onto a glass surface and surrounded by silicone oil, for incoming light, propagating along the positive <i>z</i> -axis direction, with polarization along (left) and across (right) the NR (as indicated with the yellow arrows) at the correspondent LSPR.	53
3.25	Simulated absolute scattering σ_{abs} (dashed line), absorption (dot-dashed line) σ_{sca} and extinction σ_{ext} (solid line) cross-section spectra of an exemplary SiAuNR ($D_{\text{rod}} = 40$ nm, $L_{\text{rod}} = 68$ nm ($AR = 1.7$), $R_{\text{tip}} = D_{\text{rod}}/(2.5)$, $t_{\text{shell}} = 10$ nm with $f_{\text{oil}} = 0$) obtained with the presented model (see text) and using $\epsilon_{\text{Au}}(\lambda)$ by Olmon et al., for linear polarization excitation along the NR long axis (red, σ^L) and linear polarization excitation across the NR (black, σ^T).	55
3.26	Pump (left) and Stokes (right) input field amplitude distributions, computed in COMSOL considering focusing microscope objective with NA=1.45. The simulated volume is centered at $\mathbf{r} = 0$ and has a radius $R_{\text{sim}} = 600$ nm. A focused wavefront has been used, with polarization along the <i>x</i> -axis and a Gaussian field profile in the BFP of the focusing lens.	56
3.27	Result of the first EWFD interface. Pump (left) and Stokes (right) scattered (top) and total (bottom) fields normalized to the maximum of the input field ($A_{\text{P}}^{\text{max}} = 2.41 \times 10^8$ V/m and $A_{\text{S}}^{\text{max}} = 1.84 \times 10^8$ V/m, see Fig.3.26), resulting for a SiAuNR placed at $\mathbf{r} = 0$ surrounded by silicone oil and on top of a substrate index matched with the bulk material (such as the glass coverslip).	57
3.28	Complex third-order susceptibility $\chi^{(3)}_{\text{oil}}$ of silicone oil relative to glass (microscope slide)	59
3.29	Nonlinear current \mathbf{J}_{CARS} (contour plot) and emitted field \mathbf{E}_{CARS} amplitude (false colours) generating focusing pump and stokes beam at the interface between a SiAuNR placed onto a non resonant substrate (glass coverslip) and surrounded by a resonant material (silicone oil).	60
4.1	(a)Single particle extinction spectrum of nominal 25 nm×71 nm with 5 nm silica shell (acquired as explained in 3.3.1) for different in-plane linear polarization angles of the white-light illumination as indicated. Measurements settings: spectra are averages over 200 acquisitions, 11 ms exposure time. (b) $\sigma_{\text{ext}}(\lambda_{\text{LSPR}})$ versus polarizer angle θ fit with Eq.4.1.1	63
4.2	(a) Unpolarized wide field extinction image (1196x62 pixels) of single nominal 40×68 nm-SiAuNRs taken using a 100 W halogen lamp and a band-pass filtered centered at 650 nm, a 100x 1.45 NA oil objective, and a sCMOS camera. The two circled particles are used as exemplary particles in Fig.4.2(b) and in Fig.4.3. (b)Polarization resolved wide field extinction of the particle red circled in (a), setting the rotatable polarizer at 0°, 30°, 60°, 90°, 120°, 150°. Gray bar scale for all these images: white=-0.17 and black=0.21. A 10 μm scale bar is shown in (a) and in (b) the polarization angle is noted in each image. (measurement settings: $\times 128$ averages, $N=10$ repeats, $S=2$ μm)	64

4.3	Extinction cross-section of two nominal 40 nm×68 nm-SiAuNRs extracted from wide field extinction imaging measurements performed using a 100 W halogen lamp and band-pass filters with the different reported center wavelengths, for in-plane linear polarization as indicated. (a) red-circled NP and (b) blue-circled NP of Fig.4.2(a).	64
4.4	Extinction cross-section of two nominal 50 nm×100 nm-SiAuNRs (a,b) extracted from wide field extinction imaging measurements performed using a 100 W halogen lamp and band-pass filters with the different reported center wavelengths, for in-plane linear polarization as indicated.	65
4.5	Simulated absolute absorption σ_{abs} (dashed line), scattering (dash-dotted line) σ_{sca} and extinction σ_{ext} (solid line) cross-section spectra of three different NRs (as indicated) placed at a glass substrate and surrounded by index matching silicon oil ($n=1.52$), obtained with the presented model (see text) and using $\epsilon_{\text{Au}}(\lambda)$ by Olmon et al., for (a) linear polarization excitation along the NR (σ^L) and (b) linear polarization excitation across the NR (σ^T).	66
4.6	Solution of the elastic scattering model for three NR whose size and silica shell thickness are set to be equal to the nominal specification of the NRs employed within this project, as indicated (see Sec.3.1). The local field enhancement $\mathbf{E}_{\text{tot}}/\mathbf{E}_{\text{back}}$ is plotted. The exciting field \mathbf{E}_{back} (yellow arrow) propagates along \hat{z} , is polarized along the rod axis (i.e. along \hat{x}) and excited the NP at their longitudinal LSPR.	67
4.7	Left: simulated longitudinal σ^L_{ext} . Right: solution of the elastic scattering model and NF enhancement $\mathbf{E}_{\text{sca}}/\mathbf{E}_{\text{back}}$ plotted. The exciting field (at the indicated wavelength) resonantly excites the longitudinal LSPR. Each row refers to a particle characterized by $AR=2.84$, $R_{\text{tip}}=D/(2.5)$, $t_{\text{shell}}=10$ nm and $D=3$ nm (top), 5 nm (middle) and 10 nm (bottom), as indicated.	69
4.8	Simulated extinction (left), absorption (middle) and scattering (right) cross-section of a gold NR with $D=40$ nm and $AR=1.7$ for different tip shapes: $R_{\text{tip}}=D_{\text{rod}}/2$ (black), $R_{\text{tip}}=D_{\text{rod}}/3$ (red) and $R_{\text{tip}}=D_{\text{rod}}/4$ (blue).	70
4.9	Example, for nominal 50 nm×100 nm-SiAuNRs, to show how the main rod geometrical characteristics have been extracted from TEM images. Yellow arrows and values: diameter D ; green arrows and values: rod length L ; Red arrows and values: tip shape R_{tip} .	70
4.10	Particle size distribution from the TEM images analysis for nominal 50 nm×100 nm-SiAuNRs. (a) Diameter (D) (mean = 53.37 nm, standard deviation = 4 nm), (b) Aspect ratio (AR) (mean = 1.52, standard deviation = 0.28), (c) Tip length defined as D/x . (mean = 3, standard deviation = 0.57).	71
4.11	Fit of the experimental permittivity Olmon dataset with the Drude model in the range 600-850 nm.	72

- 4.12 Fit of the experimental permittivity Olmon dataset with the Drude model and additional damping considering NP#1 (i.e. $D=40$ nm, $AR=1.7$ and $R_{tip}=D/3$). (a) Real part, Olmon data (circles), and model (line) for $g=0.75$, $g=1.00$, $g=1.25$ and $g=1.5$. b) Imaginary part, Olmon data (circles), and model (line) for $g=0.75$, $g=1.00$, $g=1.25$ and $g=1.5$ 73
- 4.13 Fit of the experimental permittivity Olmon dataset with the Drude model and additional damping. (a) Real part and (b) imaginary part. Olmon data set (circles) and model (line) for $g=0.75$, $g=1.5$ and $R_{eff}=26$ nm (NP#1, i.e. $D=40$ nm, $AR=1.7$ and $R_{tip}=D/3$), $R_{eff}=31.8$ nm (NP#2, i.e. $D=50$ nm, $AR=1.6$ and $R_{tip}=D/3$). 74
- 4.14 Simulated extinction (left), absorption (middle) and scattering (right) cross-section for $R_{eff}=26$ nm (NP#1) (black), $R_{eff}=31.8$ nm (NP#2) (red), using ϵ_{Olmon} (solid line) and $\epsilon_{g=1}$ (dashed line). 75
- 4.15 Resulting simulated absorption (top line) and scattering (bottom line) cross-sections for polarization aligned along (a) and across (b) a NR characterized by $(D, AR, g)=(52$ nm, 1.40, 1) in a wavelength range going from 430 nm to 720 nm in steps of 5 nm (solid lines) and for the corresponding filtered results assuming filters centered at 450 nm, 500 nm, ..., 700 nm with 40 nm bandwidth (star symbol). 77
- 4.16 Extinction cross-section of a nominal 50 nm \times 100 nm-SiAuNRs (a,b) extracted from wide field extinction imaging measurements performed using a 100 W halogen lamp and band-pass filters at the different reported center wavelengths, for different in-plane linear polarizations, as indicated. 78
- 4.17 (a) Errors (nm²) 2D map obtained via the error minimization procedure introduced in the text, comparing experimental and simulated extinction cross-sections. The latter were computed for $g=0.75$, varying the rod diameter D from 53 nm to 57 nm in steps of 1 nm and varying the AR from 1.35 to 1.39 in steps of 0.01. Minimum error (equal to 768 nm²) found for $(D, AR)=(55$ nm, 1.37). (b) Comparison between experimental extinction cross section (same as Fig.4.16) and simulated extinction cross section calculated via Eq.4.1.14 using $A_{\perp}=1.0201$, $A_{//}=1.2276$ and $\phi_0=158^\circ$, resulting from the error minimization procedure (obtained with for $(g, D, AR)=(0.75, 55$ nm, 1.37), see text), for $\phi=158^\circ$ (dark red dash-dotted line, indicated as 'fit ext l' as this is the case of only longitudinal plasmon mode contribution) and for $\phi=68^\circ$ (blu dash-dotted line, indicated as 'fit ext t' as this is the case of only transversal plasmon mode contribution). 79
- 4.18 Errors (nm²) 2D map obtained (via the error minimization procedure introduced in the text) comparing experimental and simulated extinction cross-sections. (a) Simulations carried out for $g=0.5$ varying the rod diameter D from 55 nm to 57 nm in steps of 1 nm and varying the AR from 1.35 to 1.37 in steps of 0.01. Minimum error (equal to 769 nm²) found for $(D, AR)=(56$ nm, 1.36). (b) Simulations carried out for $g=1.0$, varying the rod diameter D from 54 nm to 56 nm in steps of 1 nm and varying the AR from 1.36 to 1.38 in steps of 0.01. Minimum error (equal to 770 nm²) found for $(D, AR)=(55$ nm, 1.37). 79

4.19	Schematic representation (top view) of AuNB and incident light, propagating in z direction, with polarization aligned along (blue arrow) and across (red arrow) the AuNB main axis, exciting the longitudinal and transversal LSPs respectively.	80
4.20	Spectral extinction cross-section of AuNBs characterized by $l=60$ nm. (a) $\alpha=80^\circ$, (b) $\alpha=90^\circ$ and (c) $\alpha=100^\circ$. Left: Extinction cross-section for each individual particle, indicated here with the number n_p , measured at 450 nm, 500 nm, ..., 750 nm, for longitudinal (top line) and transversal (bottom line) LSPR excited. Right: ensemble median spectrum and error bars indicating the 0.1 and 0.9 quantiles.	81
4.21	Spectral extinction cross-section of AuNBs characterized by $l=75$ nm. (a) $\alpha=100^\circ$ and (b) $\alpha=90^\circ$. Left: Extinction cross-section for each individual particle, indicated in here with the number n_p , measured at 450 nm, 500 nm, ..., 750 nm, for longitudinal (top line) and transversal (bottom line) LSPR excited. Right: ensemble median spectrum and error bars indicating the 0.1 and 0.9 quantiles.	83
4.22	Spectral extinction cross-section of AuNBs characterized by $\alpha=90^\circ$. (a) $l=50^\circ$, (b) $l=55^\circ$ and (c) $l=60^\circ$. Left: Extinction cross-section for each individual particle, indicated here with the number n_p , measured at 450 nm, 500 nm, ..., 750 nm, for longitudinal (top line) and transversal (bottom line) LSPR excited. Right: ensemble median spectrum and error bars indicating the 0.1 and 0.9 quantiles.	84
5.1	Extinction cross-section of two nominal $40\text{ nm} \times 68\text{ nm}$ -SiAuNRs surrounded by silicone oil extracted from wide field extinction imaging measurements (see Chapter 3.3.1) performed using a 100 W halogen lamp and band-pass filters with the different reported center wavelengths, for in-plane linear polarization, as indicated. Left: before the laser exposure. Right: after the laser exposure in the CARS experiment.	86
5.2	Sketch of the polarization acquired by the fields when a $\lambda/2$ wave plate is used in the beam path. Left: Without NR in beams focus. Right: NR in the beam focus, oriented so that the beams polarization is aligned along its main axis. LP: Linear Polarization. WP: wave plate.	87
5.3	Left: Two photon fluorescence from linear excitation polarization. Middle and Right: Polarization resolved eH-CARS amplitude at silicone oil resonance (2904 cm^{-1}) with linear excitation polarization aligned along the longitudinal axis of the NR, as measured, lock-in offset corrected; Co-(middle) and Cross-(right) rod components correspond to horizontal (H) and vertical detected components, respectively (see text). Measurement acquired at the particle focus, with 1.45NA objective. Actual exciting power at the sample: $P_p=1.2\text{ mW}$ (pump) and $P_s=4\text{ mW}$ (Stokes). Gray scales from m (black) to M (white). Values are in units of electron per second for TPF intensity and volts for eH-CARS amplitude.	88
5.4	Sketch of the polarization assumed by the fields when a $\lambda/4$ wave plate is used in the beam path. Left: Without NR in beams focus. Right: NR in the beam focus. LP: Linear Polarization, CP: Circular Polarization.	89

5.5	Left: Two photon fluorescence from linear excitation polarization. Middle and Right: Polarization resolved eH-CARS amplitude at silicone oil resonance (2904 cm^{-1}) with circular excitation polarization, as measured, lock-in offset corrected (see Chapter 3.3.4.); Co- (middle) and Cross- (right) circular components correspond to vertical (V) and horizontal (H) detected components, respectively (see text). Actual exciting power at the sample: $P_P P_S^{1/2} = 1.22\text{ mW}^{3/2}$. Gray scales from m (black) to M (white). Values are in units of electron/second for TPF intensity and volts for eH-CARS amplitude.	90
5.6	Projection of the detected eH-CARS signal shown in Fig. 5.5, along (co-) and across (cross-) the longitudinal axis of the NR. Gray scales from m (black) to M (white). Values are in units of volts.	91
5.7	R factor, i.e. signal measured at the particle in unit of silicone oil signal. A polarization resolved eH-CARS 2D scan is acquired and the signal measured at the x-cut passing through the center of the NR PSF, as real and imaginary part, is offset with respect the signal emitted by the silicone oil and normalized to the amplitude of this last one. Different excitation modality (see text) have been used. Left: linear excitation polarization. Middle: circular excitation polarization. Right: circular excitation polarization and projection of the detected eH-CARS signal along(co-) and across(cross-) the longitudinal axis of the NR. Dot: experimental data; line: Gaussian amplitude fit.	93
5.8	Sketch represented the polarization configuration sequence (1-5) assumed by the beams travelling through the setup, until the detector axes, i.e horizontal (H) and vertical (V), when the $\lambda/2$ wave plate is inserted in the beam path (see text). Blue line: exciting beams; Gray dotted line: rotation of the $\lambda/2$ wave plate; Gold dotted line: hypothesized NR in-plane orientation; Gold line: NR emitted field; Red line: detected signal after projection.	94
5.9	a) Single particle extinction cross-section of a nominal $25\text{ nm} \times 71\text{ nm}$ -SiAuNR with 5 nm silica shell extracted from wide field extinction imaging measurements and band-pass filters with the different reported center wavelengths, for in-plane linear polarization as indicated, measured before (a1) and after (a2) the laser exposure. See Chapter3.3.1 for details about how these measurement have been carried out. b) LFE eH-CARS amplitude polarization dependence behaviour, for $\text{IFD} = 2904\text{ cm}^{-1}$ and measured at the NR in (a), using linear exciting polarization. Black: detected H component (black square) and fit (black line); Red: detected V component (red square) and fit (red line).	95

5.10	(a-b) Single particle extinction spectrum, of nominal 25 nm×71 nm-SiAuNR with 5 nm silica shell, for different in-plane linear polarization angles of the white-light illumination, as indicated, measured before (a) and after (b) the laser exposure. Measurements were performed as explained in Chapter 3.3.1. (c-d) LFE eH-CARS power dependence measurement, at IFD = 2904 cm ⁻¹ , performed at the NR in (a-b), using circular exciting polarization. (c) R _{co} (circle) and R _{cross} (square) factors computed from (d) as explained in Sec.5.2. The error bars come from the uncertainty of the exact amplitude of the Gaussian function used to fit the data to retrieve the R factor value. (d) eH-CARS amplitude measured at glass-oil interface away from NR (black circle) and signal measured at the NR in the co- (red circle) and cross- (red square) circular polarized detection channels. The dashed black line represents the linear interpolation performed on the interface signal to check its value for low power.	97
5.11	(a-b) Single particle extinction spectrum, of nominal 25 nm×71 nm-SiAuNR with 5 nm silica shell, for different in-plane linear polarization angles of the white-light illumination, as indicated, measured before (a) and after (b) the laser exposure. Measurements were performed as explained in Chapter 3.3.1. (c-d) LFE eH-CARS power dependence measurement, at IFD = 2904 cm ⁻¹ , performed at the NR in (a-b), using linear exciting polarization. (c) R _{co} (circle) and R _{cross} (square) factors computed from (d) as explained in Sec.5.2. The error bars come from the uncertainty of the exact amplitude of the Gaussian function used to fit the data to retrieve the R factor value. (d) eH-CARS amplitude measured at glass-oil interface away from NR (black circle) and signal measured at the NR in the co- (red circle) and cross- (red square) circular polarized detection channels. The dashed black line represents the linear interpolation performed on the interface signal to check its value for low power.	99
5.12	(a-b) Single particle extinction spectrum, of nominal 25 nm×71 nm-SiAuNRs with 5 nm silica shell, for different in-plane linear polarization angles of the white-light illumination, as indicated, measured before (a) and after (b) the laser exposure. Measurements were performed as explained in Chapter 3.3.1. c) LFE eH-CARS stability measured, at IFD = 2904 cm ⁻¹ , performed at the NR in (a-b), using circular exciting polarization and P _P =2.3 mW and P _S =7.9 mW. The same measurement was repeated five times and for each of them, the R _{co} (circle) and R _{cross} (square) factors have been computed as explained in Sec.5.2. The error bars come from the uncertainty of the exact amplitude of the Gaussian function used to fit the data and to retrieve the R factors value.	100

- 5.13 (a-b) Single particle extinction spectrum, of nominal $25\text{ nm} \times 71\text{ nm}$ -SiAuNRs with 5 nm silica shell, for different in-plane linear polarization angles of the white-light illumination, as indicated, measured before (a) and after (b) the laser exposure. Measurements were performed as explained in Chapter 3.3.1. c) LFE eH-CARS stability measured, at $\text{IFD} = 2904\text{ cm}^{-1}$, performed at the NR in (a), using linear exciting polarization and $P_P=1.2\text{ mW}$ and $P_S=4.3\text{ mW}$. The same measurement was repeated five times and for each of them the R factor has been computed as explained in Sec.5.2. The error bars come from the uncertainty of the exact amplitude of the Gaussian function used to fit the data to retrieved the R factor value. 100
- 5.14 Left: pump and Stokes powers with the resulting overall powers exciting at the sample used in the power dependence measurement reported in Fig.5.15. Right: eH-CARS amplitude measured at glass-oil interface away from NR for the indicated power and its linear interpolation (dashed black). 101
- 5.15 (a-b) Single particle extinction cross-section of nominal $40\text{ nm} \times 68\text{ nm}$ -SiAuNR with 10 nm silica shell extracted from wide field extinction imaging measurements and band-pass filters with the different reported center wavelengths, for in-plane linear polarization as indicated, measured before (a) and after (b) the laser exposure. See Chapter 3.3.1 for more details about how these measurements have been carried out. (c-d) LFE eH-CARS power dependence and reproducibility measurements, measured with $\text{IFD} = 2904\text{ cm}^{-1}$, performed focusing at the NR in (a-b), using circular exciting polarization. (c) $R_{\text{co-circ}}$ (circle) and $R_{\text{cross-circ}}$ (square) factors, computed from (d) as explained in Sec.5.2. The error bars come from the uncertainty of the exact amplitude of the Gaussian function used to fit the data and to retrieve the R factor value. (d) eH-CARS amplitude measured at glass-oil interface away from NR (black circle) and signal measured at the NR PSF in the co- (red circle) and cross- (red square) circular polarized detection channels. The overall power employed in each repetition is reported in the right scale for clarity (green data). . . . 102
- 5.16 Left: pump and Stokes powers with the resulting overall powers exciting at the sample used for the power dependence measurement reported in Fig.5.17. Right: eH-CARS amplitude measured at glass-oil interface away from NR for the indicated power and its linear interpolation (dashed black). 103

5.17	(a-b) Single particle extinction cross-section of nominal 40 nm × 68 nm-SiAuNR with 10 nm silica shell extracted from wide field extinction imaging measurements and band-pass filters with the different reported center wavelengths, for in-plane linear polarization as indicated, measured before (a) and after (b) the laser exposure. See Chapter 3.3.1 for more details about how these measurements have been carried out. (c-d) LFE eH-CARS power dependence and reproducibility measurements, measured with IFD = 2904 cm ⁻¹ , performed focusing at the NR in (a-b), using linear exciting polarization. (c) R factor, computed from (d) as explained in Sec.5.2. The error bars come from the uncertainty of the exact amplitude of the Gaussian function used to fit the data and to retrieve the R factor value. (d) eH-CARS amplitude measured at glass-oil interface away from NR (black circle) and signal measured at the NR PSF in the co- (red circle) and cross- (red square) circular polarized detection channels. The overall power employed in each repetition is reported in the right scale for clarity (green data).	103
5.18	Left: pump and Stokes powers with the resulting overall powers exciting at the sample used for the power dependence measurement reported in Fig.5.19. Right: eH-CARS amplitude measured at glass-oil interface away from NR for the indicated power and its linear interpolation (dashed line).	105
5.19	(a-b) Single particle extinction cross-section of nominal 50 nm × 100 nm-SiAuNR with 10 nm silica shell extracted from wide field extinction imaging measurements and band-pass filters with the different reported center wavelengths, for in-plane linear polarization as indicated, measured before (a) and after (b) the laser exposure. (c-d) LFE eH-CARS power dependence and reproducibility measurements, measured with IFD = 2904 cm ⁻¹ , performed focusing at the NR in (a-b), using circular exciting polarization. (c) R _{co-circ} (circle) and R _{cross-circ} (square) factors, computed from (d) as explained in Sec.5.2. The error bars come from the uncertainty of the exact amplitude of the Gaussian function used to fit the data and to retrieve the R factor value. (d) eH-CARS amplitude measured at glass-oil interface away from NR (black circle) and signal measured at the NR PSF in the co- (red circle) and cross- (red square) circular polarized detection channels. The overall power employed in each repetition is reported in the right scale for clarity (green data).	105
5.20	Left: pump and Stokes powers with the resulting overall powers exciting at the sample used for the power dependence measurement reported in Fig.5.21. Right: eH-CARS amplitude measured at glass-oil interface away from NR for the indicated power and its linear interpolation.	106

- 5.21 (a-b) Single particle extinction cross-section of nominal $50\text{ nm} \times 100\text{ nm}$ -SiAuNR with 10 nm silica shell extracted from wide field extinction imaging measurements and band-pass filters with the different reported center wavelengths, for in-plane linear polarization as indicated, measured before (a) and after (b) the laser exposure. (c-d) LFE eH-CARS power dependence and reproducibility measurements, measured with $\text{IFD} = 2904\text{ cm}^{-1}$, performed focusing at the NR in (a-b), using linear exciting polarization. (c) R factor, computed from (d) as explained in Sec.5.2. The error bars come from the uncertainty of the exact amplitude of the Gaussian function used to fit the data and to retrieve the R factor value. (d) eH-CARS amplitude measured at glass-oil interface away from NR (black circle) and signal measured at the NR PSF in the co- (red circle) and cross- (red square) circular polarized detection channels. The overall power employed in each repetition is reported in the right scale for clarity (green data). . . . 106
- 5.22 Energy diagram showing the resonant contribution to the CARS signal by the target molecule for (a) ideal single diatomic molecule and (b) real molecule with quantized energy levels not evenly spaced. (a.1) and (b.1) show how pump (green) and Stokes (red) are able to resonantly drive the coherence between two well defined levels. (a.2) and (b.2) show how pump and Stokes would be able to drive subsequently another vibrational coherence which involves higher vibrational states only in the case of the ideal molecule. Solid lines indicate the ground (g) and vibrational state (v_1, v_2, v_3) levels, while the virtual states are represented by dashed lines. 108
- 5.23 LFE eH-CARS time traces and extinction spectra measured before (left) and after (right) eH-CARS acquisition, on two different silica coated gold NRs of nominal $25\text{ nm} \times 71\text{ nm}$ size and 5 nm shell thickness. a) LFE eH-CARS performed with circular polarization excitation; b) LFE eH-CARS performed with linear polarization excitation rotated to be along the rod. All the LFE eH-CARS time traces were performed with an overall power on the sample around $3\text{ mW}^{3/2}$. . . 111
- 5.24 LFE eH-CARS time traces and extinction spectra measured before (left) and after (right) eH-CARS acquisition, on a silica-coated gold NR of nominal $40\text{ nm} \times 68\text{ nm}$ size and 10 nm shell thickness. a) Extracted extinction spectra measured before any LFE eH-CARS time traces; b) Extracted extinction spectra measured after the first LFE eH-CARS, performed with circular polarization excitation; c) Extracted extinction spectra measured after the first LFE eH-CARS, performed with linear polarization excitation (along the rod); d) LFE eH-CARS time trace performed with circular polarization excitation; e) LFE eH-CARS time trace performed for linear polarization excitation rotated to be along the rod. All the LFE eH-CARS time traces were performed with an overall power on the sample around $3\text{ mW}^{3/2}$. 112

- 5.25 LFE eH-CARS time traces and extinction spectra measured before and after eH-CARS acquisition, on a silica-coated gold NR of nominal $50\text{ nm}\times 100\text{ nm}$ size and 10 nm shell thickness. a) Extracted extinction spectra measured before any LFE eH-CARS time traces; b) Extracted extinction spectra measured after the first LFE eH-CARS, performed with circular polarization excitation; c) Extracted extinction spectra measured after the first LFE eH-CARS, performed with linear polarization excitation (along the rod); d) LFE eH-CARS time trace performed for circular polarization excitation; e) LFE eH-CARS time trace performed with linear polarization excitation rotated to be along the rod. All the LFE eH-CARS time traces were performed with an overall power on the sample around $3\text{ mW}^{3/2}$ 113
- 5.26 Nonlinear source current \mathbf{J}_{CARS} (contour plot) and local CARS field \mathbf{E}_{CARS} amplitude (false colours) obtained considering a SiAuNR (with $D=25\text{ nm}$, $AR=2$, $R_{\text{tip}}=D/(2.5)$, $t_{\text{shell}}=5\text{ nm}$) placed onto a glass substrate and surrounded by silicone oil, setting the NP to be in a homogeneous third order nonlinear and resonant medium ($\chi_{\text{B}}^{(3)}=\chi_{\text{oil}}^{(3)}$). Left: \mathbf{J}_{CARS} and \mathbf{E}_{CARS} obtained when only the oil has a third order nonlinear contribution. Center: \mathbf{J}_{CARS} and \mathbf{E}_{CARS} obtained when only the NP gold core has a third order nonlinear contribution. Right: \mathbf{J}_{CARS} and \mathbf{E}_{CARS} obtained when only the NP silica shell has a third order nonlinear contribution. 115
- 5.27 Simulated extinction cross-section spectra (left) and (right) consequent LSPR position in wavelength, obtained varying the NR aspect ratio AR , keeping constant all the other geometrical characteristics. (a) $D=25\text{ nm}$, $R_{\text{tip}}=D/(2.5)$ and $t_{\text{shell}}=5\text{ nm}$. (b) $D=50\text{ nm}$, $R_{\text{tip}}=D/(2.5)$ and $t_{\text{shell}}=10\text{ nm}$ 117
- 5.28 Study of the third order nonlinear contribution in the simulated-detected eH-CARS amplitude (Eq.3.4.21) obtained separately investigating the NP gold core (black, indicated with $\chi_{\text{Au}}^{(3)}$), the oil (red, indicated with $\chi_{\text{oil}}^{(3)}$) and the NP silica shell (blue, indicated with $\chi_{\text{shell}}^{(3)}$) third order contributions (see text) for a SiAuNRs surrounded by silicone oil and placed onto a glass substrate (index matched with the bulk material). The NP is considered as placed in a homogeneous material from the third-order non linearity point of view (see Eqs.5.6.2). Each LSPR corresponds to a different NP with (a) $D=25\text{ nm}$, $R_{\text{tip}}=D/(2.5)$, $t_{\text{shell}}=5\text{ nm}$ and (b) $D=50\text{ nm}$, $AR=2$, $R_{\text{tip}}=D/(2.5)$, $t_{\text{shell}}=10\text{ nm}$, for which the AR has been varied. The results for three driven molecular vibration are shown: (Left) $\Omega_{\text{vib}}=2860\text{ cm}^{-1}$, (Center) $\Omega_{\text{vib}}=2904\text{ cm}^{-1}$, to whom corresponds the oil CARS resonance, and (Right) $\Omega_{\text{vib}}=2860\text{ cm}^{-1}$ 118

5.29	Study of the third order nonlinear contribution in simulated-detected eH-CARS amplitude (Eq.3.4.21), for $\Omega_{\text{vib}}=2904\text{ cm}^{-1}$, obtained separately investigating the NP gold core (left, indicated with $\chi_{\text{Au}}^{(3)}$), the oil (center, indicated with $\chi_{\text{oil}}^{(3)}$) and the NP silica shell (right, indicated with $\chi_{\text{shell}}^{(3)}$) third order contributions (see text) for a SiAuNRs surrounded by silicone oil and placed (red, BG) in an homogeneous third order nonlinear material and (black, BG) onto a glass substrate (index matched with the bulk material) with $\chi_{\text{B}}^{(3)}=0$. Each LSPR corresponds to a different NP with $D=25\text{ nm}$, $R_{\text{tip}}=D/(2.5)$, $t_{\text{shell}}=5\text{ nm}$ for which the AR has been varied.	120
5.30	Local field enhancement (LFE) of the CARS signal, considering the CARS process taking place at a silica coated NR (with $D=25\text{ nm}$, $AR=2$, $R_{\text{tip}}=D/(2.5)$, $t_{\text{shell}}=5\text{ nm}$) in the case of (a) plasmonic gold core (ϵ_{Au} as in Chapter 4.1.3.1) and (b) dielectric core ($n=1.52$). . .	121
5.31	Top: eH-CARS amplitude as a function of the IFD, experimentally measured at the oil-glass interface away from the NR(red) and at the NR (black). Bottom: R factors wavenumber dependence.	123
5.32	Gaussian function ($\sigma=8.48\text{ cm}^{-1}$) used in the convolution onto the simulated eH-CARS signals to take into account the spectral resolution characterizing the real experiments. μ is translated in the convolution from 2840 cm^{-1} to 2960 cm^{-1} in steps of 5 cm^{-1} and here two examples are given for $\mu=2860\text{ cm}^{-1}$ (blue) and $\mu=2860\text{ cm}^{-1}$ (red).	125
5.33	Comparison between simulated eH-CARS signal, as a function of Ω , obtained neglecting (solid lines) and taking into account (dashed line) the spectral resolution that affects the experiment (see text). Both real (red) and imaginary (blue) components of the eH-CARS are displayed. The simulation was performed for four different cases: (a) in the absence of the NR at the oil-glass interface, (b) with the NR and $\chi_{\text{Au}}^{(3)}=0\text{ m}^2/\text{V}^2$, (c) with the NR and $\chi_{\text{Au}}^{(3)}=3\times 10^{-19}\text{ m}^2/\text{V}^2$ and (d) with the NR and $\chi_{\text{Au}}^{(3)}=1\times 10^{-18}\text{ m}^2/\text{V}^2$. Where the NR is present is has been modeled with $D=56\text{ nm}$, $AR=1.37$, $g=0.75$ $R_{\text{tip}}=D/3$ and $t_{\text{shell}}=10\text{ nm}$. The following third order materials properties have been used: $\chi_{\text{B}}^{(3)} = 7.8 \times 10^{-23}\text{ m}^2/\text{V}^2$ for the borosilicate glass coverslip, $\chi_{\text{Au}}^{(3)} = 3 \times 10^{-19}\text{ m}^2/\text{V}^2$ for the NR gold core, $\chi_{\text{shell}}^{(3)} = 0.6\chi_{\text{B}}^{(3)}$ for the silica shell.	126
5.34	Top: Simulated eH-CARS amplitudes, as function of the IFD, obtained in presence (black) and absence (red) of the NR, neglecting (solid lines) and taking into account (dashed line) the spectral resolution that affects the real experiments. Bottom: Comparison for the computed R factor neglecting (solid lines) and taking into account (dashed line) the spectral resolution that affects the real experiments. The simulation were performed considering a NR with $D=55\text{ nm}$, $AR=1.37$, $g=0.75$ $R_{\text{tip}}=D/3$ and $t_{\text{shell}}=10\text{ nm}$. The following third order materials properties have been used: $\chi_{\text{B}}^{(3)} = 7.8 \times 10^{-23}\text{ m}^2/\text{V}^2$ for the borosilicate glass coverslip, $\chi_{\text{Au}}^{(3)} = 3 \times 10^{-19}\text{ m}^2/\text{V}^2$ for the NR gold core, $\chi_{\text{shell}}^{(3)} = 0.6\chi_{\text{B}}^{(3)}$ for the silica shell.	127

- 5.35 Top: eH-CARS amplitude as a function of the IFD, experimentally measured at the glass-oil interface (circle red symbols) and at the NR PSF (square red symbol) and simulated from the glass-oil interface only (dashed black line) and from the NR (solid black line). The log scale was adjusted to improve the qualitative comparison between the signals related to the glass-oil interface. Bottom: Quantitative comparison between the R factors resulting from the experimental (red symbols) and simulated (black solid line) eH-CARS dataset. The $\chi_{Au}^{(3)}$ employed in the simulation performed in presence of the NR has been set to $0\text{m}^2/\text{V}^2$ (left), $3 \times 10^{-19}\text{m}^2/\text{V}^2$ (center) and $1 \times 10^{-18}\text{m}^2/\text{V}^2$ (right). 128
- 5.36 R factor versus power of incident fields from polarization resolved eH-CARS. Left: Nominal 25×71 nm NR with 5 nm of SiO_2 shell; Selected silicone oil resonance is 2904cm^{-1} ; Circular polarization excitation and R factor computed considering the projection of the detected eHCARS signal along(co-) the longitudinal axis of the NR. Middle: Nominal 40×68 nm NR with 10 nm of SiO_2 shell; Selected silicone oil resonance is 2904cm^{-1} ; Circular polarization excitation and R factor computed considering the projection of the detected eH-CARS signal along(co-) the longitudinal axis of the NR. Right: Nominal 50×100 nm NR with 10 nm of SiO_2 shell; Selected silicone oil resonance is 2904cm^{-1} ; Circular polarization excitation and R factor computed considering the projection of the detected eH-CARS signal along(co-) the longitudinal axis of the NR. 130
- 5.37 Polarization resolved single particle extinction spectra σ_{ext} measured before and after the local field enhanced eH-CARS (LFE eH-CARS) set of measurements reported in Fig.5.36. Each row refers to the particle whose size and silica shell thickness are reported in the corresponding sketch. For details about the acquisition procedure of the extinction measurement see Chapter3.3.1. 131
- 5.38 Left: Simulated extinction cross-section spectra σ_{ext} of silica coated gold NR, placed at a glass substrate and surrounded by index matching silicone oil ($n=1.52$), with diameter D equal to 25 nm (top, black), 40 nm (middle, red) and 50 nm (bottom, blue), and silica shell thickness t_{shell} set to 5 nm, 10 nm and 10 nm respectively. The aspect ratio (AR) of each NR was varied, as indicated, to shift the corresponding LSPR as about 560 nm (circle), 660 nm (square) and 760 nm (triangles). Right: Computed R factor as a function of the LSPR position of silica-coated gold NRs with $D=25$ nm $t_{\text{shell}}=5$ nm (black), $D=40$ nm $t_{\text{shell}}=10$ nm (red) and $D=50$ nm $t_{\text{shell}}=10$ nm (blue). The different symbols refers to the legend in (Right) to indicate the AR value used to obtain a given LSPR position. 133

5.39	Bar plot providing a visual representation of the number of particles investigated during the various characterizations. Distinct particle groups are shown on the x-axis, with the height of each colored box within the columns representing the number of particles characterized with the corresponding measurement. Each color denotes a specific characterization method, providing a visual overview of the distribution of analyses across different particle groups. Example: Among the nominal 50nm×100nm SiAuNRs group, a total of 60 rods underwent characterization. Specifically, 10 of these rods were specifically utilized for the eH-CARS wavenumber dependence characterization.	134
6.1	Sketch of the sample used in Chapter 6.4.2. HEK293 cells expressing C-terminally GFP-His-tagged rat P2X7 receptors are seeded onto a microscopic coverslip containing multiple AuNB nanoantennas. The inset (adapted from Ref.[1]) shows P2X7 associated with a membrane region that is enriched in sphingolipids and cholesterol (liquid ordered phase).	137
6.2	Measured SRS spectra of polystyrene (PS) and Gibco™ FluoroBrite™ DMEM. Spectra acquired tuning the OPO to have $\text{IFD}_c=2950\text{ cm}^{-1}$ and scanning the pump-Stokes delay over 500 ps. As the relative peaks intensities observed are affected by the pump-Stokes overlap from the spectral focusing method and temporal ordering for $\text{IFD}>2950\text{ cm}^{-1}$, we also plotted here for comparison the retrieved, normalized $\Im(\chi_P^{(3)} S)$.	138
6.3	Transmission wide-field image of an AuNBs array with indication about how the periodicity and orientation are determined (yellow) and the order followed to successively and automatically measure nine nanoantennas in a row (blue).	139
6.4	Representative fluctuation correlation time traces between (from top to bottom rows) nominal SHG-, TPF-, and eH-CARS signal (real component (\Re), imaginary component (\Im), amplitude (Abs) and phase (Φ)). Sample: AuNBs surrounded by Gibco™ FluoroBrite™ DMEM with 25mM HEPES. Time traces of 20 s (as indicated) were recorded with 0.1 ms sample period at the antenna’s site and downsampled to 10 ms. $\text{IFD}=2904\text{ cm}^{-1}$. Exciting power at the sample: $P_P=0.86\text{ mW}$ and $P_S=1.84\text{ mW}$. For the PMTs channels, we reported an indication of the detected bandwidth for clarity. See reliability check in Fig.6.5.	142

6.5	Four criteria to be checked to consider the correlative time trace recorded (shown in Fig.6.16) at the antenna as reliable. (a) A 2D eH-CARS amplitude image ($2\ \mu\text{m}\times 2\ \mu\text{m}$) measured at the AuNB focus, before and after the correlative measurement, shows that the antenna remained reasonably centered (yellow cross) during the time trace. Rainbow scales from m (black) to M (white) as indicated. Exciting power at the sample: $P_P=1.2\ \text{mW}$ (pump) and $P_S=4\ \text{mW}$ (Stokes). (b) Single particle extinction cross-sections, measured before and after the laser exposure, show that the antenna was not affected by significant structural changes during the laser exposure. (c) Galvo mirrors positions (along x and y directions) recorded during the time traces, to visualize possible instabilities affecting the recorded signal. (d) Four BPD currents (i_0, i_1, i_2, i_3) recorded during the time trace measurement were balanced (symmetric around the x-axis). Additionally, the $\bar{i} = \frac{i_\Sigma}{\langle i_\Sigma \rangle}$ used to correct the recorded time trace eH-CARS is shown.	144
6.6	Representative fluctuation correlation time traces between (from top to bottom row) nominal SHG, TPF, RED fluorescence, and SRS signals. Sample: 200 nm diameter YG fluorescent PS bead in a 50% glycerol/water (v/v) solution. Time traces of 20 s were recorded simultaneously in the mentioned channels with 0.1 ms sample period, downsampled to 10 ms. Powers employed at the sample: $P_P=4.7\ \text{mW}$ and $P_S=12.29\ \text{mW}$. (Left) $\text{IFD}=2904\ \text{cm}^{-1}$, (Right) $\text{IFD}=3050\ \text{cm}^{-1}$. For the PMTs channels, we reported an indication of the detected bandwidth for clarity.	146
6.7	Specification emission spectra of YG Fluorescent Microspheres (adapted from Ref.[2]) where the bandwidth of the detection of SHG-, TPF-, and RED- channels are highlighted with the corresponding representative colors (blue, green, and red). The resulting integrals of the emission curve in the different regions are reported.	147
6.8	Raman spectrum of glycerol	147
6.9	Illustration of the optical trapping taking place in a sample given by PS beads moving in a bulk medium and encountering a tightly focused beam.	148
6.10	Representative fluctuation correlation time traces between (from top to bottom row) nominal SHG-, TPF-, RED- fluorescence and SRS-signals. Sample: 200 nm diameter YG fluorescent PS beads in fully DI water solution. Time traces of 20 s were recorded simultaneously (with 0.1 ms sample period) and downsampled to 10 ms. Powers employed: $P_P=4.7\ \text{mW}$ and $P_S=12.29\ \text{mW}$. (Left) $\text{IFD}=2904\ \text{cm}^{-1}$, (Right) $\text{IFD}=3050\ \text{cm}^{-1}$. For the PMTs channels, we reported an indication of the detected bandwidth for clarity.	149

6.11	Representative fluctuation correlation time traces between (from top to bottom row) nominal SHG, TPF, RED fluorescence and SRS signals. Sample: 200 nm diameter YG fluorescent PS bead in fully DI water solution. Time traces of 20 s (as indicated) were recorded simultaneously with 0.1 ms sample period and downsampled to 10 ms. Powers employed: $P_P=2.45$ mW and $P_S=5.96$ mW. (Left) $IFD=2904$ cm^{-1} , (Right) $IFD=3050$ cm^{-1} . For the PMTs channels, we reported an indication of the detected bandwidth for clarity.	150
6.12	Zoom in into two intervals (indicated in the horizontal axis) of the representative fluctuation correlation time traces of Fig.6.11-left (left) and Fig.6.11-right (right)	151
6.13	Illustration of a possible configuration where PS beads, moving in a bulk medium, encounters a tightly focused beam, emitting SHG signal (represented with the blue bold arrows) compared to the TPF signal (represented with the green bold arrows), which is anyway emitted by the bead. The TPF field reaches its maximum when the bead is at the center of the focal volume, i.e. where the pump beam intensity is maximum.	152
6.14	Nominal SHG- and TPF- channels of Fig.6.12-left fitted with Eq.6.3.4 and Eq.6.3.3 respectively. Parameters: $A_{TPF} \simeq 1 \times 10^8$ el/s, $A_{SHG} \simeq 1.5 \times 10^5$ el/s, $\gamma_1 \simeq 5.8\text{s}^{-1}$, $\gamma_2 \simeq 2.4\text{s}^{-1}$, $t_0 \simeq 6.76\text{s}$	152
6.15	Representative fluctuation correlation time traces between (from top to bottom row) nominal SHG-, TPF-, RED- fluorescence and SRS-signals. Sample: 100 nm diameter YG fluorescent PS bead in a 50% glycerol/water (v/v) solution. Time traces of 20 s were recorded simultaneously with 0.1 ms sample period and downsampled to 10 ms. Powers employed: $P_P=5.12$ mW and $P_S=10.2$ mW. (Left) $IFD=2904$ cm^{-1} , (Right) $IFD=3050$ cm^{-1} . For the PMTs channels, we reported an indication of the detected bandwidth for clarity.	154
6.16	Representative fluctuation correlation time traces between (from top to bottom rows) nominal SHG-, TPF-, RED fluorescence and eH-CARS signal (real component (\Re), imaginary component (\Im), amplitude (Abs) and phase (Φ)). Sample: AuNBs sample with 200 nm diameter YG fluorescent PS bead in 50% glycerol/water (v/v) solution (see Chapter 3.2). Time traces of 20 s were recorded with 0.1 ms sample period at the antenna's site and downsampled to 10 ms. $IFD=2904$ cm^{-1} ; Exciting power at the sample: $P_P=0.76$ mW and $P_S=1.74$ mW. For the PMTs channels, we reported an indication of the detected bandwidth for clarity. See reliability check in Fig.A.4. .	155
6.17	Representative fluctuation correlation time traces between (from top to bottom rows) nominal SHG-, TPF-, RED fluorescence and eH-CARS signal (real component (\Re), imaginary component (\Im), amplitude (Abs) and phase (Φ)). Sample: AuNBs sample with 200 nm diameter YG fluorescent PS bead in 50% glycerol/water (v/v) solution (see Chapter 3.2). Time traces of 20 s (as indicated) were recorded with 0.1 ms sample period at the antenna's site and downsampled to 10 ms. $IFD=3050$ cm^{-1} ; Exciting power at the sample: $P_P=0.67$ mW and $P_S=1.21$ mW. For the PMTs channels, we reported an indication of the detected bandwidth for clarity. See reliability check in Fig.A.5.	156

6.18	Representative fluctuation correlation time traces between (from top to bottom rows) nominal SHG-, TPF-, RED fluorescence and eH-CARS signal (real component (\Re), imaginary component (\Im), amplitude (Abs) and phase (Φ)). Sample: AuNBs sample with 100 nm diameter YG fluorescent PS bead in 50% glycerol/water (v/v) solution (see Chapter 3.2). Time traces of 20 s were recorded with 0.1 ms sample period at the antenna's site and downsampled to 10 ms. IFD=3050 cm^{-1} . Exciting power at the sample: $P_P=0.63$ mW and $P_S=1.35$ mW. For the PMTs channels, we reported an indication of the detected bandwidth for clarity. See reliability check in Fig.A.6. .	159
6.19	Representative fluctuation correlation time traces between (from top to bottom rows) galvo mirrors position, nominal SHG-, TPF-, and eH-CARS signals (real component (\Re), imaginary component (\Im), amplitude (Abs) and phase (Φ)). Sample: HEK293 wild-type living cells onto AuNBs. Time traces of 20 s (as indicated) were recorded with 0.1 ms sample period at the antenna's site and downsampled to 10 ms. IFD=2904 cm^{-1} . Exciting power at the sample: $P_P=0.86$ mW and $P_S=1.79$ mW. For the PMTs channels, we reported an indication of the detected bandwidth for clarity. See reliability check in Fig.A.13.	161
6.20	Representative fluctuation correlation time traces between (from top to bottom rows) nominal SHG-, TPF-, and eH-CARS signal (real component (\Re), imaginary component (\Im), amplitude (Abs) and phase (Φ)). Sample: HEK293 cells expressing C-terminally GFP-His-tagged rat P2X7 receptors onto AuNBs. Time traces of 20 s (as indicated) were recorded with 0.1 ms sample period at the antenna's site and downsampled to 10 ms. IFD=2904 cm^{-1} . Exciting power at the sample: $P_P=0.9$ mW and $P_S=2$ mW. For the PMTs channels, we reported an indication of the detected bandwidth for clarity. See reliability check in Fig.A.14.	162
6.21	Representative fluctuation correlation time traces between (from top to bottom rows) nominal SHG-, TPF-, and eH-CARS signal (real component (\Re), imaginary component (\Im), amplitude (Abs) and phase (Φ)). Sample: HEK293 cells expressing C-terminally GFP-His-tagged rat P2X7 receptors onto AuNBs. Time traces of 20 s (as indicated) were recorded with 0.1 ms sample period at the antenna's site and downsampled to 10 ms. IFD=2904 cm^{-1} . Exciting power at the sample: $P_P=0.9$ mW and $P_S=2$ mW. For the PMTs channels, we reported an indication of the detected bandwidth for clarity. See reliability check in Fig.A.15.	163
6.22	Bar chart plot providing a visual representation of the main categories of events observed during our experimental study with cells.	164
A.1	Example of the lock-in offset correction for a eH-CARS signal applied to the real and imaginary parts of the measured eH-CARS signal. . .	173

- A.2 Example of reliability checks with negative outcome due to mechanical drifts. (a) A 2D eH-CARS amplitude scan ($2\mu\text{m}\times 2\mu\text{m}$) measured at the AuNB focus, before and after the correlative measurement. Rainbow scales from m (black) to M (white). (b) Single particle extinction cross-sections, measured before and after the laser exposure. (c) Galvo mirror positions (along x and y directions) recorded during the time traces. (d) Four BPD currents (i_0, i_1, i_2, i_3) recorded during the time trace measurement were balanced (symmetric around the x-axis). Additionally, the $\bar{i} = \frac{i_\Sigma}{\langle i_\Sigma \rangle}$ used to correct the recorded time trace eH-CARS is shown as well. 174
- A.3 Example of reliability checks with negative outcome due to particle damage. (a) A 2D eH-CARS amplitude scan ($2\mu\text{m}\times 2\mu\text{m}$) measured at the AuNB focus, before and after the correlative measurement. Rainbow scales from m (black) to M (white). (b) Single particle extinction cross-sections, measured before and after the laser exposure. (c) Galvo mirror positions (along x and y directions) recorded during the time traces. (d) Four BPD currents (i_0, i_1, i_2, i_3) recorded during the time trace measurement were balanced (symmetric around the x-axis). Additionally, the $\bar{i} = \frac{i_\Sigma}{\langle i_\Sigma \rangle}$ used to correct the recorded time trace eH-CARS is shown as well. 175
- A.4 Four criteria to be checked to consider the correlative time trace recorded at the antenna (shown in Fig.6.16) as reliable. (a) A 2D eH-CARS amplitude scan ($2\mu\text{m}\times 2\mu\text{m}$) measured at the AuNB focus, before and after the correlative measurement, shows that the antenna remained reasonably centered (yellow cross) during the time trace. Rainbow scales from m (black) to M (white). (b) Single particle extinction cross-sections, measured before and after the laser exposure, show that no significant structural changes affected the antenna during the laser exposure. (c) Galvo mirror positions (along x and y directions) recorded during the time traces to visualize possible instabilities affecting the recorded signal. (d) Four BPD currents (i_0, i_1, i_2, i_3) recorded during the time trace measurement were balanced (symmetric around the x-axis). Additionally, the $\bar{i} = \frac{i_\Sigma}{\langle i_\Sigma \rangle}$ used to correct the recorded time trace eH-CARS is shown as well. 176
- A.5 Four criteria to be checked to consider the correlative time trace recorded at the antenna (shown in Fig.6.17) as reliable. (a) A 2D eH-CARS amplitude scan ($2\mu\text{m}\times 2\mu\text{m}$) measured at the AuNB focus, before and after the correlative measurement, shows that the antenna remained reasonably centered (yellow cross) during the time trace. Rainbow scales from m (black) to M (white). (b) Single particle extinction cross-sections, measured before and after the laser exposure, show that no significant structural changes affected the antenna during the laser exposure. (c) Galvo mirror positions (along x and y directions) recorded during the time traces to visualize possible instabilities affecting the recorded signal. (d) Four BPD currents (i_0, i_1, i_2, i_3) recorded during the time trace measurement were balanced (symmetric around the x-axis). Additionally, the $\bar{i} = \frac{i_\Sigma}{\langle i_\Sigma \rangle}$ used to correct the recorded time trace eH-CARS is shown as well. 177

- A.6 Four criteria to be checked to consider the correlative time trace recorded at the antenna (shown in Fig.6.18) as reliable. (a) A 2D eH-CARS amplitude scan ($2\mu\text{m}\times 2\mu\text{m}$) measured at the AuNB focus, before and after the correlative measurement, shows that the antenna remained reasonably centered (yellow cross) during the time trace. Rainbow scales from m (black) to M (white). (b) Single particle extinction cross-sections, measured before and after the laser exposure, show that no significant structural changes affected the antenna during the laser exposure. (c) Galvo mirror positions (along x and y directions) recorded during the time traces to visualize possible instabilities affecting the recorded signal. (d) Four BPD currents (i_0, i_1, i_2, i_3) recorded during the time trace measurement were balanced (symmetric around the x-axis). Additionally, the $\bar{i} = \frac{i_\Sigma}{\langle i_\Sigma \rangle}$ used to correct the recorded time trace eH-CARS is shown as well. 178
- A.7 Representative fluctuation correlation plot between (from top to bottom rows) nominal SHG-, TPF-, RED fluorescence and eH-CARS signal (real component (\Re), imaginary component (\Im), amplitude (Abs) and phase (Φ)). Sample: 200nm diameter YG fluorescent PS beads in 50% glycerol/water (v/v) solution (see Chapter 3.2). Time traces of 20s (as indicated) were recorded with 0.1 ms sample period at the antenna's site and downsampled to 10ms. IFD= 3050cm^{-1} . Exciting power at the sample: $P_P=1.4\text{mW}$ and $P_S=2.5\text{mW}$. For the PMTs channels, we reported an indication of the detected bandwidth for clarity. 179
- A.8 Representative fluctuation correlation plot between (from top to bottom rows) nominal SHG-, TPF-, RED fluorescence and eH-CARS signal (real component (\Re), imaginary component (\Im), amplitude (Abs) and phase (Φ)). Sample: 200nm diameter YG fluorescent PS beads in 50% glycerol/water (v/v) solution (see Chapter 3.2). Time traces of 20s (as indicated) were recorded with 0.1ms sample period at the antenna's site and downsampled to 10ms. IFD= 3050cm^{-1} . Exciting power at the sample: $P_P=5\text{mW}$ and $P_S=11.5\text{mW}$. For the PMTs channels, we reported an indication of the detected bandwidth for clarity. 180
- A.9 Four criteria to be checked to consider the correlative time trace recorded (shown in Fig.A.10) at the antenna as reliable. (a) A 2D eH-CARS amplitude scan ($2\mu\text{m}\times 2\mu\text{m}$) measured at the AuNB focus, before and after the correlative measurement, shows that the antenna remained reasonably centered (yellow cross) during the time trace. Rainbow scales from m (black) to M (white). (b) Single particle extinction cross-sections, measured before and after the laser exposure, show that not significant structural changes affected the antenna during the laser exposure. (c) Galvo mirror positions (along x and y directions) recorded during the time traces to visualize possible instabilities affecting the recorded signal. (d) Four BPD currents (i_0, i_1, i_2, i_3) recorded during the time trace measurement were balanced (symmetric around the x-axis). Additionally, the $\bar{i} = \frac{i_\Sigma}{\langle i_\Sigma \rangle}$ used to correct the recorded time trace eH-CARS is shown as well. 181

- A.10 Representative fluctuation correlation plot between (from top to bottom rows) nominal SHG-, TPF-, RED fluorescence and eH-CARS signal (real component (\Re), imaginary component (\Im), amplitude (Abs) and phase (Φ)). Sample: AuNBs sample with 200nm diameter YG fluorescent PS bead in fully DI water (see Chapter 3.2). Time traces of 20s (as indicated) were recorded with 0.1ms sample period at the antenna's site and downsampled to 10ms. IFD=2904cm⁻¹. Exciting power at the sample: P_P=0.68mW and P_S=1.56mW. For the PMTs channels, we reported an indication of the detected bandwidth for clarity. 182
- A.11 Four criteria to be checked to consider the correlative time trace recorded at the antenna (shown in Fig.A.12) as reliable. (a) A 2D eH-CARS amplitude scan (2μm×2μm) measured at the AuNB focus, before and after the correlative measurement, shows that the antenna remained reasonably centered (yellow cross) during the time trace. Rainbow scales from m (black) to M (white). (b) Single particle extinction cross-sections, measured before and after the laser exposure, show that not significant structural changes affected the antenna during the laser exposure. (c) Galvo mirror positions (along x and y directions) recorded during the time traces to visualize possible instabilities affecting the recorded signal. (d) Four BPD currents (i₀, i₁, i₂, i₃) recorded during the time trace measurement were balanced (symmetric around the x-axis). Additionally, the $\bar{i} = \frac{i_{\Sigma}}{\langle i_{\Sigma} \rangle}$ used to correct the recorded time trace eH-CARS is shown as well. 183
- A.12 Representative fluctuation correlation plot between (from top to bottom rows) nominal SHG-, TPF-, RED fluorescence and eH-CARS signal (real component (\Re), imaginary component (\Im), amplitude (Abs) and phase (Φ)). Sample: AuNBs sample with 200nm diameter YG fluorescent PS bead in fully DI water (see Chapter 3.2). Time traces of 20s (as indicated) were recorded with 0.1ms sample period at the antenna's site and downsampled to 10ms. IFD=3050cm⁻¹. Exciting power at the sample: P_P=0.68mW and P_S=1.56mW. For the PMTs channels, we reported an indication of the detected bandwidth for clarity. 184
- A.13 Four criteria to be checked to consider the correlative time trace recorded (shown in Fig.6.19) at the antenna as reliable. (a) A 2D eH-CARS amplitude scan (2μm×2μm) measured at the AuNB focus, before and after the correlative measurement, shows that the antenna remained reasonably centered (yellow cross) during the time trace. Rainbow scales from m (black) to M (white). (b) Single particle extinction cross-sections, measured before and after the laser exposure, show that no significant structural changes affected the antenna during the laser exposure. (c) Galvo mirror positions (along x and y directions) were recorded during the time traces to visualize possible instabilities affecting the recorded signal. (d) Four BPD currents (i₀, i₁, i₂, i₃) recorded during the time trace measurement were balanced (symmetric around the x-axis). Additionally, the $\bar{i} = \frac{i_{\Sigma}}{\langle i_{\Sigma} \rangle}$ used to correct the recorded time trace eH-CARS is shown as well. 185

- A.14 Four criteria to be checked to consider the correlative time trace recorded (shown in Fig.6.20) at the antenna as reliable. (a) A 2D eH-CARS amplitude scan ($2\mu\text{m}\times 2\mu\text{m}$) measured at the AuNB focus, before and after the correlative measurement, shows that the antenna remained reasonably centered (yellow cross) during the time trace. Rainbow scales from m (black) to M (white). (b) Single particle extinction cross-sections, measured before and after the laser exposure, show that no significant structural changes affected the antenna during the laser exposure. (c) Galvo mirror positions (along x and y directions) were recorded during the time traces to visualize possible instabilities affecting the recorded signal. (d) Four BPD currents (i_0, i_1, i_2, i_3) recorded during the time trace measurement were balanced (symmetric around the x-axis). Additionally, the $\bar{i} = \frac{i_\Sigma}{\langle i_\Sigma \rangle}$ used to correct the recorded time trace eH-CARS is shown as well. 186
- A.15 Four criteria to be checked to consider the correlative time trace recorded (shown in Fig.6.21) at the antenna as reliable. (a) A 2D eH-CARS amplitude scan ($2\mu\text{m}\times 2\mu\text{m}$) measured at the AuNB focus, before and after the correlative measurement, shows that the antenna remained reasonably centered (yellow cross) during the time trace. Rainbow scales from m (black) to M (white). (b) Single particle extinction cross-sections, measured before and after the laser exposure, show that no significant structural changes affected the antenna during the laser exposure. (c) Galvo mirror positions (along x and y directions) were recorded during the time traces to visualize possible instabilities affecting the recorded signal. (d) Four BPD currents (i_0, i_1, i_2, i_3) recorded during the time trace measurement were balanced (symmetric around the x-axis). Additionally, the $\bar{i} = \frac{i_\Sigma}{\langle i_\Sigma \rangle}$ used to correct the recorded time trace eH-CARS is shown as well. 187

List of Tables

3.1	Estimated diffusion times of 100 nm and 200 nm diameter polystyrene (PS) beads passing through the focal volume ($V_f \sim 0.5 \mu\text{m}^3$) and through the volume probed by the antennas ($V_{\text{NB}} \sim 50 \text{nm}^3$), in case of fully DI water solution (0%) and 50% glycerol/water solution	34
4.1	Parameter used in Eq.4.1.14 within this work.	76
6.1	IFD (cm^{-1}), pump wavelength (nm), IFD _c (cm^{-1}), Stokes wavelength (nm), CARS wavelength (nm) used within this Chapter.	139

Abstract

Coherent anti-Stokes Raman scattering (CARS) micro-spectroscopy is a promising technology for label-free chemical sensing and imaging at high-speed. It has been extensively developed over the last two decades, allowing for mapping of endogenous biomolecules in living systems, from single cells to large area tissues, without the drawback of staining artifacts and photobleaching associated with fluorescence microscopy, at speeds up to video rate. To date, we are still missing a label-free non-invasive detection method able to achieve single-molecule detection and measure nanoscale regions of interest such as lipid nanodomains in living cells with high spatio-temporal resolution. Despite all the advantages, with a CARS-based technique is still not possible to achieve single-molecule detection. The strong enhancement of the light field occurring at the nanoscale region near the surface of a metallic nanostructure has helped to overcome this limitation. In plasmon-enhanced CARS, the generated anti-Stokes signal is the result of the locally enhanced pump and Stokes laser fields with an additional amplification of the generated anti-Stokes field by the plasmonic nanostructure.

In this work, we first show proof-of-principle experiments to chemically detect lipid molecules label-free using an epi heterodyne detected CARS (eH-CARS) technique and exploiting the local field enhancement (LFE) occurring in the nanoscale region near a single plasmonic silica-coated gold nanorod (SiAuNR). Such technique is thus named LFE eH-CARS. For optimum LFE effect, the localized surface plasmon resonance (LSPR) of the selected SiAuNRs was chosen to coincide with the CARS wavelength of the CH stretch vibration in lipid ($\sim 2900\text{cm}^{-1}$), i.e. 660 nm in our set-up. For this purpose, the extinction cross-section spectrum of each individual SiAuNR was measured. We additionally developed an optical sizing tool able to estimate parameters describing the geometry of SiAuNRs via comparison of quantitative experimental and numerical results. Furthermore, we developed an elaborate simulation model, reproducing the experimental setup, both from the point of view of the excitation and detection, to gain a better understanding of the LFE provided by a gold nanorod (NR) in CARS. Such a model has been a significant new development, to date not shown in the literature. The established technique was then used to perform correlative fluorescence and LFE eH-CARS sensing measurements at single gold nanobowtie (AuNB) antennas, by exploiting fluorescently labeled PS beads moving in and out of the antenna LFE volume. Moving forward, we interrogated the plasma membrane of HEK293 living cells over-expressing a GFP-tagged P2X7, which is a membrane receptor thought to partition in lipid nanodomains, rich in cholesterol and saturated lipids. The AuNBs were entirely designed and fabricated within the project and protocols to attach the HEK293 cells on top of the nanoantennas and keep them alive sufficiently long to perform the sensing measurements were successfully established. While eH-CARS from the PS beads in the absence

of the nano-antenna was not sufficiently strong to be detected and correlated with two photon fluorescence (TPF) simultaneously detected in our set-up, we found evidence of LFE eH-CARS correlatively with TPF fluorescence when measuring onto the antennas. Notably, we detected LFE eH-CARS correlatively with TPF fluorescence also when measuring on living cells, suggesting the presence of transient lipid nanodomains/raft, exhibiting CARS signals, close to a GFP-tagged P2X7. Further studies are needed to draw robust conclusions. The proposed LFE eH-CARS correlatively with TPF technique is biocompatible and serves as the foundation to investigate the dynamics of individual proteins within living cell membranes and their association with lipid nanodomains, with chemical specificity and sensitivity at the nanoscale.

Acknowledgements

I would first like to express my sincere gratitude to my two supervisors, Prof. Paola Borri and Prof. Wolfgang Langbein, for their invaluable guidance, unwavering support, and immense expertise throughout my PhD project. They have been instrumental in shaping my understanding, providing constructive feedback, and fostering an environment conducive to intellectual growth. Thank you for being exemplary mentors, for playing a significant role in my academic and professional journey, and for letting me be part of the European Training Network MUSIQ, funded by the European Union's Horizon 2020 research and innovation program under the Marie Skłodowska-Curie grant agreement No 812992.

I am also indebted to many members of our Quantum Optoelectronics & Biophotonics group, particularly to all those in the School of Biosciences where I have been based over the years of my PhD. Particularly, I would like to thank Dr. Iestyn Pope, Dr. Francesco Masia, Dr. Lukas Payne, Dr. David Regan, and Dr. Sion Harlow for the training they have provided in developing the sample preparation procedures and in utilizing microscopy techniques, as well as the various analysis software. I extend my sincere thanks to Dr. Attilio Zilli for his exceptional support in introducing me to the realm of numerical simulation. I am truly grateful for his help, which has paved the way for my growth in this area. I would like to extend a heartfelt thank you to Ediz and Marika, with whom I collaborated in the final part of my PhD journey. Working with them was not only professionally enriching but also personally fulfilling.

Thanks to my Cardiff family. The warmth, friendship, and support I received from this special group of individuals went far beyond the confines of work. To each member of my Cardiff family, you made Cardiff not just a place of study and research but a home away from home. Your encouragement during challenging times and shared joys during the successes have made this experience unforgettable. In particular, I want to express my gratitude to Carmen, Elena, Nicole, Rhod, Furqan, Sam, and Marialuce. Your friendship has been really a source of strength. Thank you, Cardiff family, for turning this academic journey into a shared adventure filled with laughter, support, and lasting connections.

I want to express my deepest gratitude to my family. They believed in me since the very first day and consistently followed my adventure, even from another country. Your unwavering support and encouragement have been a guiding light throughout my journey. To my boyfriend, Luca, thank you for being my partner in every sense, your support and shared dreams have made every step worthwhile. We made it through these three-year distance relationship, and this was because we always made sure that the distance was just a circumstance and not a separation. Your unconditional love is a constant source of comfort. To our kitty Basil, thanks for your presence that has added warmth and joy to my writing days.

Chapter 1

Introduction

The formidable potential of optical microscopy as a tool for investigating biological samples, with a specific focus on cells and their intricate components, has long been a driving force for scientific inquiry and discovery. Optical microscopy is extensively used to study the morphology, structure, and function of individual cells. Additionally, when used for live cell imaging, it allows researchers to monitor and record dynamic processes such as cell division, migration, and response to stimuli (Ref.[3]). Brightfield microscopy (Ref.[4]) is one of the oldest and most widely used techniques among researchers and medical experts. Briefly, a homogeneous and sufficiently intense illumination is achieved by using a condenser lens, which focuses the light onto the sample. This light subsequently passes through the sample and is ultimately collected by the compound lens system of the microscope. Variations in the transparency of the sample create contrast in the resulting image. Among the various brightfield techniques, differential interference contrast (DIC) (Ref.[5]) microscopy is a contrast-enhancing technique, used to visualize transparent and unstained specimens. In such a technique, the variations in optical path length are detected and it is possible to effectively create a 3D-like appearance of the sample. The bright field techniques are diffraction-limited, which means the diffraction of light inherently limits them. This limitation restricts the resolution to a few hundred nanometers, preventing the visualization of finer structural details and molecular-level features. In fact, as stated by Abbe's law, the resolution limit (d), i.e. the smallest resolvable distance between two points in optical microscopy is determined by the wavelength of light used (λ) and the numerical aperture (NA) of the optical system, as $d = \frac{\lambda}{2NA}$. The spatial resolution is also closely related to the point spread function (PSF) associated with the optical system. The PSF is a fundamental concept in imaging which describes how a point source is spread out in an image. It is a mathematical representation of the response of an imaging system to a point source or point object. A smaller and more compact PSF generally leads to higher spatial resolution because it means that the system can better distinguish between closely spaced objects. Moreover, bright field techniques do not provide chemical specificity. As a result, these techniques cannot differentiate between different types of molecules or specific chemical components within a sample. For researchers interested in molecular or chemical information, auxiliary techniques, such as fluorescence microscopy or vibrational microscopy, are often necessary.

Fluorescence microscopy, widely employed by biologists, is renowned for its sensitivity achieved through the utilization of fluorescence markers. These markers can be either endogenous (e.g., fluorescent proteins) (Ref.[6]) or exogenous (e.g., dyes or

semiconductor quantum dots) (Ref.[7]) into cells or tissues. Fluorescence nanoscopy (Ref.[8]) has opened up the exciting possibility of breaking the diffraction limit, enabling researchers to image and explore nanoscale structures and phenomena with unprecedented precision. For example, in the techniques that belong to the group of reversible saturable optical fluorescence transitions (RESOLFT) (Ref.[9], Ref.[10]), a subdiffraction resolution is achieved by temporarily preventing the fluorescence of fluorophores located outside the central region of the focal spot. By using specific techniques and laser patterns, such as reversible transitions between different states of the fluorophores, the emitting volume is confined to a region much smaller than the diffraction-limited spot. This focused spot, smaller than the diffraction limit, is scanned across the specimen to create a super-resolved image. The specific terms used to describe these modalities, such as stimulated emission depletion (STED) (Ref.[11]) and ground state depletion (GSD)(Ref.[12]), depend on the particular molecular transition utilized to induce the transition of fluorophores into a non-emissive or "dark" state. A different approach is instead used in PALM (photoactivated localization microscopy) and STORM (stochastic optical reconstruction microscopy), where the key principle is to use photoactivatable or photoswitchable fluorophores, controlling their activation and deactivation, to determine the center position of the PSF with higher precision than its width. In PALM (Ref.[13]), specific fluorescent molecules are switched on and off sequentially, and their precise positions are determined through mathematical analysis. This process is repeated for a large number of molecules, ultimately creating a super-resolved image. In STORM (Ref.[14]), the stochastic blinking behavior of certain fluorophores is exploited. The blinking is inherently random, and by capturing and analyzing the positions of blinking fluorophores over time, a super-resolved image is constructed. However, fluorescence microscopy techniques exhibit several drawbacks. To begin with, relying solely on fluorescence restricts the ability to distinguish a limited number of structures due to the broad emission bandwidths of fluorescent proteins, which often overlap. Furthermore, fluorophores can lose their fluorescence capability as they may undergo photobleaching. In fact, upon transition from an excited singlet state to the excited triplet state, which is characterized by a relatively long lifetime, fluorophores may interact with other molecules ending up with irreversible covalent modifications. Additionally, fluorescent molecules tend to generate reactive chemical species when exposed to light, exacerbating the phototoxic effects on biological samples. Finally, the introduction of fluorescent markers can perturb the specific structures that have been labeled for fluorescence.

Vibrational microscopy (Ref.[15]) is a technique that combines microscopy with vibrational spectroscopy to study the chemical composition and molecular structure of materials on a microscopic scale. It is a non-invasive label-free technique, which avoids sample treatments and artifacts associated with staining protocols and is not limited by fluorophore photo-bleaching and related cytotoxicity. There are two primary types of vibrational microscopy: mid-infrared (MIR) microscopy and Raman microscopy. In MIR microscopy (Ref.[16]) a mid-infrared light source ($\lambda \sim 3 \mu\text{m}$ - $10 \mu\text{m}$) is used to illuminate and resonantly probe the vibrational modes of the sample, and the transmitted or reflected light is analyzed. The main limitation in the use of the MIR technique is related to the strong absorption of water in the mid-infrared range. This water absorption can obscure the signals from the biological molecules of interest. Biological samples often contain a significant amount of water, and this can complicate the interpretation of IR spectra. Additionally, the spatial

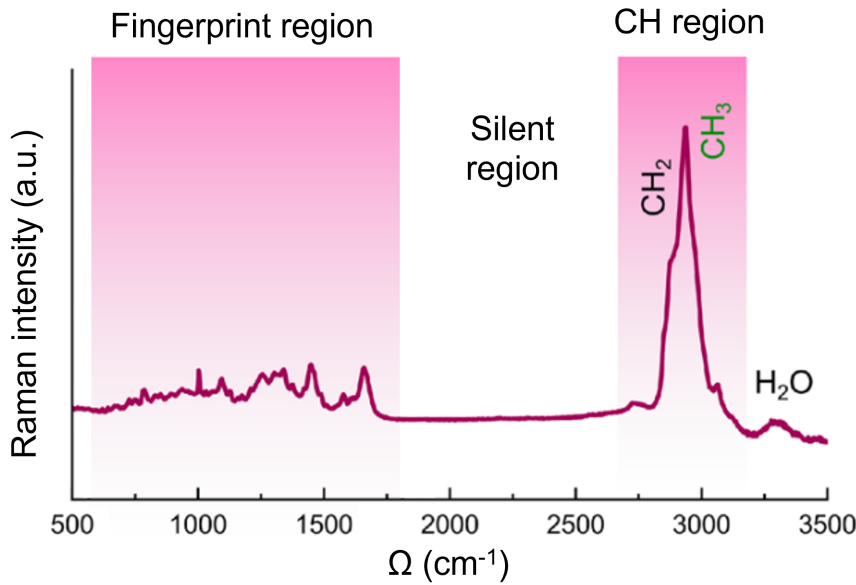


Figure 1.1: Representative biological Raman spectrum adapted from Ref.[21].

resolution is typically limited by the longer wavelength employed in MIR, although lately it has been developed a technique called optical photothermal IR microscopy (see Ref.[17]) where visible probes are used to overcome the limitation of IR spatial resolution.

Raman-based techniques are often preferred for investigating biological samples, such as tissues and cells (Ref.[18], Ref.[19]) when water compatibility and the need for high spatial resolution are essential. The simplest and first exploited technique belonging to this family is the spontaneous Raman (SR) (Ref.[20]), where a monochromatic light source, typically from a laser, interacts with a sample, and some of the incident photons undergo inelastic scattering. In this process, the energy of the scattered light is up- or down-shifted depending on the vibrational and rotational energies of the molecules in the sample. This shift, known as the Raman shift, is directly related to the molecular vibrations within the material. Figure 1.1, shows a representative biological Raman spectrum. The spectrum may be divided into three main spectral windows:

- The spectral window from 400cm^{-1} to 1800cm^{-1} is named fingerprint region. Here, numerous small and closely spaced vibrational bands can be found, which correspond to low-energy bending and twisting vibrations that can take place in lipids, proteins, and nucleic acids.
- The spectral window from 1800cm^{-1} to 2700cm^{-1} is known as the Raman-biological silent region, because typically evident peaks are not present. It can be exploited to introduce Raman-tag molecules in a given sample, which provide characteristic peaks within this spectral window, e.g. deuterated molecules with C-D stretch bonds vibrating around 2200cm^{-1} (Ref.[22]).
- Finally, the spectral window from 2700cm^{-1} to 3100cm^{-1} displays broad peaks associated with the CH, CH₂, and CH₃ symmetric and antisymmetric stretching through which one can discern lipids, proteins, and DNA.

The main drawback of the spontaneous Raman technique is its low scattering cross-section, which means that the phenomenon probability is very low and typically requires a long integration time (up to 1s) to acquire a vibrational spectrum from a single spatial position in the sample, with sufficient signal to noise ratio.

The latter drawback of SR is overcome by coherent Raman scattering (CRS) (Ref.[23]). It is a third-order nonlinear optical process which uses the interference between a first short laser pulse, called pump, and a second one, red-shifted, called Stokes, to coherently drive molecular vibrations at the beat frequency difference. In this way, the induced collective molecular oscillations from all bonds of the same type in the focal volume give rise to a constructive interference of the Raman scattered light generated by every single molecule. This process allows a sufficient coherent signal enhancement which enables high acquisition speed and the direct view of real-time movement of living samples on the few second per frame imaging scale. Moreover, CRS techniques, being based on a nonlinear optical process where the signal generation takes place only in the focal volume, exhibit three-dimensional (3D) spatial resolution without the requirement for any physical confocal apertures (Ref.[24]).

A common implementation of CRS is called CARS (Ref.[25], Ref.[26]). In this technique the initial vibrational coherence induced by the interaction between the pump and the Stokes photons with the sample is probed by a further interaction with another pulse, often chosen to coincide with the pump pulse, in a two-beam implementation. The detected frequency is then the up-shifted Raman scattering of the higher excitation frequency (pump). This signal detection is free from excitation background since the CARS optical frequency ω_{CARS} is spectrally well separated from the frequency of the exciting pump and Stokes pulses, being $\omega_{\text{CARS}} = 2\omega_{\text{P}} - \omega_{\text{S}}$. The CARS field can be expressed as (Ref.[23]):

$$E_{\text{CARS}} \propto \chi^{(3)} E_{\text{P}}^2 E_{\text{S}} \quad (1.0.1)$$

where E_{P} and E_{S} are the pump and Stokes fields and $\chi^{(3)}$ is the complex non-linear CRS susceptibility, which is the quantity of interest, being proportional to the local material composition.

The CARS technique's simplest implementation employs narrowband pump and Stokes beams. Despite its image acquisition speed (down to hundreds of nanoseconds or tens of microseconds per pixel) (ref.[27]), it does not offer the same wealth of information provided by SR as it only probes a single vibrational mode at a time. The implementation of broadband CARS (Ref.[28]), either as hyperspectral CARS (Ref.[29]) or as multiplex CARS (Ref.[30]), allows to interrogate multiple vibrational modes in one acquisition. The first is based on the coupling of pump pulses with tunable Stokes pulses, whose frequency detuning sequentially matches the Raman modes of the samples. Instead, the second one relies on the combination of narrowband pump pulses with broadband Stokes, thus interrogating multiple vibrational modes in parallel.

The detection of the CARS intensity is proportional to the modulo square of the $\chi^{(3)}$, which has a vibrationally resonant and non-resonant component. For this reason, the CARS intensity is affected by both the vibrationally resonant and non-resonant parts of the complex non-linear CRS susceptibility, whose interference gives rise to an asymmetric spectral lineshape for a resonant response. The non-resonant part also causes a background, reducing image contrast for microscopy applications (Ref.[31]). Various methods have been developed to suppress the influence of the

non-resonant background in the detected signal. As the non-resonant response is temporally instantaneous, it can be removed by temporal filtering (Ref.[32]). Alternatively, assuming an isotropic non-resonant background, once the exciting pump and Stokes polarization are defined as elliptical and ensuring that the resonant contribution has a cross-polarized intensity, the non-resonant background has a given polarization that can be filtered in the detection (Ref.[33]). Frequency modulation (FM) CARS (Ref.[34]) and dual/differential-CARS (Ref.[35], Ref.[36]) are two other implementations that suppress the non-resonant background while allowing for high-speed acquisition. In FM-CARS, a modulated CARS signal, obtained via the frequency modulation of pump and Stokes beams, is detected using a lock-in amplifier, suppressing the non-resonant background whilst maintaining video rate imaging. In dual/differential CARS, linearly-chirped femtosecond laser pulses are used to excite a pair of CARS vibrations alternatively, within the pulse train sequence. The resulting CARS intensities are detected by a single photomultiplier as sum and difference using phase-sensitive frequency filtering which suppresses the non-resonant CARS background and improves the chemical sensitivity.

The detection of the CARS signal can be performed in the forward or epi-direction. Forward and backward CARS signals can offer complementary insights into a sample (Ref.[31]). In contrast to fluorescence emission and spontaneous Raman scattering, the radiation pattern of CARS relies on both the size and shape of a scatterer (Ref.[37]). When the size of the scatterer is much smaller than the exciting wavelengths the CARS radiation is emitted in the forward and backward directions symmetrically. For an increasing sample size, the CARS radiation is emitted into a small cone propagating in the forward direction. Forward-detected CARS (F-CARS) microscopy is well-suited for imaging objects of a size comparable to or larger than the excitation wavelength. Conversely, when dealing with smaller objects, an epi-detected CARS (e-CARS) microscopy turns out to be a more sensitive approach to image objects with an axial length significantly smaller than the excitation wavelength, such as nanoparticles, or lipid bilayers in a bulk medium (Ref.[38], Ref.[39], Ref.[40], Ref.[41]), being able to exclude the detection of signal coming from the bulk which is propagating in the forward direction.

Most of the CARS implementations detect the field intensity. The implementation of an interferometric detection technique instead allows us to measure directly the amplitude and phase of the CARS field (Ref.[42]) and enables us to suppress any incoherent contribution. The interferometric detection involves the interference between the CARS field from the sample and a local oscillator (i.e. a non-resonant CARS field used as reference). Such interference is then detected by an interferometer. From the total phase difference between the two arms of the interferometer, the phase difference introduced by the sample can be extracted and the real and imaginary component of the CARS field from the sample determined. Another possibility to detect amplitude and phase of the CARS field is via a heterodyne detection scheme (Ref.[43], Ref.[44]). The heterodyne detection also involves the interference of two optical signals, but it combines the signal with a local oscillator characterized by a slightly different frequency. The signal at the frequency difference (beat frequency) can be detected in amplitude and phase by using a dual-channel lock-in amplifier. Initially, the realizations of heterodyne CARS involved a reference beam at the sample overlapped with both pump and Stokes beams, and scanned with them across the sample.

The starting point of this project is the CARS technique implementation called

eH-CARS (Ref.[45], Ref.[46]) which exploit an epi-geometry scheme and a dual-polarisation heterodyne detection via balanced photodiodes detector. Differently from the previous implementations, it exploits an external reference, temporally and spatially overlapped with the epi-CARS signal (see Chapter 3.3.2). The eH-CARS is characterized by several advantages. The epi-detection is mostly sensitive to interface and nano-objects, rejecting forward CARS background from bulk media. A balanced photodiode detection is essential to suppress the classical noise of the reference itself, e.g., due to laser instabilities. Additionally, compared to PMTs typically used, photodiodes have higher quantum efficiencies and do not suffer from amplification excess noise. The choice of reference power can be made without the risk of sample photodamage, as it does not pass through the sample, and such that it is dominant to obtain a shot-noise limited signal using balanced photodiode detection. The dual-polarization detection allows the measurement of both co- and cross-polarization components of the field in one acquisition.

Despite all the advantages, two main limitations affect are still present. First, the coherent signal enhancement is proportional to the number of identical chemical bonds in the focal volume and usually requires at least 10^6 bonds to allow high-speed imaging (Ref.[47]). Second, CARS is still limited in spatial resolution by diffraction.

The strong enhancement of the light field occurring at nanoscale regions near the surface of metallic (hence plasmonic) nanostructures can overcome both of these limitations. Metal nanostructures, upon coherent optical illumination, show localized charge density oscillations consisting of a coherent and collective motion of electrons. The consequent electric field, associated with the charge density oscillations enhances the exciting one. CARS performed in the presence of a plasmonic nanostructure is typically named surface-enhanced CARS (SECARS) in the literature. However, as the enhancement provided by the nanostructure is spatially confined to the nanostructure surface, in a small region whose size is of the same order of magnitude of the nanostructure itself, we prefer later in this thesis calling this effect local field enhancement (LFE) and, accordingly, local field enhanced CARS (LFE CARS).

The possibility of SECARS from molecules located near the surface of a small silver particle was theoretically predicted (Ref.[48]). Then its first observation was actually achieved in 1994 (Ref.[49]), using nanosecond pulses and an ensemble of colloidal plasmonic silver spheres dispersed in a net liquid given by benzene, chlorobenzene, and toluene separately tested. Another pioneering experiment has shown how recorded pyridine Raman spectrum can be enhanced by the addition of silver colloids (Ref.[50]). The SECARS experiments on metallic particle colloids demonstrated how the SECARS signal is affected by several parameters such as the properties of the particle colloids, their concentration, and the exciting laser wavelength. In general, to optimize the SECARS generation a more direct approach is to work with a single plasmonic designed nanostructure. In 2003 the adenine CARS spectrum was measured while enhanced by isolated gold nanoparticles (Ref.[51]) and later tip-enhanced CARS techniques for both spectroscopy and vibrational nanoimaging were accomplished (Ref.[52], Ref.[53]). The latter could successfully visualize the DNA network structure and subcellular organelles. Furthermore, researchers started to exploit the field enhancement occurring at plasmonic nanojunctions, i.e. nanometric size gaps in between plasmonic nanostructures. For example, in 2014, it has been demonstrated the detection of single organic molecules (trans-1,2-bis-(4-pyridil) ethylene) via the SECARS at the gap of a large gold nanoparticle (NP) dimer, encapsulated

in a porous silica shell (Ref.[54]). In the same year, a quadrumer structure formed by gold nanodisks was proposed (Ref.[55]), which minimized losses at the pump frequency and displayed superradiant properties at the anti-Stokes frequency. The spectral contrast in that case was sufficient to discriminate between the spectra of different molecular targets used in the experiments, i.e. paramercaptoaniline (p-MA) and adenine molecules, characterized by clearly distinguishable Raman spectra. The latter experiment also demonstrated how the gold nanostructure itself produced a significant four wave mixing (FWM) background, most of which could be suppressed by a polarization-sensitive detection. Only a few biological applications of SECARS have been shown so far in spite of more than 30 years since the first demonstration. In 2011 (Ref.[56]) Immuno-SECARS microscopy was demonstrated as the first application of the SECARS detection contrast for bio-imaging onto prostate tissue biopsies labeled with p63-antibody-conjugated plasmonic NPs.

The goal of this PhD project is to develop a method able to measure the chemical composition and heterogeneity in living cell membranes at the nanoscale with high speed. We exploited the combination of the mentioned eH-CARS with the LFE of the CARS field, from molecules placed in close proximity to *single* plasmonic nanoparticles. The LFE obtained for each field involved in the process mainly depends on nanostructures' composition, shape, and size. Such characteristics determine the LSPR, i.e. the frequency at which the nanostructure has to be excited to have the higher achievable enhancement and the strength of such plasmon. The dielectric environment also affects the wavelength position of the LSPR. Additionally, the incident fields, in particular its frequency and its polarization strongly influence the LFE. Depending on the shape of the nanostructure, it is possible to have a certain direction that ensures the optimal coupling between the exciting field and the excited plasmon.

In principle, both pump, Stokes, and the CARS field generated by the molecule resonantly excited can take advantage of the enhancement provided by the plasmonic nanostructure. We actually choose to work with nanostructure such that the associated LSPR involved in the process turns out to be as much as possible close to the CARS wavelength, to optimize the enhancement of such field while minimizing the enhancement of pump and Stokes. This choice was made in view of the future application in living cell membranes. In fact, the enhancement of the pump and Stokes corresponds to an amplification of these beams that could lead to an overheating of the sample and of the nanoparticles themselves, causing damage. Within this project particular attention was given to the enhancement and detection of CARS signal arising from the excitation of lipid molecules.

In order to establish a proof of principle for the LFE eH-CARS technique, we initially examined samples featuring various sizes of SiAuNR surrounded by a bulk medium with a well-defined Raman spectrum, specifically silicone oil. We utilized gold as the material for these nanostructures due to its established biocompatibility, as evidenced in previous research (Ref.[57], Ref.[58]). Additionally, a silica coating was inserted to prevent the gold nanorods from reshaping upon laser excitation, as this is a well-known issue associated with these nanoparticles (Ref.[59]). We opted for the nanorod structure as it exhibits a split in the localized surface plasmon band into two distinct bands: the longitudinal band (occurring at longer wavelengths) and the transversal band (occurring at shorter wavelengths). These bands correspond to the oscillation of free electrons along and across the main (longer) axis of the NR. The choice of rod size and aspect ratio plays a crucial role in tuning the position of

the longitudinal plasmon bands in terms of wavelength. We selected aspect ratios so that the longitudinal LSPR coincides with the wavelength of the CARS signal associated with lipids.

As colloidal synthesis typically generates a variety of sizes and shapes, we investigated the optical properties of these SiAuNRs via single-particle optical extinction microscopy measurements (see Chapter 4.1). Furthermore, we developed an *optical sizing* tool able to quantify the rod shape and size by comparing the measured extinction cross-sections with simulations. The latter were obtained via an elaborate model developed with the commercial software COMSOL Multiphysics (see Chapter 3.4), reproducing the experimental measurements. In Chapter 5, a detailed characterization of the LFE eH-CARS technique with SiAuNRs, both experimentally and via simulations was conducted to determine the enhancement provided by the NRs in the far field (FF). We compared the enhancement obtained with different NR sizes, in different exciting polarization conditions. A study to test the SiAuNRs resistance against reshaping upon laser exposure, was also carried out. Additionally, exploiting the COMSOL Multiphysics mimicking the LFE eH-CARS, we investigated the different contributions of the overall detected CARS signal. After the proof-of-principle demonstration, we moved forward employing AuNB. The idea is to use such nanostructures as antennas to detect the presence of sub-micron objects moving in their proximity. Conversely, to the SiAuNRs, which were provided by a manufacturer, the design and fabrication of the AuNBs was part of the project, and it was made in collaboration with the Single Molecule Biophotonics group, based at The Institute of Photonic Science (ICFO, Barcelona, Spain), led by Prof. Dr. Maria Garcia-Parajo. The detailed design development was guided by the outcomes of the extinction spectrum related to structures with different geometrical properties (see Chapter 4.2). As shown in Chapter 6, the designed AuNBs were then employed in correlative fluorescence and LFE eH-CARS sensing measurements, performed by exploiting fluorescently-labeled polystyrene beads, as proof of principle, and successively preliminary measurements in living cells.

Chapter 2

Background Theory

2.1 Principle of non-linear optics

Nonlinear optics is the branch of physics that deals with the study of phenomena occurring when the interaction between light and a material changes the optical properties of the latter, in such a way that its response is not proportional to the incident light's intensity (Ref.[60]). Typically, a nonlinear response is observed for very high light intensities, such as the ones provided by lasers ($\sim 10^{16}\text{W}/\text{cm}^2$, Ref.[61]). As the linear optical process, the nonlinear ones can be understood considering the polarization (or dipole moment per unit volume), induced by an applied electric field in a material. The induced polarization is mainly related to the response of the material atom's outer electrons. In fact, these electrons are not as massive as the atomic nuclei and not as tightly bound as the inner-core electrons, so when an external oscillating electric field is applied to the material, they start to oscillate around their equilibrium position. In the case of a weak applied electric field $\mathbf{E}(t)$ (i.e. in linear optics regime), the polarization $\mathbf{P}(t)$ is linearly dependent on the field strength and is typically expressed as:

$$\mathbf{P}(t) = \epsilon_0 \chi^{(1)} \mathbf{E}(t) \quad (2.1.1)$$

where $\chi^{(1)}$ is the material linear susceptibility and ϵ_0 is the free space permittivity. When the oscillation becomes larger as a consequence of a more intense applied electric field, $\mathbf{P}(t)$ becomes non-linearly dependent on the field strength and can be expanded with a power series in the field strength, i.e.:

$$\mathbf{P}(t) = \epsilon_0 \left[\chi^{(1)} \mathbf{E}(t) + \chi^{(2)} \mathbf{E}^2(t) + \chi^{(3)} \mathbf{E}^3(t) + \dots \right] = \mathbf{P}^{(1)}(t) + \mathbf{P}^{(2)}(t) + \mathbf{P}^{(3)}(t) + \dots \quad (2.1.2)$$

where $\chi^{(2)}$ and $\chi^{(3)}$ are the second- and third-order nonlinear susceptibilities, respectively, and thus $\mathbf{P}^{(1)}$, $\mathbf{P}^{(2)}$, and $\mathbf{P}^{(3)}$ are the first-, second-, and third-order induced polarizabilities. The different order susceptibilities of a material describe the material's response to an applied field. In general, they are tensors, not simple scalar quantities. When the applied field is related to ultrashort pulses, provided by a laser source, the nonlinear terms of the series become significant. Second-order nonlinear optical interactions are limited to noncentrosymmetric crystals. In materials with inversion symmetry, the second-order nonlinear susceptibility $\chi^{(2)}$ vanishes, thereby preventing the occurrence of second-order nonlinear optical interactions. Conversely, third-order nonlinear optical interactions, described by a $\chi^{(3)}$ susceptibility, can take place in both centrosymmetric and noncentrosymmetric media.

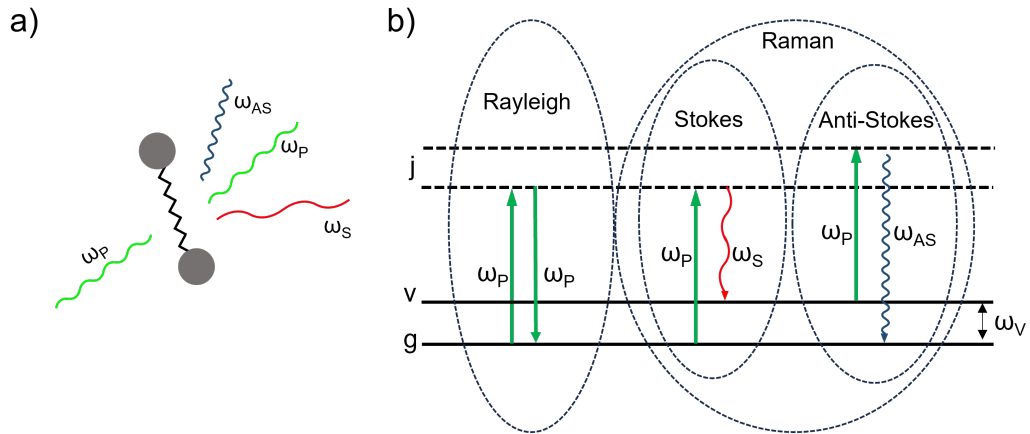


Figure 2.1: Schematic of spontaneous Raman scattering. (a) Generic molecule which scatters an incoming light, at ω_P , into Rayleigh (ω_P), Stokes ($\omega_S = \omega_P - \omega_V$) and anti-Stokes ($\omega_{AS} = \omega_P + \omega_V$) components. (b) Energy diagram for Stokes Raman scattering and anti-Stokes Raman scattering. The vibrational state (solid line) are labeled with g and v , while the virtual state (dashed line) is labeled j . The incoming light is represented by solid arrows, while the wiggled ones represent the emitted radiation.

2.1.1 Coherent Raman scattering (CRS)

In 1928, Sir Raman was the first to observe the so-called spontaneous Raman scattering phenomenon (Ref.[62]). When light interacts with molecules, the incident light is either absorbed or scattered. Raman observed that when a monochromatic light of frequency ω_P impinges on molecules, the scattered light contains an array of colors. The majority of light is scattered elastically, thus has the same frequency as the incident light and is referred to as Rayleigh scattering contribution. The additional, and weaker contributions, are frequency shifted at $\omega_P \pm \omega_V$ and are called Raman scattering components. More precisely, the red-shifted frequency is called Stokes component and the blue-shifted frequency is called the anti-Stokes component. ω_V corresponds to a specific characteristic molecular vibrational mode, i.e. to a specific chemical bond and symmetry of the probed molecules. In general, a molecule has several vibrational frequencies, so that its spontaneous Raman spectrum is characterized by discrete bands. The spontaneous Raman spectrum represents the unique combination of chemical bonds that make the molecule different from others, thus ensuring the univocal identification of the molecule itself. For this reason, spontaneous Raman provides a way of identifying selectively many types of biomolecules found in human tissues and cells (Ref.[18],Ref.[19]). Figure 2.1 gives a schematic representation of the Raman scattering phenomenon (a) together with the related energy diagrams (b) for both Rayleigh, Stokes and anti-Stokes contribution. The spontaneous Raman scattering process is typically rather weak, which means that the number of scattered photons due to the spontaneous Raman inelastic scattering is very little. The consequent very low scattering cross-section ($\sim 10^{-29} \text{cm}^2$, Ref.[63]) severely complicates many applications, including the measurements on diluted species and the vibrational imaging of biological samples, as long integration times (from 100ms to 1s per pixel) are required in order to reach a sufficient signal-to-noise ratio (S/N). The limitation of the spontaneous Raman scattering can be overcome by moving to the CRS techniques.

CRS is a class of third-order nonlinear optical processes. In this kind of process, the simultaneous interaction of three input fields in a material led to the generation of a fourth new field by means of $\chi^{(3)}$ of the material itself. The $\chi^{(3)}$ material acts as a frequency mixer, which allows energy exchange between the four fields, with an exchange rate and spectral behavior that reflects electronic, magnetic, and vibrational features typical of the material under study.

The first verification of CRS, which was possible after the first working laser demonstration (Ref.[?]) was in the form of stimulated Raman scattering (SRS) in 1962 (Ref.[64]) when a research group, lead by Woodbury, found out that the spectrum output of their Ruby laser was showing an extra line whose energy was depending on the specific liquid inserted in a cell working as a Kerr shutter in the Ruby laser cavity to achieve pulsed operation regime. By this first demonstration, the SRS phenomenon was explained theoretically both in terms of classical waves (Ref.[65]) and of quantized fields (Ref.[66]). Briefly, the fundamental of the laser exciting the liquid inside the cell induces a red-shifted emission throught spontaneous Raman, and some of this new generated light returns to the medium, after a roundtrip in the cavity, to stimulate the generation of new Stokes photons. Later, in 1965, the first demonstration of coherent anti-Stokes Raman scattering radiation generation was reported (Ref.[67]) by performing an experiment, outside a laser cavity and with different crystals and liquids and sending onto them two coherent light beams.

The most used CRS layout involves the combination of two input light pulses called pump, at ω_P , and Stokes, at ω_S , with $\omega_P > \omega_S$, to set up a collective oscillation, at $\Omega = \omega_P - \omega_S$, within an ensemble of molecules inside the laser focus. In fact, the two input fields give rise to an effective force acting on the molecular nuclei that as a consequence are driven to vibrate. In this way, all identical molecules in the focal volume are driven coherently and vibrate in sync. Then the third input field acts as a probe for Raman scattering, generating Stokes and anti-Stokes Raman scattering sidebands. The coherent superposition of the field scattered into these sidebands forms the basis of the coherent Raman signal.

An intuitive picture of the CRS process is given by its classical description. This model derives the induced material polarization when two external fields are applied. In the adiabatic approximation, while nuclei move, electrons move much faster (due to their lighter mass) so that they can adjust their molecular orbitals which can be described as parametric functions of the nuclei positions considered as fixed on the time scale of the electron motion. In turn, the nuclear motion can be described as decoupled from the electronic one, where however the electronic energy contributes to an effective nuclear potential energy. The response of the molecule to an incident light field is described by the polarizability α . This polarizability is perturbed by the presence of nuclear vibration and can be expressed in terms of the nuclear displacement coordinate Q , expanding it in a Taylor series:

$$\alpha(t) = \alpha_0 + \left(\frac{\partial \alpha}{\partial Q} \right)_0 Q(t) + \dots \quad (2.1.3)$$

where α_0 is the constant polarizability obtained in absence of nuclei modes and $\frac{\partial \alpha}{\partial Q}$ represents the coupling strength between the nuclear and electronic coordinates (Ref.[68]). Considering two optical fields, indicated as pump (P) and Stokes (S) and modeled as plane waves, i.e.

$$E_P(t) = A_P(t)e^{-i\omega_P t} + cc \quad (2.1.4)$$

$$E_S(t) = A_S(t)e^{-i\omega_S t} + cc, \quad (2.1.5)$$

when they impinge on a molecule, the nuclear mode will experience a force $F(t)$. This force can be computed considering that the potential energy of an induced dipole moment in an external field E is $-\frac{1}{2}\alpha E^2$. The derivative of the energy with respect to the nuclear coordinate defines a force $F = -\frac{1}{2}\frac{\partial\alpha}{\partial Q}E^2$. In CRS the driving force originates from the interference between pump and Stokes fields, in other words E^2 is given by the interference term between E_{pump} and E_{stokes} (namely $E_P E_S^*$ and CC) and oscillates at $\omega_P - \omega_S$. The time-dependent nuclear displacement $Q(t)$ can be described as a damped harmonic oscillator (Ref.[69]). Hence, $Q(t)$ can be obtained from the solution of the equation:

$$\frac{d^2Q(t)}{dt^2} + 2\gamma\frac{dQ(t)}{dt} + \omega_V^2 Q(t) = \frac{F(t)}{m} \quad (2.1.6)$$

where γ is the damping constant, m is the nuclear oscillator reduced mass and ω_V is the harmonic oscillator resonance frequency. A solution to Eq.2.1.6 can be found by adopting the trial solution of the form

$$Q(t) = Q(\Omega)e^{-i\omega t} + cc, \quad (2.1.7)$$

that lead to the following equation for the vibration amplitude (Ref.[70]):

$$Q(\omega_v) = \frac{1}{m}\left(\frac{\partial\alpha}{\partial Q}\right)_0\left(\frac{A_1 A_2^*}{\omega_V^2 - \Omega^2 - 2i\Omega\gamma}\right) \quad (2.1.8)$$

Clearly from Eq.2.1.8, the nuclear mode is efficiently driven when the difference frequency between the Pump and the Stokes fields, Ω , approaches the resonance frequency ω_V .

When in the interaction volume of $E_P(t)$ and $E_S(t)$ there is an ensemble of N equal molecules, the total induced polarization is given by:

$$P(t) = N\alpha(t)\{E_P(t) + E_S(t)\} = N\left[\alpha_0 + \left(\frac{\partial\alpha}{\partial Q}\right)_0 Q(t)\right]\{E_P(t) + E_S(t)\} \quad (2.1.9)$$

The terms proportional to α_0 correspond to the linear polarization of the material, while the terms proportional to $\left(\frac{\partial\alpha}{\partial Q}\right)_0$ describe the contribution to the third-order polarization due to the driven Raman mode. Inserting in Eq.2.1.9 the general form of the fields (Eqs.2.1.4) and the general solution of Q (Eq.2.1.7), the nonlinear polarization results have four different contributions (Ref.[71]):

$$P_{NL}^{(3)}(t) = P_{CSRS}e^{-i(\omega_S - \Omega)t} + P_{SRG}e^{-i\omega_S t} + P_{SRL}e^{-i\omega_P t} + P_{CARS}e^{-i(\omega_P + \Omega)t}. \quad (2.1.10)$$

Eq.2.1.10 expresses that four possible CRS interaction schemes that take place (Ref.[72]), each one generating a new field which is the result of a four-wave mixing process:

- the CARS field at frequency $\omega_{CARS} = \omega_P + (\omega_P - \omega_S)$,
- the coherent Stokes Raman scattering (CSRS) field at frequency $\omega_{CSRS} = \omega_S - (\omega_P - \omega_S)$,
- the stimulated Raman gain (SRG) at frequency ω_S ,
- the stimulated Raman loss (SRL) at frequency ω_P .

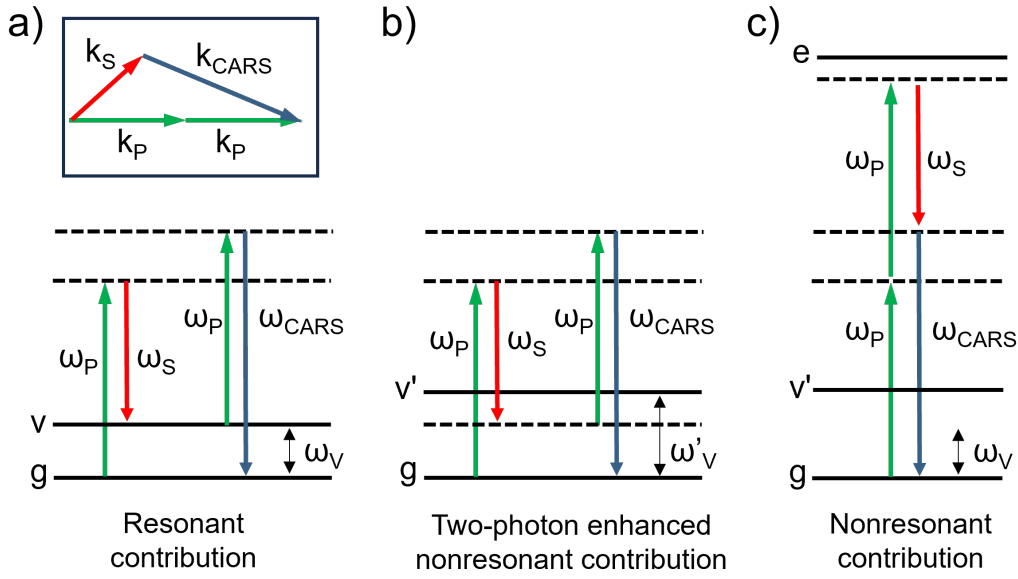


Figure 2.2: (a) Energy diagram showing the resonant contribution to the CARS signal. Insert: schematic diagram for phase matching in CARS. (b) Energy diagram showing the non-resonant contribution to the CARS signal coming from FWM processes involving the electrons of other molecules different from the target ones. (c) Energy diagram showing an electronic contribution enhanced by a two-photon resonance of the pump beam associated with an excited electronic state. The ground state is labeled with g , while the vibrational states are labeled with v (v') and the electronically excited state with e . Solid lines indicate the real state levels, while dashed lines represent the virtual states.

The SRG and SRL processes are part of the SRS interaction. Combining Eq.2.1.8 and Eq.2.1.9 with the general form of polarization, $P(t) = P(\omega)e^{-i\omega t}$, it is possible to find the amplitude of the different polarization components. Focusing for example on the component at ω_{CARS} :

$$P_{\text{CARS}} = \frac{N}{m} \left(\frac{\partial \alpha}{\partial Q} \right)_0^2 \left(\frac{A_P^2 A_S^*}{\omega_V^2 - \Omega^2 - 2i\Omega\gamma} \right) = 6\epsilon_0 \chi^{(3)}(\Omega) A_P^2 A_S^* \quad (2.1.11)$$

where the non linear susceptibility $\chi^{(3)}$ for Raman interaction, is defined as (Ref.[23]):

$$\chi^{(3)}(\Omega) = \frac{N}{6\epsilon_0 m} \left(\frac{\partial \alpha}{\partial Q} \right)_0^2 \left(\frac{1}{\omega_V^2 - \Omega^2 - 2i\Omega\gamma} \right). \quad (2.1.12)$$

The factor 6 comes from the number of permutations of the interacting fields leading to the same non-linear polarization. $\chi^{(3)}$, which quantifies the frequency-dependent material response, is thus linearly proportional to the number of molecules interacting with the input fields.

In the following, we will focus more on the CARS and SRS processes.

2.1.1.1 Coherent anti-Stokes Raman scattering (CARS)

The energy level diagram for the CARS process is shown in Fig.2.2(a). The length of the arrow in the diagram indicates the energy of a pump and a Stokes photon and a Stokes photon in the driving process. The combination of pump and Stokes photons drives the

molecule to an excited vibrational level. This creates a vibrational coherence in all the molecules within the focal volume. The anti-Stokes scattering of pump photons with this vibrational coherence generates the CARS signal at ω_{CARS} .

Under a semiclassical approach, starting from the Maxwell's equations and assuming a condition of negligible pump and Stokes intensity depletion, it is possible to extract the amplitude of the CARS field propagating through an active Raman medium, which turns out to be (Ref. [71], Ref.[23]):

$$E_{\text{CARS}} \propto -i\chi^{(3)}(\Omega)E_{\text{P}}^2E_{\text{S}}^*L \operatorname{sinc}\left(\frac{\Delta kL}{2}\right)e^{\frac{i\Delta kL}{2}} \quad (2.1.13)$$

where $\Delta k = k_{\text{CARS}} + k_{\text{S}} - 2k_{\text{P}}$ is the *phase matching term* for the CARS process which determines the direction of CARS field emission (see insert of Fig.2.2(a)). The sinc function is maximized when its argument is close to zero. This expression shows why for objects extended over a length L larger than the light wavelength, the phase matching requires propagation in the forward direction (which minimizes $\Delta k = 0$). Notably, the formula assumes a well-defined propagation direction. Under tight focusing conditions, a range of wave vectors are involved, and the size of the focal volume is such that the phase-matching condition is practically fulfilled.

The spectral shape of CARS signal is strongly dependent on the frequency behavior of the third-order non-linear susceptibility, as it is suggested by Eq.2.1.12. In practice, in the CARS process it is given by a vibrationally resonant contribution ($\chi_r^{(3)}$) and a non-resonant one ($\chi_{nr}^{(3)}$):

$$\chi^{(3)} = \chi_{nr}^{(3)} + \chi_r^{(3)} = \chi_{nr}^{(3)} + \Re(\chi_r^{(3)}) + i\Im(\chi_r^{(3)}) \quad (2.1.14)$$

The resonant contribution is related to the combination of incident frequencies, which drives a vibrational mode of the targeted molecules. The non-resonant term results from non-resonant vibrational contributions (indeed Eq.2.1.12 is non zero for $\Omega \rightarrow 0$) and electronic transitions supporting a four-wave mixing nonlinearity (see Fig.2.2(b) and (c)). Near a vibrational resonance (i.e. $\Omega \sim \omega_V$), $\chi_{nr}^{(3)}$ can be approximated as real and spectrally flat, so that it can be treated as a constant. Instead $\Re(\chi_r^{(3)})$ and $\Im(\chi_r^{(3)})$ can be retrieved by Eq.2.1.12. In particular, under a 'near resonance approximation', i.e. $\Omega \sim \omega_V$, $\omega_V^2 - \Omega^2 = (\omega_V - \Omega)(\omega_V + \Omega) \sim 2\omega_V(\omega_V - \Omega)$ and $\Omega\gamma \sim \omega_V\gamma$, so that $\Re(\chi_r^{(3)})$ and $\Im(\chi_r^{(3)})$ can be seen as:

$$\Re(\chi_r^{(3)}) \propto \frac{\Omega^2 - (\omega_P - \omega_S)^2}{(\omega_V - \Omega) + \gamma} \quad (2.1.15)$$

$$\Im(\chi_r^{(3)}) \propto \frac{\Omega\gamma}{(\omega_V - \Omega) + \gamma} \quad (2.1.16)$$

$\Im(\chi_r^{(3)})$ represents the actual third-order Raman response, and it has a Lorentzian spectral lineshape, centered at ω_V . $\Re(\chi_r^{(3)})$, on the other hand has a dispersive line shape around the resonance frequency.

In the easier implementation of a CARS set-up, the CARS intensity is measured. The presence of the non-resonant contribution leads to the distortion of the resonant signal of interest. In fact:

$$I_{\text{CARS}} \propto |\chi^{(3)}|^2 \quad (2.1.17)$$

$$\propto |\Re(\chi_r^{(3)}) + i\Im(\chi_r^{(3)}) + \chi_{nr}^{(3)}|^2 \quad (2.1.18)$$

$$\propto |\Re(\chi_r^{(3)})|^2 + |\Im(\chi_r^{(3)})|^2 + |\chi_{nr}^{(3)}|^2 + 2|\Re(\chi_r^{(3)})||\chi_{nr}^{(3)}| \quad (2.1.19)$$

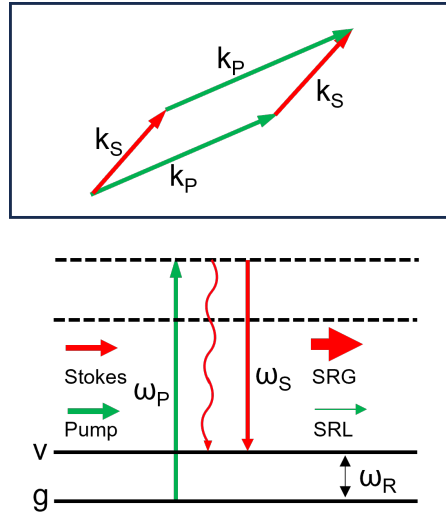


Figure 2.3: Energy diagram showing the SRS process. Insert: phase matching automatically satisfied in SRS. The solid line indicates the ground (g) and vibrational (v) state levels, while the virtual states are represented by dashed lines.

Both the terms $|\chi_{nr}^{(3)}|^2$ and $2|\Re(\chi_r^{(3)})||\chi_{nr}^{(3)}|$ constitute the so-called non-resonant background (NRB).

2.1.1.2 Stimulated Raman scattering (SRS)

To understand the SRS process, a photon stimulation picture is often provided, whereby the Stokes incoming photons stimulate the transfer of energy from pump to Stokes and the creation of a vibrational quantum. Consequently, both depletion of the pump beam and the amplification of the Stokes beam take place. The first effect is the so-called stimulated Raman loss (SRL) while the second is the so-called stimulated Raman gain (SRG). Both SRL and SRG can be measured and they carry the same Raman information. Figure 2.3 shows the energy diagram of the described SRS process.

Similarly to the case of the CARS, the expression for the SRL and SRG field can be retrieved by assuming small variations of pump and Stokes fields during the interaction (Ref.[23]). Note that the phase matching condition is directly satisfied in the SRS process (as $\Delta k = k_S + k_P - k_P + k_S = 0$, see insert of Fig.2.3). Considering the SRG process, the SRG signal is emitted in the same direction as the incoming Stokes field and the two fields interfere. The total detected intensity is therefore :

$$I(\omega_S) \propto |E_S + \Delta E_S|^2 = I_S + \Delta I_S + 2\Re\{E_S^* \cdot \Delta E_S\} \quad (2.1.20)$$

where I_S is the Stokes intensity, ΔI_S is the intensity of the non-linear radiated field, which is typically negligible, and the third term gives the amplification of ΔE_S , which is the nonlinear field ($\Delta E_S \propto -i\chi^{(3)}|E_P|^2 E_S$, Ref.[71]), interfering with the incident Stokes field. Typically, the third term is extracted via the modulation of the pump beam and probing the modulation transfer to the Stokes beam by phase-sensitive detection employing a lock-in amplifier detection technique. Thanks to such implementation I_S is rejected and the SRG signal can be written as :

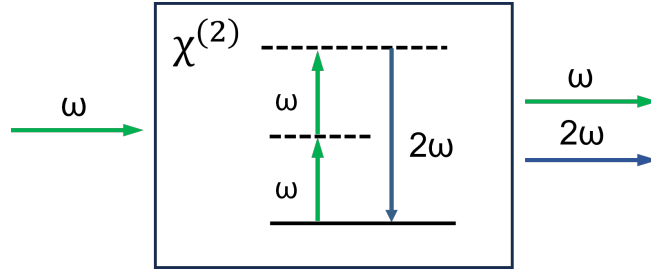


Figure 2.4: Schematic representation of SHG geometry and energy-level diagram, where solid line indicates the ground state level, while the virtual states are represented by dashed lines.

$$I_{SRG}(\omega_S) \propto 2\Re\{E_S^* \cdot \Delta E_S\} \quad (2.1.21)$$

$$\propto 2\Re\{E_S^* \cdot (-i\chi^{(3)}|E_P|^2 E_S)\} \quad (2.1.22)$$

$$\propto 2\Re\{-i\chi^{(3)} I_P I_S\} \quad (2.1.23)$$

$$\propto 2\Re\{-i(\chi_{nr}^{(3)} + \Re(\chi_r^{(3)}) + i\Im(\chi_r^{(3)})) I_P I_S\} \quad (2.1.24)$$

$$\propto 2\Im(\chi_r^{(3)} I_P I_S) \quad (2.1.25)$$

As it is clear from Eq.2.1.21, I_{SRG} has a linear dependence on both pump and Stokes intensity, it is not affected by NRB, and its signal spectral shape is directly comparable to the spontaneous Raman spectra (Ref.[73]).

2.1.2 Second harmonic generation (SHG)

The second-harmonic generation process was first discovered by Franken et al. in 1961 (Ref.[74]) and essentially it is the nonlinear optical process in which two photons with the same frequency combine, thanks to the interaction with a non-centrosymmetric material, to generate a single photon at twice their frequency. In a non-centrosymmetric material, a specific type of symmetry called inversion symmetry is lacking. Inversion symmetry means that the crystal structure of the material is identical when the position of all its constituent atoms or molecules is reversed. For example, inverting the material like in a mirror image, the arrangement of particles would remain the same. The lack of inversion symmetry results in a permanent electric polarization within the material so that $\chi^{(2)} \neq 0$. The illustration of the second harmonic generation (SHG) is depicted in Fig.2.4. When a driving field associated with a laser beam and modeled as a plane wave ($\mathbf{E}_i(t) = Ae^{-i\omega t} + cc$) is incident on a material with $\chi^{(2)} \neq 0$, the induced nonlinear polarization results to be:

$$\mathbf{P}^{(2)}(t) = \epsilon_0 \chi^{(2)} \mathbf{E}_i^2(t) = 2\epsilon_0 \chi^{(2)} AA^* + (\epsilon_0 A^2 e^{-i2\omega t} + cc). \quad (2.1.26)$$

The first contribution is at zero frequency, while the second term, at 2ω frequency, represents the source term for the second-harmonic frequency generation. Starting from Maxwell equations, the wave equation for a wave propagating in a medium with refractive index n can be derived. Then, exploiting the *three wave mixing* approach, where two incoming fields, with the same frequency, interact with a sample giving a third field that corresponds to the SHG, under the *No Depletion Approximation*

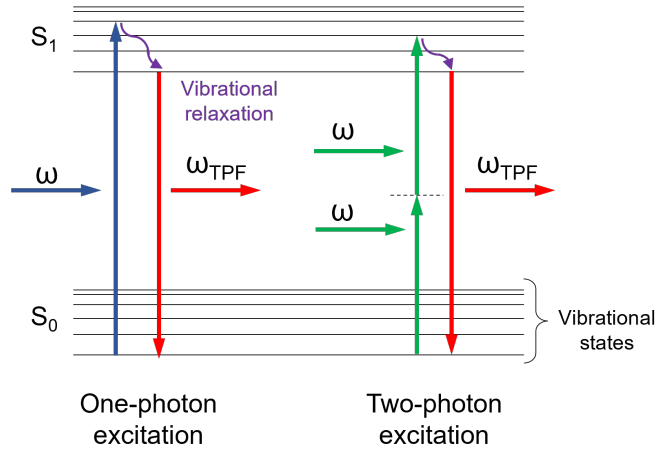


Figure 2.5: Jablonski diagram for one-photon (left) and two-photon excitation. S_0 and S_1 are the ground electronic state and the first electronic excited state respectively. The solid black lines represent the vibrational states associated with each electronic state.

(i.e. the input field is not appreciably modified by the nonlinear interaction), the intensity of the SHG field is given by:

$$I_{\text{SHG}} \propto I_1^2 \left(\frac{\sin(\frac{1}{2}\Delta kz)}{\frac{1}{2}\Delta kz} \right)^2 \frac{z^2}{4} \quad (2.1.27)$$

where I_1 is the input intensity, $\Delta k = k_{2\omega} - 2k_\omega$ is the phase-mismatch between the input and output field and z represents the distance traveled by the input field within the material. In the more general case, Δk is different from zero because, since $k(\omega) = \frac{n(\omega)\omega}{c}$, it would imply:

$$\begin{aligned} k(2\omega) &= 2k(\omega) \\ \frac{n(2\omega)2\omega}{c} &= 2 \frac{n(\omega)\omega}{c} \\ n(2\omega) &= n(\omega) \end{aligned}$$

which is a condition that can be reached in the specific case of using birefringent media (Ref.[75]). When $\Delta k \neq 0$, for a given input intensity, the SHG intensity reaches a maximum at a distance $\frac{\pi}{\Delta k}$, which is known as coherent length, and then diminishes to zero, repeating sinusoidally with period $\frac{2\pi}{\Delta k}$.

2.1.3 Two photon fluorescence (TPF)

In 1931, Maria Goppert Mayer formulated the hypothesis that a group of lower-energy photons could collectively induce an excitation as done by the absorption of a single higher-energy photon (Ref.[76]). This phenomenon was subsequently termed multiphoton excitation. After the confirmation of such hypothesis, thanks to the invention of pulsed ruby lasers, Denk et al. published the first work about the so-called two photon fluorescence (TPF) microscopy (Ref.[77]). For both single-photon and two-photon fluorescence, the excitation of a molecule occurs between the ground state (S_0) and the vibrational levels of the first electronic excited state (S_1), as shown in Fig.2.5. In the first case one photon of energy $\hbar\omega$ is needed for the

excitation, while in the second case, two photons with lower energy ($\sim \hbar\omega/2$) are needed. After either excitation process, the molecule relaxes to the lowest energy level of the first excited electronic states (via vibrational processes). A subsequent fluorescent emission brings the molecule back to the ground state. The background physics of this phenomenon can be found in Ref.[78]. In the two-photon excitation, as the photons need to arrive nearly simultaneously on the sample ($\sim 10^{-16}$ s), we have quadratic dependence of the output intensity (I_{TPF}) on the incident light intensity (I_i) rather than a linear dependence as in conventional one-photon fluorescence:

$$I_{\text{TPF}} \propto \sigma_{\text{TPF}} I_i^2. \quad (2.1.28)$$

σ_{TPF} is the two-photon induced fluorescence cross-section, i.e. a quantitative measure of the probability for the two-photon fluorescence phenomenon to take place. Typically, the probability of two-photon absorption is quite low, so that high incident photon flux needs to be delivered to the sample to generate efficient absorption. As

$$I_i \propto \frac{E}{\Delta\tau w^2} \quad (2.1.29)$$

with E the pulse energy, $\Delta\tau$ the pulse duration, and w the beam waste, it is clear that, in order to maximize the I_{TPF} generation, it is crucial to have as input ultra-short pulses (i.e. a laser) and a high NA.

TPF is commonly used in biological applications and provides some important advantages compared to its single-photon counterpart (Ref.[79], Ref.[80]). In single-photon confocal microscopy, a laser is used to illuminate a single point in the specimen. A pinhole aperture in front of the detector is needed to detect only the light emitted from the focal point, rejecting out-of-focus light. In TPF a pinhole aperture is not needed thanks to the physical principle that two-photon absorption depends on the square of the excitation intensity. In fact, the two-photon absorption probability at the center of the focal point is definitely greater than outside the focus, ensuring that the detected light is associated with the emitters in the center of the focal volume. Additionally, as the two-photon microscopy uses two photons of lower energy to achieve excitation, the probability of photodamage is reduced and again restricted only to the focal volume. It also ensures an increased penetration depth, thanks to the longer wavelength employed, allowing for deeper imaging into thick biological specimens. Cells or tissues can be visualized by utilizing their intrinsic autofluorescence, which includes the emission of various cell constituents like NADH, flavins, and collagen fibers. However, in certain situations, the natural autofluorescence is insufficient. Additionally, the goal of the measurements can be to precisely distinguish different cellular components or track protein movements. In these situations, it becomes necessary to apply external fluorophores or fluorescent dyes for labeling. They are organic compounds initially designed for single-photon excitation but can also be employed with two-photon excitation. Thus, when a fluorescent molecule absorbs photons of a specific wavelength, it becomes excited and emits light at a longer wavelength. However, over time and with continued exposure to light, the molecule can undergo chemical changes that make it unable to fluoresce. This process is called photobleaching.

2.2 Optical response of metallic nanoparticles

In this Section, we give some key information for this project, related to metallic nanoparticles and their optical response. The theoretical treatment in this work will

be conducted within the Rayleigh scattering regime, which is applicable as far as the size of the studied metallic nanoparticles is much smaller than the incident field wavelength. In this regime, the dipole approximation, which allows us to consider particles small enough to be treated as a point-like oscillating electric dipole upon excitation by an external electric field, can be used. The induced dipole moment \mathbf{p} induced by an applied field \mathbf{E} on a metal NP is given by:

$$\mathbf{p} = \epsilon_0 \epsilon_m \hat{\alpha} \mathbf{E} \quad (2.2.1)$$

where ϵ_0 and ϵ_m are the dielectric function in vacuum and of the surrounding medium, respectively. $\hat{\alpha}$ is the polarisability tensor associated with the NP. In the less complicated case of a spherical NP, being an isotropic system, $\hat{\alpha}$ reduces to be a scalar, that, in the Rayleigh regime, is given by (Ref.[81], Ref.[82]):

$$\alpha = 4\pi R^3 \frac{\epsilon_{\text{NP}} - \epsilon_m}{\epsilon_{\text{NP}} + 2\epsilon_m} \quad (2.2.2)$$

where R is the radius of the particle and ϵ_{NP} the dielectric function of a metallic NP. As the latter is a complex quantity, the polarizability is a complex quantity as well. When studying more complicated NP characterized by an ellipsoidal shape the polarizability becomes a tensor and can be derived via the Gans theory (Ref.[83], Ref.[84]). Considering an ellipsoidal NP, its polarisability tensor is given by:

$$\hat{\alpha} = \begin{pmatrix} \alpha_1 & 0 & 0 \\ 0 & \alpha_2 & 0 \\ 0 & 0 & \alpha_3 \end{pmatrix} \quad (2.2.3)$$

where α_1 , α_2 and α_3 represent the polarizability along the three ellipsoid semi-axis of length a_1 , a_2 and a_3 respectively. In analogy with the case of a spherical particle, the polarizability α_i , with $i = 1, 2, 3$, when an external field is applied parallel to the i^{th} axis, are given by:

$$\alpha_i = 4\pi a_1 a_2 a_3 \frac{\epsilon_{\text{NP}} - \epsilon_m}{3\epsilon_m + 3L_i(\epsilon_{\text{NP}} - \epsilon_m)} \quad (2.2.4)$$

To arrive at analytical solutions, it is necessary to assume two of the three semi-axis with the same length, e.g. $a_3 = a_2$, so that $\alpha_3 = \alpha_2$ (Ref.[85]). L_i represent the depolarization factors, which are given by:

$$L_1 = \left(1 - \frac{1}{e^2}\right) \left(1 - \frac{1}{2e} \ln \left(\frac{1+e}{1-e}\right)\right) \quad (2.2.5)$$

and

$$L_2 = \frac{1 - L_1}{2} \quad (2.2.6)$$

where $e = \sqrt{1 - (a_2/a_1)^2}$ describing the eccentricity of the ellipsoid. The polarizability determines the interaction of the particle with the incident field, thus it determines the extinction cross-section of the NP.

The extinction cross-section represents the total effective area of interaction between the NP and an incident field and it is defined as:

$$\sigma_{\text{ext}} = \frac{P_{\text{ext}}}{I_i} \quad (2.2.7)$$

with I_i the incident intensity and P_{ext} the total power lost due to both absorption and scattering. It is also possible to separate the two different contributions in the following way:

$$\sigma_{\text{ext}} = \sigma_{\text{abs}} + \sigma_{\text{sca}} \quad (2.2.8)$$

Within the assumption and approximation regime used in this section, σ_{abs} and σ_{sca} can be derived, considering also that the dielectric function of the metal is a complex quantity ($\epsilon_{\text{NP}} = \Re(\epsilon_{\text{NP}}) + i\Im(\epsilon_{\text{NP}})$). For a spherical NP, or an ellipsoidal NP interacting with an electric field collinearly polarized with one of its principal axes (so that just one of the diagonal terms of Eq.2.2.3 has to be taken into account), σ_{abs} and σ_{sca} can be expressed as (Ref.[83]):

$$\sigma_{\text{abs}} \propto \frac{V}{\lambda} \frac{\Im(\epsilon_{\text{NP}})}{(\Re(\epsilon_{\text{NP}}) + C\epsilon_m)^2 + \Im(\epsilon_{\text{NP}})^2} \quad (2.2.9)$$

$$\sigma_{\text{sca}} \propto \frac{V^2}{\lambda^4} \frac{(\Re(\epsilon_{\text{NP}}) - \epsilon_m)^2 + \Im(\epsilon_{\text{NP}})^2}{(\Re(\epsilon_{\text{NP}}) + C\epsilon_m)^2 + \Im(\epsilon_{\text{NP}})^2} \quad (2.2.10)$$

with $C=2$ when considering a spherical NP (Ref.[83]), and $C = \frac{1-L_i}{L_i}$ when considering an ellipsoidal NP (Ref.[86]). The roles of $\Re(\epsilon_{\text{NP}})$ and $\Im(\epsilon_{\text{NP}})$ can be understood considering the analogy between Eqs.2.2.10 and a Lorentz distribution described by :

$$f(x, x_0, \Gamma) = \frac{1}{\pi} \frac{\Gamma}{\Gamma^2 + (x - x_0)^2} \quad (2.2.11)$$

where x_0 specifies the location of the peak of the distribution, and Γ specifies the half-width at half-maximum (HWHM). $\Re(\epsilon_{\text{NP}})$ (corresponding to x_0) determines the resonance position, i.e. for $\Re(\epsilon_{\text{NP}}) = -C\epsilon_m$. Additionally, the resonance red-shifts for surrounding media with larger ϵ_m . This red-shift phenomenon is caused by increased charge shielding, which occurs when the refractive index of the surrounding environment is higher. $\Im(\epsilon_{\text{NP}})$ (corresponding to Γ) determines resonance linewidth. A smaller $\Im(\epsilon_{\text{NP}})$ gives a narrow linewidth at the resonance, with smaller damping, and larger cross-sections.

The largest extinction cross-section occurs at the so-called LSPR, i.e. the resonance frequency at which the NP polarizability reaches its maximum. The more an incident light has a frequency close to this, the stronger will be the induced coherent collective motion of NP conductive electrons, the so-called localized plasmon. As the LSPR is defined as the frequency at which the polarizability is maximum, it is the frequency at which the polarizability denominator is minimized. For a spherical NP this condition is satisfied for $\Re(\epsilon_{\text{NP}}) = -2\epsilon_m$, while for an ellipsoidal NP for $\Re(\epsilon_{\text{NP}}) = -((1 - L_1)/L_1)\epsilon_m$. The real part of the dielectric function of metals can be negative, making such requirements possible. In the case of a gold ellipsoidal NP, thanks to its aspect ratio, the longer axis-related LSPR (e.g. associated to $i=1$) displays a red-shift compared to the LSPR of a gold spherical NP. In fact, considering an ellipsoidal NP with aspect ratio equal to 2 and surrounded by oil, thus with $L_1=0.174$ and $L_2=0.413$, the condition becomes $\Re(\epsilon_{\text{NP}}) = -4.74\epsilon_m$. The $\Re(\epsilon_{\text{NP}})$ needed to minimize the denominator of the polarizability in the case of an ellipsoidal NP is more negative than in the case of a spherical NP and so a longer wavelength to get the minimization condition (see Fig.2.6).

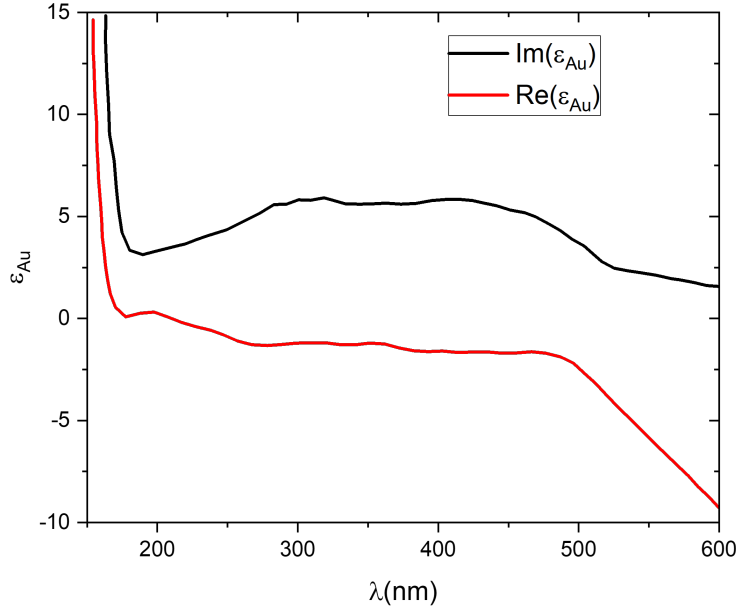


Figure 2.6: Complex dielectric function of gold (adapted from Ref.[87]): $\Re(\epsilon_{\text{Au}})$ (red lines) and $\Im(\epsilon_{\text{Au}})$ (black lines).

2.3 CARS in the presence of a plasmonic antenna

The first experimental observation of CARS in the presence of a plasmonic antenna was by Liang et al. in 1994 (Ref.[49]). But in 1980, the properties of the radiation from a molecular dipole near a spherical polarizable particle was treated by Kerker et al. (Ref.[88]). When a pump (E_P) and a Stokes (E_S) fields, at ω_P and ω_S respectively, are incident on a molecule placed at \mathbf{r} and near a metallic NP, the actual local fields experienced by the molecule can be written as

$$E_{loc}(\mathbf{r}, \omega_i) = E_i(\mathbf{r}, \omega_i) + E_{NP}(\mathbf{r}, \omega_i) \quad (2.3.1)$$

with $i=P,S$, and $E_{NP}(\mathbf{r}, \omega_i)$ the field elastically scattered by the NP. Note that the driving phase of the local fields can be different from the phases of the incident fields, as they are dressed by the spectral resonance of the antenna. Let us rewrite $E_i(\mathbf{r}, \omega_i) = A_i(\omega_i)S_i(\mathbf{r})$. Considering that the fields scattered by the NP is proportional to the amplitude A_i of the incident field, we can write $E_{loc}(\mathbf{r}, \omega_i) = f(\mathbf{r}, \omega_i)A_i(\omega_i)$, where the factor f describes the field enhancement introduced by the NP. $E_{loc}(\mathbf{r}, \omega_P)$ and $E_{loc}(\mathbf{r}, \omega_S)$ are the fields that set up the CARS polarization in the molecule, so that in analogy with Eq.2.1.11, the consequent CARS field is driven by:

$$\begin{aligned} P_{\text{CARS}}(\mathbf{r}, \omega_{\text{CARS}}) &\propto \chi^{(3)}(\omega_P - \omega_S) E_{loc}^2(\mathbf{r}, \omega_P) E_{loc}^*(\mathbf{r}, \omega_S) = \\ &= \chi^{(3)}(\omega_P - \omega_S) f^2(\mathbf{r}, \omega_P) A_P^2(\omega_P) f(\mathbf{r}, \omega_S) A_S^*(\omega_S) \end{aligned} \quad (2.3.2)$$

The generated CARS field by the molecule $E_{\text{CARS},m}$ will be then scattered by the NP, as it happens for pump and Stokes, so that the overall CARS field radiated can

be written as

$$\begin{aligned} E_{\text{CARS}}(\mathbf{r}, \omega_{\text{CARS}}) &\propto f(\mathbf{r}, \omega_{\text{CARS}}) A_{\text{CARS},\text{m}} = \\ &= f^2(\mathbf{r}, \omega_P) f(\mathbf{r}, \omega_S) f(\mathbf{r}, \omega_{\text{CARS}}) \chi^{(3)}(\omega_P - \omega_S) A_P^2(\omega_P) A_S^*(\omega_S) \end{aligned} \quad (2.3.3)$$

From this simple analysis, we can see that the local enhanced CARS field is characterized by an enhancement coming from the enhancement of all the beams involved in the process. On the other hand, the latter analysis does not take into account the coherent background at ω_{CARS} originating from the third-order susceptibility of the metal. In reality, the field measured at the detector (in the generic far field position \mathbf{R}) will be given by the interference of the field related to the vibrational excitation of the molecule and the non-resonant contribution of the metal NP (E_{M}), i.e.

$$E_{\text{tot}}(\omega_{\text{CARS}}, \mathbf{R}) = E_{\text{CARS}}(\omega_{\text{CARS}}, \mathbf{R}) e^{i\Delta\phi(\omega_{\text{CARS}})} + E_{\text{M}}(\omega_{\text{CARS}}, \mathbf{R}) \quad (2.3.4)$$

$e^{i\Delta\phi(\omega_{\text{CARS}})}$ is a phase term to make clear that the two contributions can differ in their phase as they originate from different phenomena. Extensive numerical COMSOL simulations of all these fields and effects have been carried out as it will be discussed later in the thesis.

Chapter 3

Materials and Methods

3.1 Silica coated gold nanorods (SiAuNRs) and sample preparation

We investigated three types of silica-coated gold nanorods (SiAuNRs), purchased from Nanopartz. From the specifications provided by the manufacturer, they have the following characteristics:

- 25 nm×71 nm (aspect ratio 2.8), silica shell thickness 5 nm, longitudinal LSPR in H₂O at 646 nm
- 40 nm×68 nm (aspect ratio 1.7), silica shell thickness 10 nm, longitudinal LSPR in H₂O at 620 nm
- 50 nm×100 nm (aspect ratio 2), silica shell thickness 10 nm, longitudinal LSPR in H₂O at 620 nm

The specified LSPR positions in wavelength were deducted from UV-VIS absorption spectroscopy measurements in water. The TEM images of the introduced NRs are reported in Figure 3.1. From Fig.3.1, it is possible to notice that the real size of the largest SiAuNRs, deviates from the nominal 50 nm×100 nm, being typically smaller. The sketch of the sample used to characterize all the nanorods is reported in Fig.3.2. In this section a detailed description of the sample preparation procedure will be

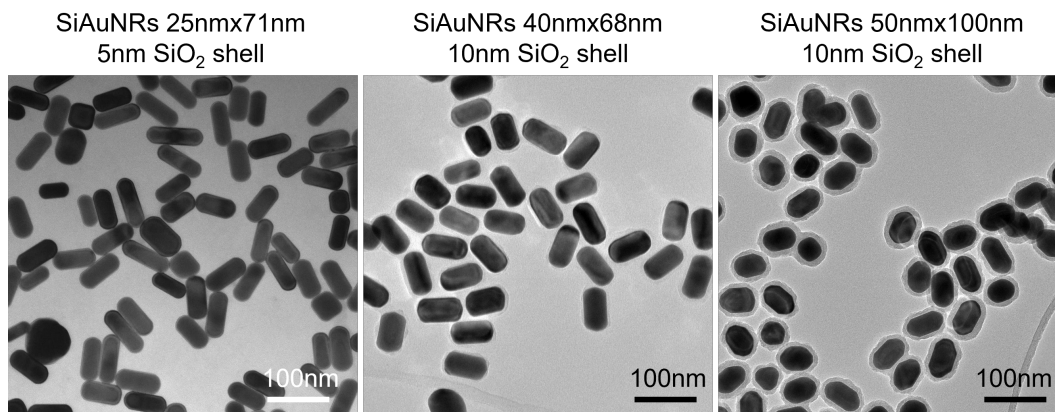


Figure 3.1: TEM images of SiAuNRs. Left: provided by Nanopartz. Middle and right: measured exploiting the electron microscopy facilities at Cardiff University.

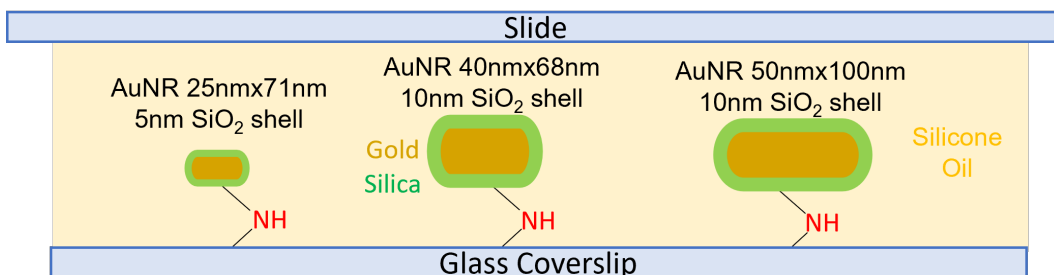


Figure 3.2: Sketch of the sample used for particle characterization: SiAuNR covalently bound to a microscope coverslip in silicone oil bulk

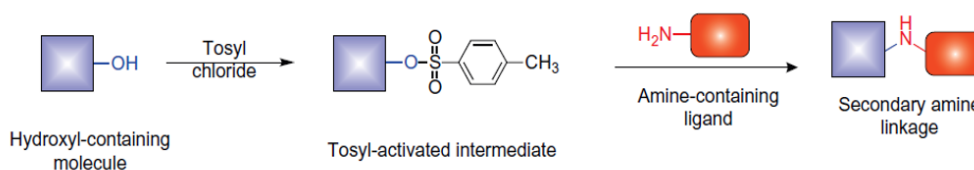


Figure 3.3: The tosyl reagent is used for reaction with glass hydroxyl groups, forming a reactive tosyl ester. The sulfonyl ester reacts with amines to form secondary amine linkages. See Ref.[89],[90],[91].

given.

When performing high-sensitivity and high-resolution optical microscopy measurements on single nanostructures at a glass interface, it is important that the glass surfaces are free from debris visible with the measurement resolution. Defocus aberration from large debris on the glass slide can cause distortion blur at the focus imaging plane. Debris at the glass coverslip can give a significant background in the extinction analysis. To prevent the presence of such debris, the cleaning protocol presented in the following was used on the glass slides and Menzel-Gläser coverslips (24 mm×24 mm, thickness #1.5). This cleaning protocol employs a 30% H₂O₂ solution, which is also fundamental for the following sample preparation steps as it gives the possibility of having the hydroxylation of the coverslips. In fact, although the glass is made mainly by silica (silicon dioxide, SiO₂), during the manufacturing process, silica is melted to then rapidly cool down, forming a non crystalline or amorphous structure with some silicon-oxygen bonds not fully formed. The formation of silanol groups (Si-OH) occurs due to the incorporation of hydroxyl (OH) groups coming from hydroxyl-containing species, in our case hydrogen peroxide. To avoid particles moving during the lasers exposure, a protocol to covalently bind the particles on the coverslip was developed, avoiding the introduction in the sample of extra-CH chains, to not create unwanted signal during the eH-CARS measurements of lipids. Since the chosen nanorods are all coated by silica with integrated amine (NH₂) groups, the chemistry represented in Fig.3.3 was selected to covalently bind our NPs onto the glass surface. The 4-toluenesulfonyl chloride, also referred to as tosyl chloride or TsCl, is an organic sulfonyl chloride able to activate agents that can facilitate the conjugation of hydroxyl-containing compounds, as our glass, to other nucleophiles, particularly amine-containing ligands, as our NRs, forming a secondary amine linkage.

The next sections will describe in detail all the sample preparation steps.

Glass preparation and cleaning

First, the glass slides have to be cut by hand to have a size around 50mm×25mm, to fit in the sample stage of our inverted microscope (see Section 3.3). This glass slide preparation is done before the cleaning procedure to minimize the risk of glass dust contamination in the final sample. To achieve clean glass breakages with minimal rough edges, the glass is lightly wetted with acetone and a diamond scribe pen was utilized to create a fault straight line on the glass slide. Subsequently, the fault line is gently tapped from underneath, and the glass is broken by applying upward pressure through the scribe line from underneath, as opposed to bending it from above.

The following cleaning procedure is then used both for glass slides and coverslips. Using some optics paper free from lint and wetted with acetone, the glass surfaces are scrubbed until any debris could be seen by eyes. This step helps remove inorganic debris, which may need physical agitation for removal. The acetone-scrubbed glassware is then placed in a beaker containing toluene, which exhibits a good ability to dissolve a range of organic compounds (including many polymers and hydrocarbon-based oil) and sonicated for 20 minutes in a sonicator bath. In the following, the glass slide and coverslip are placed in a beaker containing acetone and again sonicated for 20 minutes. The acetone is important to remove toluene residues and dissolve any water based contaminants thanks to its carbonyl group (C=O). After the sonication in acetone, the glass is rinsed thoroughly in Milli-Q water and placed in another beaker filled with Milli-Q water. The latter beaker is then placed in the microwave. The water was brought to the boiling point and left boiling for 3 minutes. Finally, the glass is taken from the Milli-Q water and left in a bath of 30% H₂O₂ solution to be then sonicated for 20 minutes. This step is needed to make sure the removal of contaminants, by both the heating and vigorous motion of boiling, and to make any acetone traces evaporate. Following the sonication the coverslips are kept submerged in the hydrogen peroxide at 4°, for at least 24 hrs, allowing oxidation of remaining surface contaminants, as well as hydrophilizing the glass surfaces. All the passages in which glass is transferred from one bath to the following, are carried out under a fume hood.

Coverslips functionalisation

After at least 24 hours from the cleaning procedure, the coverslips are rinsed with DI water, dried with nitrogen flow, brought under the fumehood, and placed into an acetone bath to ensure the glass is water-free. The tosyl chloride, used in this stage of the sample preparation, must be kept at room temperature, under inert atmosphere and away from metal and water. In fact, it corrodes metals on contact, decomposes on heating producing toxic and corrosive fumes (sulfur oxides and hydrogen chloride) and reacts with water and moist air producing hydrogen chloride, which forms white fumes of hydrochloric acid upon contact with atmospheric water vapor. For this reason, all the following passages were performed under the fumehood and all the instrumentation undergoing in contact with the TsCl must be cleaned with acetone before and after being used. A solution of 10% (w/v) tosyl chloride and acetone is prepared. To allow the complete dissolution of the TsCl powder, an acetone rinsed magnetic stir is inserted in the beaker used and the overall solution is mixed gently

with a magnetic stirrer. Once the tosyl chloride is dissolved completely in acetone, the coverslips are transferred from the acetone bath to the TsCl solution. The beaker has to be covered with a teflon lid and left for up to 2hrs. Once past those two hours, the coverslips are retrieved from the tosyl chloride and deeply rinsed with acetone first and the DI water after. Finally, they are dried with nitrogen flow.

NPs solution preparation and sample mounting

The starting NR colloid solution is diluted in a buffer given by DI filtered water and acetic acid, added to have a final pH between 4.5 and 5 to maintain the Z potential given by the NP specification data sheet and to avoid particles aggregation. Additionally, to decrease the probability of particle aggregation, each solution is sonicated in a sonicator bath, prior to being used. The choice of the concentration to be reached was dictated by the need to have an average distance between particles of 5-10 μm , such that most NPs can be resolved by optical microscopy with well-separated PSF. So, if we consider to cover 80% of the overall coverslip area, which is nominally 24mm \times 24mm, in the ideal 1D case where particles dispose equally distant between each other, the total covered distance can be written as $D = d * (N - 1)$ where D is the total distance of about 21mm, d is the average inter-particle distance and N is the number of particles. Typically $N \gg 1$, so that the 1 can be neglected. Imposing $d = D/N = 7.5\mu\text{m}$, we obtain $N \approx 3000$. Then considering our 2D case, $N_{2D} = N_{1D}^2 \approx 10^7$. The latter is the concentration we aim for the NR diluted solutions. After the dilution of the NR colloid stock concentration, a particle wet sedimentation technique follows. The functionalized coverslips are placed on a piece of lint-free optics paper and on top of them a 100 μl droplet of the prepared NR diluted solution is deposited. A piece of paper towel soaked in H₂O is placed near them inside a petri dish. Everything was then placed under a large inverted water bath for up to 1 hr (see Fig.3.4). The paper towel is needed to increase the humidity beneath the water bath, minimising the amount of evaporation that would cause aggregation of particles at the edges of the droplet. After 1 hr, the coverslips are rinsed one last time with DI H₂O and dried with nitrogen flow. The side of the coverslip containing the NRs was coated with $\approx 30 \mu\text{l}$ silicone oil (refractive index $n=1.52$) and covered with a slide. When imaging the sample, the use of a squeezed sample minimized the presence of unfocused debris aberration. For this reason, the unsealed construction is then slowly pressed in a table vice, so that the final space between the two glasses turns out to be of the order of a few micrometers. The unsealed construction is wrapped in optical paper and shielded by placing a sacrificial slide and a cardboard cutout above and below it. The purpose of the cardboard is to safeguard the glass from the sharp edges of the vise, while the sacrificial glass ensures uniform compression, reducing lateral drift. To avoid scratches, optical paper is also introduced. The entire setup was then clamped securely within a vertically mounted vise (see Fig.3.5), paying particular attention to compression alignment by placing the stationary portion of the vise at the bottom. After removing excess oil, the original coverslip and slide were then sealed with clear nail varnish.

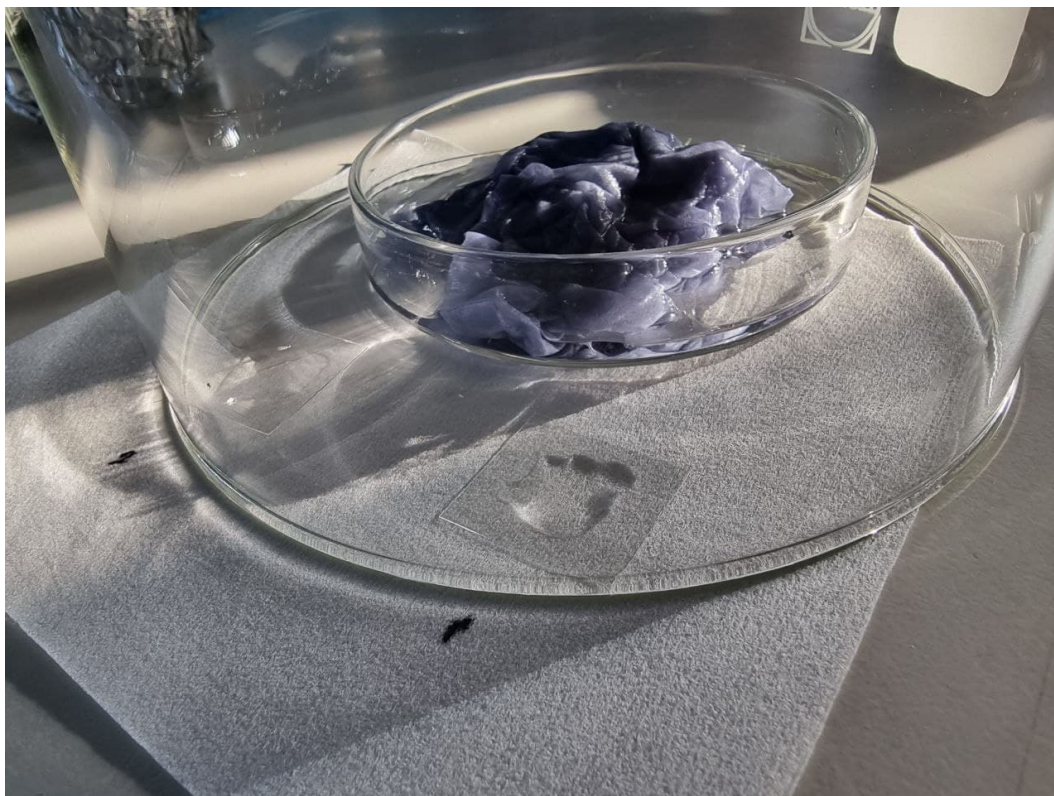


Figure 3.4: Functionalized coverslip covered by 100 μ l of NRs solution in wet atmosphere to prevent particle aggregation.

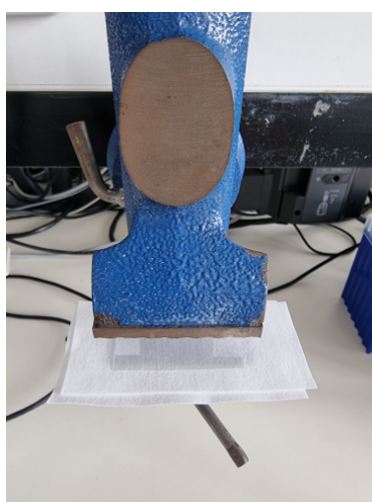


Figure 3.5: Sample mounted in the table vise.

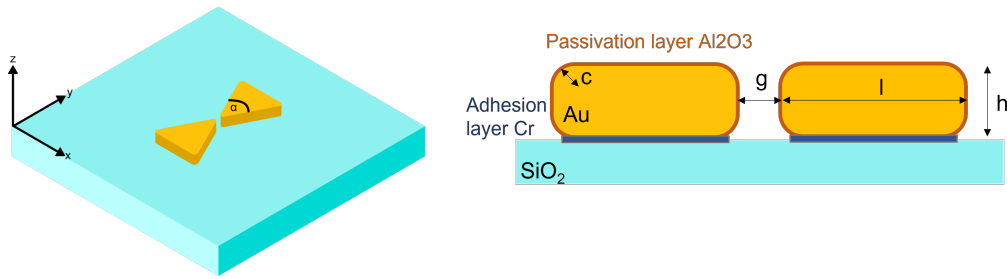


Figure 3.6: AuNB sketch. Left: 3D view; Right: lateral view. α : apex angle; l : length; h : height; c : radius of curvature; g : gap size.

3.2 Gold nanobowties (AuNBs) and samples preparation

In collaboration with the Single Molecule Biophotonics group, based at The Institute of Photonic Science (ICFO, Barcelona, Spain), led by Prof. Dr. Maria Garcìa-Parajo, we successfully designed and fabricated gold nano-bowties (AuNBs) antennas. AuNBs have been used in this PhD project to perform correlative fluorescence and SRS/eH-CARS sensing measurement using samples where the antennas were surrounded by PS beads moving around in a bulk media as well as biological samples made by HEK293 living cells laying on the antennas.

3.2.1 AuNB design and fabrication

AuNB design

Figure 3.6 represents a sketch of the designed AuNBs. As depicted in the sketch, these nanostructures are characterized by different parameters as the apex angle (α), the length (l), equivalent to the distance from the nanoantenna tip to the triangle base, the height (h), defined as the antennas thickness, the radius of curvature (c) and gap (g) size. A Cr adhesion layer has been used to attach the antennas onto the BK-7 glass substrate, since gold does not adhere well to glass. Additionally, an Al_2O_3 passivation layer coats the nanoantennas and substrate to improve the thermal stability. For the fabrication, an electron beam lithography (EBL) based lift-off process was developed and some of the mentioned antenna parameters were dictated by fabrication requirements:

- The thickness of the Cr layer was chosen to be 1 nm thick. It is kept as thin as possible to minimize energy dissipation through non-radiative pathways (Ref.[92]), but sufficiently thick to allow a good adhesion with the deposition method deployed during the nanofabrication.
- The coating Al_2O_3 layer was chosen to be 3 nm thick to improve the antennas thermal stability of nanoantennas without strongly reducing the local field enhancement (Ref.[93])
- The height h of the gold nanoantennas is fixed at 50 nm. A reduced antennas thickness would introduce additional interfacial damping (Ref.[94]), while an increase of it would effectively reduce the achievable lateral resolution in the fabrication process.

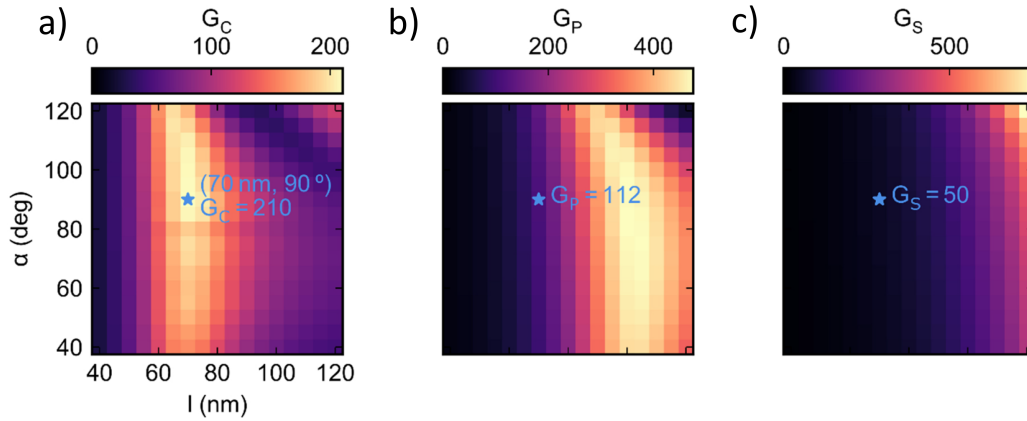


Figure 3.7: FDTD simulations of gold bowtie nanoantennas. (a-c) Intensity enhancement G (defined in Eq.3.2.1) at the gap center for the CARS ($\lambda_C=660$ nm), pump ($\lambda_P=820$ nm), and Stokes ($\lambda_S=1080$ nm) wavelength for different lengths l and apex angles α . The optimal parameters are chosen to maximize G_C and indicated by the blue star in (a).

- A gap size g of 20 nm is the minimal one that can be reliably achieved with the EBL-based fabrication process.
- The limited lateral resolution of the fabrication process imposes an edge and corner curvature radius of $c=20$ nm.

With the above mentioned parameters being constrained as explained, only the nanoantenna length l and apex-angle α remain available for optimization. To have a first estimation about the optimized l and α for a CARS experiment, a commercial finite-difference time-domain (FDTD) simulation software (Lumerical) was employed to predict the parameters yielding the desired optical response. The simulations were carried out by Ediz Herkert (PhD student at ICFO under the supervision of Prof. Dr. Maria Garcia-Parajo), assuming an aqueous environment surrounding the excited antenna. The exciting fields have been simulated as plane waves linearly polarized along the nanoantennas axis. The wavelengths of the fields used in the simulations were 660 nm, 820 nm, 1080 nm as CARS (λ_C), pump (λ_P) and Stokes (λ_S) wavelength respectively, very close to the ones used in our eH-CARS experiments (see Sec.3.3.2). An intensity-enhancement parameter as been defined in the following way:

$$G(\lambda, l, \alpha) = \left| \frac{E(\lambda, l, \alpha)}{E_0(\lambda)} \right|^2 \quad (3.2.1)$$

where $E_0(\lambda)$ represents the incident field, while $E(\lambda, l, \alpha)$ represents the field due to the presence of the antenna. $G(\lambda, l, \alpha)$ has been used to quantify the enhancement obtained with different (l, α) combinations.

Figure 3.7 shows the intensity-enhancements (G_C , G_P and G_S) obtained in the center of the gap, at 28 nm distance from the glass substrate, exciting the antennas at λ_C (a), λ_P (b), and λ_S (c). As indicated by the star symbol, the maximum intensity-enhancement at the CARS wavelength is obtained for $l=70$ nm and $\alpha=90^\circ$. For these parameters, the enhancement at the CARS wavelength is 210, whereas it is 112 and 50 at the pump and Stokes wavelengths, respectively. Due to the nonlinear nature of the CARS process such antenna thus theoretically provides a total CARS enhancement $G_{\text{tot}} = G_C \times G_P^2 \times G_S = 1.32 \times 10^8$.

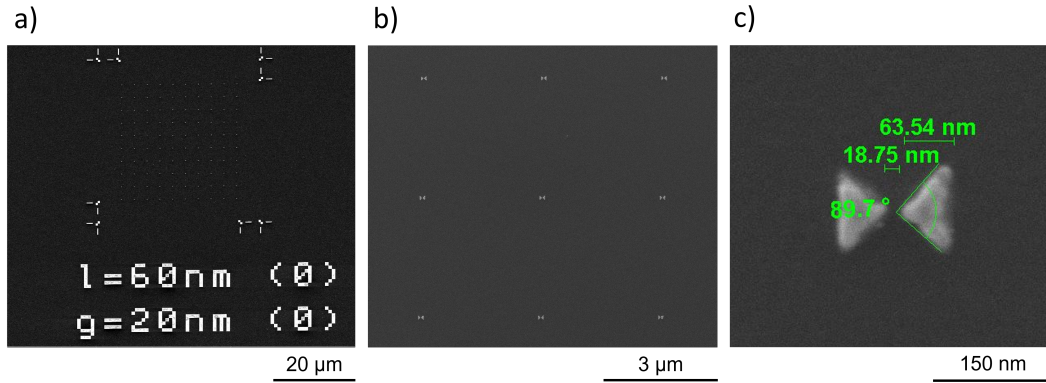


Figure 3.8: SEM images of the gold bowtie nanoantennas. (a) Writefield containing 10×10 nominally equal gold bowtie nanoantennas and labeled with the nominal parameters l and g as well as a unique identifier (here, $(0, 0)$). (b) Zoom-in showing 3×3 exemplary nanoantennas. (c) Zoom-in showing one single nanoantenna with its real antenna length l , gap size g , and apex angle α .

AuNB fabrication

As already mentioned, an EBL based lift-off process was developed and a range of nominally different (l, α) combinations, around the one suggested by the simulations, were used. Moreover, the gap size (g) has been investigated making it ranging around 20 nm. This choice of changing the structure parameters around the theoretically optimized ones was made to then test the different nanostructure in the actual experiments, which can differ from the ideal simulation condition. It was also useful to take in mind the proximity effect (Ref.[95]) which can take place during the EBL process and can lead the parameters to be different from the nominal ones. Figure 3.8 shows some SEM images related to one AuNB writefield characterized by $l=60$ nm, $g=20$ nm (as indicated) and $\alpha=90^\circ$. Each writefield contains 10×10 nominally equal gold bowtie nanoantennas (a). In Fig.3.8(b) it is possible to find a zoom-in showing 3×3 exemplary nanoantennas with a periodicity of about $3 \mu\text{m}$ in both directions to avoid coupling effects. In Fig.3.8(c) a zoom-in on one single antenna is reported, which shows that the real antenna length, gap size, and apex angle can be different from the nominal parameters. The following sections provide a concise overview of Electron Beam Lithography, followed by a comprehensive description of the nanofabrication process developed by Ediz Herkert.

Introduction to Electron Beam Lithography

In EBL systems (Ref.[96]) a highly focused and accelerated beam of electrons is scanned over a surface covered by a resist (the so-called e-beam resist), sensitive to electron radiation, to pattern features down to sub-10 nm. The e-beam can expose different areas and geometries of the substrates thanks to deflector coils or stage movement. Based on the type of resist used, the exposed areas become more or less soluble in organic solvents, enabling selective removal of either the exposed or non-exposed regions of the resist. Afterward, a layer of metal is deposited on the obtained structure. Typically a lift-off process is used to remove the remaining resist covered by the redundant metal. After a final cleaning of the sample, the plasmonic metallic pattern is obtained (Fig.3.9). The primary advantage of electron beam lithography comes from the very small electron wavelength (typically less than 0.01 nm at 20 keV)

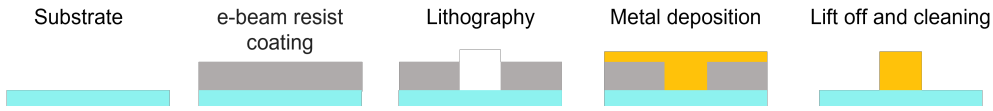


Figure 3.9: Schematic overview of individual steps in the EBL fabrication process of plasmonic structures.

and thus it can write custom patterns with sub-10 nm resolution. Based on the system, the resolution is mostly limited by imperfections in the electron optics and electron backscattering from the substrate. When fabricating small nanostructures with thin details, it is desirable to favor the resolution, which implies the employment of an electron beam with a small diameter obtained in the case of a small current and low throughput (understood as the quantity of electrons arriving on the sample).

Fabrication Procedure

The process is based on the positive-tone resist named ARP6200.04 and allows a lateral resolution between 30-40 nm. For the EBL process, the Raith Elphy Plus system is used. It is characterized by an acceleration voltage of up to 30 kV and an electron-beam aperture chosen to be the smallest possible (30 μ m, spot size 1), together with a step size of 5 nm to achieve the required lateral resolution. Each writefield contains 10 \times 10 bowtie nanoantennas with a periodicity of 3 μ m. A dose of 422.5 $\frac{\mu\text{C}}{\text{cm}^2}$ has been used to impress the desired pattern on the resist. The writefields also contain alignment markers being here only used for easier identification of the nanoantenna arrays and are labeled with the respective parameters and two unique numbers specifying the location in the writefield arrays (see Figure 3.8(a)).

The process is divided into steps:

1. Glass substrate cleaning:
24mm \times 24mm, #1.5 BK-7 coverslips are cleaned with 15 min sonication in acetone followed by rigorous rinsing with IPA and ultrapure water (MilliQ). They are then dried with nitrogen flow and dry-baked on a hot-plate for 3-5min at 155 $^{\circ}$ C to make sure all the water molecules evaporate.
2. Glass preparation for EBL:
 - 150ml of the positive-tone resist is added on the cleaned coverslip by drop-coating and subsequent spin-coating for 60 s at 4000rpm to obtain a thin and homogenous layer. The resist is baked on a hot-plate for 2min at 155 $^{\circ}$ C to evaporate the residual resist solvent.
 - A thin layer of the water-soluble conductive polymer EspacerTM 300Z is applied by drop-coating 150ml of the polymer on the coverslip and spin-coating for 60s at 5000rpm. The conductive polymer is necessary since it mitigates charging effects induced by the electron beam during the EBL process due to the insulating glass substrate.
3. Sample Development:
 - The coverslip is rinsed for 15s in MilliQ to remove the water-soluble conductive polymer EspacerTM 300Z and then dry-blown with nitrogen.

- Following, it is dipped in AR600-546 for 2 min and then rinsed sequentially for 15s with isopropanol and MilliQ. With this passage the development is stopped. Finally, it is blow-dried again with nitrogen.
4. Cr and Au layers deposition with a Leybold Univex 350 evaporator:
 - Cr is deposited by means of e-beam evaporation, at 1\AA s^{-1} at pressures around 2×10^{-6} mbar.
 - Au is deposited by means of e-beam evaporation, at 2\AA s^{-1} at pressures around 2×10^{-6} mbar.
 5. Lift-off:

After the metal deposition, the coverslips are placed for 90-120 min without sonication and another 30 min with sonication in the remover AR600-71 for the lift-off process. The lift-off process is then ended by rinsing the nanostructured coverslips with isopropanol and MilliQ and dry-blowing with nitrogen.
 6. Antennas coating:

The coverslips with the nanoantennas are coated with a 3 nm Al_2O_3 layer using atomic layer deposition (ALD) with a Cambridge Nanotech Savannah 200 system. The ALD process is run at 200°C at ~ 0.3 mTorr and consists of three 0.015 s H_2O pulses followed by three 0.05 s pulses of trimethylaluminium (TMA). The series of pulses is repeated 27 times with 10 s pauses between each pulse at an approximate growth rate of 1.1\AA s^{-1} per pulse series, yielding the 3 nm Al_2O_3 layer.

3.2.2 Polystyrene (PS) beads

The PS beads used to test the sensing ability of the AuNBs were 200 nm diameter Fluoresbrite[®] YG Fluorescent Microspheres, with 5% diameter coefficient of variation, and 100 nm diameter Fluoresbrite[®] YG Carboxylate Microspheres, with 10 % diameter coefficient of variation (Polyscience, Inc). Being YG (yellow-green), both of them have 441 nm and 486 nm as wavelengths for maximum excitation and emission, respectively (see fluorescence emission/excitation spectrum in Fig.3.10). Although the size of these beads is well larger than the gap size in the antenna, such sizes have been chosen for the first preliminary test to be sure of having enough polystyrene material providing a sufficiently high SRS to be detected, even when an enhancement from an antenna is not present. As consequent of the large beads sizes, we need to take into account that they will not be able to fit within the gap of the antenna, thus we do not work in the optimized condition to have the highest field enhancement. Both bead solutions were shipped in DI water. The starting solution concentration (C_S [particles/ml]) can be computed with the following formula provided by the manufacturer in the technical data sheet:

$$C_S = \frac{6W10^{12}}{\rho\pi\phi^3} \quad (3.2.2)$$

where W is the weight/volume concentration of the solution, in grams of polymer per ml (0.025g for a 2.5% latex), ϕ is the diameter in micrometers of latex particles and ρ is the density of polymer in grams per ml (1.05 for polystyrene). Using this formula we obtain a starting concentration of 5.7×10^{12} particles/ml for the 200 nm diameter PS beads and 4.55×10^{13} particles/ml for the 100 nm diameter PS beads.

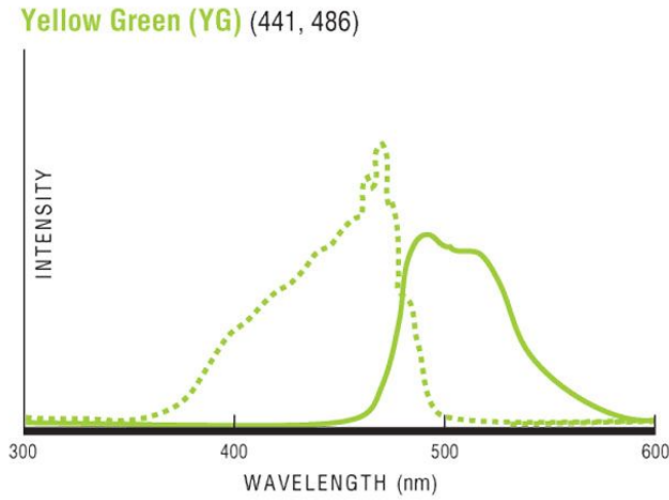


Figure 3.10: Fluorescence emission/excitation spectrum of YG Fluorescent Microspheres and YG Carboxylate Microspheres from Ref.[2].

In order to be able to detect a PS bead passing by a AuNB as clearly isolated spikes in time, the initial PS beads solution had to be diluted, reaching a given final concentration C_F , such that the probability of finding a PS beads in the focal volume of our measurements ($V_f \sim 0.5 \mu\text{m}^3$) turns to be lower than 1. This probability can be computed as $P = C_F V_f$. To a final concentration $C_F \sim 10^{10}$ particles/ml corresponds a probability around 0.71%. For this reason, the two starting solutions have been diluted to have 5.7×10^{10} particles/ml for the 200 nm diameter PS beads and 8×10^{10} particles/ml for the 100 nm diameter PS beads. For dilution, rather than pure water, a solvent of glycerol-water mixture was chosen to control the viscosity and in turn diffusion on the PS beads. According to the theory of the Brownian motion, the diffusion length in each dimension of a translational motion is given by

$$\langle x^2 \rangle = 2D_t t \quad (3.2.3)$$

D_t is the translational diffusion constant, that for a spherical particle is given by

$$D_t = \frac{k_B T}{6\pi\eta_s r_p} \quad (3.2.4)$$

where t is the diffusion time, k_B is the Boltzmann's constant (1.38×10^{-23} J/K), T is the temperature in units of [K] (typically 300 K for room temperature), η_s is the solvent dynamic viscosity in units of [Ns/m²] and r_p is the particle radius in units of [m]. By diluting the starting solution with a glycerol-DI water solution it is possible to change the diffusion time of the PS beads in a probed area, as we change the viscosity of the bulk media where the beads are moving. The 200 nm diameter PS beads have been diluted both with fully DI water and with a 50% glycerol/water (v/v) diluting solution, while for the 100 nm diameter PS beads, only the latter has been employed. According to Ref.[?], η_s for a solution of water is 0.0010 Pa.s, while a solution given by 50% of water and 50% of glycerol gives $\eta_s = 0.0060$ Pa.s. Using Eq.3.2.3 and Eq.3.2.4, it is possible to derive the time required by a PS bead to pass through a probed volume. Table 3.2.2 provided the estimated diffusion times of the introduced PS beads when they pass through the focal volume (V_f) and the volume

Diameter	V_f		V_{NB}	
	0%	50%	0%	50%
100 nm	30 ms	170 ms	0.3 ms	1.7 ms
200 nm	62 ms	341 ms	0.62 ms	3 ms

Table 3.1: Estimated diffusion times of 100 nm and 200 nm diameter PS beads passing through the focal volume ($V_f \sim 0.5 \mu\text{m}^3$) and through the volume probed by the antennas ($V_{NB} \sim 50 \text{nm}^3$), in case of fully DI water solution (0%) and 50% glycerol/water solution

probed by the antennas ($V_{NB} \sim 50 \text{nm}^3$), in case of fully DI water solution (0%) and 50% glycerol/water solution.

After having prepared the PS beads solution, on the nanostructured coverslips a $3.16 \mu\text{l}$ drop of polystyrene is placed next to the area where the nanostructures are. The polystyrene drop is required at a later stage for the alignment of the SRS /eHCARS signal (see calibration in Sec.3.3.2). After the polystyrene drop solidified, a double-sided adhesive imaging gasket is mounted on a cut microscopy slide (prepared as in Sec.3.1) and filled with about $16 \mu\text{l}$ of PS solution. The coverslip with nanostructures is then mounted on the other side of the gasket so that the gasket is sealed.

3.2.3 HEK293 Cells

To successfully perform measurements with living cells onto the antennas, it is important to establish a sample preparation protocol ensuring that the cells (Human Embryonic Kidney - HEK293 cells in our case) attach onto the nanoantennas without harming them. It is also necessary to identify the right conditions in which the cells can survive a prolonged time without causing a strong vibrational or fluorescent background. The following protocol has been developed in collaboration with Dr. Mark Young from Cardiff University, who provided us with the cell lines cultured in his laboratory. Stable cell lines of HEK293 cells wild type and HEK293 cells expressing C-terminally GFP-His-tagged rat P2X7 receptors (P2X7-GFP-His) are cultured in DMEM:F12 medium with 10% FBS. To detach the cells from the flask the medium is replaced by 5ml trypsin, which is neutralized after 5min with DMEM:F12. To achieve the desired cell concentration, the detached cells are resuspended in the required volume of medium. Different concentrations of cells have been tested as reported in Fig.3.11. From our tests, we found out that $5 \times 10^6 \mu\text{l}^{-1}$ leads to a good coverage of cells ensuring that enough cells settle on top of the nanoantennas avoiding too much cell-cell overlap. Meanwhile, the nanostructured coverslips undergo a 30-minutes cleaning process using 100% ethanol. After cleaning, as in the case of the PS beads sample, a $3.16 \mu\text{l}$ drop of polystyrene is placed adjacent to the region containing the AuNB arrays. Once the polystyrene droplet has solidified, a suspension of $15 \mu\text{l}$ with $5 \times 10^6 \mu\text{l}^{-1}$ cells is introduced on the central portion of the coverslip, on top of the nanostructures. The coverslip with the drop of concentrated cell suspension is then incubated for 30min to let the cells settle. Then 3mL of DMEM:F12 is added to protect the cells from drying out during the next 24hr incubation. Following the incubation period, the coverslips undergoes three rounds of washing with PBS to ensure the complete removal of dead cells and the DMEM:F12 medium. The presence of phenol red in the medium can contribute to a substantial fluorescent background, hence its removal is crucial. Subsequently, the

PBS is meticulously eliminated from the coverslip using blotting paper, taking care not to come into contact with the cells. Again a double-sided adhesive imaging gasket is mounted on a microscopy slide. It is filled with about 12 μl of phenol red-free FluoroBrite DMEM (GibcoTM FluoroBriteTM DMEM) with 25mM HEPES, which is needed to stabilize the pH of the medium in the absence of a stabilizing carbon dioxide atmosphere. The coverslip with the cells and nanostructures is then mounted on the other side of the gasket so that the gasket is sealed, therein containing the medium with the cells on the nanoantennas. The FluoroBrite DMEM with 25 mM HEPES has been also used for a control sample to test the response of the bowties in the absence of cells. The widefield z-stacks shown in Figure 3.12(a) and 3.12(b) were captured about 3hours apart. We can see that this protocol provides good coverage of cells attached to the coverslip on top of the antennas. The cells appear to be still alive after 3 hours. Indeed, the distribution of cells being different before (a) and after (b) indicates that they were alive.

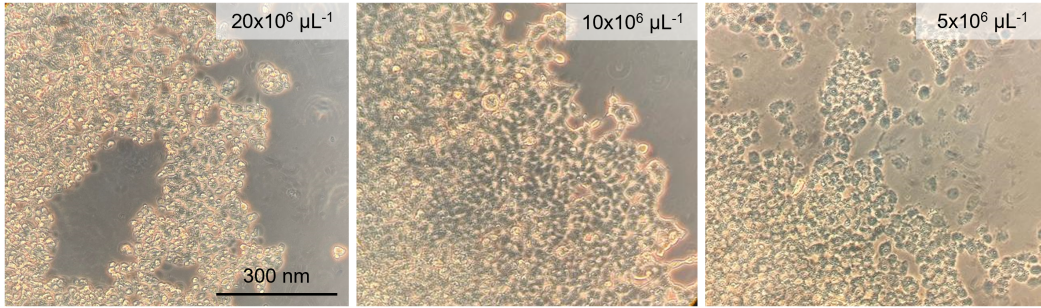


Figure 3.11: Wide field images of HEK293 cells (Objective 60x). The optimal cell concentration was determined visually through a wide-field microscope. For that, a 15 μl drop containing cells at $5 \times 10^6 \mu\text{l}^{-1}$, $10 \times 10^6 \mu\text{l}^{-1}$, or $20 \times 10^6 \mu\text{l}^{-1}$ was applied on top of an empty coverslip. After about 30 min the cells settled onto the coverslip and were incubated for 24 h before taking the images.

3.3 Multimodal microscope setup

3.3.1 Polarization resolved extinction

The optical cross-section is a physical property that characterizes a particle and determines its interaction with light. In fact, when some light encounters a particle the interaction can be of various modalities. The optical cross-section quantifies the likelihood of this interaction to occur. It is expressed in units of area. The extinction cross-section σ_{ext} is a specific type of optical cross-section that is associated with the extinction of light. σ_{ext} quantifies the NP efficiency in absorbing and scattering an incoming light, leading to its overall extinction. It is defined as:

$$\sigma_{\text{ext}} = \frac{P_{\text{ext}}}{I_i} \quad (3.3.1)$$

where I_i is the incident intensity and P_{ext} is the total power lost due to both absorption and scattering. It is possible also to separate the two different contributions in the following way:

$$\sigma_{\text{ext}} = \sigma_{\text{abs}} + \sigma_{\text{sca}} \quad (3.3.2)$$

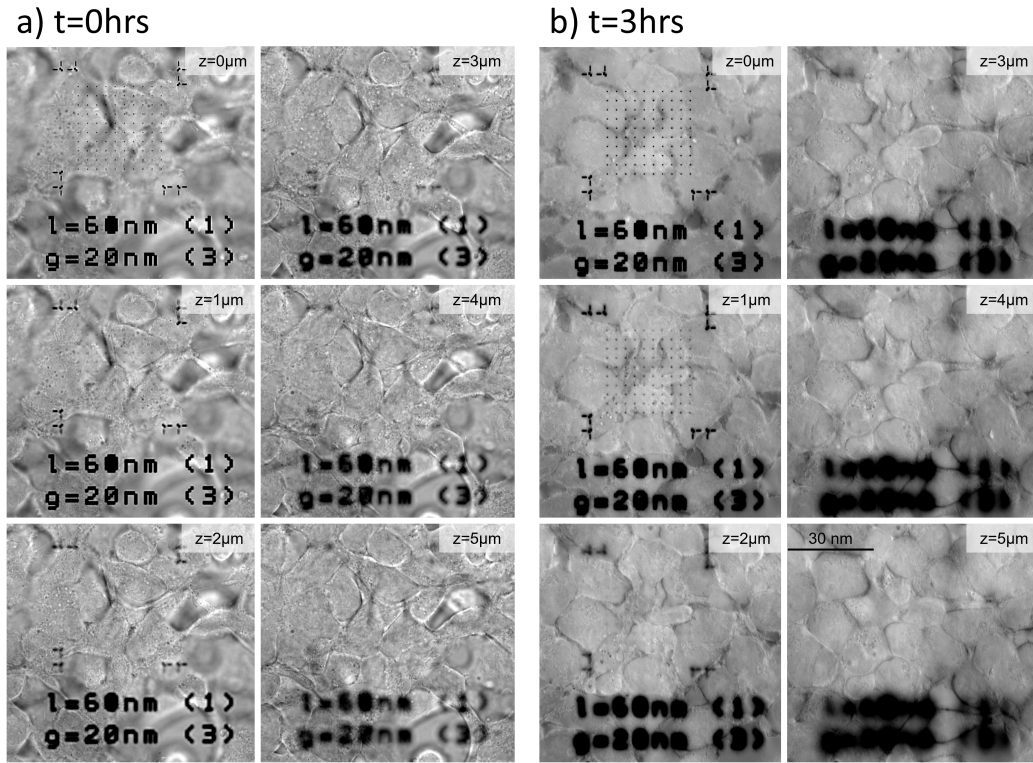


Figure 3.12: Widefield transmission images (Objective 100x) of HEK293 cells. The cells were deposited on top of the nanostructures and were imaged before (a) and after (b) the correlative fluorescence-eHCARS measurements with the focus at different z-sections (as indicated) with $z = 0 \mu\text{m}$ coinciding with the focus of the AuNBs.

The extinction cross-section intrinsically depends on the NP size and shape but also on host materials. By measuring σ_{ext} for different wavelengths we can obtain information about the particle geometrical characteristics and determine the position of the LSPR. Moreover, in this context, the extinction measurements have been used also to check an eventual change of NP geometrical characteristics due to the laser exposure.

The polarization resolved wide-field extinction micro-spectroscopy and polarization resolved extinction spectroscopy techniques, developed in our lab, are useful for the purpose of measuring σ_{ext} . A brief explanation of the basic principle of these techniques is given in the following. More details about them can be found in Ref. [97],[98] and [99].

Both wide-field extinction and extinction spectroscopy measurements were performed on a Nikon Ti-U inverted microscope (microscope stand shown in Fig.3.13), using as an illumination source a 100 W halogen lamp. The Nikon Ti-U inverted microscope stand was setup with a 1.34NA, $n=1.518$ oil-immersion condenser (Nikon MEL41410) and a 1.45NA, 100 \times , $n=1.518$ oil immersion objective (Nikon MRD00405) coupled with 1x tube-lens. Before the condenser, a rotatable linear polarizer is inserted allowing to change the illumination field polarization in the plane of the nanorod. This allows to measure the extinction properties for different polarization of the illumination light (see Fig.3.14). Six different polarization directions, indicated with θ in Fig.3.14, were used. They have a 30 $^\circ$ angle difference at the back

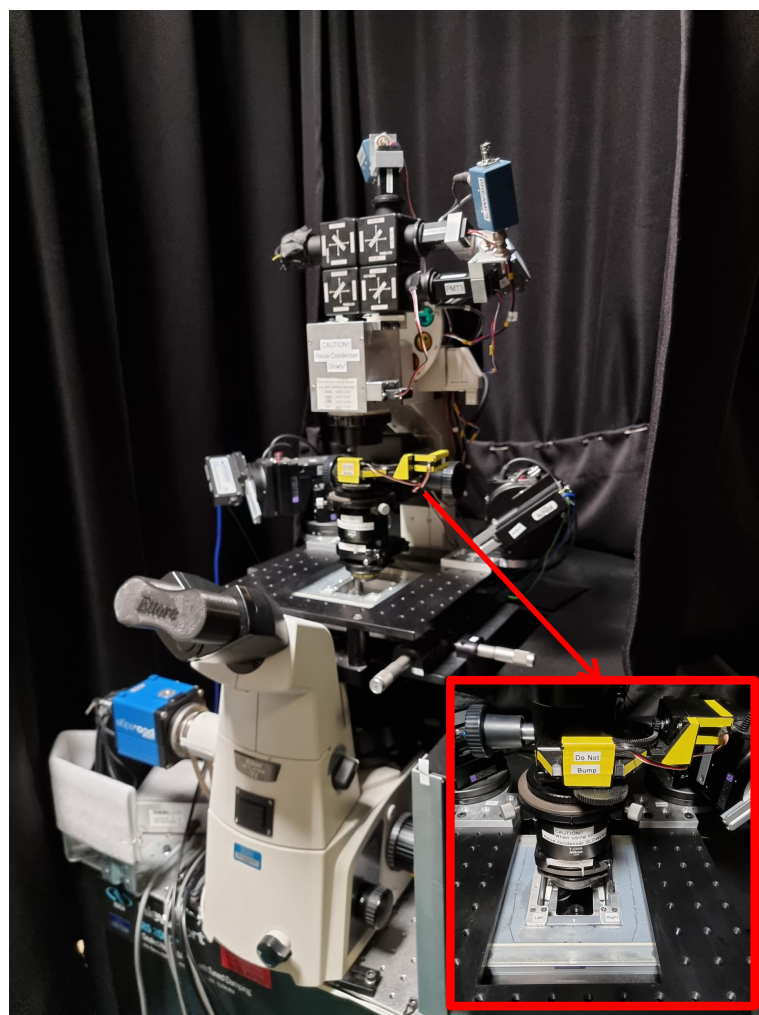


Figure 3.13: Nikon Ti-U inverted microscope with a zoom-in on the sample holder.

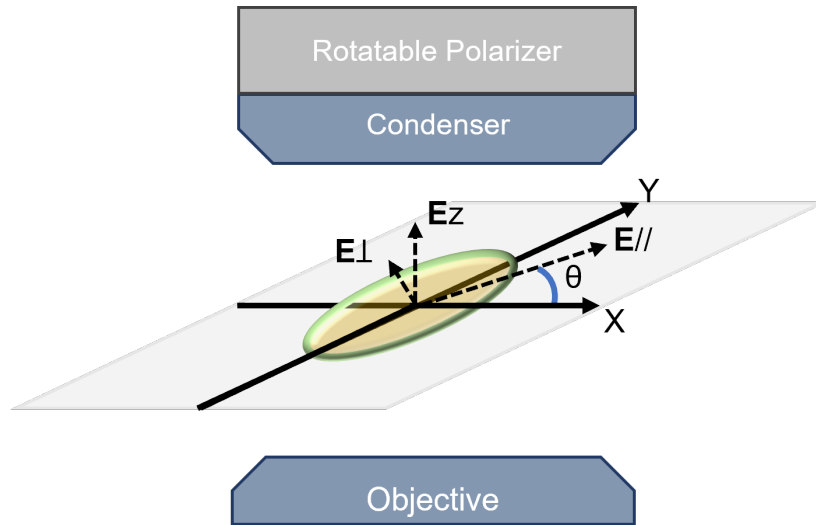


Figure 3.14: Sketch of the geometry of the NP in the measurement reference system. E_{\perp} and $E_{//}$ are in the xy plane. θ represents the angle at which the linear polarizer is set compared to the x axis in the back focal plane of the condenser. Although $E_{//}$ is the predominant field component in the field focus, E_{\perp} and E_z are still present due to the high NA employed (see Ref. [99])

focal plane of the condenser and are called respectively 0° , 30° , 60° , 90° , 120° , 150° .

Our wide-field extinction is a transmission based wide field imaging method to rapidly perform both the detection of single nano-objects and to extract a quantitative measurement of σ_{ext} . From a practical point of view, extinction microscopy is performed by taking two bright-field images, one with the NPs in a given in-plane position and the other with the NPs laterally shifted. The amount of the lateral shift needed, which depends on the NA of the objective and on the wavelength (λ) used, can be computed as:

$$S = 2R_i + 100\text{nm} \quad (3.3.3)$$

with

$$R_i = \frac{3\lambda}{2NA} \quad (3.3.4)$$

R_i is approximately the radius of the second Airy ring in the PSF for a given illumination wavelength λ (Ref.[97]). Choosing a lateral shift longer than S assures to avoid significant overlap of airy patterns. In our measurements, we adopted a lateral shift of $2 \mu\text{m}$. Then a background image is taken for blocked illumination. Calling the background-subtracted transmitted intensity of the bright-field image with the NP of interest in the center I_f , and the shifted one I_0 , the extinction cross-section of a NP located within the circular area A_i centered at the NP, with radius R_i , in the image can be expressed as

$$\sigma_{\text{ext}} = \int_{A_i} \Delta dA \quad (3.3.5)$$

where $\Delta = (I_0 - I_f)/I_0$. Basically, Δ represents the final extinction image, in which the NP appears as two spots, one bright and one dark, due to the lateral shifting. A wavelength-dependent spectroscopic analysis is possible using band-pass filters in the excitation beam path to select the wavelength of the exciting light from the white light lamp source. The image data was recorded using a scientific-complementary metal-oxide-semiconductor (CMOS) camera (PCO Edge 5.5), set to

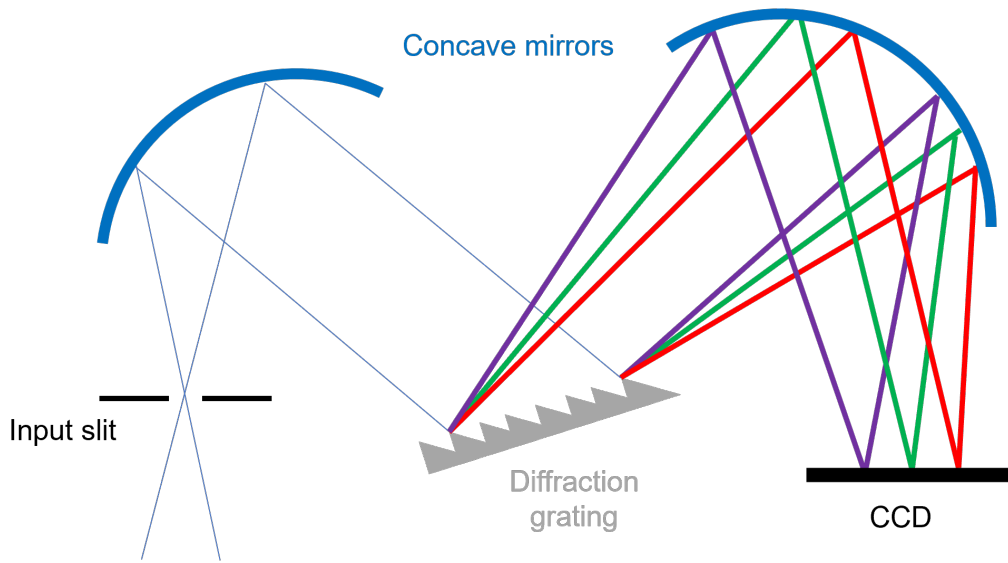


Figure 3.15: Simplified ray diagram of the spectroscopy setup. The rays arriving at the input slit are the ones collected by the Objective lens.

the maximum capability of acquiring 100 frames per second at 1196×621 pixels with 16-bit digitization, 0.54 electrons per count, and a full well capacity of $N_{fw} = 30000$ electrons. The adjustment of the illumination lamp power was done by maximizing it, without bringing the camera to saturation. Generally, I_f and I_0 are averaged over a number, N_i , of individual acquisitions, to reduce shot noise in the final image. To further reduce shot noise, this procedure is repeated N_r , moving the sample between the two positions. As explained in Ref.[99], this leads to a shot-noise limited noise in the measurement of σ_{ext} given by:

$$\hat{\sigma}_{ext} = \frac{R_i d_{px}}{M} \sqrt{\frac{\pi}{N_i N_r N_{fw}}} \quad (3.3.6)$$

where d_{px} is the pixel size ($6.5 \mu\text{m}$) and M (100) is the magnification onto the camera. For our measurements, we adopted $N_i=128$ and $N_r=10$, thus obtaining an $\hat{\sigma}_{ext} \sim 12 \text{ nm}^2$. The quantitative wide-field extinction image analysis is performed via a home built image analysis program written in IMAGEJ macro language, developed by Lukas Payne, that given the extinction images, returns the single particle σ_{ext} (see Ref.[97] for details).

With the same basic principle just explained, it is possible also to perform an extinction spectroscopy measurement using a spectrometer in the detection beam path, while retaining the white light illumination. In this case, all the wavelengths contained in the illumination light can be analyzed at the same time, giving also an accurate knowledge about the LSPR spectral positions. For the spectroscopy measurements the transmitted light collected by the microscope objective is sent to an imaging spectrometer (Horiba Jobin-Yvon iHR 550). As depicted in Fig.3.15, the light enters the spectrometer through a rectangular open slit, with adjustable opening. A first concave mirror collimates and redirects the input light toward a diffraction grating, equipped with 100 lines per mm, where it is spread out into a spectrum. Following this, a second concave mirror refocuses the spectrally dispersed light onto a charge-coupled device (CCD) camera (Andor Newton DU-971N), characterized by a 1600×400 pixels sensor with pixel pitch $16 \mu\text{m}$. The input slit is imaged

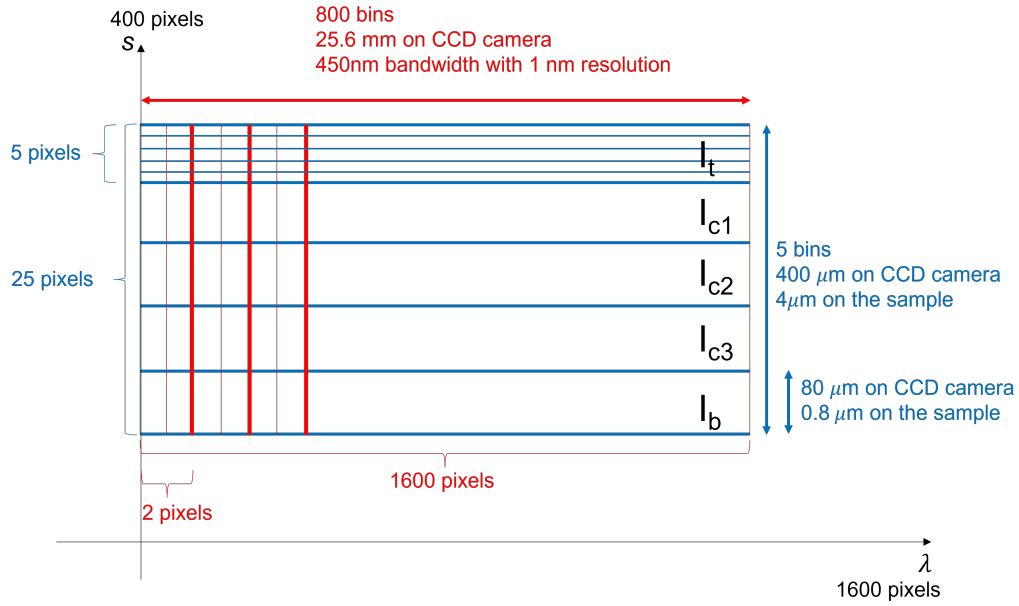


Figure 3.16: Schematic explanation of how the binning for the CCD camera pixels was performed in both horizontal (spectral) and vertical (spatial) direction.

1:1 onto the CCD. The CCD horizontal pixels are used for spectroscopy while the vertical ones allow spatial imaging of the sample. From the spectral point of view the resolution depends on the grating (which determines the detectable bandwidth that in our case is ~ 450 nm, as measured), on the CCD pixel pitch, on number of pixels used and on slit width related to the spectral dimension. In acquisition modality, we adopted a $80\mu\text{m}$ wide slit and exploited all the 1600 available pixels so that the spectral resolution turned to be ~ 1.7 nm. As the pixel bandwidth turned to be $450\text{ nm}/1600 \sim 0.3$ nm we could apply a 2 horizontal binning to double the signal without losing information. Regarding the spatial dimension, we decided to use 25 of the 400 pixels available on the CCD. As the square pixel size is $(16\mu\text{m})^2$, we occupy in this way $25 \times 16\mu\text{m} = 400\mu\text{m}$ on the CCD vertical axis. The magnification of the slit at the sample is simply the width divided by the magnification, this means that to the $400\mu\text{m}$ obtained on the CCD corresponds $4\mu\text{m}$ at the sample. As it is done in the spectral dimension, also in the spatial dimension we apply a binning so that we obtain 5 bins, each containing 5 pixels. Consequently, each bin corresponds $0.8\mu\text{m}$ on the sample. Figure 3.16 gives a representation of the binning used in both the horizontal and vertical axis of the CCD. The 2×5 binning is actually performed in the software (i.e. adding individual pixel counts) rather than on-chip to avoid saturation. The sample is moved (via the MCL nanostage) to have the nanoparticle under study, which has a typical PSF of ~ 500 nm radius, placed in the central vertical bin. We collected two shifted spectra, I_0^s and I_1^s , where the s indicate a spectrum, by taking 200 acquisitions for each, with an exposure time of 11 ms (obtaining intensity counts around 4×10^4). In the extinction spectroscopy measurement we perform a double referencing. The spatial referencing is similar to that of the wide-field method, shifting to an area nearby, without any NPs, and capturing spectra with the same settings. This first referencing is done so that each pixel point on the NR corresponds to a reference signal acquired via the same pixel of the CCD camera. The temporal referencing is instead given considering the top and bottom

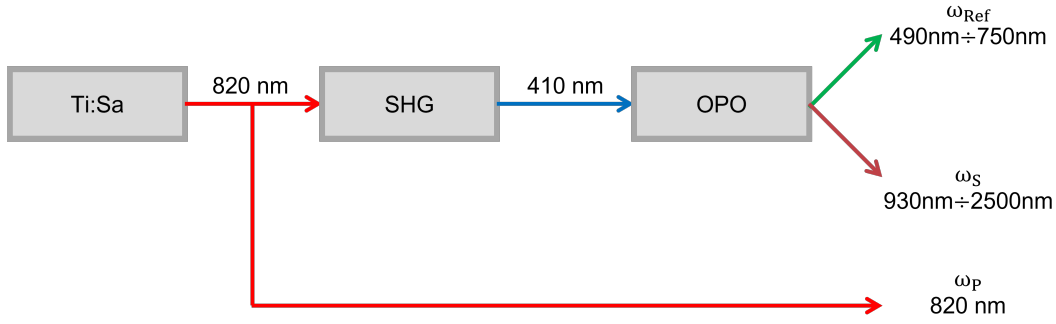


Figure 3.17: Sketch of laser source and wavelength outputs for multimodal nonlinear microscopy. The Ti:Sa laser source provides a laser beam with fundamental wavelength at 820 nm, 80 MHz repetition rate and 150 fs pulse duration. This is used both as Pump beams and also to pump an OPO, after being frequency-doubled via a second harmonic generation crystal, which provides both the Stokes and Reference beam for eH-CARS measurements.

bins and this is needed to compensate for eventual lamp intensity fluctuation. We actually used the three central bins to improve the vertical particle localization. Let us call the signal collected for the top (bottom) stripe I_t (I_b), and the signal from the center stripes I_{c1} , I_{c2} , I_{c3} , as in Fig.3.16. The differential transmission spectrum is calculated using:

$$\Delta^s = 1 - \left(\frac{I_{c1}^0 + I_{c2}^0 + I_{c3}^0}{I_t^0 + I_b^0} \frac{I_t^1 + I_b^1}{I_{c1}^1 + I_{c2}^1 + I_{c3}^1} \right) \quad (3.3.7)$$

where I^0 (I^1) is used to indicate the spectrum acquired at (away from) the nanoparticle.

3.3.2 Heterodyne epi-detected CARS (eH-CARS)

A complete and detailed description of the setup used to perform the eH-CARS, previously developed in our lab, can be found in Ref.[45]. The setup is shown diagrammatically in Fig.3.17 and Fig.3.18. Notably, this is a multimodal microscope built also to perform conventional forward-CARS (F-CARS), SRS, TPF, and SHG measurements as depicted in Figure 3.18.

In our implementation, we need a pump, a Stokes, and a reference beams. A mode-locked Titanium:Sapphire (Ti:Sa) laser source (Mai-Tai HP, Spectra Physics) provides pulses characterized by a repetition rate ν_L of 80MHz and 150fs duration. It is a tunable laser (from 690 nm to 1040 nm), but its fundamental is kept at 820 nm and used as pump (λ_P). The laser source then is also frequency-doubled to pump an optical parametric oscillator (Inspire OPO, Radiantis). The optical parametric oscillator (OPO) provides an idler, used as a Stokes beam, with a tunable wavelength in the range 930-2500 nm (λ_S). Consequently, the signal, used as a reference, results in the range 490 nm-750 nm (λ_{ref}) (see Fig.3.17). The tunability of the Stokes wavelength allows to excite a wide range of vibrational frequency Ω , as shown in Fig.3.19 (black). They are in fact connected by the relation $\Omega = \omega_P - \omega_S$, where ω_P is constant as we keep λ_P at 820 nm. The reference wavelength will consequently result equal to the CARS wavelength, which can be derived using the relation $\omega_{CARS} = \omega_P + \Omega$ (see Fig.3.19 (red)). Using 820 nm for the pump and for example 1080 nm and 660 nm as

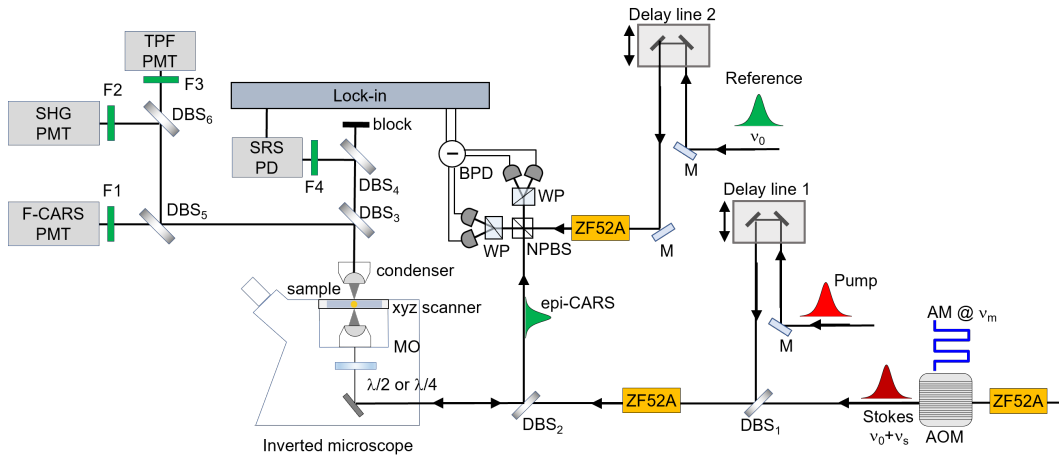


Figure 3.18: Sketch of the multimodal SRS /SHG/TPF/F-CARS/eH-CARS microscope. Stokes pulses are amplitude-modulated at ν_m and radio-frequency shifted at ν_s using an AOM. Spectral focusing is applied via H-ZF52A glass blocks. The pump travels through a delay line for IFD optimization. Pump and Stokes are coupled via DBSs into an inverted microscope. F-CARS/SHG/MPF are detected in transmission using a bandpass filters (F1, F2, F3) and a PMT. SRS is detected using a bandpass filter F4 and a resonant photodiode (PD) and filtered at ν_m by using a lock-in amplifier. eH-CARS is collected in epi-geometry and combined with a reference pulse (which travels through a delay line for temporal overlap optimization) by using a non-polarizing beam splitter (NBS), polarization split by using a Wollaston prism (WP) and detected by using pairs of balanced photodiodes (BPD).

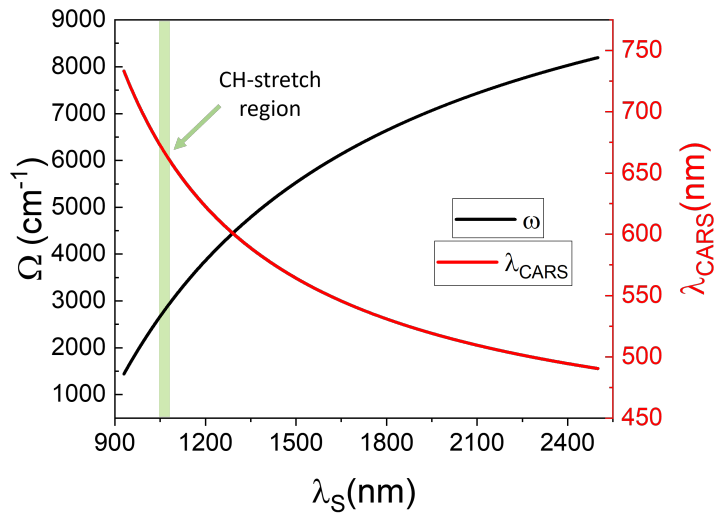


Figure 3.19: Dependence of exited vibrational frequency Ω and CARS wavelength λ_{CARS} on the Stokes wavelength (λ_S), keeping the pump wavelength (λ_P) fixed at 820nm.

central wavelengths for Stokes and reference signal respectively, it is possible to drive vibrational resonances in the CH-stretch region (around 3000 cm^{-1}), which is the spectral region on which this project focus. Figure 3.18 gives all the details about how the excitation of the sample and the detection of the consequent generated CARS signal are performed. To selectively drive a molecular vibration of interest the spectral focusing method is used (see Ref.[100] for more details). In practice, all the involved laser pulses, having a duration of 150 fs, are spectrally broad, with a width typically 10 times larger than Raman linewidths of biomolecules of interest, e.g. lipids. In spectral focusing, an equal linear chirp is applied to both pump and Stokes, using glass blocks (ZF52A), creating a constant instantaneous frequency difference (IFD) between the two beams. The temporal envelope of such pulses can be elongated, by the linear chirp, to a few picoseconds. The spectral resolution achieved, determined by the Fourier-limit of the temporal envelope, is around 20 cm^{-1} , which coincides with typical Raman linewidths of CH stretch vibrations. To tune the IFD, the pump beam travels also through a motorized delay line (delay line 1). Also the reference is chirped by glass blocks to acquire the same linear chirp as the generated CARS signal at the non-polarizing beam splitter (NPBS) of the balanced detector. The chirp applied to the reference is determined assuming that the CARS signal will have the same chirp as pump and Stokes with the additional chip due to the microscope objective and the tube lens. Moreover, the reference travels through a motorized delay line (delay line 2), in order to provide spectral and temporal overlap with the CARS field, allowing for heterodyning. For the heterodyne detection, an acousto-optic modulator (AOM) driven at the radiofrequency $\nu_s=77\text{MHz}$ is used to frequency up-shift the Stokes beam. Then, pump and Stokes beams are recombined by a dichroic beam splitters (DBS), in the sketch DBS1, and sent onto a commercial inverted microscope (the same in Section 3.3.1) via a second dichroic beam splitter DBS2. Finally, they are focused onto the sample by a high NA microscope objective, a 1.45NA $100\times$ oil-immersion objective (Nikon MRD00405) used with $1\times$ tube-lens. We have the possibility of inserting a wave plate before the objective, in order to change beam polarization onto the sample plane. In this work, both a $\lambda/2$ and $\lambda/4$ wave plate have been used. The sample is positioned and moved with respect to the focal volume of the objective by scanning an xyz sample stage with nanometric position accuracy (resolution of 0.4 nm over a range in XYZ of $200\text{ }\mu\text{m}^3$ with 15 ms response time). After the excitation of the sample, the generated CARS signal is collected in reflection (epi-CARS). This implementation is useful taking into account the size of the microscope PSF, which extends axially (along the z direction) about $1\text{ }\mu\text{m}$, and the typical thickness of thin lipid bilayer (4-5 nm). The epi-detection allows to remain sensitive to the interfaces because most of the CARS contribution from bulk media, excited within the PSF, mainly propagates in the forward direction. After being transmitted by DBS2, the epi-CARS is recombined in a NPBS with the reference beam for interferometric detection. Through this interferometric detection the measured signal is also free from any incoherent background (such as fluorescence). Moreover, non-resonant contributions given by electronic FWM processes can be spatially, spectrally and temporally distinguished in the detection. Specifically, the delay time between the reference pulse and the CARS signal can be adjusted to maximize the interference with the vibrationally resonant response having a coherence time of picoseconds, against instantaneous non-resonant nonlinearities. The interference between the epi-CARS signal and the reference field is separated by using a Wollaston prism (WP) into two orthogonal polarization com-

ponents (nominally, vertical (V) and horizontal (H)) and these are detected by a balanced photodiodes (BPD), characterized by high quantum efficiency. This detection scheme, which measures the current difference in the interferometer arms, allows to reject classical noise and to reach shot noise limitation. The heterodyne technique is implemented by exploiting the frequency down-shifting of the epi-CARS resulting from the shift applied to the Stokes frequency. The interference between the CARS field and the reference is then detected at 3MHz using a dual-channel lock-in amplifier (ZI HF2), providing amplitude and phase components. Thanks to the heterodyne method it is possible to measure the amplitude and phase of the field.

3.3.3 Forward-CARS, SRS, SHG, and TPF

Conventional forward-CARS (F-CARS), SRS, SHG, and TPF detection are implemented in the microscope setup.

For SRS, the Stokes beam was amplitude modulated by the AOM, driven with a square wave amplitude modulation of frequency $\nu_m = 2.5\text{MHz}$. F-CARS, SRS, SHG, and TPF are collected by a 1.34 NA oil condenser in transmission geometry. A dichroic beam splitter DBS3 reflects the F-CARS, SHG, and TPF signals and transmits the Pump and Stokes beams. SRS, in the form of stimulated Raman loss, is measured on the Pump beam, selected by using an additional dichroic (DBS4), which reflects the signal at 820 nm (and transmits the Stokes beam that is then blocked), together with a short-pass filter F4 (790 nm - 860 nm), and detected as an intensity modulation at $\nu_m = 2.5\text{MHz}$ via a PD and the dual phase lock-in amplifier (ZI HF2), taking the in-phase component of the SRS modulation. The other dichroic beam splitters (DBS5 and DBS6) and filters (F1, F2, and F3) are ordered in such a way that DBS5 transmits the F-CARS signals and reflects the SHG and the TPF one. Then, DBS6 transmits the TPF, which passes through a bandpass filter F3 (bandwidth:468 nm-552 nm) and is detected by a photomultiplier (TPF photonmultiplier (PMT)) and reflects the SHG signal, which passes through a bandpass filter F2 (bandwidth:391 nm-437nm) and is detected by another photomultiplier (SHG PMT). Finally, the F-CARS signal passes through the correspondent bandpass filter F1 (bandwidth:642 nm-707 nm) and is detected by another photomultiplier (F-CARS PMT). Additionally, even if in the standard configuration wavelengths of 642 nm-707 nm are sent to the CARS PMT, the latter filter can be exchanged to measure fluorescence for wavelengths longer than 540 nm.

3.3.4 Setup calibration for eH-CARS measurements in silicone oil

As mentioned in Section 3.1, the NRs were characterized while surrounded by silicone oil. The Raman spectrum of silicone oil exhibits typical stretching and bending vibration bands of CHx aliphatic groups at $2800\text{-}3000\text{ cm}^{-1}$, with a main peak centered at 2904 cm^{-1} (Ref.[101]). The latter was the wavenumber at which most of the characterization was performed.

To initiate the setup calibration, the primary step involves configuring the appropriate OPO parameters. The user must provide the wavelength value at which the OPO signal (and consequently the OPO idler) should be generated, considering the pump wavelength set at 820 nm. This configuration dictates the initial IFD, denoted as IFD_c . Subsequently, the spectral focusing technique is employed to achieve both high spectral resolution and to fine-tune the IFD within the pulse's spectral

width. The wavelength inserted in the OPO is the one that allows us to have an $\text{IFD}_c \sim +50 \text{ cm}^{-1}$ higher than the IFD at which we have to measure. In Ref.[102], which is a prior publication by our research group, this choice is explained. When measuring a CARS phenomenon is necessary to guarantee the right time ordering of the pulses involved in the process and interacting with the sample. It has been demonstrated both theoretically and experimentally that an $\text{IFD}_c \sim \text{IFD} + 50 \text{ cm}^{-1}$ is the optimal choice, taking into account the finite coherence time of the Raman resonances, to then have the pump pulse arrival and temporal width such that it is able both to drive the coherence (together with the Stokes beam) and to act as a probe. In our experiment, we typically addressed the vibrational excitation at 2904 cm^{-1} . Thus, the OPO was set to provide an IFD_c at $\sim 2950 \text{ cm}^{-1}$. The relation between the wavenumber (Ω) corresponding to the excited vibration and the exciting wavelengths (λ_P and λ_S) is:

$$\Omega = \frac{1}{\lambda_P} - \frac{1}{\lambda_S} \quad (3.3.8)$$

Given the $\lambda_P = 820 \text{ nm}$, for $\Omega = 2950 \text{ cm}^{-1}$, the consequent Stokes wavelength has to be 1081 nm . The Stokes corresponds to the idler by the OPO, so that from its value we can compute the wavelength the OPO requires as input, which corresponds to the CARS wavelength (λ_{CARS}). Given λ_P and λ_S , λ_{CARS} is given by:

$$\frac{1}{\lambda_{\text{CARS}}} = \frac{2}{\lambda_P} - \frac{1}{\lambda_S} \quad (3.3.9)$$

which gives 660 nm . The OPO signal has to be set to have the same wavelength as the CARS one as it will be used as the reference in the heterodyne detection. To this setting, follows a fine calibration of the IFD in SRS modality. SRS in this case is preferred over F-CARS and eH-CARS because it only contains the resonant contribution of the signal, which is proportional to $\text{Im}\{\chi_{\text{oil}}^{(3)}\}$. Another possibility would have been to measure the CARS spectrum, but it is affected by both the resonant and non-resonant contribution of the signal. The interference between the resonant and non-resonant part led to a broader and dispersive lineshape for the spectrum compared to the one obtainable with an SRS scan. As explained before, the pump beam is scanned over a delay, typically few ps to tune the IFD over a range of 500 cm^{-1} , while both pump and Stokes beams are focused in silicone oil bulk (as shown in the sketch of Fig.3.21), to then select the pump delay which gives the maximum SRS signals. An example of SRS spectrum obtained after the calibration is given in Fig.3.21(a)). The typical power used for these calibration steps is around 5 mW for pump and 10 mW for Stokes at the beam focus. In general, when subsequently measuring at different IFD, the same value of IFD_c can be kept as far as the delay time between pump and Stokes, required to address the specific IFD, ensures that the two pulses remain temporally overlapped, allowing them to interact effectively with the sample. Figure 3.20 illustrates how, once IFD_c is established, variations in the pump-Stokes delay result in an IFD tuning accompanied by a change in the intensity of the pump-Stokes overlap, with a full width at half maximum around 150 cm^{-1} . In fact, it shows a measurement of F-CARS, acquired after pump and Stokes alignment, focusing the laser beams within the non resonant glass coverslip, with $\text{IFD}_c \sim 2900 \text{ cm}^{-1}$ and scanning the pump-Stokes delay to tune the IFD over a 400 cm^{-1} range. Being the material non resonant, the detected CARS does not depend on the time ordering between pump and Stokes beams but only depends on

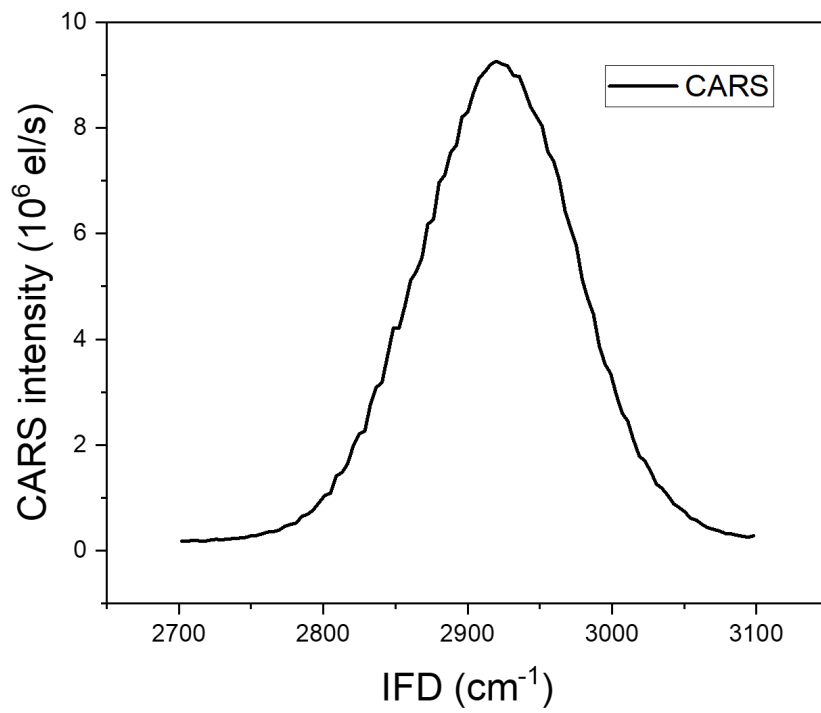


Figure 3.20: F-CARS intensity acquired after OPO tuning to have $\text{IFD}_c \sim 2900 \text{ cm}^{-1}$, focusing pump and Stokes laser beams within the non resonant glass coverslip ($P_P=5 \text{ mW}$, $P_S=10 \text{ mW}$), tuning the IFD by varying pump-Stokes delay to tune the IFD over a 400 cm^{-1} range.

their overlap. Once the IFD is calibrated, we need to calibrate the delay between the epi-CARS signal and the reference so that they result temporally overlapped at the NPBS. This calibration is performed by focusing pump and Stokes beams at the glass-oil interface (again shown in Fig. 3.21 sketch). The reference delay is scanned over a range from 10 to 50 ps. Figure 3.21(b) shows a eH-CARS amplitude (A) and phase (Φ) xz image ($5\mu\text{m}\times 5\mu\text{m}$, 54×501 steps), taking centering at the glass-oil interface, performed selecting the optimized epi-CARS - reference delay. In this case, a $\lambda/4$ wave plate was inserted in the beam path, with the consequent detection of a signal coming from the glass-oil interface nearly fully vertically polarized (see Sec.5.1 for more information about the use of a $\lambda/4$ wave plate). In general, the imaging measurements need a lock-in offset correction, to compensate for any offset or baseline signal present in the output of the lock-in amplifier. The correction was carried out treating the signal as a complex quantity and centering at zero independently both its real and imaginary components. The offset mainly arises from electronic noise. An example of lock-in correction is given in Fig.A.1. From Fig.3.21(b), it is clear how the detection of an epi-CARS signal is possible only if the beams are focused at an interface. In fact, the epi-CARS signal can arise from both a backward reflection of CARS signal generated in the forward direction, or it can be directly generated in the backward direction. The first case takes place if there is a step in the $\chi^{(1)}$ at an interface, which corresponds to a change in the refractive index, while a backward generated signal arises from a step in the $\chi^{(3)}$. Since the coverslip glass and the silicone oil are refractive index matched, the detection of the epi-CARS signal is due to the second case. The amplitude reached its maximum at the glass-oil interface z position and it doesn't show any fringes because it represents the overall magnitude of the superimposed waves used for interferometric detection. Fringes can be instead observed in the phase, reflecting the constructive and destructive interference pattern depending on the phase difference between the epi-CARS and the reference.

3.4 Numerical simulations via COMSOL

Among the several numerical available approaches for electromagnetic simulations, the finite element method (FEM) has been chosen for this project. It is essentially a mathematical algorithm to discretize and solve partial differential equations, able to handle irregular geometries and fine features within large domains. In fact, the non-regular tetrahedral adaptive mesh used to discretize space in the FEM can accurately approximate curved surfaces and be selectively refined in specific areas of interest, minimizing discretization errors compared to other approximations that use rectangular division. With the commercial software COMSOL Multiphysics[®], it is possible to implement the FEM within a convenient user interface. A comprehensive explanation of the developed model is outside the scope of this work, but a thorough description can be found in Ref.[103] by Attilio Zilli. Here, our focus will be on the part of the model exploited within this project and the modifications made to align it with the required specifications.

The models discussed in this work have been solved via the electromagnetic waves frequency domain (EWFD) interface, included in the *Wave optics module* and *RF module*. In COMSOL, the term interface refers to a specific partial differential equation being solved. Within each module, all the interfaces related to a given class of phenomenon are grouped. The EWFD interface is particularly use-

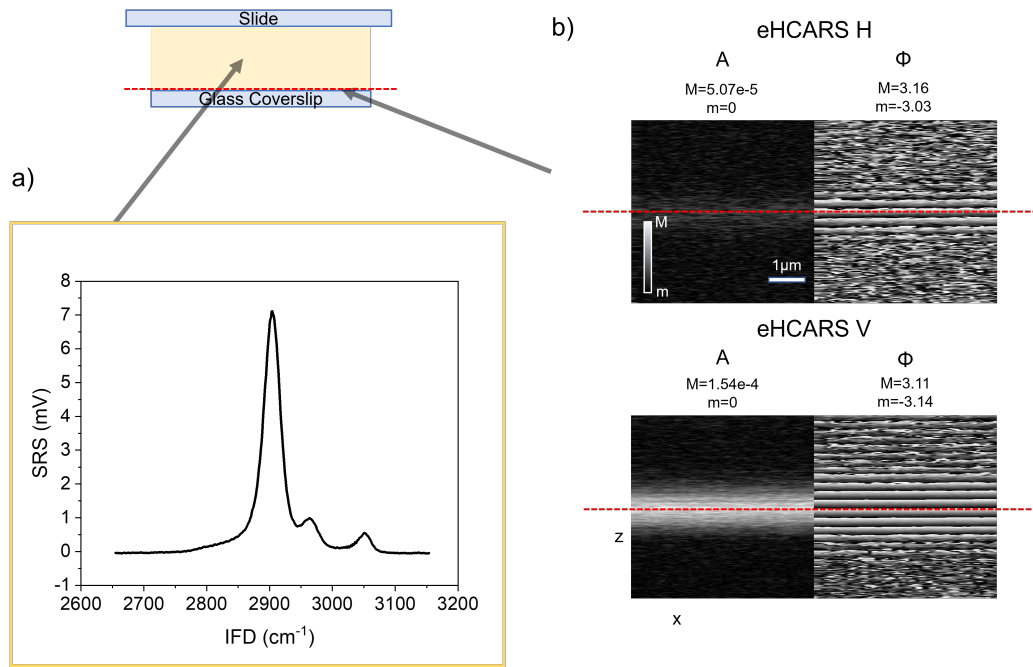


Figure 3.21: Calibration measurements. The sketch illustrates the point of the sample where the laser beams were focused during the two calibration measurements (center, within silicone oil bulk, for the IFD calibration via SRS and red dotted line, at glass-silicone oil interface, for reference delay optimization). (a) Measured SRS spectrum of Silicone oil. (b) eH-CARS amplitude (A) and phase (Φ), for both detected components (horizontal (H) and vertical (V)) of xz scan at glass-oil interface, at IFD=2904 cm^{-1} and with the optimized Reference delay (see text).

ful for analyzing and simulating electromagnetic wave propagation, scattering, and radiation phenomena. It allows to solve Maxwell's equations in the frequency domain, looking for a monochromatic solution, assuming a harmonic time dependence ($e^{-i\omega t}$) for all fields and sources. The Maxwell's equations can be expressed in the frequency domain as follows:

$$\nabla \cdot \mathbf{D} = \rho \quad (3.4.1)$$

$$\nabla \cdot \mathbf{B} = 0 \quad (3.4.2)$$

$$\nabla \times \mathbf{E} = i\omega \mathbf{B} \quad (3.4.3)$$

$$\nabla \times \mathbf{H} = -i\omega \mathbf{D} + \mathbf{J} \quad (3.4.4)$$

where \mathbf{E} (\mathbf{B}) is the electric (magnetic) field in free space while \mathbf{D} (\mathbf{H}) is the electric (magnetic) field propagating in a material. Exploiting the constitutive relation $\mathbf{B} = \mu \mathbf{H}$ and $\mathbf{D} = \epsilon \mathbf{E}$ it is possible to reformulated electromagnetics in terms of \mathbf{E} alone, as :

$$\nabla \times \mu^{-1}(\nabla \times \mathbf{E}) - \omega^2 \epsilon \mathbf{E} = i\omega \mathbf{J} \quad (3.4.5)$$

In Eq.3.4.5, μ (permeability) and ϵ (permittivity) represent the material properties, while the external current \mathbf{J} represents a source term introduced in the simulation volume, which does not originate from the fields. It is important to underline that under the EWFD interface, the inelastic scattering process can not be treated, as the equation is solved only for a ω per time. Additionally, the EWFD interface relies on

a time-independent formulation of electromagnetism, so that transient phenomena can not be described. In COMSOL, when using the EWFD interface, two possible approaches to solve a problem can be followed:

- *Full field formulation:*
It directly solves Eq.3.4.5 and it is used when it is necessary to introduce an analytical expression for $\mathbf{J}(\mathbf{r})$.
- *Scattered field formulation:*
It is convenient to be used when a scattering phenomenon is treated. In this formulation the total field \mathbf{E}_{tot} is seen as given by $\mathbf{E}_{\text{sca}} + \mathbf{E}_{\text{back}}$ with \mathbf{E}_{sca} the scattered field and \mathbf{E}_{back} the background field that represents a radiative excitation coming from a distant source. Writing $\mathbf{E}_{\text{tot}} = \mathbf{E}_{\text{sca}} + \mathbf{E}_{\text{back}}$, Eq.3.4.5 can also be rewritten as

$$(\nabla \times \mu^{-1} \nabla \times - \omega^2 \epsilon) \mathbf{E}_{\text{sca}} = i\omega \mathbf{J} - (\nabla \times \mu^{-1} \nabla \times - \omega^2 \epsilon) \mathbf{E}_{\text{back}} \quad (3.4.6)$$

so that \mathbf{E}_{sca} is the variable solved by COMSOL and \mathbf{E}_{back} is defined by the user with either an analytical description or a numerical vector field.

In this work, depending on the type of problem under study, both approaches have been exploited.

To combine the requirement imposed by the FEM of having a finite-sized simulation volume together with the need of mimicking open boundaries for radiation, the tools provided by COMSOL of introducing a perfectly matched layer (PML) are exploited. A PML can be seen as a perfectly absorbing layer that avoids a simple truncation of the simulated domain, which would lead to unwanted artificial reflection of the radiations into the computational domain. Mathematically, a PML is implemented by introducing a complex-valued permittivity ϵ and permeability μ , so that the PML acts as a region where the electromagnetic waves are attenuated exponentially as they propagate away from the boundary. This attenuation converts propagating waves into decaying ones, ensuring that they do not reflect back into the domain (Ref.[104]). In order to build models that properly describe the experimental conditions, we have to take into account that in our microscopy systems, the condenser and objective lenses are placed in the *far-field* (FF) of the studied object. The *far-field* domain refers to the region or zone in which electromagnetic waves have propagated a sufficient distance from their source and exhibit characteristics that are independent of the specific details of the source. Once arrived in the *far-field* domain, the radiation is collected over a finite solid angle, the so-called acceptance. COMSOL provides in post-processing the possibility of using the so-called *far-field variables* in specified domains. A field in the FF domain (E_{FF}) is computed via the Stratton-Chu transform (Ref.[105]):

$$E_{\text{FF}} = -\frac{ik}{4\pi} \hat{\mathbf{r}} \times \int_{\Gamma_{\text{FF}}} \left[\hat{\mathbf{r}} \times \mathbf{E} - \sqrt{\frac{\mu}{\epsilon}} \hat{\mathbf{r}} \times (\hat{\mathbf{n}} \times \mathbf{H}) e^{ikr} \cdot \hat{\mathbf{r}} \right] d\Gamma \quad (3.4.7)$$

where $\hat{\mathbf{r}}$ represent the direction, the surface integration is performed over the outer boundary Γ_{FF} of the FF domain and $\hat{\mathbf{n}}$ identifies the normal to Γ_{FF} in every point. Essentially, the analytical solution, as a function of $\hat{\mathbf{r}}$, of the simulated field at the surface, delimiting the simulation volume is converted as a function of the emission angles to then compute the amount of the field being collected by the acceptance angle of the objective. It is important to underline that E_{FF} is not an electric field as its unit of measurement results to be in Volt, thus it represents the measured far field, given the correspondent near field.

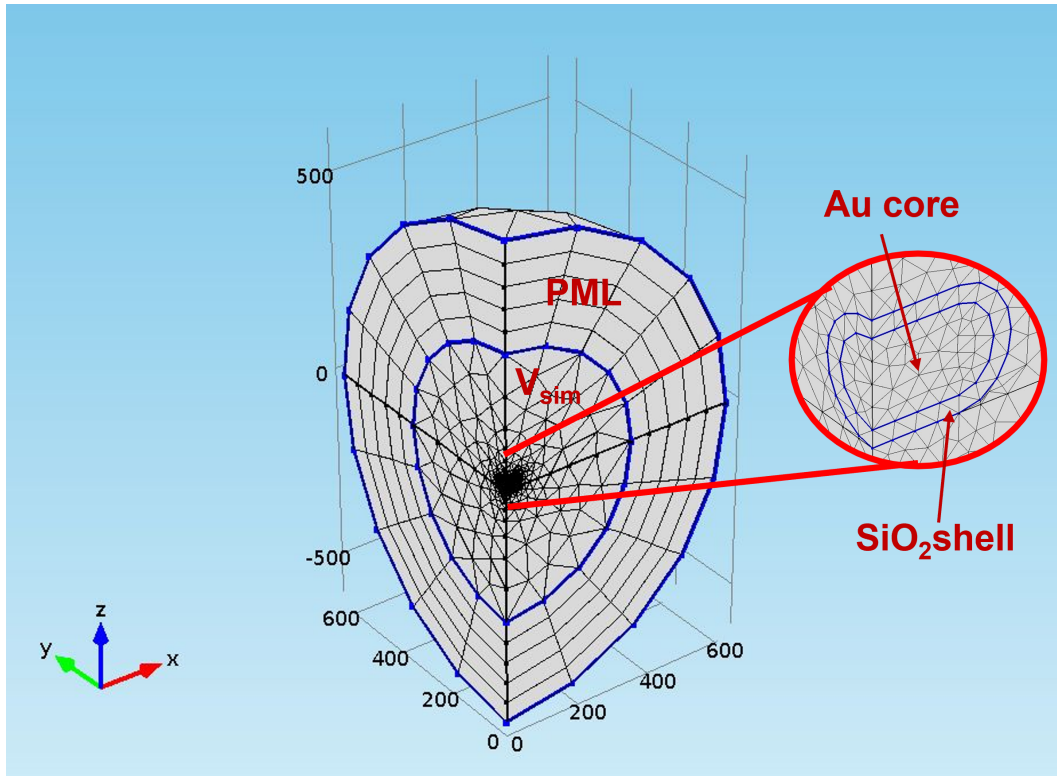


Figure 3.22: Typical geometry and meshing of the COMSOL models adopted within this work. Overview of the simulated volume V_{sim} , a quarter of a sphere encircled by a PML of homogeneous thickness. An NR is placed in the middle of V_{sim} , above the $z = 0$ optical interface and the NR close-up is reported to make visible its Au core and the SiO_2 shell.

Geometry of the models

Within this project, two models have been developed to simulate both the elastic linear scattering phenomenon and the nonlinear scattering phenomenon. The geometry of the models were built according to the real experimental configuration. In this Section, all the common characteristics of the built models will be given. The tested sample is given by a silica-coated NR placed on a dielectric interface (the BK-7 coverslip, $n_B = 1.52$), surrounded by silicone oil ($n_{\text{oil}} = 1.523$) (Ref.[106]). The typical geometry adopted together with its mesh is reported in Fig.3.22. The simulation volume (V_{sim}) is implemented as a quarter of a sphere with radius $r_{\text{sim}} = \lambda_0/2n_0$, encircled by a PML of homogeneous thickness $t_{\text{PML}} = \lambda_0/2n_0$, where λ_0 is the wavelength adopted during the simulation and n_0 generally is the average of the involved refractive index. The choice of r_{sim} was made to ensure simulation boundaries outside the reactive near field (NF) region of the NR. The implementation of the simulation volume (V_{sim}) as a quarter of a sphere, instead of using a complete sphere, speeds up the solutions as well as the FF calculations and is possible given the symmetry of the problems. For an object having $x = 0$ and $y = 0$ as mirror planes (as our NRs) only a quarter of the geometry needs to be solved. The symmetry is implemented by assigning a perfect electric conductor (PEC) boundary and a perfect magnetic conductor (PMC) boundary at either $x = 0$ or $y = 0$ planes depending on the polarization of the exciting field. As explained in the following, in our simulation we will use exciting fields with fixed polarization along and across the NR. A

PEC boundary reverses the sign of the normal component of the electric field while preserving the sign of the tangential component, while a PMC boundary conserves the sign of the normal component and reverses the sign of the tangential component across the interface. Regarding the adopted mesh, V_{sim} is meshed with a free tetrahedral mesh having a maximum element size of $\lambda/5n_0$, which ensures a sufficient sampling of the electric field, while the PML is meshed with a swept mesh of five elements of constant thickness along the radial direction. The NR, placed above the $z = 0$ optical interface surrounded by silicone oil, is built combining a cylinder, as the rod main body, with an ellipsoid, to recreate the rod tip. The longitudinal axis of the NR is chosen to be along the x-axis of the reference system. The system was built so that L_{rod} represents the total rod length (from tip to tip), D_{rod} represents the rod diameter, and R_{tip} , defined as the x-semi-axis of the ellipsoid, represents the tip length. Again, the NR aspect ratio (AR) is given by $AR=L_{\text{rod}}/D_{\text{rod}}$. In a similar way as the NR, the silica shell, with a homogeneous thickness t_{shell} , has been built. Regarding the refractive index of the silica shell, the following expression has been used:

$$n_{\text{shell}} = (1 - f_{\text{oil}})n_{\text{SiO}_2} + f_{\text{oil}}n_{\text{oil}} \quad (3.4.8)$$

where we take into account the possibility of having a porous silica shell and f_{oil} represent the fraction of oil within the shell due to its porosity. In the case of no-porous shell $f_{\text{oil}}=0$ and $n_{\text{shell}}=n_{\text{SiO}_2} = 1.458$ (Ref.[107]).

3.4.1 Extinction

To simulate a linear elastic scattering phenomenon, the *Scattered field formulation* has been exploited. Radiative excitation, represented by \mathbf{E}_{back} , is introduced in the model as a plane wave propagating along the positive direction of the z -axis:

$$\mathbf{E}_{\text{back}} = E_i e^{-in_0 \mathbf{k}z} \quad (3.4.9)$$

with \mathbf{k} the wave vector and a nominal amplitude E of 1 V/m. Within this work, we simulated the extinction cross-section of a nanorod for exciting light linearly polarized along and across the particle. This translates into imposing \mathbf{E}_{back} to have just one component on the x - or the y -axis respectively for the two cases. When simulating the field linearly polarized along the NR, the PEC boundary is set to be on the $x = 0$ plane, while the PMC boundary to the $y = 0$ plane. Vice versa for the case of the excitation linearly polarized across the NR. A solution of this model consists of the value of the electromagnetic field components at every node of the spatial mesh. The field itself and also other derived quantities can be visualized in space as false color maps. All figures and results in this section refer to an exemplary NR with the following characteristics: $D_{\text{rod}} = 40$ nm, $L_{\text{rod}} = 68$ nm ($AR= 1.7$), $R_{\text{tip}} = D_{\text{rod}}/(2.5)$, $t_{\text{shell}} = 10$ nm with $f_{\text{oil}} = 0$. Here, the single-crystal $\epsilon_{\text{Au}}(\lambda)$ dataset by Olmon et al. (Ref.[108]), shown in Fig.3.23, has been used and more detailed study about the optimized dataset for $\epsilon_{\text{Au}}(\lambda)$ will be presented in Sec.4.1.3.1.

Figure 3.24 displays the computed $\mathbf{E}_{\text{sca}}/\mathbf{E}_{\text{back}}$ (top) and $\mathbf{E}_{\text{tot}}/\mathbf{E}_{\text{back}}$ (bottom) obtained when the exemplary NR is excited resonantly with its longitudinal LSPR at 645 nm (left) and its transversal LSPR at 540 nm (right) by plane wave (\mathbf{E}_{back}) linearly polarized along and across the NR respectively, as indicated with the yellow arrows. The simulated and plotted fields amplitude obey across interfaces to the boundary condition $\epsilon_1 E_1^\perp = \epsilon_2 E_2^\perp$ and $E_1^{\parallel} = E_2^{\parallel}$. We can notice that at the glass-oil interface, the field amplitude does not show any discontinuity as the two

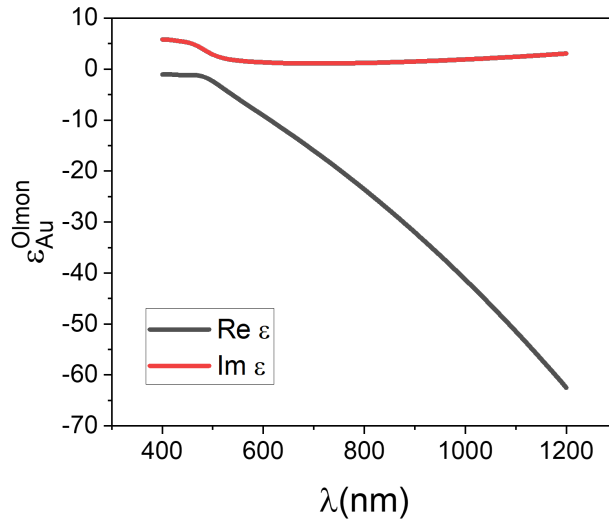


Figure 3.23: Dielectric function of gold, both real (black) and imaginary (red) parts in the visible spectral region measured via spectroscopic ellipsometry measurements on single crystal thick gold surface, reported in Ref.[108].

materials are refractive index matched. In both cases, the scattered field displays a field distribution peculiar to the emission of a dipole oriented along the \mathbf{E}_{back} polarization direction. At the gold-shell interface, in the direction of the \mathbf{E}_{back} oscillations, there is the field discontinuity coming from the boundary condition. In fact $\epsilon_{\text{Au}} E_{\text{Au}}^{\perp} = \epsilon_{\text{shell}} E_{\text{shell}}^{\perp}$ and $\epsilon_{\text{Au}} \gg \epsilon_{\text{shell}}$, so that consequently $\mathbf{E}_{\text{shell}} \gg \mathbf{E}_{\text{Au}}$. It is less evident in the case of excitation at 540 nm the step in ϵ starts to be less large due to the value of $\epsilon_{\text{Au}}(540 \text{ nm})$.

The total field is the result of the interference between the incoming and scattered fields and its values is the one that has to be used to see the actual field enhancement, comparing it with the incoming field. The resonant excitation of the plasmon modes results in an enhanced electric field localized at the end tip of the nanorod in Fig.3.24-left case and along the transverse field direction in the Fig.3.24-right, with a field enhancement reaching a factor of 20 and 6 respectively. It is interesting to see how in the case of the transversal plasmon excitation, thanks to the lower enhancement given by the plasmon itself, the field generated inside the metal at the rod tip is better visible. This is a geometrical effect taking place. In fact, the incoming field oscillating across the NR is able to induce a current in the metal surface that at the tip can penetrate inside the metal itself. As a result, a field inside the metal is generated in this NP volume region. Going toward the main body of the NP, in our model, inside the cylinder volume, the induced currents can penetrate less and this results in a decreased internal field.

The experimental observables can be computed from the microscopic derived quantities. For example, the extinction cross-section, which is the observable quantity we are interested in, can be rewritten and computed as:

$$\sigma_{\text{ext}} = \frac{P_{\text{sca}} + P_{\text{abs}}}{I_i} \quad (3.4.10)$$

where:

- $I = \frac{1}{2} n_0 c_0 \epsilon_0 E_i^2$ results directly from the model input parameters.

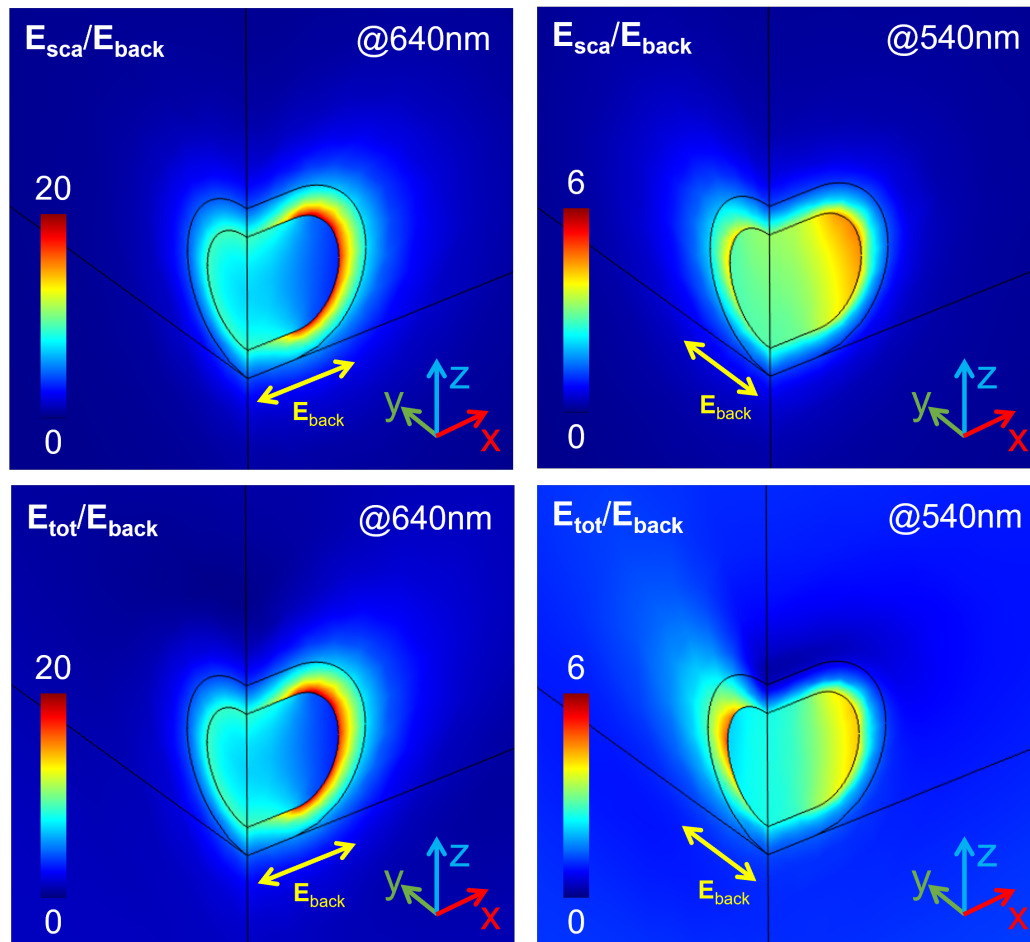


Figure 3.24: Normalized amplitude of the scattered (top) and total (bottom) electric fields obtained, with a $40\text{ nm} \times 68\text{ nm}$ NR, having a 10 nm SiO_2 shell, placed onto a glass surface and surrounded by silicone oil, for incoming light, propagating along the positive z -axis direction, with polarization along (left) and across (right) the NR (as indicated with the yellow arrows) at the correspondent LSPR.

- The absorbed power P_{abs} can be computed by integrating, over the NP volume, the density of power dissipated through *Joule heating*, which is directly computed by COMSOL as $Q_{\text{Joule}} = 0.5[\text{Re}(\mathbf{J}_c \cdot \mathbf{E}_{\text{tot}}^*)]$ (with \mathbf{J}_c the current density):

$$P_{\text{abs}} = 4 \int_{V_{\text{NR}}} Q_{\text{Joule}} dV \quad (3.4.11)$$

The *Joule heating* occurs when the exciting electric field (\mathbf{E}_{back}) accelerates the free electrons within the metal, causing them to collide with the ion lattice. This collision converts their kinetic energy into thermal energy, leading to lattice vibrations and the generation of heat. The factor 4 before the integrals is needed since the simulation volume is a quarter of the real NP volume.

- The scattered power P_{sca} is the flux of the time-averaged scattered Poynting vector \mathbf{P}_{sca} , across the NP surface:

$$P_{\text{sca}} = 4 \int_{\Gamma_{\text{NR}}} \mathbf{P}_{\text{sca}} \cdot \hat{\mathbf{n}} d\Gamma \quad (3.4.12)$$

Again the factor 4 is inserted to take into account the simulation over a quarter of the real NP volume, \mathbf{P}_{sca} is computed directly by COMSOL as $\mathbf{P}_{\text{sca}} = 0.5[\text{Re}(\mathbf{E}_{\text{sca}} \times \mathbf{H}_{\text{sca}}^*)]$ and $\hat{\mathbf{n}}$ is the versor normal to Γ_{NR} in each point.

Figure 3.25 shows the simulated absolute extinction (solid line), scattering (dashed line), and absorption (dot-dashed line) spectra via the COMSOL model presented, for exciting polarization aligned along (red, σ^L) and across (black, σ^T) the NR long axis. By looking at and comparing σ_{abs}^L and σ_{abs}^T , it is clear how the plasmon resonance absorption band splits into two bands. The high-energy band, at a shorter wavelength centered around 525 nm, and the lower-energy band centered at 645 nm.

3.4.2 LFE eH-CARS

In order to simulate the nonlinear microscopy experiment performed, the implemented solving scheme is divided into two sequential steps. The first EWFD interface computes the scattering of the input pump and Stokes beams and for this reason, it is run twice at λ_P and λ_S . λ_P and λ_S are chosen as in our experiments to drive a particular molecular vibration at $\Omega_{\text{vib}} = \omega_P - \omega_S$. For example to drive the molecular vibration at $\Omega_{\text{vib}} = 2904 \text{ cm}^{-1}$, λ_P is set to 820 nm and λ_S to 1076 nm. In this interface, the scattered field formulation is used. Both pump and Stokes are simulated as linearly polarized beams along the NR longitudinal axis, tightly focused by the high numerical aperture of the objective lens $\text{NA}_{\text{obj}}=1.45$. They are characterized by Gaussian field profile at the back focal plane (BFP) of the objective. Ref.[103] gives the exact vectorial description of such beams. Here we report just the field amplitude which is given by:

$$A_{\text{Gauss}} = \frac{\omega}{NA} \sqrt{\frac{2\pi n^3}{\epsilon_0 c^3} \frac{P_{\text{pulse}}}{\frac{F}{2}(1 - e^{-\frac{2}{F^2}})}} \quad (3.4.13)$$

where P_{pulse} is the pulse power and F is the filling factor (see Ref.[103]), which expresses the objective lens efficiency in collecting light. The P_{pulse} can be computed as:

$$P_{\text{pulse}} = \frac{P_{\text{avg}}}{R_{\text{pulse}} T_{\text{pulse}}} \quad (3.4.14)$$

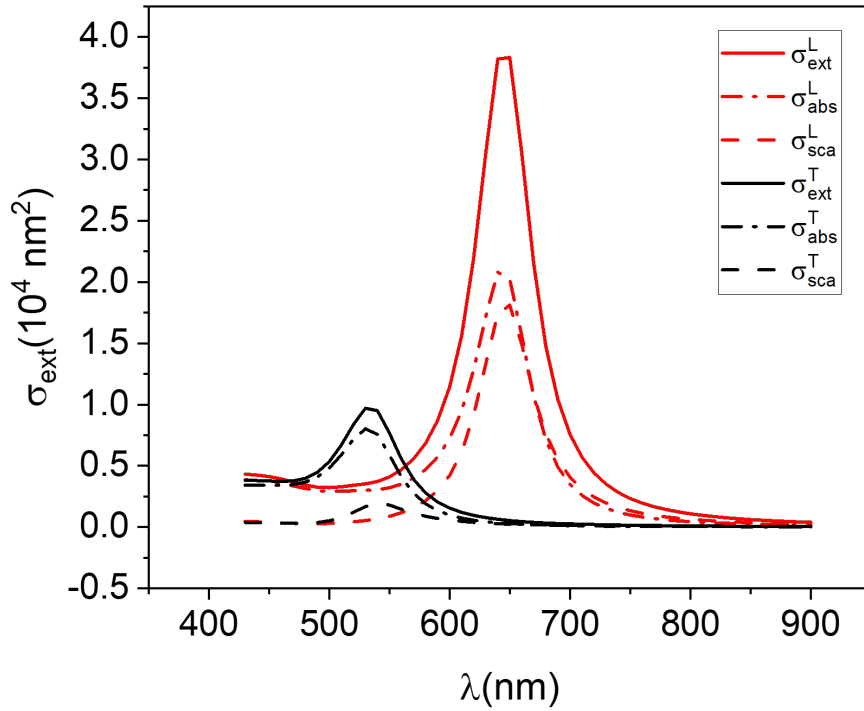


Figure 3.25: Simulated absolute scattering σ_{abs} (dashed line), absorption (dot-dashed line) σ_{sca} and extinction σ_{ext} (solid line) cross-section spectra of an exemplary SiAuNR ($D_{\text{rod}} = 40$ nm, $L_{\text{rod}} = 68$ nm ($AR = 1.7$), $R_{\text{tip}} = D_{\text{rod}}/(2.5)$, $t_{\text{shell}} = 10$ nm with $f_{\text{oil}} = 0$) obtained with the presented model (see text) and using $\epsilon_{\text{Au}}(\lambda)$ by Olmon et al. (Ref.[108]), for linear polarization excitation along the NR long axis (red, σ^L) and linear polarization excitation across the NR (black, σ^T).

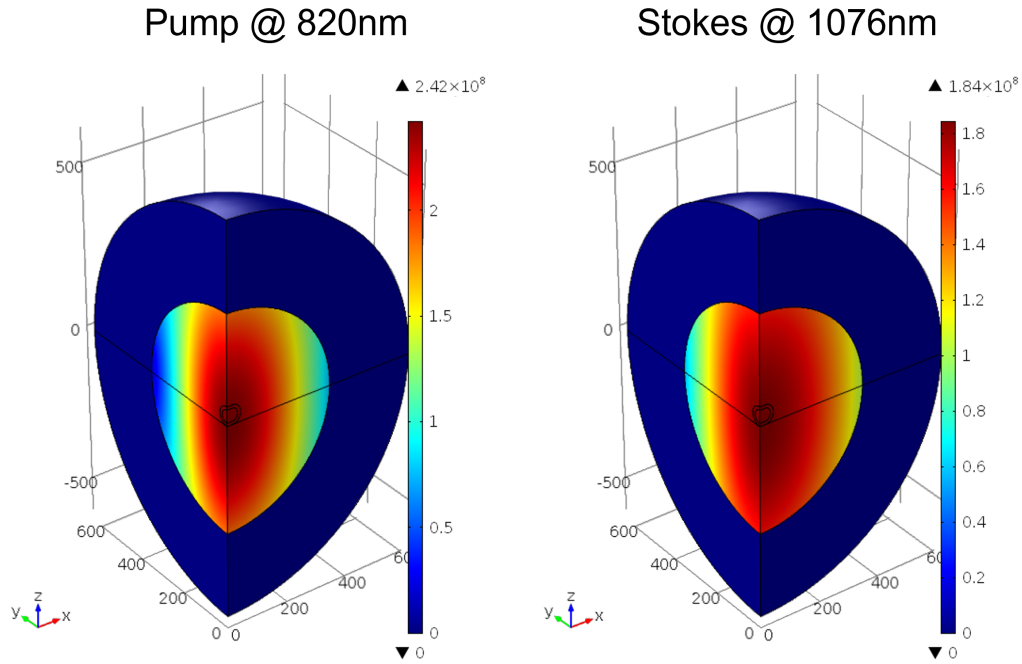


Figure 3.26: Pump (left) and Stokes (right) input field amplitude distributions, computed in COMSOL considering focusing microscope objective with NA=1.45. The simulated volume is centered at $\mathbf{r} = 0$ and has a radius $R_{\text{sim}} = 600$ nm. A focused wavefront has been used, with polarization along the x -axis and a Gaussian field profile in the BFP of the focusing lens.

with P_{avg} the measured average laser power, R_{pulse} the repetition rate and T_{pulse} the pulse duration. The typical experimental values used $P_{\text{avg}} = 1$ mW, $T_{\text{pulse}} = 1$ ps, and $R_{\text{pulse}} = 80$ MHz give $P_{\text{pulse}} = 12.5$ W. In our microscope, the input beams have a filling factor F close to 1 for both pump and Stokes beams.

Figure 3.26 shows how the input fields look like for both pump (left) and Stokes (right). They are both characterized by a regular shape and centered at the nominal focus $\mathbf{r}=0$. They are not axially symmetric, but slightly elongated along the direction of the exciting polarization. Two lateral fringes are visible as well, analogous to the characteristic rings of the Airy pattern. Even if the input power is always the same, the pump amplitude is higher than the Stokes one, as it is proportional to the field frequency, which is higher in the pump case. The opposite occurs for the beam waist, which is proportional to the field wavelength so that the pump's waste is smaller.

The typical results of the first interface are summarized in Fig.3.27, which shows pump (left) and Stokes (right) scattered (top) and total (bottom) fields normalized to the maximum of the correspondent input fields ($A_{\text{P}}^{\text{max}} = 2.41 \times 10^8$ V/m and $A_{\text{S}}^{\text{max}} = 1.84 \times 10^8$ V/m, see Fig.3.26). The presence of the particle changes the spatial distribution of the input fields (Fig.3.26). It is interesting to compare the spatial distribution of the scattered and total fields as the first one is the response of the metal particle to compensate for the background field inside its gold core. In fact, by looking at the total field, which is again the result of the interference between scattered and background fields, we see that the field inside the NP gold core tends to be zero. Note that in the case of the Stokes beam, the total field is

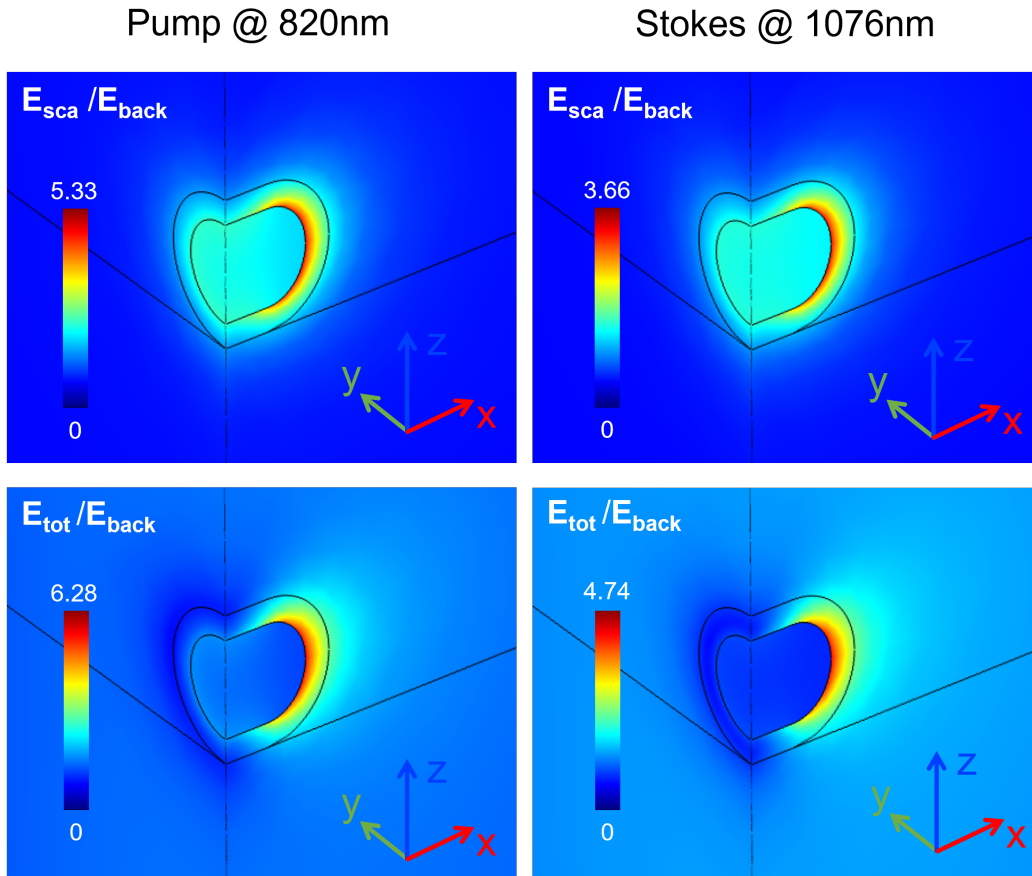


Figure 3.27: Result of the first EWFD interface. Pump (left) and Stokes (right) scattered (top) and total (bottom) fields normalized to the maximum of the input field ($A_{\text{P}}^{\text{max}} = 2.41 \times 10^8 \text{ V/m}$ and $A_{\text{S}}^{\text{max}} = 1.84 \times 10^8 \text{ V/m}$, see Fig.3.26), resulting for a SiAuNR placed at $\mathbf{r} = 0$ surrounded by silicone oil and on top of a substrate index matched with the bulk material (such as the glass coverslip).

even more screened inside the NP and this is the result of having a higher negative value for ϵ_{Au} at 1076 nm than at 820 nm. The total field, outside the gold core shows a more elongated shape than the scattered field, due to the interference with the background field displaying the same characteristic. The field enhancement at the NR tip results from the plasmon excitation, with a contribution depending on the spectral distance between the field wavelength and the longitudinal NP LSPR, together with a geometrical enhancement.

The second EWFD interface takes as input the resulting $\mathbf{E}_{\text{tot}}^{\text{P}}$ and $\mathbf{E}_{\text{tot}}^{\text{S}}$ from the first EWFD interface to drive the nonlinear emission, represented by \mathbf{E}_{CARS} . Here, the full field formulation in the absence of radiative excitation is exploited and the source is given by an external current $\mathbf{J} = -i\omega\mathbf{P}$. Since the process we are treating is the CARS phenomenon $\mathbf{P} = \mathbf{P}_{\text{CARS}}(\omega_{\text{CARS}})$, with $\omega_{\text{CARS}} = 2\omega_{\text{P}} - \omega_{\text{S}}$. A classical derivation of \mathbf{P}_{CARS} , within the scalar approximation is reported in Ref.[75]. Under the scalar approximation, the CARS polarization turns out to be:

$$\mathbf{P}_{\text{CARS}}(\omega_{\text{CARS}}) = 6\epsilon_0\chi_{\text{R}}^{(3)}(\omega_{\text{CARS}})(\mathbf{E}_{\text{P}} \cdot \mathbf{E}_{\text{S}}^*)\mathbf{E}_{\text{P}} + 3\epsilon_0\chi^{(3)}(\omega_{\text{CARS}})(\mathbf{E}_{\text{P}} \cdot \mathbf{E}_{\text{P}})\mathbf{E}_{\text{S}}^* \quad (3.4.15)$$

where the first term is the vibrational term, which describes a vibration induced by a pump and a Stokes photon and probed by another pump photon. The second term represents the nonresonant contribution arising from a FWM-induced phenomenon as a two-photon absorption. The Eq.3.4.15 will then acquire a different form depending on the material properties of the various physical domains. In our model, the resonant material is represented by the silicone oil, while the glass substrate, the silica rod shell, and the gold rod core are nonresonant.

For all the nonresonant material, in first approximation, we assumed that their contribution is just given by a FWM (nonresonant) phenomenon taking place. This is reasonable considering the possibility in glass and gold of inducing, via the absorption of two pump photons, an electronic transition with an equivalent wavelength of around 410 nm. Thus, within these physical domains $\mathbf{P}_{\text{CARS}}(\omega_{\text{CARS}}) = 3\epsilon_0\chi^{(3)}(\omega_{\text{CARS}})(\mathbf{E}_{\text{P}} \cdot \mathbf{E}_{\text{P}})\mathbf{E}_{\text{S}}^*$.

To estimate the third-order susceptibility for the glass coverslip and the silica shell we exploited results reported in Ref.[109], in which non linear refractive index n_{NL} for different glasses have been measured via THG. For the borosilicate glass substrate, the value of $n_{\text{NL,B}} = 1.38 \times 10^{-13} \text{ esu}$ was found. From this value, exploiting the relation between n_{NL} and $\chi^{(3)}$, $\chi^{(3)} = (n_{\text{NL}}n_0)/(12\pi)$, with n_0 the ordinary linear refractive index, we could compute $\chi_{\text{B}}^{(3)} = 5.6 \times 10^{-15} \text{ esu} = 7.8 \times 10^{-23} \text{ m}^2/\text{V}^2$, using in the last equality the conversion $\chi_{[\text{m}^2/\text{V}^2]}^{(3)} = 1.40 \times 10^{-8} \chi_{[\text{esu}]}^{(3)}$ suggested in Ref.[75].

Regarding the silica shell, we estimated that $\chi_{\text{SiO}_2}^{(3)} = 0.6\chi_{\text{B}}^{(3)}$. In fact, comparing the n_{NL} values obtained for silica and borosilicate glass, we have that $n_{\text{NL,SiO}_2} = 0.6n_{\text{NL,B}}$. Thus, $\chi_{\text{SiO}_2}^{(3)}$ can be written as

$$\chi_{\text{SiO}_2}^{(3)} = \frac{n_{\text{NL,SiO}_2}n_{0,\text{SiO}_2}}{12\pi} = \quad (3.4.16)$$

$$= \frac{(0.6n_{\text{NL,B}})n_{0,\text{SiO}_2}}{12\pi} \frac{n_{0,\text{B}}}{n_{0,\text{B}}} = \quad (3.4.17)$$

$$= \frac{n_{\text{NL,B}}n_{0,\text{B}}}{12\pi} \frac{0.6n_{0,\text{SiO}_2}}{n_{0,\text{B}}} \quad (3.4.18)$$

The first factor, by definition, is $\chi_{\text{B}}^{(3)}$, while computing the second, using the well-

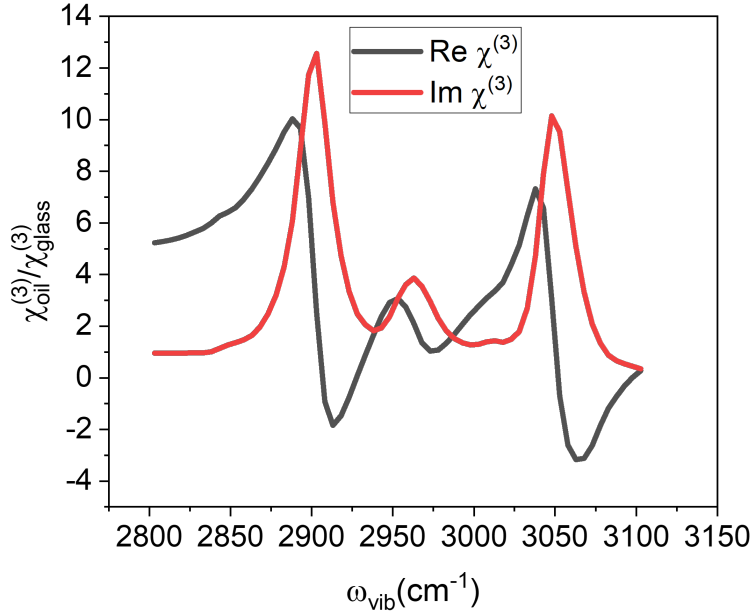


Figure 3.28: Complex third-order susceptibility $\chi_{\text{oil}}^{(3)}$ of silicone oil relative to glass (microscope slide)

known $n_{0,B} = 1.51168$ and $n_{0,\text{SiO}_2} = 1.4585$, we obtain a value \sim of 0.6.

The $\chi_{\text{Au}}^{(3)}$ values reported in the literature vary significantly across multiple orders of magnitudes, from 10^{-14} to $10^{-19} \text{m}^2/\text{V}^2$, as shown by Boyd et al. (see Ref.[61]). The variance of the different values is attributed to the utilization of different measurement procedures, which are sensitive to different contributions to the nonlinear optical response.

Concerning the Au core of the NR, in this work we initially adopted the value $\chi_{\text{Au}}^{(3)} = 2 \times 10^{-19} \text{m}^2/\text{V}^2$, measured by Renger et al. (Ref.[110]), using a FWM setup with wavelength and pulses duration very close to our experimental condition. Then, in Sec.5.8, $\chi_{\text{Au}}^{(3)}$ will be adjusted according to the comparison between simulation and experimental results.

In the resonant material, the resonant contribution given by $\chi_{\text{R}}^{(3)}$ is dominant compared to the non resonant one, so that we can write \mathbf{P}_{CARS} for silicone oil as

$$\mathbf{P}_{\text{CARS,oil}}(\omega_{\text{CARS}}) = 6\epsilon_0\chi_{\text{R}}^{(3)}(\omega_{\text{CARS}})(\mathbf{E}_{\text{P}} \cdot \mathbf{E}_{\text{S}}^*)\mathbf{E}_{\text{P}}. \quad (3.4.19)$$

The complex nonlinear optical susceptibility $\chi_{\text{oil}}^{(3)}$ of the silicone oil was retrieved from quantitatively measurement of $\bar{\chi} = \frac{\chi_{\text{oil}}^{(3)}}{\chi_{\text{B}}^{(3)}}$. These measurements were conducted using techniques that were previously developed within our research group (Ref.[111]) and the results are reported in Fig.3.28. In our model

$$\frac{\mathbf{E}_{\text{CARS,oil}}}{\mathbf{E}_{\text{CARS,B}}} \propto \frac{\mathbf{P}_{\text{CARS,oil}}}{\mathbf{P}_{\text{CARS,B}}} \propto \frac{6\chi_{\text{oil}}^{(3)}}{3\chi_{\text{B}}^{(3)}} = \bar{\chi} \quad (3.4.20)$$

Thus, the silicone oil third order susceptibility value is $\chi_{\text{oil}}^{(3)} = \frac{1}{2} \bar{\chi} \chi_{\text{B}}^{(3)}$.

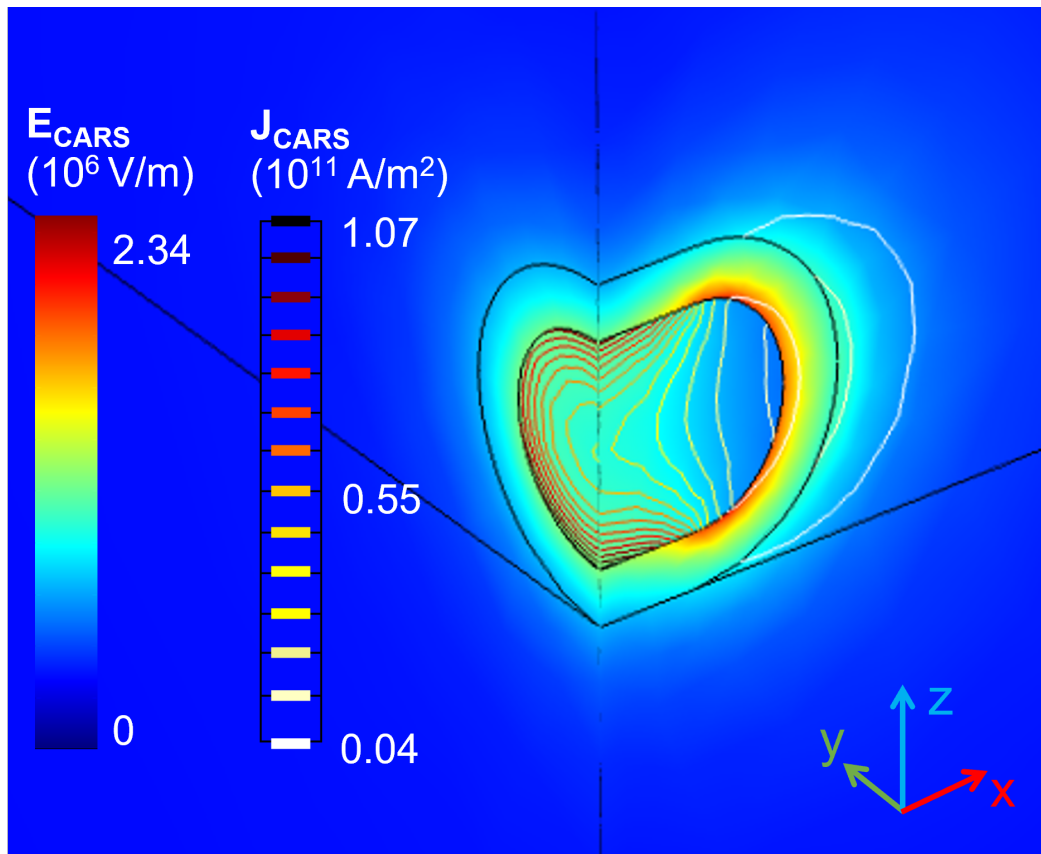


Figure 3.29: Nonlinear current J_{CARS} (contour plot) and emitted field E_{CARS} amplitude (false colours) generating focusing pump and stokes beam at the interface between a SiAuNR placed onto a non resonant substrate (glass coverslip) and surrounded by a resonant material (silicone oil).

Figure 3.29 shows the result of the second interface in the case of the chosen exemplary particle. It shows both the nonlinear current \mathbf{J}_{CARS} (contour plot), generating thanks to \mathbf{P}_{CARS} in the different material, together with the consequent \mathbf{E}_{CARS} spatial distribution. The strength of the current depends on the $\chi^{(3)}$ found in a given material and since gold is characterized by $\chi^{(3)}$ orders of magnitude higher than the other materials, the stronger current is found here. As regards the field spatial distribution, we found the highest value at the NR gold core tip outside the metal and within the silica shell.

In our experiments, the epi emission is measured in amplitude and phase using the heterodyne detection scheme described in Sec.3.3.2. The model calculates the epi-detected heterodyne signal of eH-CARS by combining the mixing term of the CARS field, projected to the FF using Eq.3.4.7, with the reference field \mathbf{E}_{ref} , described by:

$$\text{eH-CARS} = 4 \frac{1}{r_{\text{sim}}} \frac{1}{2} n c_o \epsilon_0 \int_{\Gamma_{\text{Obj}}} \mathbf{E}_{\text{CARS,FF}} \cdot \mathbf{E}_{\text{ref}}^* d\Gamma \quad (3.4.21)$$

This integration takes place over a spherical cap located on the boundary of V_{sim} , which corresponds to the acceptance region of the objective lens and the factor 4 takes into account that we simulate a quarter of the region Γ_{Obj} . Eq.3.4.21 express the pulse peak power and to obtain the average power measured in the experiments we need to multiply by the duty cycle of the source ($R_{\text{pulse}} \times T_{\text{pulse}}$). In order to reproduce in the model the spatial mode matching together with the fact that the interference between the signal and the reference takes place before the detector and that the reference doesn't pass through the objective lens, \mathbf{E}_{ref} is simulated as a Gaussian field profile in the objective BFP and co-polarized with the excitation. Its amplitude is computed considering the measured average power $P_{\text{avg,ref}} = 1mW$, its relation with the laser intensity

$$I_0 = \frac{P_{\text{peak}}}{A_{\text{spot}}} = \frac{P_{\text{avg}}}{R_{\text{pulse}} T_{\text{pulse}}} \frac{1}{\pi (0.5 \frac{\lambda}{NA})^2} \quad (3.4.22)$$

and the relation between the field amplitude and intensity

$$I_0 = \frac{1}{2} n \epsilon_0 c_0 E_0^2. \quad (3.4.23)$$

and turns out to be $8.8 \times 10^4 V/m$. As shown in Ref.[103] $\text{eH-CARS}(r_{\text{sim}})$ always exhibits oscillations well fitted by a sinusoidal function with period $L = \lambda_{\text{CARS}} / (2n)$, with n the average of the refractive index separated by the interface. This oscillation comes from a numerical artifact of the FF calculations due to the discretization introduced by the mesh at the boundary where the transform is computed. This artifact is removed by averaging any two simulations corresponding to opposite points of the circle, i.e. whose r_{sim} differ by $L/2$.

Chapter 4

Optical extinction of nanostructures

4.1 SiAuNRs

4.1.1 Experimental extinction cross-section

The optical properties of the SiAuNRs have been investigated via extinction microspectroscopy.

For the SiAuNRs characterized by nominal size $25\text{ nm} \times 71\text{ nm}$ and 5 nm silica shell, the polarization resolved extinction spectroscopy technique was used and Fig.4.1(a) reports an example of a quantitative single particle analysis performed. It shows the extracted optical extinction cross-section for all the wavelengths in the visible range and for the indicated exciting field in plane linear polarization: 0° , 30° , 60° , 90° , 120° and 150° . The selected particle has a transversal and a longitudinal LSPR centered at 525 nm and 690 nm respectively. As expected, also by comparison with simulations (see Fig.3.25), the transversal LSPR turns out to have a lower cross-section than the longitudinal one and it is not characterized by an evident polarization dependent behaviour. The reduced cross-section can be qualitatively understood considering that there is a shorter length and thus a smaller dipole moment (hence less polarisability) along the short axis compared to the long axis. Instead, the longitudinal LSPR has a larger cross-section and shows a clear polarization dependent behaviour, with a maximum and a minimum value for incoming light polarized at 120° and 30° respectively. The dependence of σ_{ext} , on the linear exciting polarization angle θ at the LSPR of the longitudinal mode is a sensitive probe of NP asphericity. Measuring this dependence, it is possible to fit the experimental $\sigma_{\text{ext}}(\lambda_{\text{LSPR}}, \theta)$ with

$$\sigma_{\text{ext}}(\lambda_{\text{LSPR}}, \theta) = \sigma_0(1 + \alpha_{\text{P}} \cos(2(\theta - \theta_0))) \quad (4.1.1)$$

where σ_0 is the polarization averaged σ_{ext} , $\alpha_{\text{P}} \leq 1$ is the amplitude of the polarization dependence and $0 \leq \theta_0 \leq \pi$ is an angular offset, indicating the in-plane orientation of the NP asymmetry. σ_0 is related to the particle size, while α_{P} is a measure of the observed NP asymmetry, with $\alpha_{\text{P}} = 0$ corresponding to absence of dipolar asymmetry and $\alpha_{\text{P}} \sim 1$ indicating a very elongated particle, with a strong LSPR preferential axis, as would be expected for the longitudinal plasmon mode of a nanorod. Fig.4.1(b) shows the fit using Eq.4.1.1. The particle under study turns out to have the following fit parameters: $\sigma_0 = 17893\text{ nm}^2 \pm 516\text{ nm}^2$ and $\alpha_{\text{P}} = 0.88 \pm 0.04$, confirming that this particle has a pronounced rod-shape.

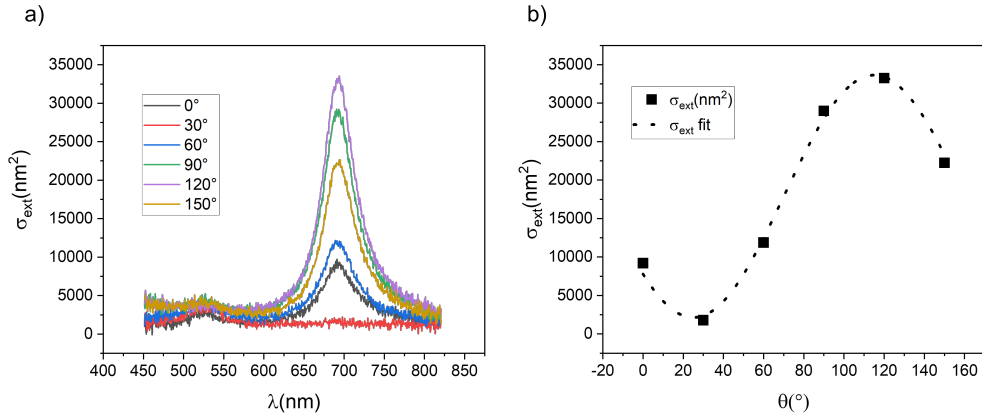


Figure 4.1: (a) Single particle extinction spectrum of nominal $25 \text{ nm} \times 71 \text{ nm}$ with 5 nm silica shell (acquired as explained in 3.3.1) for different in-plane linear polarization angles of the white-light illumination as indicated. Measurements settings: spectra are averages over 200 acquisitions, 11 ms exposure time. (b) $\sigma_{\text{ext}}(\lambda_{\text{LSPR}})$ versus polarizer angle θ fit with Eq.4.1.1

Despite the very precise knowledge of the LSPR spectral position, spectroscopy comes with the drawback of being able to measure one single particle per time. Instead, the wide field extinction technique introduced in Chapter 3.3.1, has the main advantage of being able to rapidly measure in absolute units σ_{ext} for all the NPs within the imaged field of view (FOV), without the need for calibration standards (see Ref.[97]). For this reason, moving ahead with our research, we decided to adopt the polarization resolved wide field extinction technique to investigate the σ_{ext} of the NPs belonging to the $40 \text{ nm} \times 68 \text{ nm}$ - and $50 \times 100 \text{ nm}$ - SiAuNRs groups.

Figure 4.2(a) shows an example of extinction image of nominal $40 \text{ nm} \times 60 \text{ nm}$ -SiAuNRs, taken inserting in the excitation beam path a band-pass filter centered at $650 \text{ nm} \pm 20 \text{ nm}$ and using unpolarized incident light. From the analysis of the acquired images, each NP corresponds to a bright and a dark spot. This is because we use a shifted image for reference to determine the differential transmission induced by the particle (see Chapter 3.3.1). Considering the particle circled in red in Fig.4.2(a), Figure 4.2(b) shows how the extinction image changes when different incident light polarizations are selected. Qualitatively, it is already possible to understand that, thanks to its strong polarization dependent behaviour, the selected particle has a rod shape and that its LSPR is not spectrally far from the center wavelength of the band pass filter inserted, since at the LSPR wavelength the polarization dependence is stronger. After acquiring the extinction images using different bandpass filters (in our case, centered at 450 nm , 500 nm , 550 nm , 600 nm , 650 nm , and 700 nm) and, for each filter, selecting the different polarizations, the IMAGEJ software introduced in Chapter 3.3.1 returns $\sigma_{\text{ext}}(\lambda, \theta)$ of all the NPs within the FOV. In Fig.4.3(a) the result of this analysis for the red-circled particle of Fig.4.2(a) is shown. By looking at this figure, we can confirm the rod shape of the particle, as its longitudinal LSPR, which is centered at 650 nm , exhibits a strong polarization dependent behaviour with a maximum at 150° and a minimum at 60° .

From the TEM images of Chapter 3.1 (Fig.3.1), it is evident that the particle sizes deviates from the nominal ones provided by the supplier and additionally they exhibit considerable variability. The actual size and shape of a particle determine its optical properties such as the strength of the extinction cross-section and the

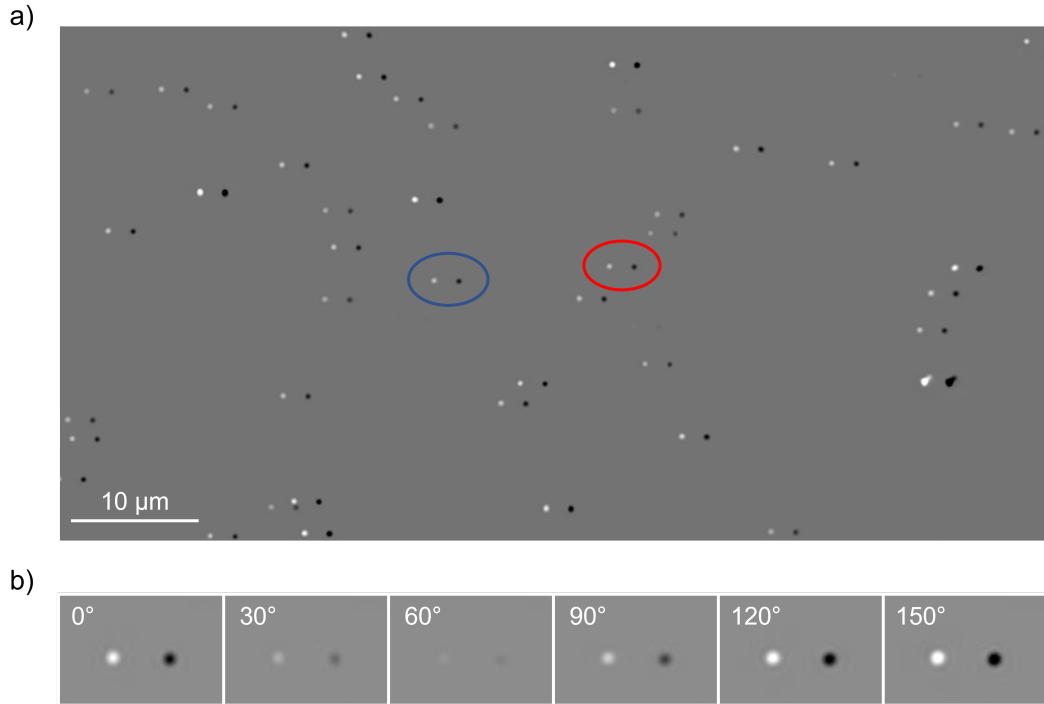


Figure 4.2: (a) Unpolarized wide field extinction image (1196x62 pixels) of single nominal 40×68 nm-SiAuNRs taken using a 100 W halogen lamp and a band-pass filter centered at 650 nm, a 100×1.45 NA oil objective, and a sCMOS camera. The two circled particles are used as exemplary particles in Fig.4.2(b) and in Fig.4.3. (b) Polarization resolved wide field extinction of the particle red circled in (a), setting the rotatable polarizer at 0° , 30° , 60° , 90° , 120° , 150° . Gray bar scale for all these images: white=-0.17 and black=0.21. A $10 \mu\text{m}$ scale bar is shown in (a) and in (b) the polarization angle is noted in each image. (measurement settings: $\times 128$ averages, $N=10$ repeats, $S=2 \mu\text{m}$)

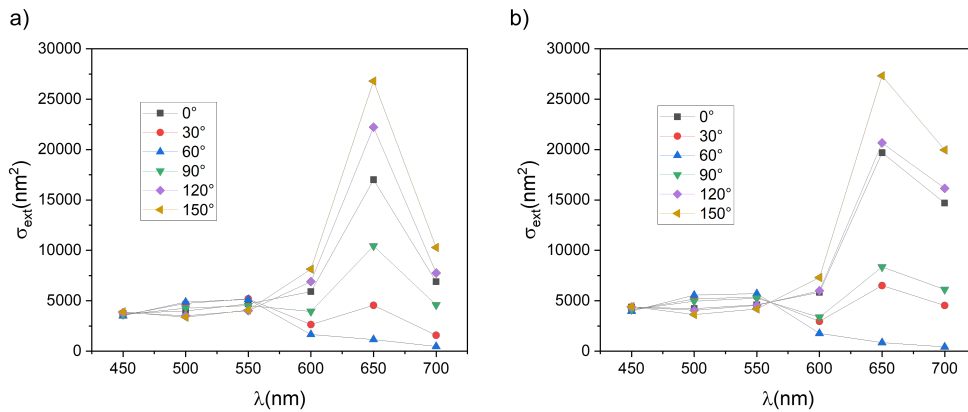


Figure 4.3: Extinction cross-section of two nominal $40 \text{ nm} \times 68 \text{ nm}$ -SiAuNRs extracted from wide field extinction imaging measurements performed using a 100 W halogen lamp and band-pass filters with the different reported center wavelengths, for in-plane linear polarization as indicated. (a) red-circled NP and (b) blue-circled NP of Fig.4.2(a).

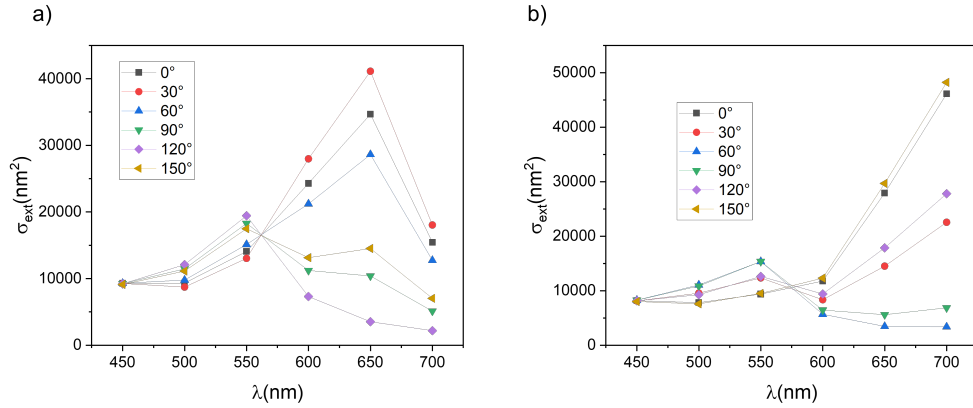


Figure 4.4: Extinction cross-section of two nominal $50 \text{ nm} \times 100 \text{ nm}$ -SiAuNRs (a,b) extracted from wide field extinction imaging measurements performed using a 100 W halogen lamp and band-pass filters with the different reported center wavelengths, for in-plane linear polarization as indicated.

spectral position of the longitudinal LSPR. The latter is a crucial parameter for our research and our target is to have a longitudinal LSPR as much as possible close to 660 nm (corresponding to the CARS wavelength), as explained in Chapter 5. The σ_{ext} , obtained from our wide field extinction technique, allows us to rapidly check how much the LSPR of an individual NR is shifted compared to our target value. Figure 4.3(b) shows the extinction spectrum of the particle circled in blue in Fig.4.2. Again, we found that this is a rod-shape particle. Comparing the two NRs, we can understand that they are characterized by a different in-plane orientation (different polarization dependent behaviour) and, most importantly by different geometrical characteristics. In fact, compared to the first NR (Fig.4.2(a)), the σ_{ext} of the second one (Fig.4.3(b)) is larger, suggesting an overall bigger volume and its longitudinal LSPR turn out to be in a different spectral position, more red-shifted, meaning that its actual AR is larger.

Similar consideration can be made for the nominal $50 \text{ nm} \times 100 \text{ nm}$ -SiAuNRs group: generally, the majority of the NPs in the ensemble are rod-shaped particles, but their actual size deviates from the nominal one with a non-negligible variability. Figure 4.4 shows the extinction cross-section spectrum obtained considering two different nominal $50 \text{ nm} \times 100 \text{ nm}$ -SiAuNRs. One should notice that the maximum σ_{ext} obtained in this case is larger than the one measured for the nominal $40 \text{ nm} \times 68 \text{ nm}$ -SiAuNRs group, which is consistent with the larger nominal size. Moreover, thanks to the larger volumes, with the nominal $50 \text{ nm} \times 100 \text{ nm}$ -SiAuNRs, in general, the transversal LSPR becomes visible in our experiments. Also in this case we notice that the spectral positions of the longitudinal LSPRs are different for different NRs. In this example, we have that the first NR (Fig.4.4(a)) has the longitudinal plasmon mode more blue-shifted, centered around 625 nm, while the second NR (Fig.4.4(b)) has the LSPR red-shifted, toward 700 nm.

4.1.2 Simulated extinction cross-section

As explained in Chapter 3.4, we developed a COMSOL model able to compute the extinction cross-section for nanorods that can have different sizes, shell thickness, and tip lengths (to vary from a more to a less rounded tip). In this Section, the

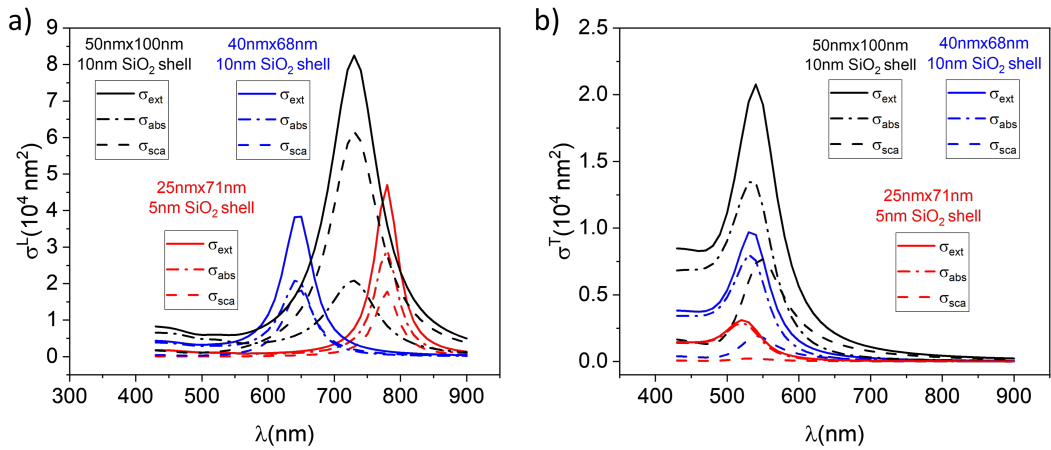


Figure 4.5: Simulated absolute absorption σ_{abs} (dashed line), scattering (dash-dotted line) σ_{sca} and extinction σ_{ext} (solid line) cross-section spectra of three different NRs (as indicated) placed at a glass substrate and surrounded by index matching silicon oil ($n=1.52$), obtained with the presented model (see text) and using $\epsilon_{\text{Au}}(\lambda)$ by Olmon et al. (Ref.[108]), for (a) linear polarization excitation along the NR (σ^L) and (b) linear polarization excitation across the NR (σ^T).

cross-sections obtained using an incident polarization aligned along the NR main axis will be indicated as σ^L , as the longitudinal mode, corresponding to electrons oscillating along the NR longer axis, is excited. Instead, σ^T will be used when the exciting polarization will be aligned along the NR transversal axis.

Figure 4.5 shows the absolute extinction (solid line), absorption (dash-dotted line), and scattering (dashed line) simulated spectra, obtained with the COMSOL model presented, for NRs whose sizes and silica shell thicknesses were set to be equal to the nominal specification given for the NRs employed experimentally within this project (as indicated). The tip length was set to be $R_{\text{tip}} = D_{\text{rod}}/(2.5)$. Again, for this set of simulations, the single-crystal $\epsilon_{\text{Au}}(\lambda)$ dataset by Olmon et al. (Ref.[108]) has been used. A detailed study of the optimized dataset for $\epsilon_{\text{Au}}^{NP}(\lambda)$ will be presented in the following section. Precisely, the results on the left (right) were computed for exciting polarization aligned along (across) the NR, so that the cross-sections are indicated with σ^L (σ^T), as the longitudinal (transversal) LSPR was excited. Comparing the results for the three NPs reported in Fig.4.5(a) and (b), it is clear that a higher aspect ratio increases the energy separation between the resonance frequencies of the two plasmon bands (Ref.[112],[113]).

The transversal plasmon band, which corresponds to the oscillation of the electrons along the NR short axis, has a spectral position relatively insensitive to the NR aspect ratio (Ref.[114],[115]), while its extinction peak increases and is slightly red-shifted for longer diameter (see Fig.4.5(b)). For the smallest NR of this example, the overall extinction cross-section is dominated by the absorption contribution (σ_{abs}^T) while the scattering contribution (σ_{sca}^T) increases for a larger diameter. Notably, the NR transversal mode is comparable to the plasmon mode obtained considering a spherical particle. In the quasi-static regime, i.e. when the wavelength of the incident radiation is much greater than the particle diameter (see Chapter 2.2 and Ref.[86]),

$$\frac{\sigma_{\text{sca}}}{\sigma_{\text{abs}}} \propto \left(\frac{R}{\lambda}\right)^3 \quad (4.1.2)$$

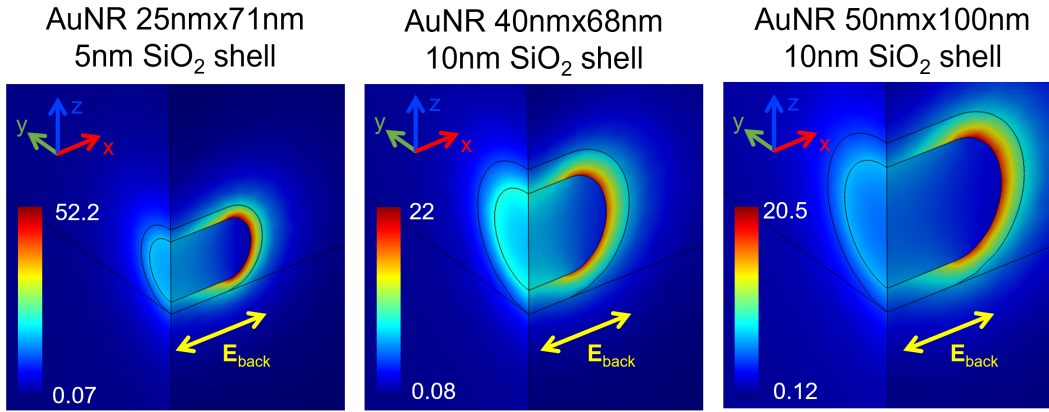


Figure 4.6: Solution of the elastic scattering model for three NR whose size and silica shell thickness are set to be equal to the nominal specification of the NRs employed within this project, as indicated (see Sec.3.1). The local field enhancement $\mathbf{E}_{\text{tot}}/\mathbf{E}_{\text{back}}$ is plotted. The exciting field \mathbf{E}_{back} (yellow arrow) propagates along \hat{z} , is polarized along the rod axis (i.e. along \hat{x}) and excited the NP at their longitudinal LSPR.

so that the scattering contribution becomes negligible compared to the absorption one, while increasing the diameter it can not be neglected anymore (as in the case of $D=40$ nm and $D=50$ nm).

The spectral position of the longitudinal LSPR depends on the aspect ratio characterizing the NR (Ref.[116]) (see Fig.4.5(a)). In fact, the highest AR , which in this example is 2.84 for the 25 nm \times 71 nm NR, gives a more red-shifted longitudinal LSPR. For the simulated particles we found the longitudinal LSPR at 780 nm for the 25 nm \times 71 nm NR, at 645 nm for the 40 nm \times 68 nm NR, and at 730 nm for the 50 nm \times 100 nm NR. In general, as expected, for both σ_{ext}^T and σ_{ext}^L the peak value increases for larger NP volume.

Figure 4.6 reports the results obtain for $\mathbf{E}_{\text{tot}}/\mathbf{E}_{\text{back}}$ when the three NRs of Fig.4.5 are selected. The exciting field \mathbf{E}_{back} (see yellow allows), resonantly excites the NRs under study at their corresponding longitudinal LSPR and has been set to be co-rod linearly polarized. The local field enhancement, at the NR gold tip, turns to be (from left to right) 52.2, 22, and 20.5. The actual value of the NF enhancement is limited by non-radiative and radiative damping of the excited LSP (Ref.[117]). The non-radiative damping is given by the NP absorption, and can be split into two contributions, the nonradiative intrinsic damping, which is independent from the particle size and is related to the excitation of interband and intraband transitions in the gold metal (Ref.[118]), and the surface scattering damping, which is dependent on the particle size and is related to the presence of the nanoparticle surface (Ref.[119]). The surface scattering damping is not taken into account within this section and it will be investigated in the following as it is taken into account via the modification of the ϵ_{Au} (see Sec.4.1.3.1). The other source of damping is the radiative contribution (Γ_{rad}), which describes the radiative emission of the collective electron oscillation energy into an optical far-field and is proportional to the NP volume. ($\Gamma_{\text{rad}} \propto V$, Ref.[120]). Thanks to the latter it is possible to understand qualitatively the decreased near field enhancement together with a broader plasmon resonance obtained in Fig.4.6 for larger sizes.

When neglecting the surface scattering contributions in the damping, by decreasing

the NP size it is possible to reach the point where the quasi-static picture of plasmon resonances can be used. Within this approximation, the NF enhancement turns out to be independent of the particle size. Figure 4.7 shows that with the COMSOL built model, we can simulate this condition of size independent NF enhancement. To make a comparison between the NF enhancement obtained with different sizes, we consider the case where the overall NR geometry remains the same, only with a varied volume. For this reason in Fig.4.7 all the simulated particles are characterized by the same AR , chosen to be equal to 2.84, to make the results consistent with the smallest particle of Fig.4.5. The thickness of the silica shell is set to 5 nm. In Figure 4.7 each row shows a NR with a given diameter (3 nm, 5 nm, and 10 nm, from top to bottom). On the left, the corresponding simulated σ_{ext}^L spectra are reported to show the spectral position of the longitudinal LSPR, which moderately red-shifts of few nanometers for bigger D . On the right, the NF enhancement ($\mathbf{E}_{\text{sca}}/\mathbf{E}_{\text{back}}$) obtained resonantly exciting the longitudinal LSPR modes is displayed. From the latter, it is possible to see that for the AuNR size 25 nm \times 71 nm in Fig.4.5 and Fig.4.7 we were not in the quasi-static limit, as the enhancement was size dependent. The quasi-static limit becomes a good approximation for $D \leq 10$ nm, as we see a decrease of the NF enhancement less than 5% for smaller sizes.

Until now we compared NRs with different sizes in terms of diameter and length, but characterized by the same tip shape. In Figure 4.8 we want to show the effect of choosing a tip more or less rounded on the extinction (left), absorption (middle), and scattering (right) cross-sections simulated for exciting light co-rod polarized (i.e. polarized along the rod long axis). To make visible the effect on the scattering cross-section, we choose for this example $D = 40$ nm and $AR = 1.7$, which is a size with a significant scattering contribution as shown in Fig.4.5. The semiaxis R_{tip} of the ellipsoid, used to build the rod tip, has been varied from $D_{\text{rod}}/2$ to $D_{\text{rod}}/4$. Both σ_{abs}^L and σ_{sca}^L , and consequently σ_{ext}^L , are affected in terms of the LSPR position, with a red-shift for shorter R_{tip} (Ref.[116]). σ_{sca}^L , besides having a more pronounced red-shift, also has a peak that increases for less rounded tips. Instead, the change in the absorption peak for different cap-lengths is less significant.

4.1.3 Optical sizing

By comparing the experimental extinction cross-section (in Sec.4.1.1), with the simulated ones (in Sec.4.1.2), both in terms of amplitudes and in terms of longitudinal LSPR spectral position, it is evident that there is a discrepancy. As already mentioned, looking at the TEM images of the different groups of SiAuNRs, we noticed a deviation of the particle sizes from the nominal ones. Considering the stock solution of the nominal 50 nm \times 100 nm-SiAuNRs ($AR=2$) with 10 nm silica shell, to have a better idea about which are the actual sizes of the particles, we took an ensemble of 100 random NPs and the geometrical characteristics have been extracted as shown for two exemplary NPs in Figure 4.9. We measured the length of the diameter D (yellow arrows), the rod length L (green arrows) from tip to tip, and R_{tip} , i.e. the distance from the cylinder base thought as the main rod body (see how a nanorod is modeled in Sec.3.4) to the rod tip (red arrows). Once obtained these 3 values we computed for each particle the aspect ratio, as $AR = L/D$, and retrieved the x value appearing in $R_{\text{tip}} = D/x$. In Figure 4.10, the statistical results for D , the AR and R_{tip} are reported. The diameter turns out to be statistically slightly larger than the one stated by the supplier (Fig.4.10(a)), while we found a consistent discrepancy for the AR (Fig.4.10(b)), with a mean of 1.52, corresponding to L of 80 nm

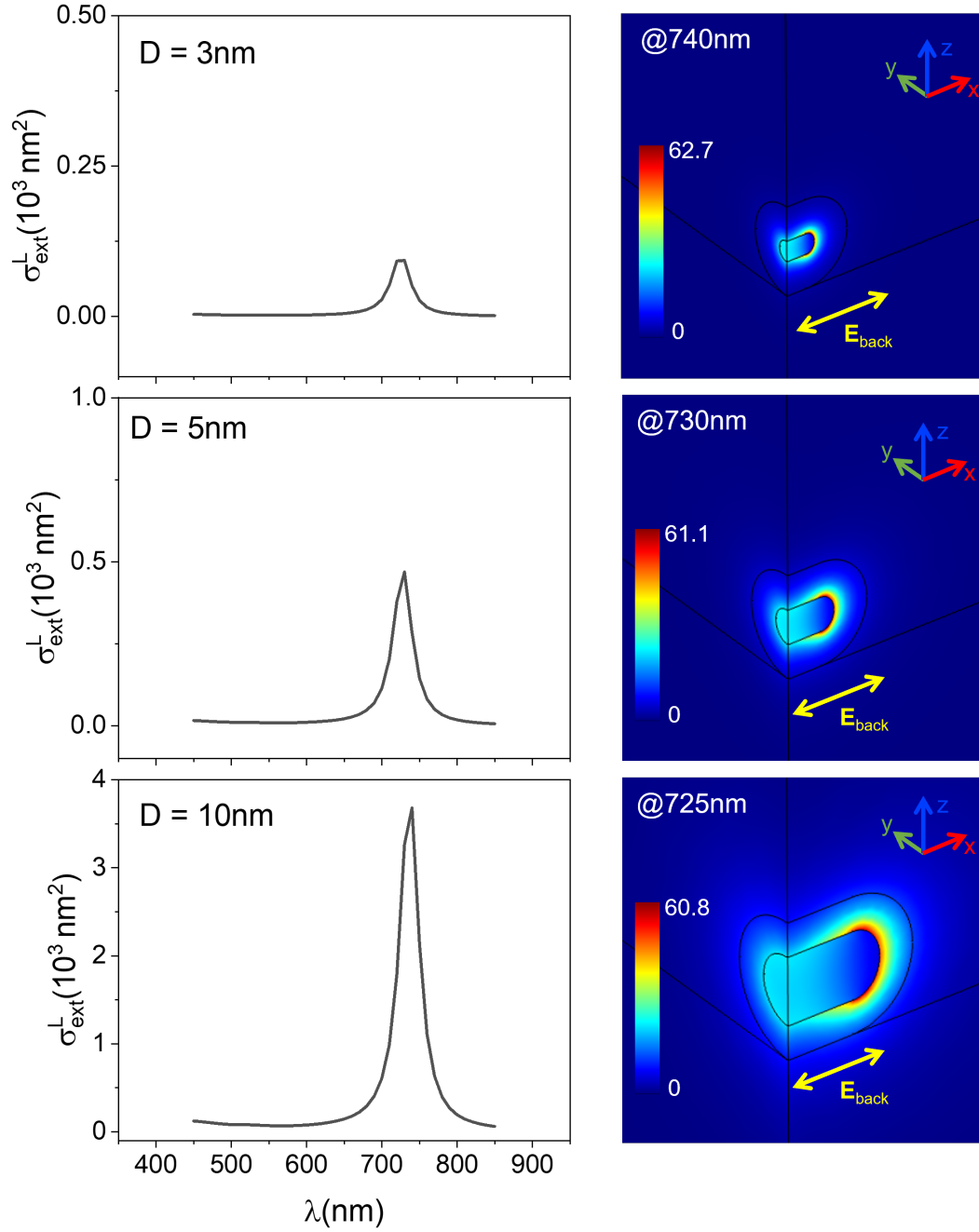


Figure 4.7: Left: simulated longitudinal σ_{ext}^L . Right: solution of the elastic scattering model and NF enhancement $E_{\text{sca}}/E_{\text{back}}$ plotted. The exciting field (at the indicated wavelength) resonantly excites the longitudinal LSPR. Each row refers to a particle characterized by $AR=2.84$, $R_{\text{tip}}=D/(2.5)$, $t_{\text{shell}}=10 \text{ nm}$ and $D=3 \text{ nm}$ (top), 5 nm (middle) and 10 nm (bottom), as indicated.

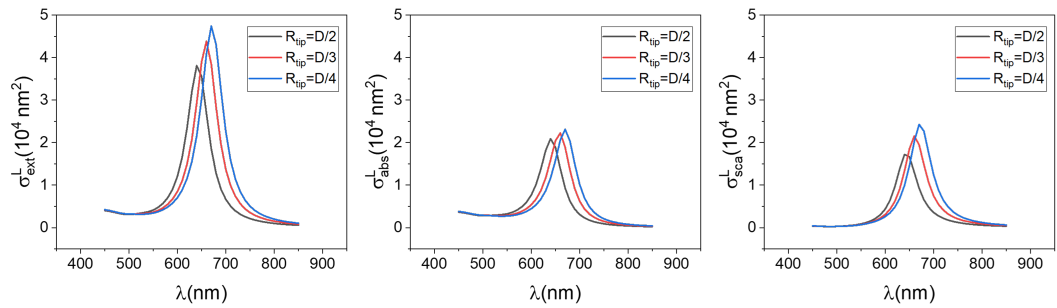


Figure 4.8: Simulated extinction (left), absorption (middle) and scattering (right) cross-section of a gold NR with $D=40$ nm and $AR=1.7$ for different tip shapes: $R_{\text{tip}} = D_{\text{rod}}/2$ (black), $R_{\text{tip}} = D_{\text{rod}}/3$ (red) and $R_{\text{tip}} = D_{\text{rod}}/4$ (blue).

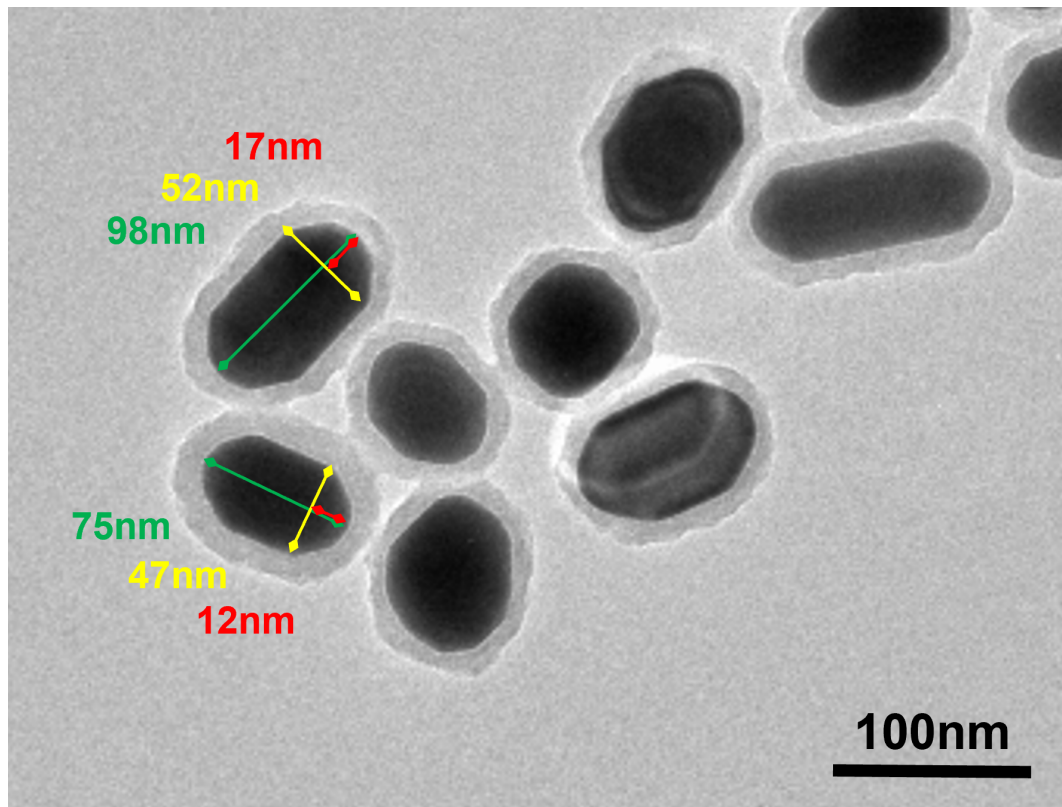


Figure 4.9: Example, for nominal 50 nm×100 nm-SiAuNRs, to show how the main rod geometrical characteristics have been extracted from TEM images. Yellow arrows and values: diameter D ; green arrows and values: rod length L ; Red arrows and values: tip shape R_{tip} .

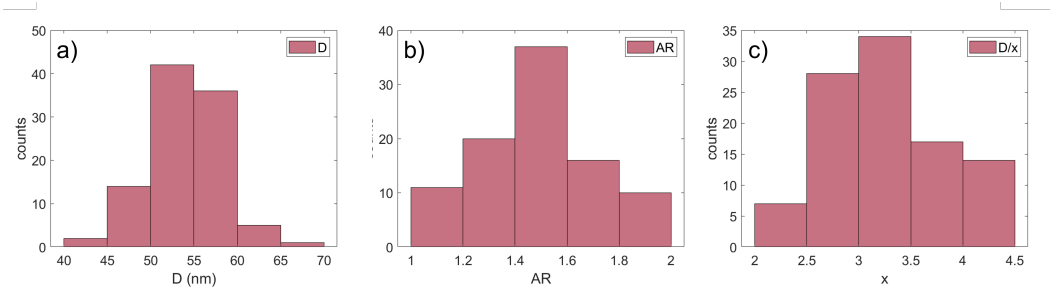


Figure 4.10: Particle size distribution from the TEM images analysis for nominal $50 \text{ nm} \times 100 \text{ nm}$ -SiAuNRs. (a) Diameter (D) (mean = 53.37 nm , standard deviation = 4 nm), (b) Aspect ratio (AR) (mean = 1.52 , standard deviation = 0.28), (c) Tip length defined as D/x . (mean = 3 , standard deviation = 0.57).

when assuming a diameter equal to the mean value 53 nm . Regarding the tip shape (Fig.4.10(c)), which was not specified by the manufacturer, assuming a nanorod well represented by our COMSOL model with an elliptical cap shape, the semiaxis characterizing the NR can be assumed as equal to $R_{\text{tip}}=D/3$ based on the mean value in the histogram in Fig.4.10(c). The geometrical characteristics of an NP are essential in determining its extinction cross-section and the enhancement provided in the LFE-eHCARS measurements (see Chapter 5). For this reason and since we cannot make assumptions on the geometrical NP characteristics because of the seen variability, we decided to build an *optical sizing* tool based on the comparison of simulated and measured extinction cross-sections for the individual AuNR under study. This method is described in the following sub-sections.

4.1.3.1 Modification of the gold permittivity

To build an optical sizing tool, the material description adopted in the exploited numerical simulation is important. The Olmon data set used until now to describe the permittivity of gold, being obtained by measuring thick gold surfaces (Ref.[108]) does not take into account the presence of the surface confining the NP.

For bulk metals, the gold permittivity ϵ_{bulk} can be written using the Drude model, since it is appropriate to describe the behaviour of quasi-free electrons in a metal, as:

$$\epsilon_{\text{bulk}} = 1 - \frac{\omega_{\text{P}}^2}{\omega^2 + i\gamma_0\omega} \quad (4.1.3)$$

where ω_{P} is the plasma frequency and γ_0 is the damping factor related to any kind of energy dissipation mechanisms (such as electron-electron or electron-phonon collisions). The Drude model takes into account the intraband transition, i.e. the optical transition of free electrons in the conductive band to a higher energy level of the same band. However, the contribution of core electrons (*d-band* electrons) promoted to the conductive band (interband transitions) is not taken into account. Thus, to have a more complete expression of ϵ_{bulk} we have to add an extra term (Ref.[29]):

$$\epsilon_{\text{bulk}}(\omega) = 1 + \epsilon_{\text{b}} - \frac{\omega_{\text{P}}^2}{\omega^2 + i\omega\gamma_0} \quad (4.1.4)$$

When working with small metallic NPs it is necessary to introduce an additional term to describe the effect of the surface delimiting the particle. This is typically

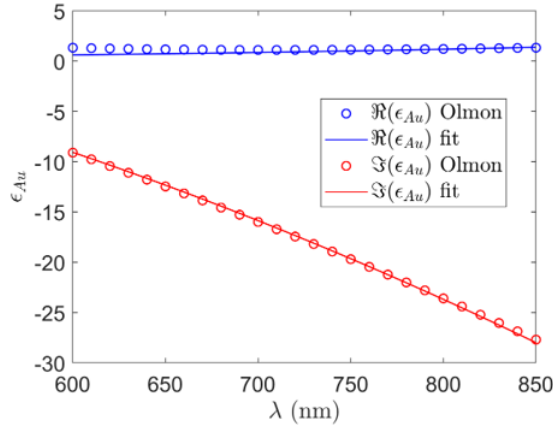


Figure 4.11: Fit of the experimental permittivity Olmon dataset with the Drude model in the range 600-850 nm.

done in the literature (Ref.[121]) by introducing a damping term:

$$\gamma_{\text{NP}} = \gamma_0 + g \frac{v_{\text{F}}}{R_{\text{eff}}} \quad (4.1.5)$$

The second term represents the surface damping contribution. v_{F} is the Fermi velocity, to describe the electrons close to the Fermi level thought to contribute to the collisions against the particle surface, and R_{eff} is the effective radius of the particle under study, i.e. the radius of an equivalent (in terms of volume) spherical particles. g is a dimensionless factor called *surface scattering coefficient* and it influences the strength of the additional surface damping. Thus, the permittivity of a metallic NP can be written as:

$$\epsilon_{\text{NP}}(\omega) = 1 + \epsilon_{\text{b}} - \frac{\omega_{\text{P}}^2}{\omega^2 + i\omega \left(\gamma_0 + g \frac{v}{R_{\text{eff}}} \right)} \quad (4.1.6)$$

The $\epsilon_{\text{NP}}^{\text{exp}}(\omega)$ experienced during a measurements can be seen as:

$$\epsilon_{\text{NP}}^{\text{exp}}(\omega) = \epsilon_{\text{Olmon}}(\omega) + \Delta\epsilon(\omega, \gamma_{\text{NP}}) \quad (4.1.7)$$

where γ_{NP} is given by Eq.4.1.5 and the correction of the permittivity from the Olmon data set is expressed as

$$\Delta\epsilon(\omega, \gamma_{\text{NP}}) = \epsilon_{\text{NP}}(\omega, \gamma_0 + g \frac{v_{\text{F}}}{R_{\text{eff}}}) - \epsilon_{\text{NP}}(\omega, \gamma_0) \quad (4.1.8)$$

We first fit (see Fig.4.11) the Olmon data set $\epsilon_{\text{Olmon}}(\omega)$ with the Drude model $\epsilon(\omega, \gamma) = \epsilon_{\infty} - \omega_{\text{P}}^2 / (\omega^2 + i\omega\gamma_0)$, in the range 600-850 nm, to avoid the region of gold interband transition influencing too much the frequency dependence, so that $1 + \epsilon_{\text{b}} \propto \epsilon_{\infty}$, getting the following fit parameters: $\epsilon_{\infty} = 8.6594$, $\omega_{\text{P}} = 1.3371 \times 10^{16} \text{s}^{-1}$ and $\gamma_0 = 1.1774 \times 10^{14} \text{s}^{-1}$. The Fermi velocity for gold is $v_{\text{F}} = 1.4 \times 10^6 \text{ m/s}$ (Ref.[122]). Let's consider for example a particle (indicated with NP#1) characterized by diameter $D = 40 \text{ nm}$, $AR = 1.7$ and tip length $R_{\text{tip}} = D/3$. To compute R_{eff} we first have to compute the volume of the NP. To remain consistent with the developed COMSOL model, the nanoparticle volume is computed as the sum of the cylinder (c) and ellipsoid (e) volumes used to build the main body and tips of the particle, i.e.:

$$V_{\text{rod}} = V_{\text{c}} + V_{\text{e}} = 2 \left(\pi \frac{D}{2} \right)^2 \left(\frac{L}{2} - \frac{D}{3} \right) + \frac{4}{3} \pi \frac{D}{2} \frac{D}{2} \frac{D}{3} \quad (4.1.9)$$

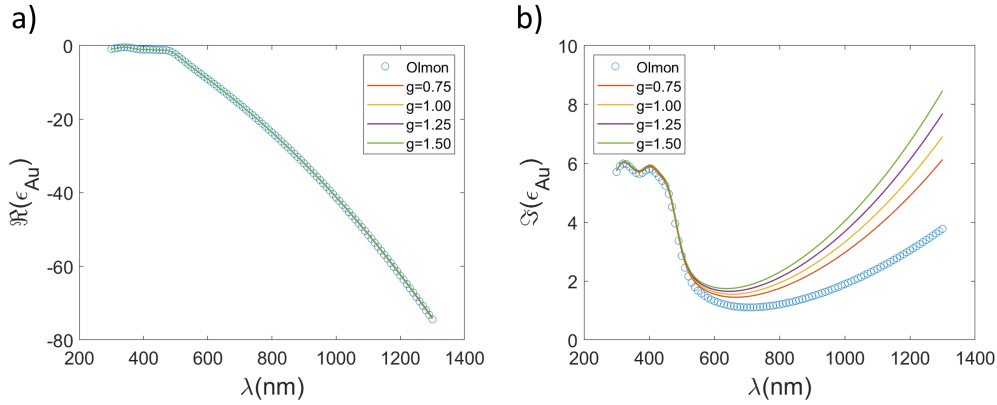


Figure 4.12: Fit of the experimental permittivity Olmon dataset with the Drude model and additional damping considering NP#1 (i.e. $D=40$ nm, $AR=1.7$ and $R_{\text{tip}}=D/3$). (a) Real part, Olmon data (circles), and model (line) for $g=0.75$, $g=1.00$, $g=1.25$ and $g=1.5$. b) Imaginary part, Olmon data (circles), and model (line) for $g=0.75$, $g=1.00$, $g=1.25$ and $g=1.5$.

From $V_{\text{rod}}^{NP\#1}$, which is in this case equal to $7.43 \times 10^4 \text{ nm}^3$, then $R_{\text{eff}}^{NP\#1}$ is computed considering an equivalent spherical particle:

$$R_{\text{eff}} = \sqrt[3]{\frac{3V_{\text{rod}}}{4\pi}} \quad (4.1.10)$$

resulting in 26 nm. In Eq.4.1.8, we vary the damping parameter g within the typical range reported previously in literature (Ref.[123]). The resulting modified $\epsilon_{\text{NP}}(\omega)$ is shown in Fig.4.12. The real part of $\epsilon_{\text{NP}}(\omega)$ (Fig.4.12(a)) changes less than 0.1% with the g parameter variation, meaning that the particle LSPR, which depends on $\Re(\epsilon_{\text{NP}})$, is not affected by the surface damping (See Section 2.2). On the contrary, $\Im(\epsilon_{\text{NP}})$ (Fig.4.12(b)), for longer λ , turns to be more affected by the introduction of the surface damping parameter and it increases for higher g values, bringing to less sharp and broader resonances (See Section.2.2).

Now, let's consider a second nanorod (NP#2) with $D=50$ nm, $AR=1.6$ and $R_{\text{tip}}=D/3$, characterized by a LSPR very close to the one obtained for NP#1, as demonstrated by the simulated extinction cross-section spectra reported in Fig.4.14, obtained using Olmon dataset. In this case $V_{\text{rod}}^{NP\#2} = 1.35 \times 10^5 \text{ nm}^3$ and $R_{\text{eff}}^{NP\#1} = 31.8$ nm. Figure 4.13 shows the comparison between the ϵ_{NP} computed for NP#1 and NP#2, using $\epsilon_{g=0.75}$, $\epsilon_{g=1.5}$ and ϵ_{Olmon} . When considering NP#2 the overall change of the permittivity imaginary component (Fig.4.13(b)) is less compared to the case of NP#1. This is because its bigger volume, and the consequent larger R_{eff} , reduces the surface damping. Again, the real part is not too affected by the different particle sizes and by the introduction of the surface damping parameter. Figure 4.14 shows the effect of the modified permittivity on the extinction (left), absorption (middle) and scattering (right) cross-section for both exciting polarization aligned along ((a), σ^L) and across ((b), σ^T) the NR main axis. For both NP#1 (black) and NP#2 (red), σ_{ext} , σ_{abs} and σ_{sca} have been simulated using ϵ_{Olmon} (solid line) and $\epsilon_{g=1}$ (dashed line). Looking at the resulting simulations, similar considerations can be made for the two NPs. As expected, when the transversal mode is excited (Fig.4.14(b)), the results in terms of cross-section are less affected by the introduction of the surface damping because of the relatively smaller change in the $\Im(\epsilon_{\text{NP}})$ around 550 nm.

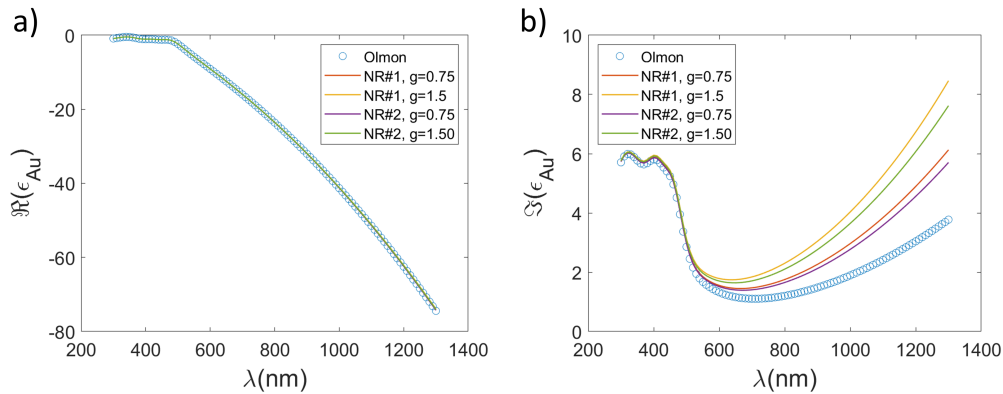


Figure 4.13: Fit of the experimental permittivity Olmon dataset with the Drude model and additional damping. (a) Real part and (b) imaginary part. Olmon data set (circles) and model (line) for $g=0.75$, $g=1.5$ and $R_{\text{eff}}=26$ nm (NP#1, i.e. $D=40$ nm, $AR=1.7$ and $R_{\text{tip}}=D/3$), $R_{\text{eff}}=31.8$ nm (NP#2, i.e. $D=50$ nm, $AR=1.6$ and $R_{\text{tip}}=D/3$).

Both the longitudinal and transversal LSPR positions are not affected by the surface damping parameter as $\Re(\epsilon_{\text{NP}})$ does not have significant changes. When the longitudinal mode is excited, the simulated absorption cross-section slightly broadens for stronger damping. The small reduction in its amplitude is attributed to numerical errors. Regarding the simulated scattering cross-section, the introduction of the surface damping and the consequent bigger $\Im(\epsilon_{\text{NP}})$ bring to a decreased LSPR peak and to a broader resonance (larger FWHM).

4.1.3.2 Error minimisation procedure

For our optical sizing tool via the comparison between experimental and simulated extinction cross-section ($\sigma_{\text{ext}}^{\text{exp}}$ vs $\sigma_{\text{ext}}^{\text{sim}}$), we assume that the overall extinction cross-section can be modeled as a weighted combination of the extinction cross-sections obtained when the two main plasmon modes are separately excited (Ref.[123]). Since in the ideal case we have the excitation of the sole longitudinal and transversal plasmon mode when the light is perfectly polarized along and across the NR respectively, the overall particle extinction cross-section can be seen as a weighted superposition of the longitudinal and transversal extinction cross-section contributions, i.e:

$$\sigma_{\text{ext}}^{\text{sim}}(\lambda) = \beta^{\perp}(\phi)\sigma_{\text{ext}}^{\perp}(\lambda) + \beta^{\parallel}(\phi)\sigma_{\text{ext}}^{\parallel}(\lambda) \quad (4.1.11)$$

where the symbols \perp and \parallel are used within this Section to represent the two cases of having the incident light polarized along and across the NR. To properly weigh the transversal and longitudinal contributions to the overall extinction cross-section, β^{\perp} and β^{\parallel} are expressed as:

$$\begin{aligned} \beta^{\perp} &= A_{\perp} \left(E_{\perp}^2 \sin^2(\phi - \phi_0) + E_z^2 \right) \\ \beta^{\parallel} &= A_{\parallel} \left(E_{\parallel}^2 \cos^2(\phi - \phi_0) \right) \end{aligned} \quad (4.1.12)$$

Let's now explain the different quantities appearing in Eq.4.1.12.

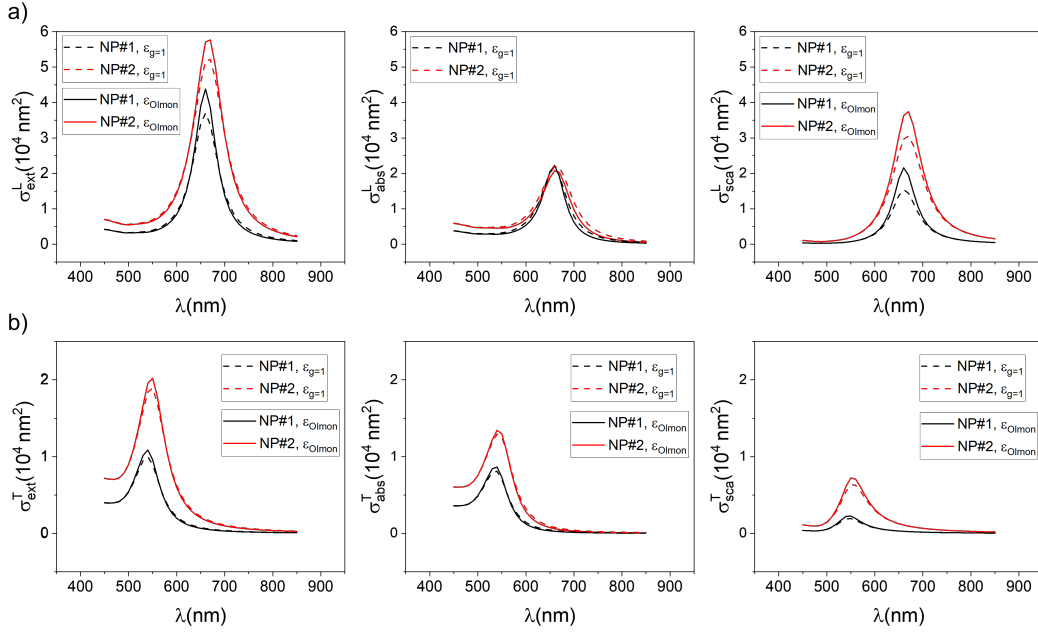


Figure 4.14: Simulated extinction (left), absorption (middle) and scattering (right) cross-section for $R_{\text{eff}}=26$ nm (NP#1) (black), $R_{\text{eff}}=31.8$ nm (NP#2) (red), using ϵ_{Olmon} (solid line) and $\epsilon_{g=1}$ (dashed line).

- Since we don't have an a priori knowledge about the exact particle orientation, the wide field extinction cross-section measurements were carried out at six different incident light polarizations (see Sec.4.1.1) at the nanorod plane, nominally 0° , 30° , 60° , 90° , 120° and 150° . To properly model and compare the simulated and experimental extinction, we have to take into account the mismatch between the light polarization used (ϕ) and the particle orientation (ϕ_0). The transversal and longitudinal contributions are depicted in the expression of β^\perp and β^{\parallel} as sinusoidal functions, dependent on ϕ , so that if $\phi - \phi_0 = 0^\circ$ only the longitudinal mode is excited and vice versa for $\phi - \phi_0 = 90^\circ$. The squares are needed to represent the contribution of the corresponding light intensity components to the cross-section.
- In Eq.4.1.12, E_\perp and E_{\parallel} are the relative cartesian components of the incident electric field in the front focal plane of an aplanatic lens, such as the condenser in a wide field optical microscope, adopting a Köhler illumination scheme and characterized by a high NA (in our case $\text{NA} = 1.34$). In the ideal case, when linearly polarized light is used, their values are equal to 1. In the experiment, we have to consider that, due to the high condenser NA employed, the incident field doesn't have just the nominal incident polarization, but also an additional component along the propagation axis (z -axis). This component, indicated as E_z , contributes to the transversal mode excitation only and this is why it appears just in the expression of β^\perp . Following Ref.[99], $E_\perp = E_{\parallel}$ and E_z were computed assuming that the illumination in the BFP of the lens propagates along the optic axis of the lens, has total spatial incoherence, has an axially symmetric intensity distribution and is linearly polarized in the BFP. Again, we consider the square of them since we need to express the correspondent field intensity.

E_{\perp}	0.909
$E_{//}$	0.909
E_z	0.409
f_{\perp}	0.362
$f_{//}$	0.384

Table 4.1: Parameter used in Eq.4.1.14 within this work.

- A_{\perp} and $A_{//}$ are dimensionless absolute factors needed to scale the simulation results to match experimental data.

Using Eq.4.1.11 with Eq.4.1.12 still does not allow us to have a quantitative comparison between $\sigma_{\text{ext}}^{\text{exp}}$ and $\sigma_{\text{ext}}^{\text{sim}}$. In fact, we still need to take into account the extent to which the objective used in the experiment collects the scattered light, and how this contributes to reducing $\sigma_{\text{ext}}^{\text{exp}}$. We took the advantage of being able to simulate and compute the absorption and scattering cross-sections separately to then write the simulated extinction as:

$$\sigma_{\text{ext}}^{\text{sim}} = (1 - f)\sigma_{\text{sca}}^{\text{sim}} + \sigma_{\text{abs}}^{\text{sim}} \quad (4.1.13)$$

where f represents the fraction of scattered power collected by the microscope objective. The f parameter depends both on the objective characteristics and on the angular distribution of the power scattered by the NR to the far-field. The latter is determined both by the electromagnetic excitation and by the NR optical response. Zilli et al. (Ref.[124]) derived the f parameter under the dipole approximation, thus assuming the electrostatic regime. This approximation is still a good one within this work as the size of the considered NR is smaller than the exciting wavelength. All the interactions of the dipole with the field it radiates were neglected, assuming a weak scatterer. The microscope illumination was taken as an incoherent superposition of plane waves and, consequently, the NR had to be seen as a collection of dipoles oscillating with unrelated phases, rather than a single dipole. Also, the scattering of the reflected radiation was not taken into account, which is a suitable approximation when there is no mismatch at the interface where the NR is placed. The optical response of the NR depends on its polarizability tensor α . When the longitudinal mode is excited, the polarizability $\alpha_{//}$ is uniaxial and parallel to the interface. Instead, for the excitation of the transversal mode, α_{\perp} can be seen as the scalar one characterizing the isotropic optical response of a sphere. These considerations lead to two different f parameters ($f_{//}$ and f_{\perp}) for the two excitation cases. In view of all the just mentioned aspects, a complete expression for $\sigma_{\text{ext}}^{\text{sim}}$ is given by Eq.4.1.14.

$$\begin{aligned} \sigma_{\text{ext}}^{\text{sim}}(\lambda, \phi) = & A_{\perp} \left(E_{\perp}^2 \sin^2(\phi - \phi_0) + E_z^2 \right) \left((1 - f_{\perp})\sigma_{\text{sca}}^{\perp}(\lambda) + \sigma_{\text{abs}}^{\perp}(\lambda) \right) + \\ & + A_{//} \left(E_{//}^2 \cos^2(\phi - \phi_0) \right) \left((1 - f_{//})\sigma_{\text{sca}}^{//}(\lambda) + \sigma_{\text{abs}}^{//}(\lambda) \right) \end{aligned} \quad (4.1.14)$$

The complete computation of the parameters E_{\perp} , $E_{//}$, E_z , f_{\perp} and $f_{//}$ can be found in Ref.[103] and Ref.[124], while here we just report the used values within this work in Table 4.1.

$\sigma_{\text{abs}}^{\perp}(\lambda)$, $\sigma_{\text{sca}}^{\perp}(\lambda)$, $\sigma_{\text{sca}}^{//}(\lambda)$ and $\sigma_{\text{sca}}^{//}(\lambda)$ in Eq.4.1.14 are computed making a sweep over different NR diameters and aspect ratio. The simulations were carried out considering the surface damping parameter in the gold permittivity and the surface

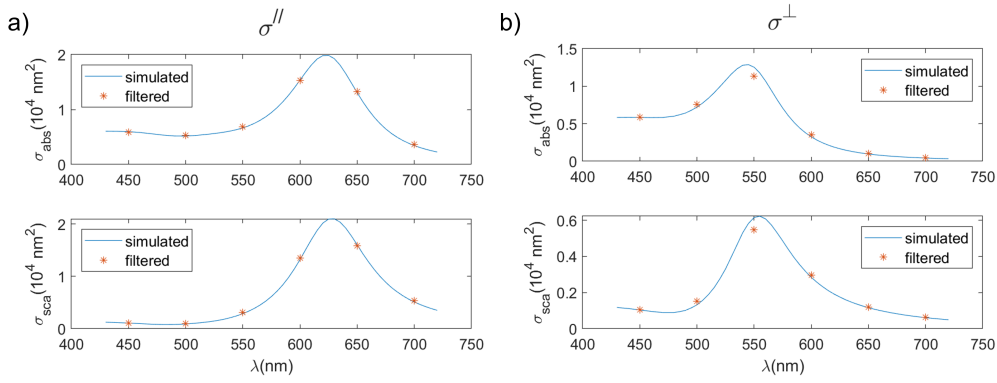


Figure 4.15: Resulting simulated absorption (top line) and scattering (bottom line) cross-sections for polarization aligned along (a) and across (b) a NR characterized by $(D, AR, g) = (52 \text{ nm}, 1.40, 1)$ in a wavelength range going from 430 nm to 720 nm in steps of 5 nm (solid lines) and for the corresponding filtered results assuming filters centered at 450 nm, 500 nm, ..., 700 nm with 40 nm bandwidth (star symbol).

scattering coefficient g has been used as a further degree of freedom to match better the simulation results with the experiments. While both the shell thickness and the rod tip shape were set to 10 nm and $D/3$ respectively (based on the TEM analysis results), the D , AR , and g parameters combination (simply indicated with (D, AR, g)) characterizing best a particle under study were estimated with the following error minimization procedure.

For each (D, AR, g) combination, we defined an error function as

$$err_{(D,AR,g)}(\lambda, \phi) = \sigma_{\text{ext}}^{\text{sim}(D,AR,g)}(\lambda, \phi) - \sigma_{\text{ext}}^{\text{exp}}(\lambda, \phi) \quad (4.1.15)$$

where $\sigma_{\text{ext}}^{\text{sim}(D,AR,g)}(\lambda, \phi)$ is structured as Eq.4.1.14. $\sigma_{\text{abs}}^{\perp}(\lambda)$, $\sigma_{\text{sca}}^{\perp}(\lambda)$, $\sigma_{\text{sca}}^{\parallel}(\lambda)$ and $\sigma_{\text{sca}}^{\parallel}(\lambda)$ were computed from simulation carried out in a wavelength range going from 430 nm to 720 nm in steps of 5 nm. Since in the wide field experiments we use filters centered at 450 nm, 500 nm, ..., 700 nm with 40 nm bandwidth, the simulated cross-section points obtained within 40 nm around the wavelength values used in the experiment were averaged to reproduce the effect of the filters bandwidth. Figure 4.15 shows how the filter bandwidth influenced the simulated $\sigma_{\text{abs}}(\lambda)$ (top) and $\sigma_{\text{sca}}(\lambda)$ (bottom) outcomes for both $\sigma^{\parallel}(\lambda)$ (a) and $\sigma^{\perp}(\lambda)$ (b). In this example $(D, AR, g) = (52 \text{ nm}, 1.40, 1)$. In Eq.4.1.14, ϕ was set to $0^\circ, 30^\circ, \dots, 150^\circ$ according to the polarizer orientation used in the experiment. For each tested (D, AR, g) , the nonlinear least-squares (nonlinear data-fitting) problems solver *lsqnonlin*, available in Matlab environment, was used to get the A_{\perp} , A_{\parallel} and ϕ_0 giving the smaller error between experiments and simulations. To each (D, AR, g) combination corresponds an error given by Eq.4.1.16, which takes into account that we have in total the comparison between 36 simulated and experimental data points (6 wavelengths and 6 light polarizations). This error is the quantity used to discriminate between the different (D, AR, g) combinations to find the best one.

$$err_{(D,AR,g)} = \sqrt{\frac{1}{36} \sum_{i=1}^{36} (err(\lambda, \phi))^2} \quad (4.1.16)$$

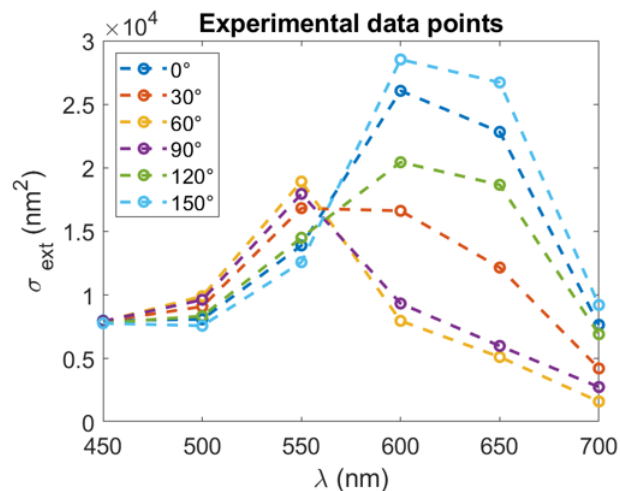


Figure 4.16: Extinction cross-section of a nominal $50 \text{ nm} \times 100 \text{ nm}$ -SiAuNRs (a,b) extracted from wide field extinction imaging measurements performed using a 100 W halogen lamp and band-pass filters at the different reported center wavelengths, for different in-plane linear polarizations, as indicated.

In the following, an example of this error minimization procedure is given. Let's consider the particle for which we measured the 36 data points (as explained in Sec.4.1.1) reported in Fig.4.16. Figure 4.17(a) shows the errors, computed via Eq.4.1.16, with $g=0.75$ and for different (D, AR) combinations. In this case the minimum error (equal to 768 nm^2) is obtained for $D=55 \text{ nm}$ and $AR=1.37$ and the correspondent fitting parameters are $A_{\perp}=1.0201$, $A_{//}=1.2276$ and $\phi_0=158^\circ$. Figure 4.17(b) shows the comparison between the experimental data points, $\sigma_{\text{ext}}^{\text{sim}}(\lambda, 158^\circ)$ and $\sigma_{\text{ext}}^{\text{sim}}(\lambda, 68^\circ)$. Additionally, the optimized surface damping coefficient g turns to be 0.75 , as demonstrated in Fig.4.18 where we report the errors obtained using $g=0.5$ and $g=1$. For these two g the minimum errors achieved were 769 nm^2 , for $(D, AR)=(56 \text{ nm}, 1.36)$, and 770 nm^2 , for $(D, AR)=(55 \text{ nm}, 1.37)$, respectively, slightly larger than the one given by $g=0.75$.

4.2 AuNBs

As explained in Chapter 3.2, the first step of the project involving the AuNBs antennas was focused on determining which antenna parameters (l, α) combination was the one optimized to have a longitudinal LSPR as close as possible to the CARS field wavelength in our experiment when measuring a lipid sample. To find the optimized combination, we exploited our polarization resolved extinction technique. To measure simultaneously the extinction of an array containing 10×10 nominally equal gold bowtie nanoantennas, as the ones reported in Fig.3.8(a), we used the wide field imaging technique. These measurements were carried out with AuNBs surrounded by a mixture of 80% Glycerol and 20% DI water.

Since in this case, all the antennas have the same orientation in space, the excitation polarization employed was the one parallel and orthogonal to the nanoantennas main axis, nominally at 0° and 90° . As in the case of nanorods, the AuNB LSPR band splits into two, i.e. a longitudinal (long axis of the antennas) and a transverse (short axis of the antennas) mode. Figure 4.19 reports a sketch (top view) of the nanobowties excited by the two polarization orthogonal to each other (red and blue

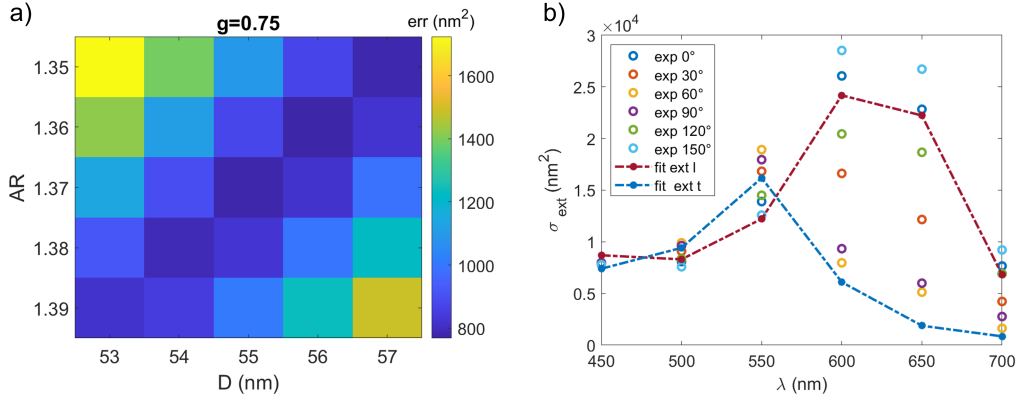


Figure 4.17: (a) Errors (nm^2) 2D map obtained via the error minimization procedure introduced in the text, comparing experimental and simulated extinction cross-sections. The latter were computed for $g=0.75$, varying the rod diameter D from 53 nm to 57 nm in steps of 1 nm and varying the AR from 1.35 to 1.39 in steps of 0.01. Minimum error (equal to 768 nm^2) found for $(D, AR)=(55 \text{ nm}, 1.37)$. (b) Comparison between experimental extinction cross section (same as Fig.4.16) and simulated extinction cross section calculated via Eq.4.1.14 using $A_{\perp}=1.0201$, $A_{//}=1.2276$ and $\phi_0=158^\circ$, resulting from the error minimization procedure (obtained with for $(g, D, AR)=(0.75, 55 \text{ nm}, 1.37)$, see text), for $\phi=158^\circ$ (dark red dash-dotted line, indicated as 'fit ext l' as this is the case of only longitudinal plasmon mode contribution) and for $\phi=68^\circ$ (blue dash-dotted line, indicated as 'fit ext t' as this is the case of only transversal plasmon mode contribution).

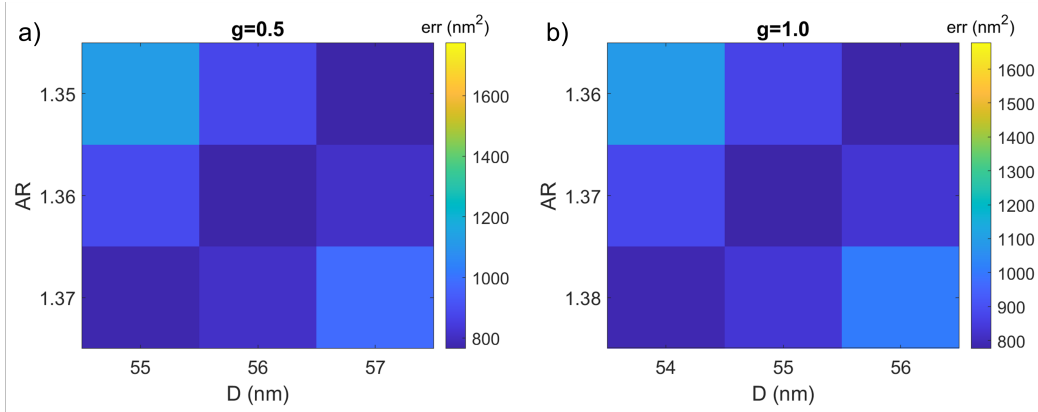


Figure 4.18: Errors (nm^2) 2D map obtained (via the error minimization procedure introduced in the text) comparing experimental and simulated extinction cross-sections. (a) Simulations carried out for $g=0.5$ varying the rod diameter D from 55 nm to 57 nm in steps of 1 nm and varying the AR from 1.35 to 1.37 in steps of 0.01. Minimum error (equal to 769 nm^2) found for $(D, AR)=(56 \text{ nm}, 1.36)$. (b) Simulations carried out for $g=1.0$, varying the rod diameter D from 54 nm to 56 nm in steps of 1 nm and varying the AR from 1.36 to 1.38 in steps of 0.01. Minimum error (equal to 770 nm^2) found for $(D, AR)=(55 \text{ nm}, 1.37)$.

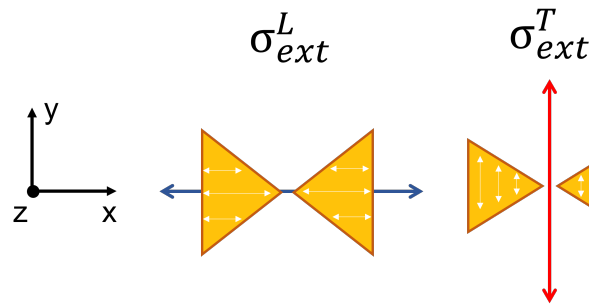


Figure 4.19: Schematic representation (top view) of AuNB and incident light, propagating in z direction, with polarization aligned along (blue arrow) and across (red arrow) the AuNB main axis, exciting the longitudinal and transversal LSPs respectively.

arrow) and the consequent direction of the oscillating electrons (white arrows). Here it is important to underline that from a practical point of view, during the mounting of the sample, when attaching the coverslip on the gasket, the coverslip, and thus also the nanostructures, can be slightly tilted in the xy plane. For each sample, the rotation of the linear polarizer was adjusted to optimize the excitation of the longitudinal and transversal plasmon mode, but due to the possible inclination of the coverslip together with the finite minimum rotation step of the polarizer, an error in defining the optimal polarizer orientation could take place in some cases. In this stage of the project, considering the good reproducibility of the antenna size, we were interested in the comparison of the LSPR spectral position rather than the absolute value of σ_{ext} . The LSPR position does not depend on the exciting polarization and it can be determined given that there is enough contribution to excite the plasmon mode. A comparison between the absolute values of the measured extinction is reliable when comparing antennas fabricated onto the same coverslip and excited in the same polarization condition. We studied how different nominal parameter combinations can lead to different extinction cross-section spectra. In this case, the extinction was measured using bandpass filters centered at 450 nm, 500 nm, 550 nm, 600 nm, 650 nm, 700 nm, and 750 nm with 40 nm bandwidth.

Figure 4.20 shows how the extracted extinction cross-section changes keeping the length parameter l fixed (in this case $l=60$ nm) and increasing the apex angle parameter α from 80° (a) to 90° (b) and then to 100° (c). In particular, on the left, we report the results obtained for each individual particle (identified by the number n_p) and for both excited LSPRs (longitudinal plasmon mode and transversal plasmon mode). On the right side of the figure, we report the correspondent extinction cross-section median value and the intervals defined by the 0.1 to 0.9 quantile, indicated with the error bars. In principle, each array should have contained 10×10 nominally equal antennas, but typically, due to error during the lift-off process, the complete removal of some antennas could take place. That is why in the n_p axis typically we have from 70 to 80 antennas that can be examined.

By looking at this result it is possible to notice that by increasing the apex angle, the absolute values of σ_{ext}^L increases. This behaviour is explained considering the overall volume of the probed nanoantennas which is 5034 nm^3 , 1200 nm^3 and 14301 nm^3 for (a), (b), and (c) respectively, and that the extinction cross section is directly proportional to the antennas volume (Ref.[86]). As mentioned, a direct comparison between the absolute value of these three sets of measurements is reasonable

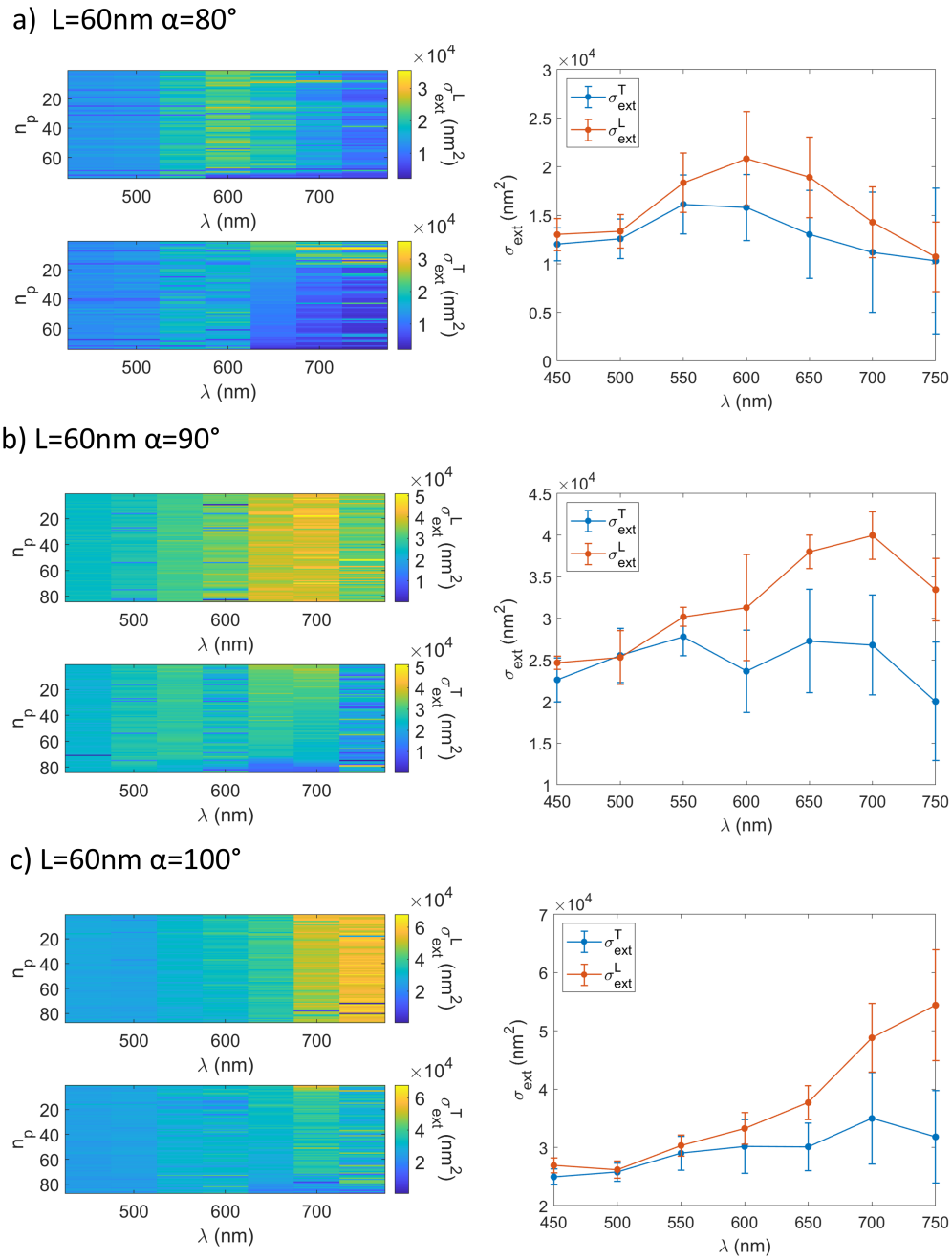


Figure 4.20: Spectral extinction cross-section of AuNBs characterized by $l=60\text{ nm}$. (a) $\alpha=80^\circ$, (b) $\alpha=90^\circ$ and (c) $\alpha=100^\circ$. Left: Extinction cross-section for each individual particle, indicated here with the number n_p , measured at 450 nm, 500 nm, ..., 750 nm, for longitudinal (top line) and transversal (bottom line) LSPR excited. Right: ensemble median spectrum and error bars indicating the 0.1 and 0.9 quantiles.

because all the nanostructures measured were fabricated onto the same coverslip, so they were affected by the same tilt coming from the coverslip attached to the imaging gasket. Additionally, the longitudinal plasmon mode undergoes a red-shift for larger α . This resonance red-shift can be understood as for an apex angle bigger than 80° , the two opposite corners (not defining the gap) of each nanotriangular are so apart from each other that two isolated LSPRs develop instead of a single one which is localized to the nanotriangular base and moves back and forth along the bowties main axis. These two plasmon modes will propagate back and forth from the corner of one nanotriangular to the opposite corner of the other nanotriangular. The two plasmon modes, interfering, give rise to a standing wave. The resonance of these standing waves will depend on the length of the oblique side of the two triangles so that it will be then more red-shifted for larger α as the electrons will have more space for the oscillations (Ref.[125]). From this set of measurements we can also see that in this experimental condition, the light polarization was slightly not optimized to be parallel and perpendicular with respect to the main axis of the antennas, as when using perpendicular polarization the longitudinal plasmon mode is still well visible (see Fig.4.20(b)). Despite this, the acquired data suggest that the optimal choice falls around the combination $(l,\alpha)=(60\text{ nm}, 90^\circ)$.

To have a direct comparison of how the extinction cross-section depends on the combination rather than just a parameter, Figure 4.21 shows the extinction data acquired on a sample where the nanostructures are characterized by $l=75\text{ nm}$ and α equal to 100° (a) and 90° (b). In both cases, the longitudinal plasmon mode turns out to be at longer wavelengths than the probed wavelength range, excluding these (l,α) combinations and l longer than 75 nm for the scope of our project.

Based on the results of Fig.4.20 and Fig. 4.21, a fine study on the extinction dependence on the l parameter once α is fixed at 90° has been carried out. Figure 4.22 shows the results for l set to be 50 nm (a), 55 nm (b), and 60 nm (c). A 5 nm increase of l corresponds to a LSPR red-shift in wavelength of 25 nm . Again these results can be understood considering a longer distance over which the electron can oscillate for longer l (Ref.[126]). Also in this case we can directly compare the absolute value of σ_{ext} as all the nanostructures measured were fabricated onto the same coverslip. As expected, we have an increase of σ_{ext} for longer l as the volume of the antennas goes from 10000 nm^3 (a), to 11000 nm^3 (b), and to 12000 nm^3 (c). Moreover, by directly comparing Fig.4.22(c) with Fig.4.20(b) is it possible to see how a less optimized incident polarization, as in the second case, change the extinction result compared to a better polarization choice. In fact, in both cases, it is clear how the longitudinal plasmon mode is centered around 675 nm , but in the second case, we have both a higher absolute value for σ_{ext}^L and also a complete decoupling between σ_{ext}^L and σ_{ext}^T when using the two orthogonal polarizations.

In general, looking at the presented results and comparisons, we confirmed that the best choice of (l,α) combination turns out to be $(60\text{ nm}, 90^\circ)$ as in this condition, the LSPR is centered closer to 660 nm .

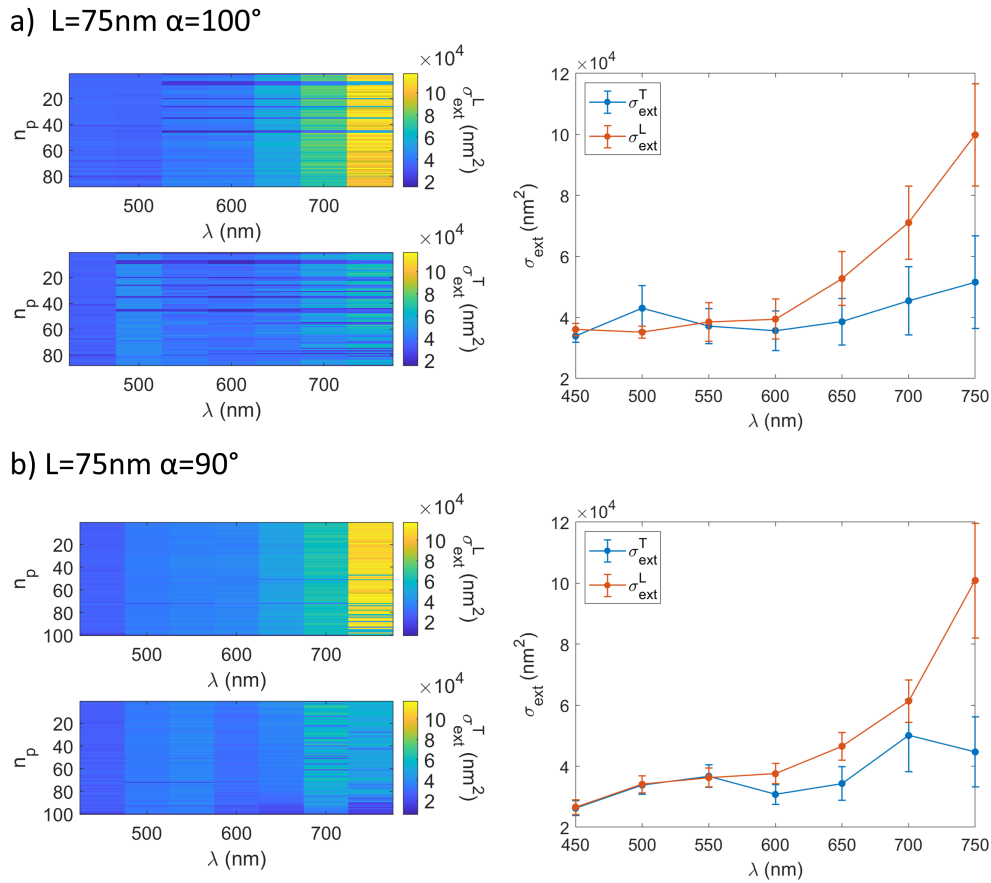


Figure 4.21: Spectral extinction cross-section of AuNBs characterized by $l=75\text{ nm}$. (a) $\alpha=100^\circ$ and (b) $\alpha=90^\circ$. Left: Extinction cross-section for each individual particle, indicated in here with the number n_p , measured at 450 nm, 500 nm, ..., 750 nm, for longitudinal (top line) and transversal (bottom line) LSPR excited. Right: ensemble median spectrum and error bars indicating the 0.1 and 0.9 quantiles.

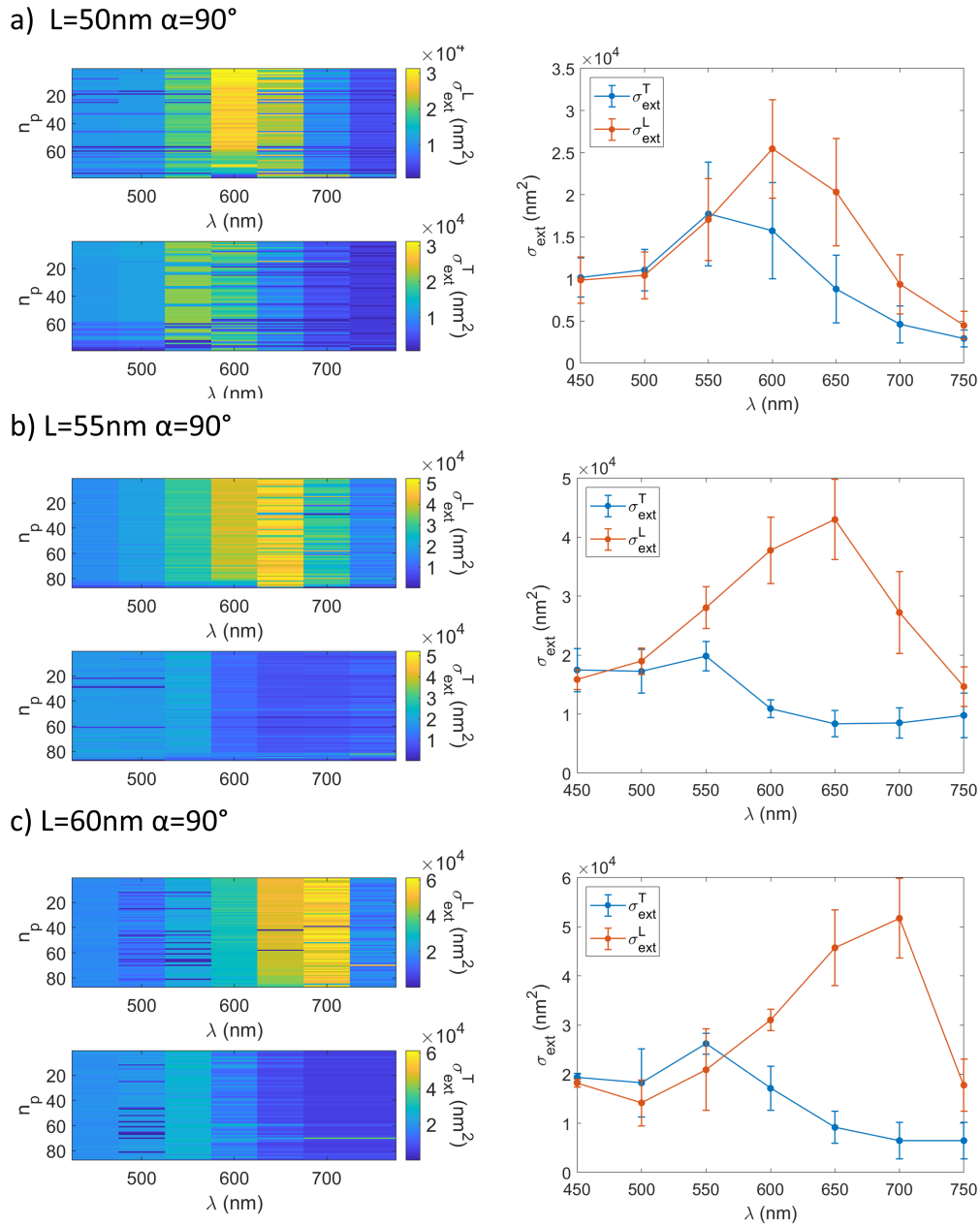


Figure 4.22: Spectral extinction cross-section of AuNBs characterized by $\alpha=90^\circ$. (a) $l=50^\circ$, (b) $l=55^\circ$ and (c) $l=60^\circ$. Left: Extinction cross-section for each individual particle, indicated here with the number n_p , measured at 450 nm, 500 nm, ..., 750 nm, for longitudinal (top line) and transversal (bottom line) LSPR excited. Right: ensemble median spectrum and error bars indicating the 0.1 and 0.9 quantiles.

Chapter 5

LFE eH-CARS with SiAuNRs

In this Chapter, our primary objective is to establish a proof of principle for the LFE eH-CARS technique. Our investigation delves into understanding the behavior of the nanorods when subjected to different excitation modalities. We aim to quantify the enhancements observed in the far field and assess the stability and reproducibility of these enhancements. Furthermore, we extend our exploration to unravel the near-field phenomena occurring in this context, utilizing COMSOL simulations.

This chapter serves as a comprehensive exploration of LFE eH-CARS and its potential applications, shedding light on both its far-field and near-field characteristics, and laying the foundation for further study and application in the field.

5.1 Circular vs Linear excitation polarization

To ensure the highest enhancement achievable when exploiting a gold nanorod, it is crucial to optimize the interaction between the rod, the incident light fields, and the CARS field to be enhanced. It is important to ensure both a spectral and a directional overlap between the CARS field and the NR LSPR. The spectral overlap is optimized by choosing a nanorod size such that its longitudinal LSPR turns out to be as close as possible to the wavelength of the field that has to be enhanced. In this work, we aim to enhance the CARS field provided by lipid (i.e. molecules vibrating in the CH stretch region), which in our experimental implementation has a wavelength of around 660 nm, while limiting the absorption of pump and Stokes field. Regarding the directional overlap, we need to adjust the CARS field polarization direction, aligning it along the NR longitudinal axis.

The polarization of the CARS field depends on the polarization of the pump and Stokes beams, which in our case have a starting horizontal linear polarization. By introducing a wave plate before the sample (as shown in Fig.3.18) it is possible to change their polarization and consequently the one of the CARS beam. In order to have a CARS field circularly polarization, a $\lambda/4$ wave plate has to be used, while a $\lambda/2$ wave plate is needed to rotate the initial linear polarization. To understand the characteristics of the detected signals when using both wave plates, it is essential to take into account that the epi-emitted signal passes through the wave plate and that the reference beam, used for the interferometric detection, is polarized at 45° to have equal vertical and horizontal components.

In the following section, we provide a qualitative explanation of how the polarization changes during the beam propagation up to the detector, for conventional

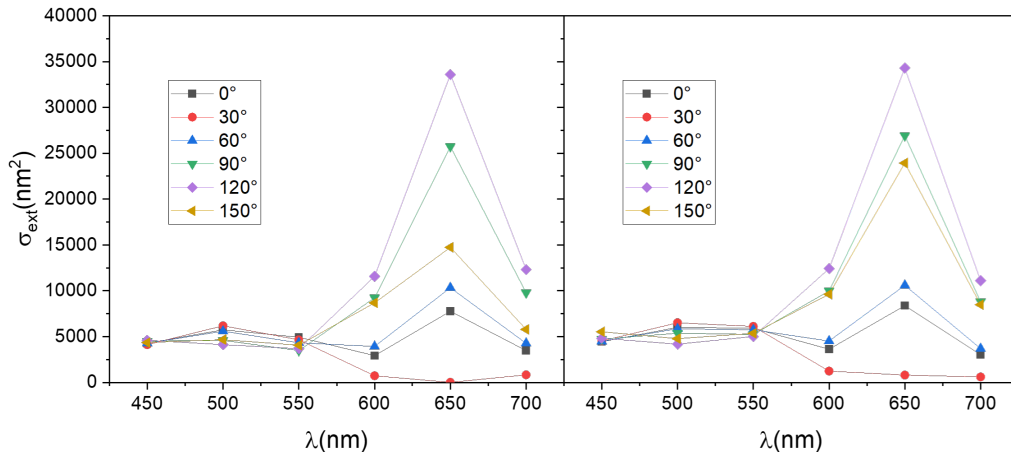


Figure 5.1: Extinction cross-section of two nominal $40 \text{ nm} \times 68 \text{ nm}$ -SiAuNRs surrounded by silicone oil extracted from wide field extinction imaging measurements (see Chapter 3.3.1) performed using a 100 W halogen lamp and band-pass filters with the different reported center wavelengths, for in-plane linear polarization, as indicated. Left: before the laser exposure. Right: after the laser exposure in the CARS experiment.

epi-detected CARS and epi-detected local-field enhanced CARS when utilizing the two wave plates mentioned. All the measurements shown in this section were acquired at the same particle. The extinction cross-section spectrum of such particle has been measured (Fig.5.1) both before (left) and after (right) all the laser exposures. The particle under study in this section did not undergo a reshaping and also its in-plane orientation did not show marked variation. This is important to confirm the consistency of the comparison between the two wave plates such that different detected fields are related to the different excitation modalities and not to particle reshaping. The selected NR is a nominal $40 \text{ nm} \times 68 \text{ nm}$ -SiAUNR with 10 nm silica shell. Its longitudinal LSPR is centered at 650 nm in a surrounding silicone oil medium (of $n=1.52$ refractive index matched to glass), close to the CARS signal wavelength from the glass-oil interface originating from the silicone oil vibrational resonance in the CH-stretch region ($\sim 2900 \text{ cm}^{-1}$) using the pump and Stokes wavelengths in our experiment (see set-up in Chapter 3.3.2).

A wave plate (or phase retarder) is an optical device that is used to modify the polarization state of light passing through it. It is made of a birefringent material which means that the refractive index experienced by the incoming field depends on the field polarization orientation compared to the two characteristic material axis. In fact, a birefringent material has a slow axis and a fast axis, both being perpendicular to the beam direction and also to each other. The names of such axis comes from the refractive index associated with their direction which makes the incoming beam travel slower and faster respectively within the material. The difference between the $\lambda/2$ and $\lambda/4$ wave plate stays in the propagation length within the wave plate, which determines how it will affect the incoming beam. When a $\lambda/2$ wave plate is inserted in the beam path, pump and Stokes linear polarizations can be rotated and the amount of the rotation depends on the angle (θ) formed by the wave plate fast axis and the incoming polarization orientation.

Exploiting the Jones formalism (Ref.[127]) we can express a field horizontally polar-

ized as

$$\mathbf{E}^H = \begin{pmatrix} 1 \\ 0 \end{pmatrix}.$$

The transformation matrix describing a $\lambda/2$ wave plate is given by (Ref.[128])

$$\mathbf{T}_{\lambda/2} = \begin{pmatrix} \cos(2\theta) & \sin(2\theta) \\ \sin(2\theta) & -\cos(2\theta) \end{pmatrix},$$

so that the resulting beam polarization (\mathbf{E}_{out}) for an horizontally polarized input field (\mathbf{E}^H) is given by

$$\mathbf{E}_{\text{out}} = \mathbf{T}_{\lambda/2} \mathbf{E}^H = \begin{pmatrix} \cos(2\theta) & \sin(2\theta) \\ \sin(2\theta) & -\cos(2\theta) \end{pmatrix} \begin{pmatrix} 1 \\ 0 \end{pmatrix}.$$

In the following we will consider a reference system where the horizontal orientation corresponds to 0° rotation and anti-clockwise rotation has a positive sign. If the $\lambda/2$ wave plate is rotated at 45° (Fig.5.2), pump and Stokes beams acquire a vertical polarization prior to excite the sample. In fact, if $\theta=45^\circ$, $\mathbf{E}_{\text{out}} = \begin{pmatrix} 0 \\ 1 \end{pmatrix} = \mathbf{E}^V$.

For any given input polarization, it can be generalized that when a $\lambda/2$ wave plate is adjusted to an angle θ , it rotates of the input polarization by twice θ . Since the silicone oil is isotropic, it doesn't affect the symmetry of the beams and the generated (unenhanced) CARS signal is linearly vertically polarized as the exciting pump and Stokes. Passing through the $\lambda/2$ wave plate, its polarization is rotated, back to horizontal (Fig.5.2(left)), so that the interference with the reference field leads to the detection of a linearly horizontally polarized field. If, in the same wave plate condition, pump and Stokes are focused in the vicinity of a NR with orientation such that the unenhanced CARS field is aligned along the NR (Fig.5.2 (right)), which represent the optimized case, the enhanced CARS field is vertically polarized as well and then the detected field horizontally polarized. Section 5.3 will investigate the consequences of having a $\lambda/2$ wave plate rotation such that the unenhanced CARS field is not aligned along the NR main axis.

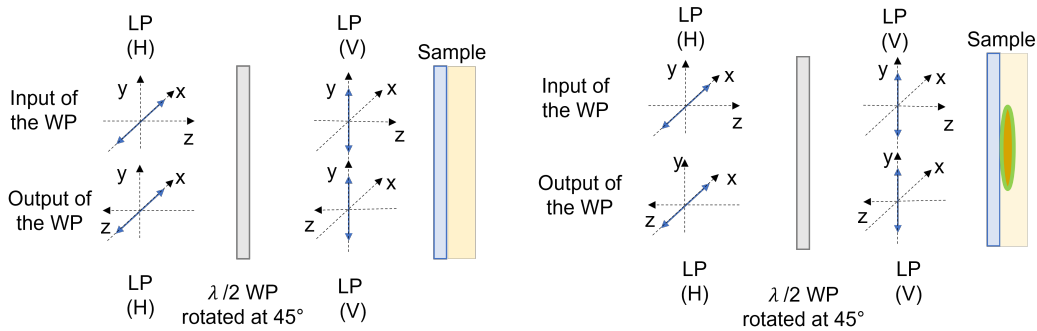


Figure 5.2: Sketch of the polarization acquired by the fields when a $\lambda/2$ wave plate is used in the beam path. Left: Without NR in beams focus. Right: NR in the beam focus, oriented so that the beams polarization is aligned along its main axis. LP: Linear Polarization. WP: wave plate.

Figure 5.3 shows TPF and LFE eH-CARS amplitude xy-images acquired at the focus of the NR presented in Fig.5.1, using linear excitation polarization. The $\lambda/2$

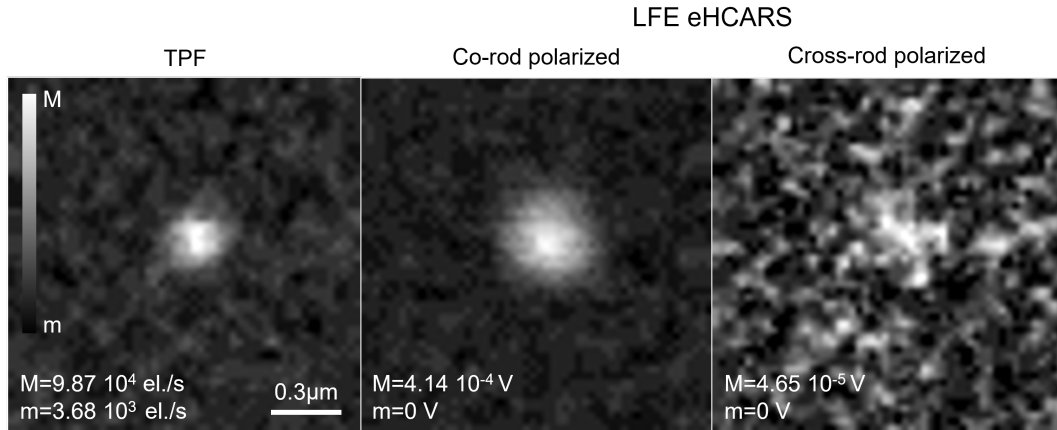


Figure 5.3: Left: Two photon fluorescence from linear excitation polarization. Middle and Right: Polarization resolved eH-CARS amplitude at silicone oil resonance (2904 cm^{-1}) with linear excitation polarization aligned along the longitudinal axis of the NR, as measured, lock-in offset corrected; Co-(middle) and Cross-(right) rod components correspond to horizontal (H) and vertical detected components, respectively (see text). Measurement acquired at the particle focus, with 1.45NA objective. Actual exciting power at the sample: $P_P=1.2\text{ mW}$ (pump) and $P_S=4\text{ mW}$ (Stokes). Gray scales from m (black) to M (white). Values are in units of electron per second for TPF intensity and volts for eH-CARS amplitude.

wave plate was rotated so that pump, Stokes and CARS field were co-rod polarized. Pump and Stokes powers at the sample focus were respectively 1.2 mW and 4 mW. The physical origin of the signal detected in the nominal TPF channel is related to the two-photon luminescence (TPL) (Ref.[129], Ref.[130]) of the gold nanorod arising from either pump or Stokes photons absorption, as it has been shown to have a broad spectral dependence (Ref.[131]). The simultaneous absorption of two photons induces the excitation from the d-band to the sp-band. The closer the wavelength of the exciting photons gets to the LSPR associated with the nanorod under study, the greater the enhancement of this phenomenon becomes. Via intraband scattering processes, the excited electrons in the sp-band move close to the Fermi energy. Subsequently, two relaxation paths can take place. Both potentially contribute to the detection of the signal (around 500 nm) in the nominal TPF channel. By inter-band radiative relaxation, the electrons and holes can recombine. Alternatively, by a sp-band electrons nonradiative decay, the two NR plasmon modes can be excited causing then the emission of photons characterized by the specific plasmon wavelength and polarization (Ref.[132]). Thus, in the nominal TPF channel, due to its bandwidth (see Chapter 3.3.3), it is measured the contribution of the transversal mode. For the LFE eH-CARS amplitude both co- and cross-rod polarized detected components, which correspond to H and V components in our detection system, are displayed, to demonstrate that, at the used laser powers and for exciting field polarization aligned along the NR, the contribution given by the NR transversal mode is negligible. Both the signal emitted by the silicone oil and the enhanced signal obtained in the presence of the particle are detected in the co-rod polarized component.

When working with the $\lambda/4$ wave plate, its rotation is set, independently from any NR in-plane orientation (Fig.5.4(left)), so that pump and Stokes (initially hor-

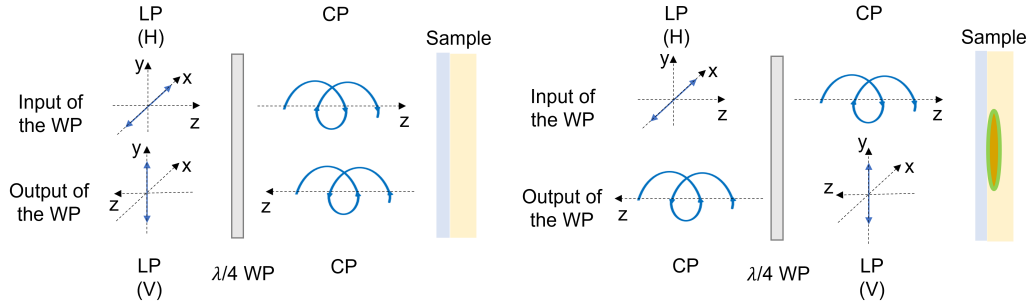


Figure 5.4: Sketch of the polarization assumed by the fields when a $\lambda/4$ wave plate is used in the beam path. Left: Without NR in beams focus. Right: NR in the beam focus. LP: Linear Polarization, CP: Circular Polarization.

izontally linearly polarized) are incident on the wave plate at 45° to its optics axis. The transformation matrix describing a $\lambda/4$ wave plate is given by (Ref.[128])

$$\mathbf{T}_{\lambda/4} = e^{-i\pi/4} \begin{pmatrix} \cos^2(\theta) + i \sin^2(\theta) & \sin(\theta)\cos(\theta) - i \sin(\theta)\cos(\theta) \\ \sin(\theta)\cos(\theta) - i \sin(\theta)\cos(\theta) & \sin^2(\theta) + i \cos^2(\theta) \end{pmatrix},$$

so that the resulting beam polarization (\mathbf{E}_{out}) for an horizontally polarized input field (\mathbf{E}^{H}) is given by

$$\mathbf{E}_{\text{out}} = \mathbf{T}_{\lambda/4} \mathbf{E}^{\text{H}}.$$

Since in our experiment, we set $\theta=45^\circ$ the Jones matrix for the $\lambda/4$ wave plate reduces to

$$\mathbf{T}_{\lambda/4} = \frac{1}{\sqrt{2}} \begin{pmatrix} 1 & -i \\ -i & 1 \end{pmatrix}.$$

As consequence,

$$\mathbf{E}_{\text{out}} = \frac{1}{\sqrt{2}} \begin{pmatrix} 1 & -i \\ -i & 1 \end{pmatrix} \begin{pmatrix} 1 \\ 0 \end{pmatrix} = \frac{1}{\sqrt{2}} \begin{pmatrix} 1 \\ -i \end{pmatrix}$$

which is the Jones matrix describing a right-circularly polarized. Thus, pump and Stokes acquire a circular polarization. The consequent glass-oil interface CARS field is circularly polarized as well. The latter, propagating in the backward direction, has then a reverse circular helicity, and passing through the $\lambda/4$ wave plate, results at the end in a vertically polarized signal. After the interference with the reference beam, it reaches the detector as fully vertically-polarized (V). When pump and Stokes excite a region where a NR is placed (Fig.5.4 (right)), this breaks the CARS field symmetry, because, in first approximation, the rod structure strongly enhances the CARS field along a well-defined linear polarization direction. Thus, the enhanced CARS signal, after the $\lambda/4$ wave plate, acquires an elliptical polarization. The relative magnitude of the ellipse semi-axes depends on the NR orientation. For example, if the particle is oriented parallel or perpendicular to the initial polarization of pump and Stokes beams, the enhanced CARS field will be circularly polarized, as it is incident at 45° to the wave plate optics axis. In both cases of elliptically or circularly polarized field, the interference with the reference gives the detection of a signal with both co-(detected in the V channel) and cross-(detected in the H channel) circularly polarized components, relative to the incident circularly polarized pump and Stokes.

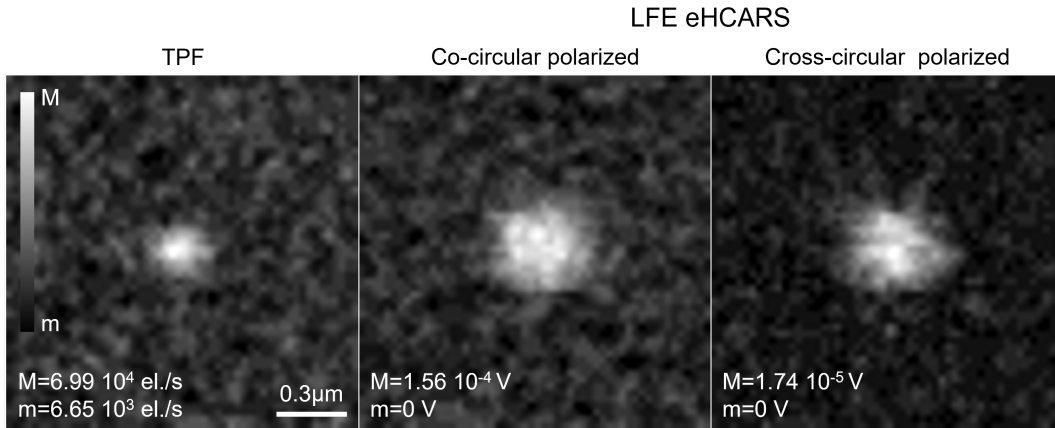


Figure 5.5: Left: Two photon fluorescence from linear excitation polarization. Middle and Right: Polarization resolved eH-CARS amplitude at silicone oil resonance (2904 cm^{-1}) with circular excitation polarization, as measured, lock-in offset corrected (see Chapter 3.3.4.); Co- (middle) and Cross- (right) circular components correspond to vertical (V) and horizontal (H) detected components, respectively (see text). Actual exciting power at the sample: $P_P P_S^{1/2} = 1.22\text{ mW}^{3/2}$. Gray scales from m (black) to M (white). Values are in units of electron/second for TPF intensity and volts for eH-CARS amplitude.

Figure 5.5 shows TPF and LFE eH-CARS amplitude xy-images, acquired again at the same NR of Fig.5.1, using this time circular excitation polarization. Here, pump and Stokes powers were respectively 1.6 mW and 5.6 mW. As expected the LFE eH-CARS signal turns out to be split in the two detected components, while the not enhanced signal coming from the glass-oil interface turns to be only in the co-circular detected component.

Comparing the TPF maximum value obtained at the NR PSF, we can see that the usage of the $\lambda/2$ wave plate allows to have a signal higher in magnitude than the case of the $\lambda/4$. For the LFE eH-CARS measurements, the utilization of the $\lambda/2$ gives a better S/N as all the signal emitted at the NR is in one detected component. From a practical point of view, since we do not have an a priori knowledge about the NR orientation, it is challenging to match the exciting beams polarization using the $\lambda/2$ wave plate with the orientation of the rod. To achieve this matching, typically the NR has to be laser exposed for a certain duration before continuing with the desired measurement. Ideally, the laser dwell time on the NR should be minimized to prevent damage. To that end, using circular polarization ensures that the longitudinal plasmon of the rod is excited, as circularly polarized light always have a component along the main NR axis. However, also in this case there are few downsides. As already mentioned, the S/R is not optimized because the NR signal is detected both in the co- and cross- circular components. Additionally, for given pump and Stokes input powers, a lower overall power is actually exciting the NR. In fact, since $E_{\text{CARS}} \propto E_P^2 E_S$ and power $P \propto E^2$, when we use linear polarization in excitation, $E_{\text{CARS}} \propto P_P \sqrt{P_S}$. When the $\lambda/4$ wave plate is used, the amplitude of the input electric field is effectively aligned along the NR axis and on average decreased by a factor $\frac{1}{\sqrt{2}}$. As consequence:

$$E_{\text{CARS}} \propto \left(\frac{E_P}{\sqrt{2}} \right)^2 \frac{E_S}{\sqrt{2}} = \frac{E_P^2 E_S}{2 \sqrt{2}} = \frac{P_P \sqrt{P_S}}{2 \sqrt{2}} \quad (5.1.1)$$

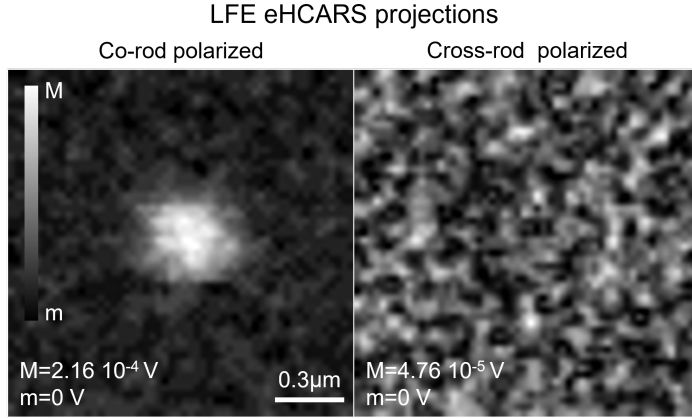


Figure 5.6: Projection of the detected eH-CARS signal shown in Fig. 5.5, along (co-) and across (cross-) the longitudinal axis of the NR. Gray scales from m (black) to M (white). Values are in units of volts.

Due to the main advantage of being able to excite the longitudinal LSPR even without knowing its in-plan orientation, we decided to develop an analysis procedure, explained in the following, to improve the S/N associated to the measurements performed employing the $\lambda/4$ wave plate. The co- (\mathbf{S}_p) and cross- (\mathbf{S}_m) circular detected fields can be expressed in terms of the fields emitted by the NR, which are linearly polarized along the longitudinal (\mathbf{S}_{co}) and transversal (\mathbf{S}_{cross}) axes, as:

$$\begin{cases} \mathbf{S}_p = \frac{1}{\sqrt{2}}(\mathbf{S}_{co} + i\mathbf{S}_{cross}) \\ e^{i\theta} \mathbf{S}_m = \frac{1}{\sqrt{2}}(\mathbf{S}_{co} - i\mathbf{S}_{cross}) \end{cases} \quad (5.1.2)$$

The relative phase between \mathbf{S}_p and \mathbf{S}_m is taken into account multiplying \mathbf{S}_m by $e^{i\theta}$, with $\theta = \theta_{S_p} - \theta_{S_m}$. Starting from Eqs.5.1.2, it is possible to derive the projection of the detected signals onto the particle main axes, obtaining:

$$\mathbf{S}_{co} = \frac{1}{\sqrt{2}} (\mathbf{S}_p + e^{i\theta} \mathbf{S}_m) \quad (5.1.3)$$

and

$$\mathbf{S}_{cross} = \frac{1}{\sqrt{2}} (-i\mathbf{S}_p + ie^{i\theta} \mathbf{S}_m) \quad (5.1.4)$$

Note that the lock-in offset correction mentioned in Chapter 3.3.4 is included in \mathbf{S}_p and \mathbf{S}_m , so that $\mathbf{S}_i = \mathbf{S}_i + \boldsymbol{\sigma}_{S_i}$, with $i=p,m$ and $\boldsymbol{\sigma}$ representing the applied offset. In Fig.5.6 is it possible to see the results of these projections starting from the data of Fig.5.5. As expected the signal provided by the rod turns out to be fully in the co-rod polarized component and there is an improvement of the S/R of a factor of $\sqrt{2}$. This improvement comes from the fact that the signal from the NR detected in the two channels constructively interference giving an improvement of 2 to the overall signal. Instead, the noise related to these acquisitions is randomly added giving for it an increase of $\sqrt{2}$. Thus the obtained signal to noise is $\sim \frac{2S}{\sqrt{2}N} = \sqrt{2} \frac{S}{N}$.

5.2 Enhancement quantification (R factor)

Within this work, the measured signal enhancement provided by a NR is quantified using a value named R-factor. The R-factor is defined considering the CARS fields

as complex quantities and evaluating the field measured at the NR spatial position and away from it. In fact, it is calculated starting from an eH-CARS 2D scan, offsetting the field obtained at the NR PSF with the field obtained at the glass-oil interface away from the NR, and applying a normalization to this difference using the amplitude measured at the glass-oil interface. In essence, the R factor expresses the signal provided by the rod in unit of glass-oil interface signal. From a practical point of view, starting from an xy scan of the particle, taken at the particle z focus (as the ones showed in Fig.5.3, 5.5 and 5.6), the R factor is computed considering a x-cut ~ 100 nm wide (in the y direction), passing through the center of the NR PSF. This 2D set of data were averaged into one pixel in the y axis to maximize the signal to noise ratio. The signal measured at the glass-oil interface is thus given by the signal at the edge of this x-cut. Going into details, we need to consider how different excitation/detection approaches will impact onto the R factor computation.

- If the $\lambda/2$ wave plate is exploited and its rotation optimized to have the CARS field along the NR main axis, both the NR and glass-oil interface detected signals will result in having only an horizontal component (see sketch in Fig.5.2). The formula used to compute the R factor in this case is:

$$R = \frac{|\mathbf{E}_{\text{NR}}^{\text{H}} - \mathbf{E}_0^{\text{H}}|}{|\mathbf{E}_0^{\text{H}}|} \quad (5.2.1)$$

where \mathbf{E}_0 represents the glass-oil interface field and \mathbf{E}_{NR} the field measured at the NR. Note that, as complex quantities are involved, $|\mathbf{E}_{\text{NR}}^{\text{H}} - \mathbf{E}_0^{\text{H}}|$ translates into $\sqrt{(\Re(\mathbf{E}_{\text{NR}}^{\text{H}}) - \Re(\mathbf{E}_0^{\text{H}}))^2 + (\Im(\mathbf{E}_{\text{NR}}^{\text{H}}) - \Im(\mathbf{E}_0^{\text{H}}))^2}$.

- When using the $\lambda/4$ wave plate, without applying any projection to the results, the signal provided by the rod is contained in both co- and cross- (vertical and horizontal) circular components. Therefore, it is a good practise to compute the R factor for both, as

$$R_{\text{co-circ}} = \frac{|\mathbf{E}_{\text{NR}}^{\text{co-circ}} - \mathbf{E}_0^{\text{co-circ}}|}{|\mathbf{E}_0^{\text{co-circ}}|} \quad (5.2.2)$$

and

$$R_{\text{cross-circ}} = \frac{|\mathbf{E}_{\text{NR}}^{\text{cross-circ}} - \mathbf{E}_0^{\text{cross-circ}}|}{|\mathbf{E}_0^{\text{cross-circ}}|} \quad (5.2.3)$$

It is important to underline that in both $R_{\text{co-circ}}$ and $R_{\text{cross-circ}}$ appears $\mathbf{E}_0^{\text{co-circ}}$ as the glass-oil interface signal is detected only in the co-circular polarized component.

- If the $\lambda/4$ is used but the projection of the NR detected signal is computed (as explained in Sec.5.1), the R factor can be computed as

$$R = \frac{|\mathbf{E}_{\text{NR}}^{\text{co-rod}} - \mathbf{E}_0^{\text{co-circ}}|}{|\mathbf{E}_0^{\text{co-circ}}|} \quad (5.2.4)$$

After the R factor calculation, the result is fitted with a Gaussian amplitude function because of the typical bell-shaped curve exhibited by the x-cut. The general form of a Gaussian amplitude fitting function is:

$$f(x) = Ae^{-\frac{(x-\mu)^2}{2\sigma^2}} \quad (5.2.5)$$

where $f(x)$ represents the value of the function at a specific x-coordinate, A is the amplitude or maximum value of the Gaussian curve, μ is the mean or center of the Gaussian curve and σ is the standard deviation, which relates to the width or spread of the curve. The R factor provided by the NR under study will be then given by the amplitude A of this Gaussian fit. While the computation of the R factor is performed across the entire PSF, the enhancement provided by a NR is generated from a region significantly smaller than the PSF. As a result, the values obtained for R do not represent the actual local field enhancement occurring at the surface of the NR. A discussion of the local field enhancement in the nanoscale region near NR will be presented in Sec.5.7.

Figure 5.7 shows the result for the R factor obtained along the x-cut passing through the center of the NR PSF and the consequent Gaussian amplitude fitting function, for the three introduced cases: (a) linear exciting polarization along the NR (R factor computed starting from the data of Fig.5.3), (b) circular polarization in both excitation and detection (R factor computed starting from the data of Fig.5.5) and (c) circular exciting polarization with projection of the detected components (R factor computed starting from the data of Fig.5.6). The highest R factor is obtained in the first case (16.6 ± 0.4), using the $\lambda/2$ wave plate in excitation. As expected using the $\lambda/4$ wave plate, since the NP signal is distributed in the two detected components, we obtained the lowest R factors ($R_{\text{co-circ}} = 3.62 \pm 0.09$ and $R_{\text{cross-circ}} = 4.33 \pm 0.09$). An intermediate R factor is obtained by exploiting the projection of the detected signal (9.66 ± 0.19), because although in this case the actual overall exciting power is reduced, all the signal emitted by the NR turns out to be in one component, with the consequent improvement of the S/R.

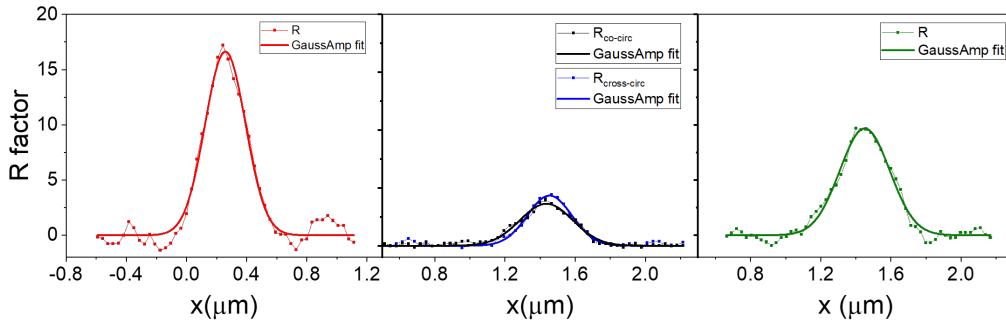


Figure 5.7: R factor, i.e. signal measured at the particle in unit of silicone oil signal. A polarization resolved eH-CARS 2D scan is acquired and the signal measured at the x-cut passing through the center of the NR PSF, as real and imaginary part, is offset with respect the signal emitted by the silicone oil and normalized to the amplitude of this last one. Different excitation modality (see text) have been used. Left: linear excitation polarization. Middle: circular excitation polarization. Right: circular excitation polarization and projection of the detected eH-CARS signal along(co-) and across(cross-) the longitudinal axis of the NR. Dot: experimental data; line: Gaussian amplitude fit.

5.3 Linear Polarization excitation dependence of LFE eH-CARS

When using the $\lambda/2$ wave plate, as mentioned before, the rotation of the latter has to be set so that the polarization of the exciting beams is aligned along the longitudinal axis of the NR under study. To do this, spatially resolved acquisitions of the eH-CARS field in the region of the NR have to be acquired prior performing the actual measurement so that the rotation of the wave plate is optimized to get the higher LFE eH-CARS signal. We took advantage of those needed pre-scan to study how the signal at the NR varies depending of the $\lambda/2$ wave plate rotation.

Figure 5.8 is a sketch representing the polarization adopted by the beams travelling through the different stages of the setup. We consider the ideal condition of a NR placed perfectly flat onto the glass surface (xy-plane) and all the fields propagating along the z direction, taken as perpendicular to the sheet. In particular, the exciting fields are represented as incoming the sheet (1,2), while the field then collected by the objected are represented as outgoing the sheet (3,4,5). In the following, we detail the polarization configuration as per sketch sequence 1-5 in Fig.5.8.

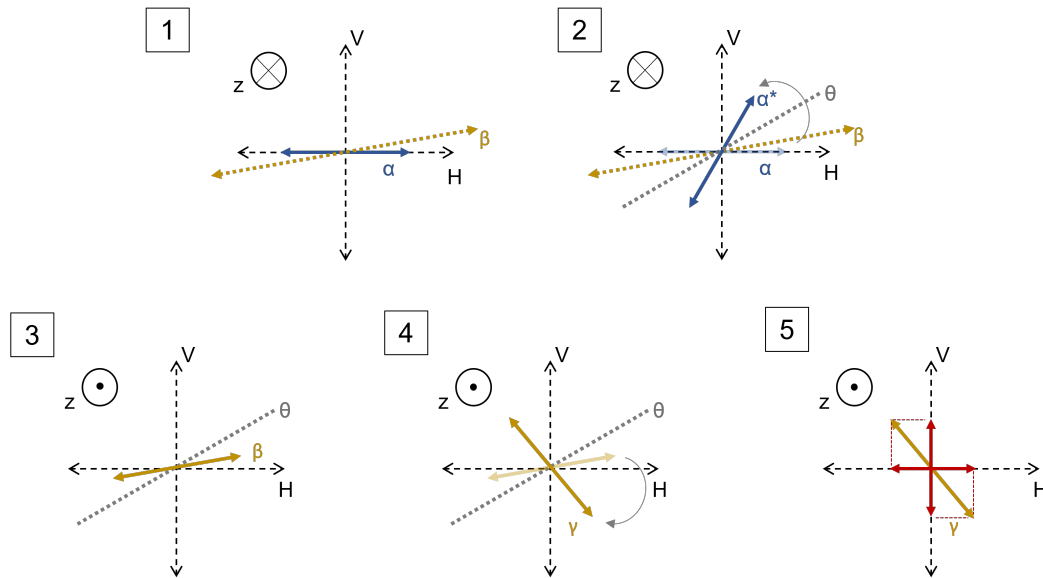


Figure 5.8: Sketch represented the polarization configuration sequence (1-5) assumed by the beams travelling through the setup, until the detector axes, i.e horizontal (H) and vertical (V), when the $\lambda/2$ wave plate is inserted in the beam path (see text). Blue line: exciting beams; Gray dotted line: rotation of the $\lambda/2$ wave plate; Gold dotted line: hypothesized NR in-plane orientation; Gold line: NR emitted field; Red line: detected signal after projection.

1. After the Mai-Tai laser source and the OPO, the exciting beams (pump and Stokes) represented in blue in the sketch, are horizontally polarized ($\alpha=0$) and in the general case, they are not polarized along the NR main axis (represented with the dotted gold line, at the angle β).
2. The exciting fields pass through the $\lambda/2$ wave plate which is rotated at a general angle θ (represented with the dotted gray line). If the incident beam is linearly polarized (as in our case) the resulting exciting polarization will be

rotated by twice the angle of the wave plate orientation (Ref.[133]). Thus the exciting polarization direction forms the angle $\alpha^* = \alpha + 2\theta$. In this sketch, we assumed that a anti-clockwise rotation has positive sign.

3. Neglecting the contribution given by the NR transversal mode, the NR emits a field which is linearly polarized along its main axis. In our setup we collect in reflection hence the detected field propagates in the opposite direction as compared to 1 and 2. The signal emitted by the NR is the enhanced CARS signal, which come from a third-order process (Ref.[134]), therefore we can represent its amplitude as:

$$E_{NR} \propto E_P^2 \cos^2(\phi) E_S \cos(\phi) \quad (5.3.1)$$

where ϕ represents the angle between the polarization of the exciting beams and the rod orientation, thus $\phi = \alpha^* - \beta = \alpha + 2\theta - \beta = 2\theta - \beta$.

4. The enhanced field pass through the $\lambda/2$ wave plate, but this time in the opposite direction so that its rotation takes place as clockwise and this field has a polarization direction forming the angle $\gamma = \beta - 2\theta$.
5. Finally, the latter field arrives at the detector, prior to interfering with the reference polarized at 45° . This corresponds to detect the projection of the field on the reference, so that the two field detected components turn to be

$$\begin{aligned} E_H &\propto \cos^3(\phi) \cos(\gamma) \\ E_V &\propto \cos^3(\phi) \sin(\gamma) \end{aligned} \quad (5.3.2)$$

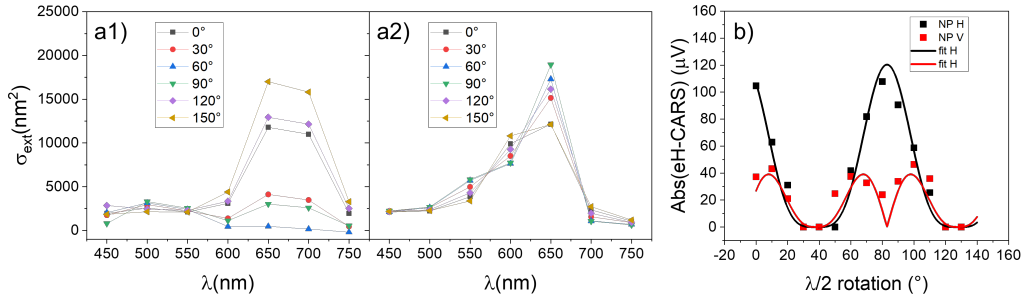


Figure 5.9: a) Single particle extinction cross-section of a nominal $25 \text{ nm} \times 71 \text{ nm}$ -SiAuNR with 5 nm silica shell extracted from wide field extinction imaging measurements and band-pass filters with the different reported center wavelengths, for in-plane linear polarization as indicated, measured before (a1) and after (a2) the laser exposure. See Chapter3.3.1 for details about how these measurement have been carried out. b) LFE eH-CARS amplitude polarization dependence behaviour, for $\text{IFD} = 2904 \text{ cm}^{-1}$ and measured at the NR in (a), using linear exciting polarization. Black: detected H component (black square) and fit (black line); Red: detected V component (red square) and fit (red line).

The study of the NR enhanced eH-CARS amplitude as a function of the $\lambda/2$ wave plate rotation θ is reported in Fig.5.9. We measure the eH-CARS signal at the the particle PSF in both the horizontal (H) and vertical (V) detected channels. The $\lambda/2$ wave plate has been rotated from 0° to 130° in steps of 10° . Particularly, in this case the NR was a nominal $25 \text{ nm} \times 71 \text{ nm}$ -SiAuNR with 5 nm silica shell. In

Fig.5.9-a the extinction cross-section spectrum before (a1) and after (a2) the laser exposure are reported. In the extinction spectrum acquired after the laser exposure two main peaks slightly shifted in wavelengths can distinguished, meaning that the NR was developing a second main axis, possibly due to the presence of a hole in the shell allowing melted gold coming out. Despite that, the detected amplitude behaviours doesn't deviate from the one expected, as it is shown in Fig.5.9-b, where the detected H and V amplitude components are fitted with Eq.5.3.2. The latter measurements were performed as explained in Chapter 3.3.2, at $\text{IFD} = 2904 \text{ cm}^{-1}$.

5.4 NRs stability against the laser exposure

In this section, separately for each kind of SiAuNRs introduced in Chapter 3.1 and starting from eH-CARS imaging measurements with $\text{IFD} = 2904 \text{ cm}^{-1}$, we retrieved the R factor, as explained in Sec.5.2. We investigated the R-factor power dependence and its reproducibility. For the power dependence characterization, pump and Stokes powers were sequentially increased. Theoretically, the R factor is independent of the pump and Stokes powers used because both the signal generated at the glass-oil interface and the one generated at the NP should vary by the same amount. The R factor exhibits a power dependence behavior when particle reshaping or saturation effect take place. It is possible to discriminate between these two scenarios by checking the NP extinction cross-section before and after the laser exposure. In fact, as it has been shown in Sec.3.3.1, the NP extinction cross-section provides information about the NR geometrical characteristics. To test the particle R factor reproducibility, pump and Stokes powers were set to be sufficiently high to get good glass-oil interface signal S/R. Once decided the scan settings, sequential repetitions have been performed and the consequent R factors compared. Also in this case the extinction spectrum of the NR was measured before and after the laser exposure. All the results presented in this section were obtained starting from $2 \mu\text{m} \times 2 \mu\text{m} \times 2 \mu\text{m}$ xyz raster scan with $54 \times 54 \times 7$ pixels. The sample period was set to be 2 ms. The xy image at the NP focus was then selected for the R factor computation. Either the $\lambda/2$ and the $\lambda/4$ wave plate were used. Here, it is important to underline that, individual NRs exhibited a different behavior in both extinction and eH-CARS measurements even when they had the same nominal size/shape, i.e. coming from the same batch provided by the manufacturer. In each batch, we aim to select for the eH-CARS characterization, NRs displaying a longitudinal LSPR fairly close to 660 nm, the wavelength of the CARS field. In the following examples, we reported different cases that represent on average the particles resistance behavior and R factor value reproducibility of each group of tested SiAuNRs for both the exciting polarization condition introduced. In this set of examples, when the $\lambda/4$ was used in the excitation path the projections of the detected field along and across the NR were not computed, as this would affect only the final R factor value, without affecting the information about the resistance. It turned out that the stability and resistance of a NR mainly depend on the thickness of its silica shell rather than the kind of exciting polarization employed, while the R factor value reproducibility could be affected by a saturation effect. The nominal $25 \text{ nm} \times 71 \text{ nm}$ -SiAuNRs with 5 nm shell turn out to be the more subjected to particle reshape/destruction even for low applied laser powers. Instead, both the nominal $40 \text{ nm} \times 68 \text{ nm}$ -SiAuNR and the nominal $50 \text{ nm} \times 100 \text{ nm}$ -SiAuNR result way more stable with occasionally a slightly blue-shifted LSPR after the laser exposure.

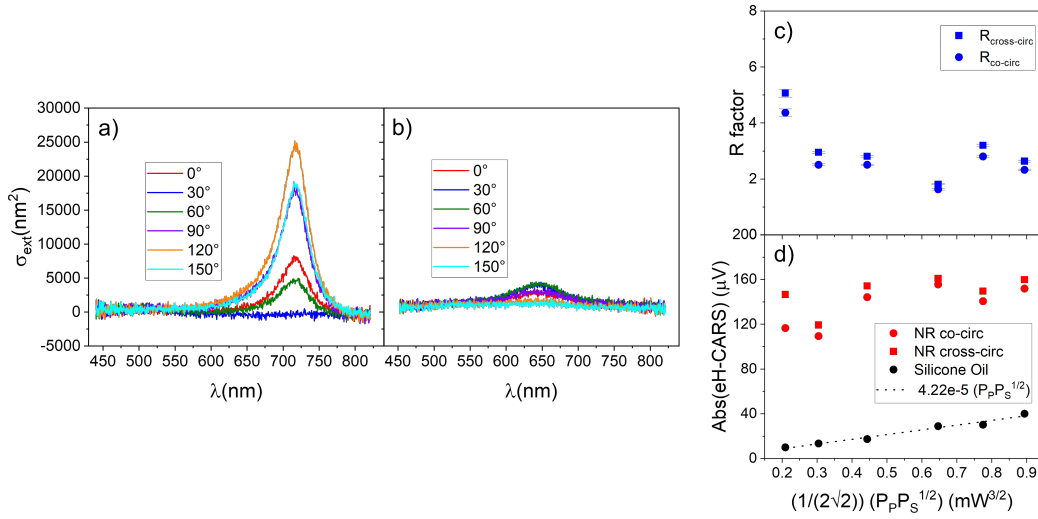


Figure 5.10: (a-b) Single particle extinction spectrum, of nominal $25 \text{ nm} \times 71 \text{ nm}$ -SiAuNR with 5 nm silica shell, for different in-plane linear polarization angles of the white-light illumination, as indicated, measured before (a) and after (b) the laser exposure. Measurements were performed as explained in Chapter 3.3.1. (c-d) LFE eH-CARS power dependence measurement, at $\text{IFD} = 2904 \text{ cm}^{-1}$, performed at the NR in (a-b), using circular exciting polarization. (c) R_{co} (circle) and R_{cross} (square) factors computed from (d) as explained in Sec.5.2. The error bars come from the uncertainty of the exact amplitude of the Gaussian function used to fit the data to retrieve the R factor value. (d) eH-CARS amplitude measured at glass-oil interface away from NR (black circle) and signal measured at the NR in the co- (red circle) and cross- (red square) circular polarized detection channels. The dashed black line represents the linear interpolation performed on the interface signal to check its value for low power.

25 nm \times 71 nm-SiAuNR, 5 nm shell

We first started to characterize the nominal $25 \text{ nm} \times 71 \text{ nm}$ NR with 5 nm silica shell. The results reported in Fig.5.10(c-d) refer to a power dependence characterization performed on the NR whose extinction cross-section spectra are shown in Fig.5.10(a-b). The latter were acquired before (Fig.5.10(a)) and after (Fig.5.10(b)) the laser exposure. For the nominal $25 \text{ nm} \times 71 \text{ nm}$ NR the extinction cross-section was measured via extinction spectroscopy, as explained in Sec.3.3.1. In this first set of measurements, an exciting circular polarization was used. Fig.5.10(d) shows the amplitudes measured (and lock-in offset corrected) at the NR (red), for both co-(circle) and cross-(square) circular detected polarization, and the amplitude measured at the glass-oil interface (black). The latter linearly depends on $P_p \sqrt{P_s}$, so that we could verify, via a linear interpolation, that the detected signal had a reasonable value, following the theoretical predicted dependence, also when it was close to the noise level, i.e. for low pump and Stokes powers. Notice that, the proportionality constant between the eH-CARS amplitude and $P_p \sqrt{P_s}$ strictly depends on the alignment of the setup and on the power used for the reference beam exploited in the detection. This leads to generally different proportionality constant for different days of measurements. The eH-CARS amplitudes values (Fig.5.10(d)) suggest that the NR provides an enhancement to the glass-oil interface signal for all the powers employed, but looking at the R factor (Fig.5.10(c)) power dependence behavior we

can clearly see that this enhancement was not constant. This particle, provided the highest enhancement during the first scan at the lowest powers. The R factor drop recorded during the second scan suggests a particle reshaping toward a more stable shape, as the R factor does not undergo other marked variation in the following scan at higher power. The comparison between the extinction spectra, before and after the laser exposure, confirms the hypothesis of the particle reshaping toward a more spherical particle. In fact it is clear that there is a blue shift of the longitudinal LSPR, which suggests a decreased aspect ratio (Ref [135]). The nanoparticle did not completely lose its rod-like shape as we can still notice a polarization dependent extinction behaviour, which also suggests a variation of the in-plane particle orientation during the laser exposure. This explains the variation in the relative $R_{\text{co-circ}}$ and $R_{\text{cross-circ}}$ between the first and the following repetitions: the orientation of the NR changed so that the enhanced CARS field after the $\lambda/4$ wave plate was more circular polarized then elliptically polarized, giving the detection of amplitudes, in the two channels, with nearly the same values.

Figure 5.11 shows a power dependence measurement, performed on another particle, this time exploiting a linear polarized excitation aligned along the main axis of the NR. As already stated in Sec. 5.1, the usage of the $\lambda/2$ wave plate ensures a higher R factor (see Fig. 5.11(c)). Also in this case, upon increasing the applied powers, the particle underwent reshaping. The comparison between extinction cross-section measurements before (a) and after (b) the laser exposure is crucial to understand which kind of reshape the NR underwent. The extinction cross-section measurements revealed again a reshaping toward a more spherical-like particle (decreased aspect ratio). The stability characterization of this kind of NRs are reported in Fig. 5.12 and Fig. 5.13, for the case of the circular and linear polarization excitation respectively. Comparing the two extinction cross-section spectra (Fig. 5.12(a) vs Fig. 5.13(a)) acquired before the laser exposure, it is clear how much nominally equal particles can differ in terms of their geometrical characteristics. The particle associated to the spectrum in Fig. 5.12(a) is clearly larger in size (higher extinction values at the longitudinal LSPR) than the second one (Fig. 5.13 (a)). The eH-CARS measurements were performed selecting similar pump and Stokes powers: $P_P=2.3$ mW and $P_S=7.9$ mW for the first case (Fig. 5.12(c)) and $P_P=1.2$ mW and $P_S=4.3$ mW for the second case (Fig. 5.13(c)). The actual strength of combined pump and Stokes powers (computed as $P_P\sqrt{P_S}$) on the sample resulted in 0.57 mW^{3/2} and 0.88 mW^{3/2}. The powers were chosen to have the glass-oil interface signal above the noise level. The particle related to Fig. 5.12 shows a good stability at the low powers applied as its R factor didn't undergo marked variation. It is interesting to see how the laser exposure affected the particle orientation, as the difference between the $R_{\text{co-circ}}$ and $R_{\text{cross-circ}}$ values increased during the second, third and fourth repetition, to then return nearly the same of the initial one in the last repetition. Instead, the particle related to Fig. 5.13 didn't have a good stability/resistance, as the R factor was decreasing already during the second repetition (Fig. 5.13(c)). The decrease is again explained by looking at the extinction variation, with a more blue-shifted LSPR after the laser exposure (Fig. 5.13(a-b)), meaning a decreased aspect ratio.

40 nm×68 nm-SiAuNRs, 10 nm shell

While measuring the NRs characterized by 10 nm silica shell, we immediately realized how their resistance against the reshaping was improved. For this reason, we decided to change the modality to characterize them. We combined the power

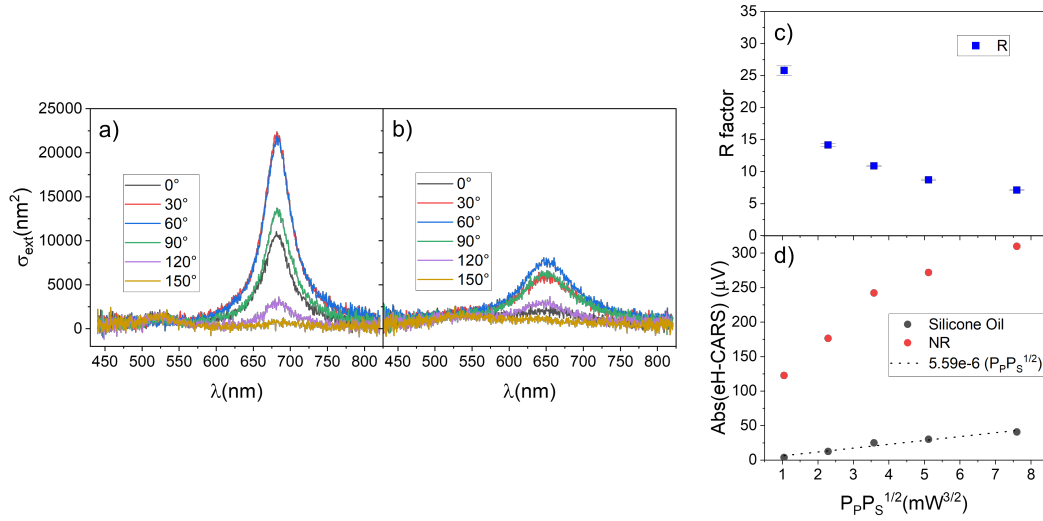


Figure 5.11: (a-b) Single particle extinction spectrum, of nominal $25 \text{ nm} \times 71 \text{ nm}$ -SiAuNR with 5 nm silica shell, for different in-plane linear polarization angles of the white-light illumination, as indicated, measured before (a) and after (b) the laser exposure. Measurements were performed as explained in Chapter 3.3.1. (c-d) LFE eH-CARS power dependence measurement, at $\text{IFD} = 2904 \text{ cm}^{-1}$, performed at the NR in (a-b), using linear exciting polarization. (c) R_{co} (circle) and R_{cross} (square) factors computed from (d) as explained in Sec.5.2. The error bars come from the uncertainty of the exact amplitude of the Gaussian function used to fit the data to retrieve the R factor value. (d) eH-CARS amplitude measured at glass-oil interface away from NR (black circle) and signal measured at the NR in the co- (red circle) and cross- (red square) circular polarized detection channels. The dashed black line represents the linear interpolation performed on the interface signal to check its value for low power.

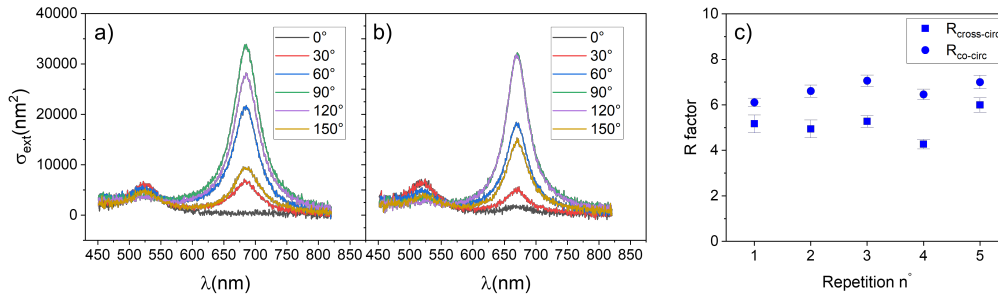


Figure 5.12: (a-b) Single particle extinction spectrum, of nominal $25 \text{ nm} \times 71 \text{ nm}$ -SiAuNRs with 5 nm silica shell, for different in-plane linear polarization angles of the white-light illumination, as indicated, measured before (a) and after (b) the laser exposure. Measurements were performed as explained in Chapter 3.3.1. c) LFE eH-CARS stability measured, at $\text{IFD} = 2904 \text{ cm}^{-1}$, performed at the NR in (a-b), using circular exciting polarization and $P_P=2.3 \text{ mW}$ and $P_S=7.9 \text{ mW}$. The same measurement was repeated five times and for each of them, the R_{co} (circle) and R_{cross} (square) factors have been computed as explained in Sec.5.2. The error bars come from the uncertainty of the exact amplitude of the Gaussian function used to fit the data and to retrieve the R factors value.

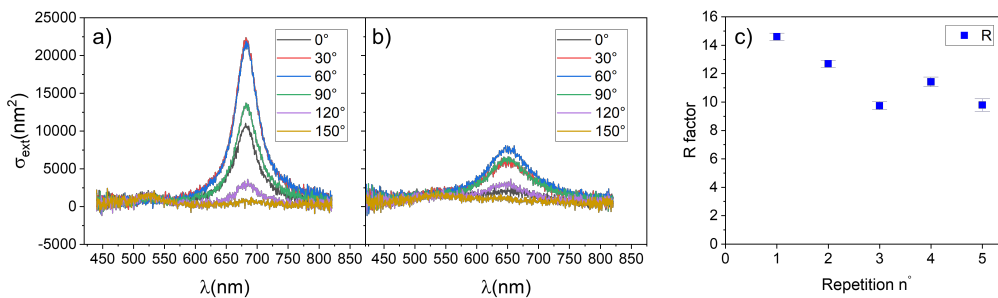


Figure 5.13: (a-b) Single particle extinction spectrum, of nominal $25 \text{ nm} \times 71 \text{ nm}$ -SiAuNRs with 5 nm silica shell, for different in-plane linear polarization angles of the white-light illumination, as indicated, measured before (a) and after (b) the laser exposure. Measurements were performed as explained in Chapter 3.3.1. c) LFE eH-CARS stability measured, at $\text{IFD} = 2904 \text{ cm}^{-1}$, performed at the NR in (a), using linear exciting polarization and $P_P=1.2 \text{ mW}$ and $P_S=4.3 \text{ mW}$. The same measurement was repeated five times and for each of them the R factor has been computed as explained in Sec.5.2. The error bars come from the uncertainty of the exact amplitude of the Gaussian function used to fit the data to retrieved the R factor value.

dependence with reproducibility measurements on the same single particle. The measurements were organized so that for a given pump and Stokes powers combination few repetition of the same scan (three in the presented cases) were performed. The laser powers were then increased until the enhanced signal was starting to not follow the increase of the correspondent glass-oil interface signal. Both the $\lambda/4$ and $\lambda/2$ wave plate have been tested in the excitation. Let us discuss now the nominal $40\text{ nm}\times 68\text{ nm}$ -SiAuNRs.

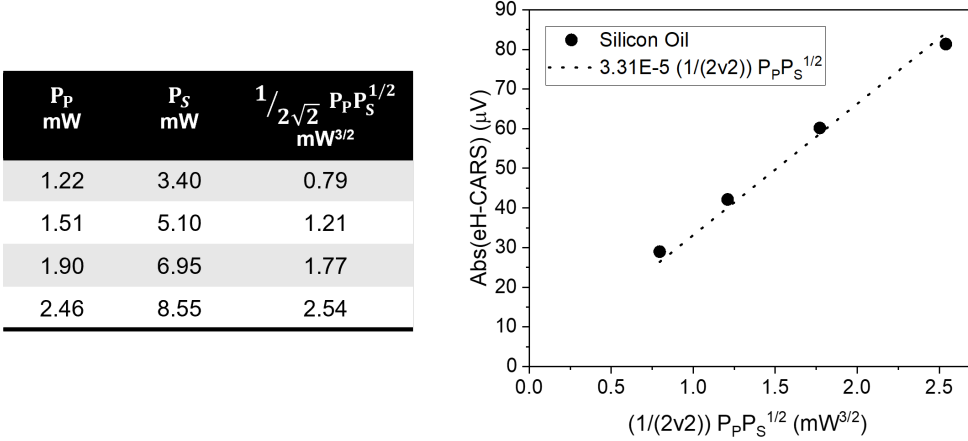


Figure 5.14: Left: pump and Stokes powers with the resulting overall powers exciting at the sample used in the power dependence measurement reported in Fig.5.15. Right: eH-CARS amplitude measured at glass-oil interface away from NR for the indicated power and its linear interpolation (dashed black).

Figure 5.14 and Figure 5.16 show on the left a table giving the pump, Stokes and the correspondent overall power exciting the sample used in the power dependence measurements. On the right it is shown the glass-oil interface eH-CARS signal obtained for each applied powers combination and the consequent linear interpolation. The latter were reported as it is important to check that the signal obtained at lower powers, used for the normalization in the R factor computation, was well defined against noise. Fig.5.14 refers to the measurement where the $\lambda/4$ wave plate was employed while Fig.5.16 to the $\lambda/2$ wave plate. In Figure 5.15 and Figure 5.17 are reported the corresponding characterization results. Fig.5.15(c-d) and Fig.5.17(c-d) are organized so that they show in (d) the eH-CARS amplitude detected at the NR PSF (blue data) and away from it (black data), while in (c) the computed R factor. As three repetitions with the same applied power have been performed, the overall power employed in each measurement is reported in the right scale for clarity (green data). Figure 5.15(a-b) and 5.17(a-b) show the extinction cross section for the particle under study measured before (a) and after (b) all the laser exposures. The particle related to Fig.5.15, excited via circularly polarized beams, showed an overall good stability during the measurements performed with the first three powers combination, as the enhanced signal increases for higher powers (Fig.5.15(d)). The more accurate R factor (Fig.5.15(c)) reveals actually a slight decrease of the provided enhancement, which can be explained by the σ_{ext} measured after the laser exposure (Fig.5.15(b)). Due to the laser exposure, the LSPR turns out to be blue shifted, resulting in a lower value of σ_{ext} at 660 nm, with a consequent weaker coupling between the exciting plasmon and both pump, Stokes and CARS fields. The

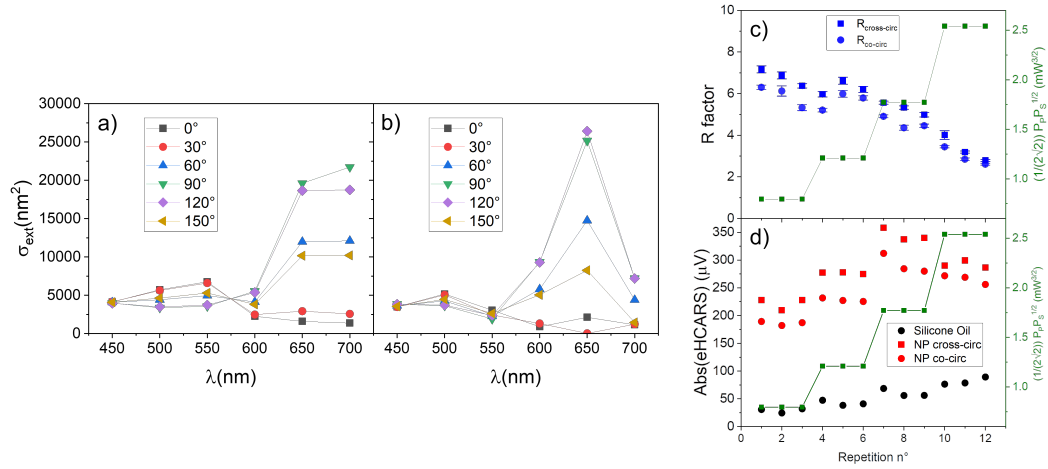


Figure 5.15: (a-b) Single particle extinction cross-section of nominal $40 \text{ nm} \times 68 \text{ nm}$ -SiAuNR with 10 nm silica shell extracted from wide field extinction imaging measurements and band-pass filters with the different reported center wavelengths, for in-plane linear polarization as indicated, measured before (a) and after (b) the laser exposure. See Chapter 3.3.1 for more details about how these measurements have been carried out. (c-d) LFE eH-CARS power dependence and reproducibility measurements, measured with $\text{IFD} = 2904 \text{ cm}^{-1}$, performed focusing at the NR in (a-b), using circular exciting polarization. (c) $R_{\text{co-circ}}$ (circle) and $R_{\text{cross-circ}}$ (square) factors, computed from (d) as explained in Sec.5.2. The error bars come from the uncertainty of the exact amplitude of the Gaussian function used to fit the data and to retrieve the R factor value. (d) eH-CARS amplitude measured at glass-oil interface away from NR (black circle) and signal measured at the NR PSF in the co- (red circle) and cross- (red square) circular polarized detection channels. The overall power employed in each repetition is reported in the right scale for clarity (green data).

decreased R factor recorded during the last experiments at higher powers can not be explained by the mentioned LSPR blue shift. This was proved by performing a last measurement (not shown here) with the lowest employed powers and computing the R factors that turned to be $R_{\text{co-circ}} = 4.8 \pm 0.2$ and $R_{\text{cross-circ}} = 5.2 \pm 0.1$, thus very close to the ones obtained for the third powers combination. Being able to revert the R factor back to its initial value, by simply decreasing the applied powers, suggests that a saturation effect took place at high powers.

The next example of power dependence-stability test (Fig.5.17), performed using the $\lambda/2$ wave plate, is notable for two reasons:

- First, this example demonstrates how the R factor gives a more reliable knowledge about the actual enhancements provided by the NR compared to the one obtained just looking at the amplitude of the signals. In fact, by looking at NR emitted signal in the second and third repetitions of the first two applied overall powers (Fig.5.17(b)-bottom), one could think that something is happening to the NR, but eventually the lower signal at the rod reflects a lower signal at the glass-oil interface, which could be also related to the deviation from the

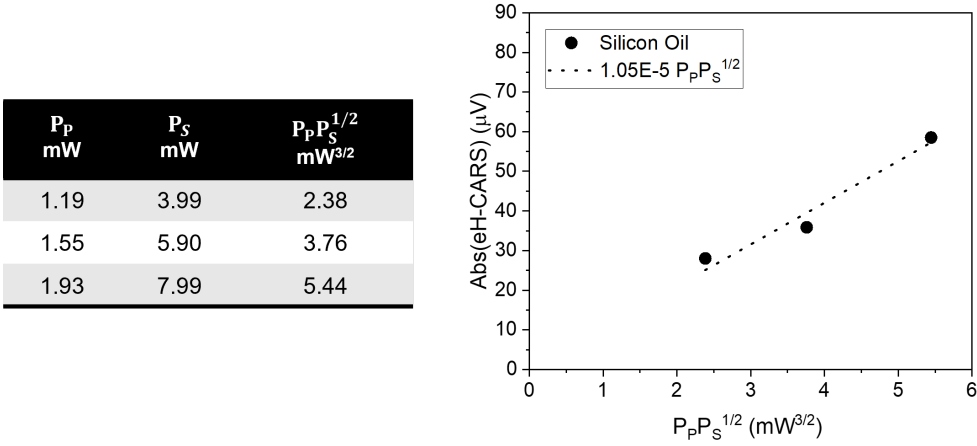


Figure 5.16: Left: pump and Stokes powers with the resulting overall powers exciting at the sample used for the power dependence measurement reported in Fig.5.17. Right: eH-CARS amplitude measured at glass-oil interface away from NR for the indicated power and its linear interpolation (dashed black).

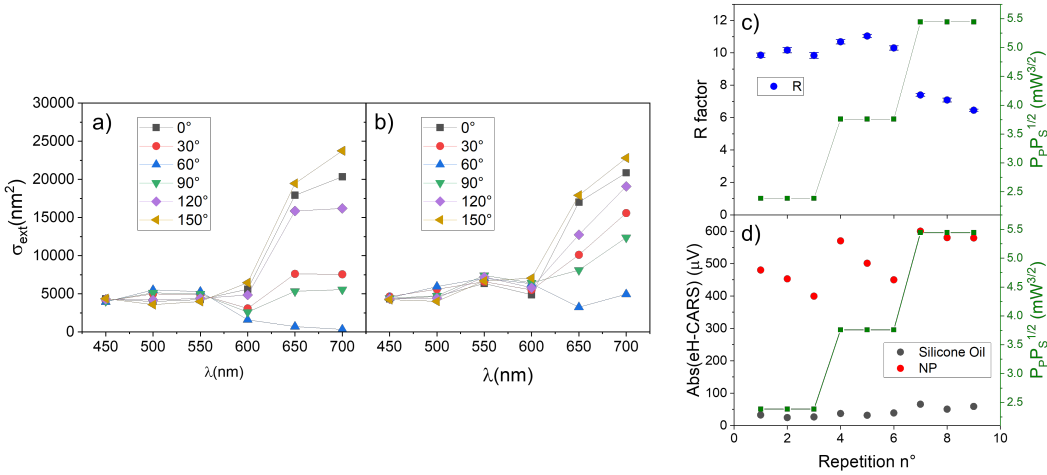


Figure 5.17: (a-b) Single particle extinction cross-section of nominal 40 nm×68 nm-SiAuNR with 10 nm silica shell extracted from wide field extinction imaging measurements and band-pass filters with the different reported center wavelengths, for in-plane linear polarization as indicated, measured before (a) and after (b) the laser exposure. See Chapter 3.3.1 for more details about how these measurements have been carried out. (c-d) LFE eH-CARS power dependence and reproducibility measurements, measured with $IFD = 2904\text{ cm}^{-1}$, performed focusing at the NR in (a-b), using linear exciting polarization. (c) R factor, computed from (d) as explained in Sec.5.2. The error bars come from the uncertainty of the exact amplitude of the Gaussian function used to fit the data and to retrieve the R factor value. (d) eH-CARS amplitude measured at glass-oil interface away from NR (black circle) and signal measured at the NR PSF in the co- (red circle) and cross- (red square) circular polarized detection channels. The overall power employed in each repetition is reported in the right scale for clarity (green data).

intended focal point of the image due to mechanical drifts. Indeed once found the NP, we were used to acquire the images at a given power sequentially to not overexpose the particle.

- Secondly, the data of the extinction cross section spectrum after the laser exposure (Fig.(Fig.5.17(a)-right) and the R factor (Fig.5.17(b)-top) obtained during the last measurements clearly confirm that a reduction of the R factor for high power can not be always explained with a particle reshaping. Comparing the initial and the final R factor, it is evident a considerable reduction, but the extinction cross section do not show an equal marked change.

The reduction of the R factor at higher powers could be explained by the saturation of CARS phenomenon itself taking place at the NR. A more detailed investigation of this aspect is given in Sec.5.4.1.

50 nm×100 nm-SiAuNRs, 10 nm shell

As also the nominal 50 nm×100 nm-SiAuNRs are coated with a 10 nm silica shell, the same approach followed to test the stability and reproducibility of the measured R factor of nominal 40 nm×68 nm-SiAuNRs, was used, namely we performed combined power dependence and stability characterizations. Similar consideration can be drawn. Fig.5.19 shows the results obtained using the $\lambda/4$ waveplate, at the laser powers indicated in Fig.5.18, for a selected NR which exhibited a stable extinction spectrum. Again the reduced R factor obtained in the last set of measurements at the highest power (Fig.5.19(b)-top), was not explained by the comparison of the extinction cross-section measured before and after the laser exposure (Fig.5.19(a), left vs right), which does not reveal any substantial particle shape changing. The particle studied the last test (Fig.5.21), using the $\lambda/2$ wave plate (laser powers applied and consequent generated glass-oil interface eH-CARS signals reported in Fig.5.20), behaved in a different way since, as can be seen by the R factor power dependence (Fig.5.21), its R factor remained nearly constant during all the measurements. In agreement with this, also the extinction cross-section spectra does not suggest a shape variation. Notice that, the powers applied to this last NR is higher than the one applied to the previous particle. This example further highlights how peculiar is the behaviour of each particle, which depends on its geometrical characteristics.

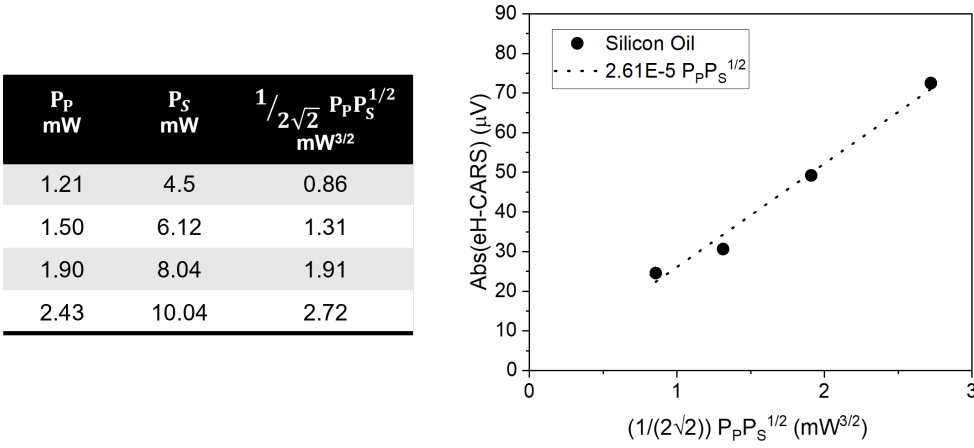


Figure 5.18: Left: pump and Stokes powers with the resulting overall powers exciting at the sample used for the power dependence measurement reported in Fig.5.19. Right: eH-CARS amplitude measured at glass-oil interface away from NR for the indicated power and its linear interpolation (dashed line).

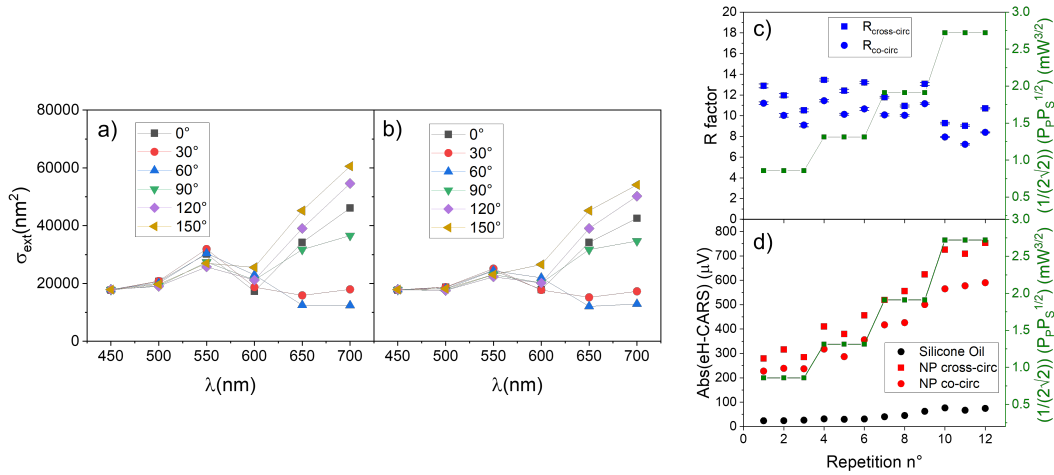


Figure 5.19: (a-b) Single particle extinction cross-section of nominal 50 nm \times 100 nm-SiAuNR with 10 nm silica shell extracted from wide field extinction imaging measurements and band-pass filters with the different reported center wavelengths, for in-plane linear polarization as indicated, measured before (a) and after (b) the laser exposure. (c-d) LFE eH-CARS power dependence and reproducibility measurements, measured with IFD = 2904 cm⁻¹, performed focusing at the NR in (a-b), using circular exciting polarization. (c) $R_{\text{co-circ}}$ (circle) and $R_{\text{cross-circ}}$ (square) factors, computed from (d) as explained in Sec.5.2. The error bars come from the uncertainty of the exact amplitude of the Gaussian function used to fit the data and to retrieve the R factor value. (d) eH-CARS amplitude measured at glass-oil interface away from NR (black circle) and signal measured at the NR PSF in the co- (red circle) and cross- (red square) circular polarized detection channels. The overall power employed in each repetition is reported in the right scale for clarity (green data).

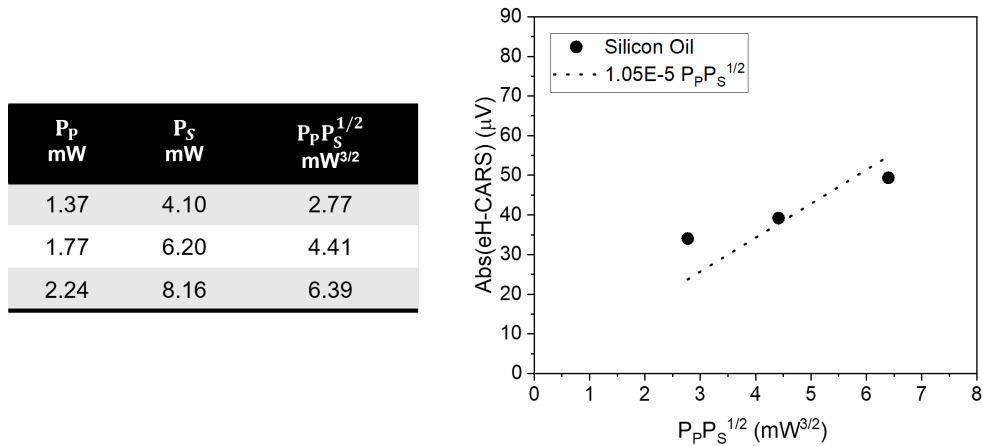


Figure 5.20: Left: pump and Stokes powers with the resulting overall powers exciting at the sample used for the power dependence measurement reported in Fig.5.21. Right: eH-CARS amplitude measured at glass-oil interface away from NR for the indicated power and its linear interpolation.

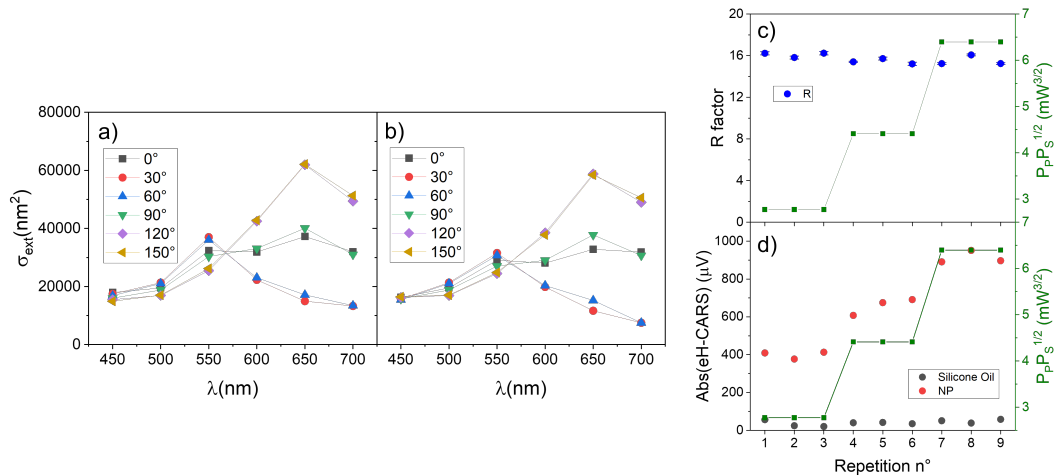


Figure 5.21: (a-b) Single particle extinction cross-section of nominal 50 nm×100 nm-SiAuNR with 10 nm silica shell extracted from wide field extinction imaging measurements and band-pass filters with the different reported center wavelengths, for in-plane linear polarization as indicated, measured before (a) and after (b) the laser exposure. (c-d) LFE eH-CARS power dependence and reproducibility measurements, measured with $IFD = 2904 \text{ cm}^{-1}$, performed focusing at the NR in (a-b), using linear exciting polarization. (c) R factor, computed from (d) as explained in Sec.5.2. The error bars come from the uncertainty of the exact amplitude of the Gaussian function used to fit the data and to retrieve the R factor value. (d) eH-CARS amplitude measured at glass-oil interface away from NR (black circle) and signal measured at the NR PSF in the co- (red circle) and cross- (red square) circular polarized detection channels. The overall power employed in each repetition is reported in the right scale for clarity (green data).

5.4.1 Saturation Effect

With increasing pump and Stokes powers, a saturation of the CARS signal may take place. This can be understood as follows. Assuming diatomic molecules treated as quantum linear harmonic oscillators, in their quantized energy levels diagram, the energy levels are equally spaced (Fig.5.22-a). In this condition, starting from molecules in the ground state undergoing a coherent Raman process, using pump and Stokes pulses such that their frequency difference matches the characteristic vibrational frequency of the molecules, no CARS saturation is expected. This is because the perturbation of the system due to the CRS process does not preclude the possibility of driving subsequently another vibrational coherence that involves higher vibrational states (Fig.5.22-a2). On the other hand, in real molecules, the potential energy governing the vibrational motion is not harmonic. In other words, real molecules are anharmonic systems with quantized energy levels not evenly spaced (Fig.5.22-b). In this condition, the interaction of the molecule with pump and Stokes is able to resonantly drive only the coherence between two well defined levels (Fig.5.22-b1). Hence the coherent driving process, via the interference between pump and Stokes, resonantly drives the coherence between ground and first vibrational state only. Further excitation into higher levels depends on the strength of the anharmonicity and the spectral width of the driving (i.e. the pulse duration used). Generally, this leads to a saturation effect as the driving becomes less effective. This brings to the CARS saturation due to the depletion of the ground state (Fig.5.22-b2), and the shift in the vibrational resonance for higher states, hence reduced effect of the coherent driving of these higher vibrational transitions. As explained in Chapter 2.1.1.1, $I_{\text{CARS}} \propto |\chi^{(3)}|^2 = |\chi_{\text{R}}^{(3)} + \chi_{\text{NR}}^{(3)}|^2$ and $\chi_{\text{R}}^{(3)} \propto \Delta N$ where ΔN represents the population difference between the vibrational and ground states (Ref.[136]). The population difference can be affected and its transient perturbation depends on pump and Stokes beams intensities, i.e.(Ref.[137],[138])

$$\frac{d(\Delta N)}{dt} \propto -I_{\text{P}}I_{\text{S}} \quad (5.4.1)$$

Therefore, for high excitation intensities, there is a decrease of the population difference, which leads to a decreased $\chi_{\text{R}}^{(3)}$ and thus I_{CARS} , producing the saturation effect.

Ref.[139] states that for C-H stretching of biomolecules the peak intensity threshold (computed as $\sqrt{I_{\text{P}}I_{\text{S}}}$) for saturation is about $1 \times 10^{12} \text{W/cm}^2$ or $1.5 \times 10^{13} \text{W/cm}^2$ for 2-ps or 100-fs lasers, respectively. For given pump and Stokes average powers employed in the experiment, the peak intensity in the laser focus is given by

$$I_{\text{peak}} = \frac{P}{R_{\text{pulse}}T_{\text{pulse}}} \frac{1}{A_{\text{spot}}} \quad (5.4.2)$$

where $A_{\text{spot}} = \pi(\frac{\lambda}{2NA})^2$. As mentioned in Chapter 3.3.2, with our setup we have repetition rate $R_{\text{pulse}}=80 \text{ MHz}$, pulse duration $T_{\text{pulse}}=1 \text{ ps}$ and $NA=1.45$. For example, considering the set of measurements shown in Fig.5.15 and the maximum pump and Stokes average powers employed ($P_{\text{P}}=2.46 \text{ mW}$ and $P_{\text{S}}=8.55 \text{ mW}$), the resulting peak intensities are $1.22 \times 10^{10} \text{W/cm}^2$ for the pump and $2.47 \times 10^{10} \text{W/cm}^2$ for the Stokes, which give $\sqrt{I_{\text{P}}I_{\text{S}}} \sim 1.73 \times 10^{10} \text{W/cm}^2$, below from the saturation threshold. This consideration is consistent with the power dependence measured at the glass-oil interface away from the NR and shown for example in Fig.5.16, which scales without showing saturation. At the NR, since pump and Stokes beams are enhanced the

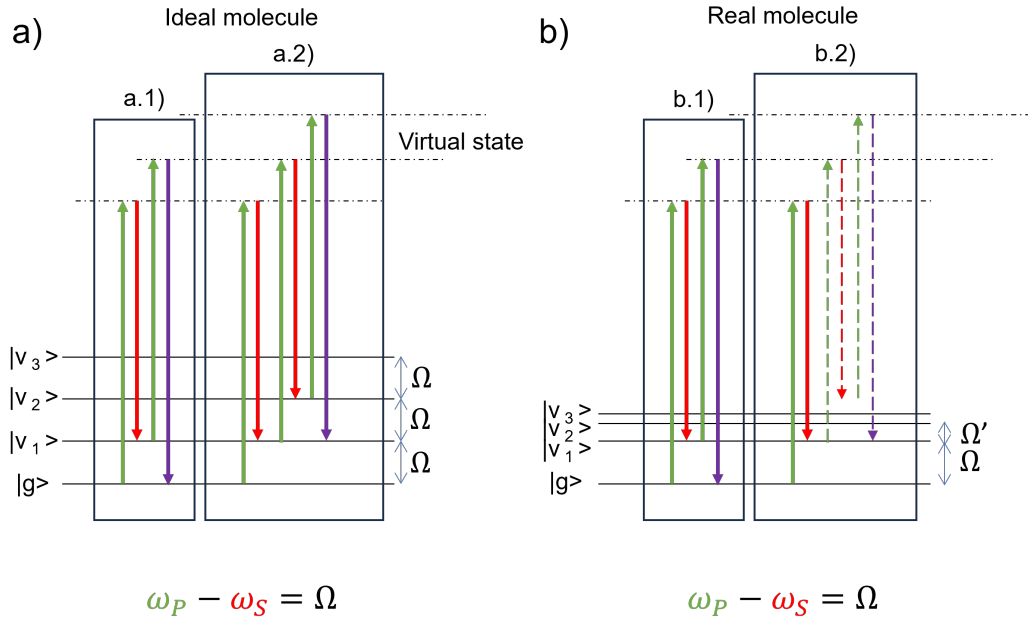


Figure 5.22: Energy diagram showing the resonant contribution to the CARS signal by the target molecule for (a) ideal single diatomic molecule and (b) real molecule with quantized energy levels not evenly spaced. (a.1) and (b.1) show how pump (green) and Stokes (red) are able to resonantly drive the coherence between two well defined levels. (a.2) and (b.2) show how pump and Stokes would be able to drive subsequently another vibrational coherence which involves higher vibrational states only in the case of the ideal molecule. Solid lines indicate the ground (g) and vibrational state (v_1, v_2, v_3) levels, while the virtual states are represented by dashed lines.

peak intensity of these beams will be higher. To estimate the experimental pump and Stokes peak intensities at the NR tip, we exploited the COMSOL model introduced in Charter 3.4.2. We simulated the pump and Stokes enhancement, as we did in Fig.3.27, for a NR with $D=40$ nm, $AR=1.7$, $R_{\text{tip}}=D/3$, $t_{\text{shell}}=10$ nm and $g=0.75$ (used to compute the modified ϵ_{Au}). 1 mW has been used in the simulation as input average powers for both pump and Stokes. Then, we evaluated the pump and Stokes fields at the NR tip in oil obtaining $E_P^{\text{sim}}=7.64 \times 10^8$ V/m and $E_S^{\text{sim}}=4.44 \times 10^8$ V/m. Since the amplitude of an electric field is proportional to the square root of its peak power, we can write

$$\begin{cases} E^{\text{sim}} &= C \sqrt{\frac{P_{\text{avg}}^{\text{sim}}}{R_{\text{pulse}} T_{\text{pulse}}}} \\ E^{\text{exp}} &= C \sqrt{\frac{P_{\text{avg}}^{\text{exp}}}{R_{\text{pulse}} T_{\text{pulse}}}} \end{cases} \quad (5.4.3)$$

Thus, the proportionality constant C can be retrieved from the simulation and the intensity peak had in the experiment can be computed with $I = cn\epsilon_0|E|^2$. Following this procedure we obtain $E_P^{\text{exp}}=1.19 \times 10^{11}$ V/m and $E_S^{\text{exp}}=1.29 \times 10^{11}$ V/m and consequently $I_P^{\text{exp}}=2.88 \times 10^{11}$ W/cm² and $I_S^{\text{exp}}=3.40 \times 10^{11}$ W/cm². Thus the overall peak intensity inducing the CARS process at the NR tip is $\sqrt{I_P I_S} \sim 3.13 \times 10^{11}$ W/cm², closer to the threshold stated in the literature.

This saturation behaviour can explain the measured decrease of R with high power, while the NR was NOT reshaped, as shown e.g in Fig.5.17 and Fig.5.19.

5.5 LFE eH-CARS time traces

The stability of the three groups of SiAuNRs was tested also measuring LFE eH-CARS time traces. Essentially, we employ a real sensing measurement condition wherein laser beams are directed at the SiAuNRs for a specified duration, without performing a 2D scan. This experimental condition is the one that will allow us to detect transient object in proximity of a nanostructure. Our attention stays on observing the alterations in the LFE eHCARS signal by a single SiAuNR, which should remain constant if the nanorod does not undergo shape changing, as the particle is in a homogeneous environment, being surrounded by silicone oil. While plotting the results of the acquired LFE eH-CARS amplitude, it is crucial to take into account that this signal is also affected by the fluctuation in the Stokes and reference beams. In this contest we neglect the fluctuation affecting the pump beam as it is directly provided by the laser source Ti:Sa (MaiTai), which is typically quite stable, while the Stokes and the reference beams are obtained from the optical parametric process taking place in the OPO (see Chapter 3.3.2). The intensity (I_{sig}) of a signal detected via the heterodyne technique is proportional to both the signal field itself (E_{sig}) and to the reference field (E_{ref}) (Ref.[140]):

$$I_{\text{sig}} \propto 2E_{\text{sig}}E_{\text{ref}}. \quad (5.5.1)$$

The intensity is then proportional to both the power ($I \propto P$) and to the square of the field amplitude ($I \propto A^2$), so that $A \propto \sqrt{P}$. In our case $E_{\text{sig}} = E_{\text{eH-CARS}} \propto E_{\text{P}}^2 E_{\text{S}}$, thus:

$$I_{\text{sig}} = I_{\text{eH-CARS}} \propto E_{\text{P}}^2 E_{\text{S}} E_{\text{ref}} \quad (5.5.2)$$

where the index P and S indicate again pump and Stokes, respectively. Exploiting then the relation between the amplitude and the power of a field, we can write:

$$A_{\text{eH-CARS}} \propto \sqrt{P_{\text{P}}}^2 \sqrt{P_{\text{S}}} \sqrt{P_{\text{ref}}}. \quad (5.5.3)$$

In our detection scheme we also employ a balanced photodiode technique (Ref.[141]), acquiring two couples of balanced photocurrents, nominally i_1, i_2, i_3, i_4 , where two of them will be positive and the other two negative. The powers of both Stokes and reference are proportional to the sum of the absolute values of such currents ($P \propto i = |i_1| + |i_2| + |i_3| + |i_4|$), so that:

$$A_{\text{eH-CARS}} \propto \sqrt{i} \sqrt{i} = i. \quad (5.5.4)$$

where we neglected the factor $\sqrt{P_{\text{P}}}^2$, assuming it to be constant. The time trace eH-CARS amplitude displayed in the following (Abs(eH-CARS)), compensated for the Stokes and reference fluctuations is therefore given by:

$$\text{Abs}(\text{eH-CARS}) = A_{\text{eH-CARS}} \frac{\langle i \rangle}{i} \quad (5.5.5)$$

where $\langle i \rangle$ is the average value of i during the considered time trace. Instead of directly dividing for the current we divide for the normalized current, so that the unit of Abs(eH-CARS) remains voltage. Also for these stability tests, both the $\lambda/4$ and the $\lambda/2$ wave plates have been, separately, employed. The status of the particle was always checked before and after each time traces measuring the extinction spectrum via the wide field technique, as explained in Chapter 3.3.1. If

during the experiment performed with the $\lambda/4$ wave plate inserted, the particle did show any marked reshaping, we subsequently conducted the experiment using the $\lambda/2$ wave plate on the same particle. The figures presented in the following two sections are organized so that they show in the first row the particle extinction spectrum acquired before and after the laser exposure, while in the second row the LFE-eH-CARS time traces. We acquired 50s time traces with a sample period of 2ms. The signal was resampled to a sample period of 0.2s to reduce the noise. In fact in this condition, where we are not sensing the environment of the particle but its stability, we don't expect to see very fast fluctuation. For all the following measurements pump and Stokes powers were set in order to have an overall power at the sample around $3\text{ mW}^{3/2}$ and the time trace was acquired at the particle focus.

25 nm \times 71 nm-SiAuNR, 5 nm shell

The particles belonging to the nominal 25 nm \times 71 nm-SiAuNRs group exhibited an unstable behavior for this kind of experimental condition, so that we could never test the same particle for both a circularly and linearly polarized excitation. Figure 5.23(a) shows an example of a time trace measured exploiting the $\lambda/4$ wave plate in the beam path, where the detected co- and cross- circular polarized component have a similar value. By looking at the behaviour of the eH-CARS amplitude (second row) we can observe some oscillations. Due to the slightly periodic trend, such oscillations can be attributed as coming from the laser source. The overall LFE eH-CARS signal is quite low compared to e.g. the results in Fig.5.10 and Fig.5.11. This could be explained by looking at the variation of the extracted extinction spectrum (first row) before (left) and after (right) the laser exposure. Initially, the longitudinal extinction peak was at 700 nm, while after the laser exposure we found it slightly red-shifted. Moreover, an additional peak centered at around 600 nm develops and, as a consequence, we have a minimum of the extinction near 660 nm. A possible explanation could be that the thin silica shell is not uniformly covering the NR, and there is a gap such that, in the first few seconds of the laser exposure, melt gold moves out from the shell, forming another particle axis (close to a cross shape). Also, the particle measured employing the $\lambda/2$ wave plate confirms a low stability (Fig.5.23(b)). Before the LFE eH-CARS measurements, the peak of the extinction was very close to 660 nm (Fig.5.23(b)-top left), but again during the laser exposure the particle underwent reshaping. The longitudinal peak becomes blue-shifted explaining the decrease in time of the recorded eH-CARS signal. In the time interval from ~ 25 s to ~ 35 s, the recorded signal improved. As the laser exposure in addition to reshaping can cause a change in NR orientation, a possible explanation is that within that interval of time the particle orientation came back to be optimized with the $\lambda/2$ wave plate rotation.

40 nm \times 68 nm-SiAuNRs and 50 nm \times 100 nm-SiAuNRs, 10 nm shell

The results related to particles belonging to the nominal 40 nm \times 68 nm-SiAuNRs and 50 nm \times 100 nm-SiAuNRs groups are shown together in this section as similar considerations could be drawn. For both of them, it was possible to perform, on the same particle, sequentially the LFE eH-CARS time traces with the $\lambda/4$ and with the $\lambda/2$ wave plates, thanks to their stability. Figure 5.24, related to a nominal 40 nm \times 68 nm-SiAuNR, and Figure 5.25, related to a nominal 50 nm \times 100 nm-SiAuNR, are organized such that they display (a) the extinction cross-section before

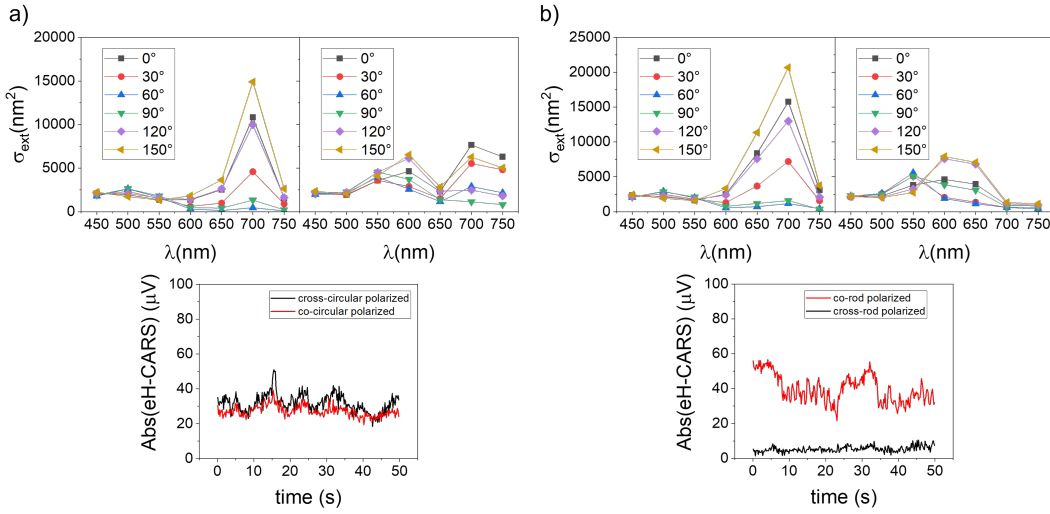


Figure 5.23: LFE eH-CARS time traces and extinction spectra measured before (left) and after (right) eH-CARS acquisition, on two different silica coated gold NRs of nominal $25\text{ nm} \times 71\text{ nm}$ size and 5 nm shell thickness. a) LFE eH-CARS performed with circular polarization excitation; b) LFE eH-CARS performed with linear polarization excitation rotated to be along the rod. All the LFE eH-CARS time traces were performed with an overall power on the sample around $3\text{ mW}^{3/2}$.

any laser exposure, (b) the one measured after the eHCARS measurements with the $\lambda/4$ (the latter shown in (d)) and (c) after the eHCARS time trace with the $\lambda/2$ (shown in (e)). The nominal $40\text{ nm} \times 68\text{ nm}$ -SiAuNR during the time trace with the $\lambda/4$ wave plate (Fig.5.24(d)) was unchanged. The extinction spectra before and after (Fig.5.24(a) and Fig.5.24(b), respectively) confirm the stability of the particle. During the second time trace, performed with the $\lambda/2$ wave plate (Fig.5.24(e)) a small decrease in eH-CARS signal was recorded in the first 10s of measurement; the signal remained then constant and with a significant value. By checking with the last extinction measurement the status of the SiAuNR, we can see a small decrease of the longitudinal peak amplitude but no resonance shift occurred. It is probable that the SiAuNR underwent slight changes, however, it can be considered still reusable.

The nominal $50\text{ nm} \times 100\text{ nm}$ -SiAuNR gave a stable signal for both LFE eH-CARS time trace with the $\lambda/2$ and the $\lambda/4$ wave plate. The latter signal, as in the case of Fig.5.23(a), is characterized by slightly periodic oscillation coming from the laser source. Nevertheless, we can see a higher value in eH-CARS amplitude compared to the other particles and good stability.

5.6 Study of third order non linear contributions to the LFE eH-CARS

In Chapter 3.4.2 we introduced the COMSOL model developed to simulate the experimental eH-CARS detected signal. In Figure 3.29 we showed the results of the COMSOL second interface, for both the overall nonlinear source current \mathbf{J}_{CARS} and for the consequent CARS near field \mathbf{E}_{CARS} . \mathbf{J}_{CARS} turns out to be very strong inside the NR gold core compared to its value in the resonant material, namely the oil and in the glass substrate and within the silica shell. In this Section we

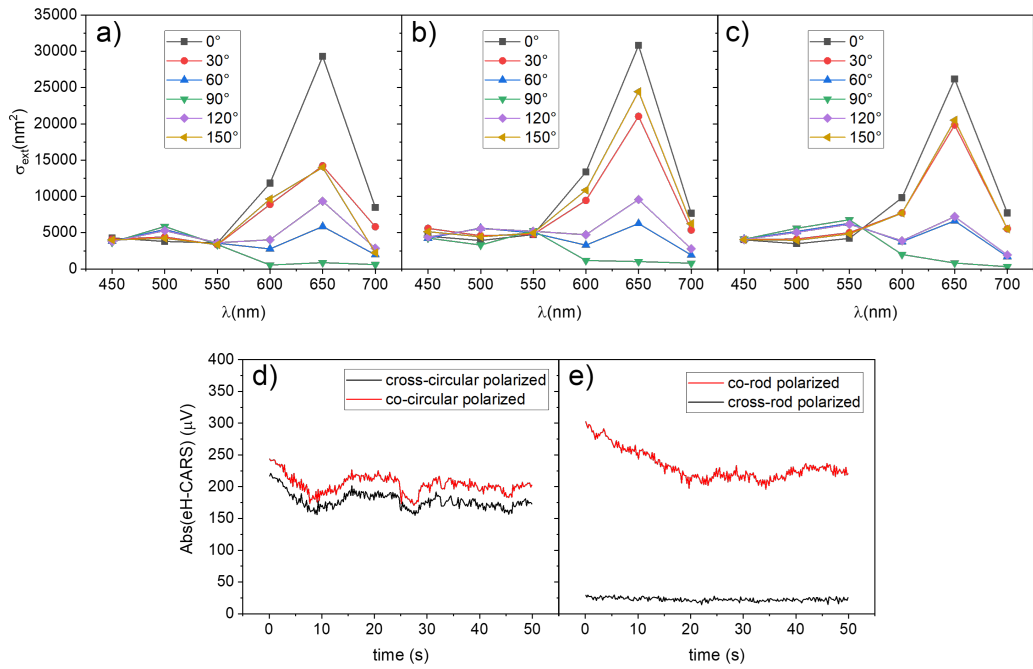


Figure 5.24: LFE eH-CARS time traces and extinction spectra measured before (left) and after (right) eH-CARS acquisition, on a silica-coated gold NR of nominal $40\text{ nm} \times 68\text{ nm}$ size and 10 nm shell thickness. a) Extracted extinction spectra measured before any LFE eH-CARS time traces; b) Extracted extinction spectra measured after the first LFE eH-CARS, performed with circular polarization excitation; c) Extracted extinction spectra measured after the first LFE eH-CARS, performed with linear polarization excitation (along the rod); d) LFE eH-CARS time trace performed with circular polarization excitation; e) LFE eH-CARS time trace performed for linear polarization excitation rotated to be along the rod. All the LFE eH-CARS time traces were performed with an overall power on the sample around $3\text{ mW}^{3/2}$.

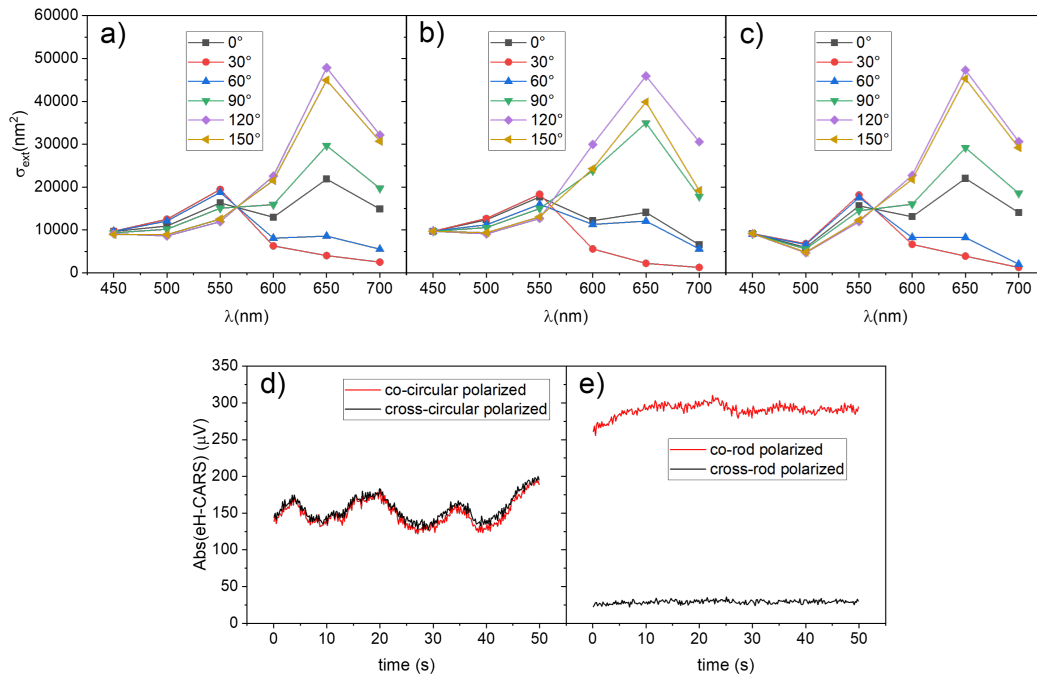


Figure 5.25: LFE eH-CARS time traces and extinction spectra measured before and after eH-CARS acquisition, on a silica-coated gold NR of nominal $50 \text{ nm} \times 100 \text{ nm}$ size and 10 nm shell thickness. a) Extracted extinction spectra measured before any LFE eH-CARS time traces; b) Extracted extinction spectra measured after the first LFE eH-CARS, performed with circular polarization excitation; c) Extracted extinction spectra measured after the first LFE eH-CARS, performed with linear polarization excitation (along the rod); d) LFE eH-CARS time trace performed for circular polarization excitation; e) LFE eH-CARS time trace performed with linear polarization excitation rotated to be along the rod. All the LFE eH-CARS time traces were performed with an overall power on the sample around $3 \text{ mW}^{3/2}$.

will investigate how the different materials in the simulation volume contribute to the overall detected signal. The experimental \mathbf{E}_{CARS} is given by the interference involving all the coherent fields generated in the near field at λ_{CARS} , either coming from a resonant process and from non resonant ones.

The strength of the source current \mathbf{J}_{CARS} in each material depends on both the third order susceptibility associated with such material and on the NP geometrical characteristics. As mentioned in Chapter 3.4.2, we have:

$$\begin{cases} \mathbf{J}_{\text{CARS}}^{\text{oil}} & \propto \mathbf{P}_{\text{CARS}} \propto \chi^{(3)}(\mathbf{E}_P \cdot \mathbf{E}_S^*) \mathbf{E}_P \\ \mathbf{J}_{\text{CARS}}^{\text{Au,shell,glass}} & \propto \mathbf{P}_{\text{CARS}} \propto \chi^{(3)}(\mathbf{E}_P \cdot \mathbf{E}_P) \mathbf{E}_S^* \end{cases} \quad (5.6.1)$$

where $\chi^{(3)}$ is the third order susceptibility related to the specific material, while \mathbf{E}_P and \mathbf{E}_S are the fields resulting from the first interface of the COMSOL model, which simulates how pump and Stokes fields are enhanced thanks to the presence of the NP.

To separately investigate the strength of each contribution, we performed parallel simulations where just one material was kept as *third order active* (i.e leaving the corresponding $\chi^{(3)}$ unchanged with respect to the value stated in Chapter 3.4.2), while all the others third order contribution were set to be off (i.e. having the corresponding $\chi^{(3)}=0$). All the material's linear properties were instead kept as stated in Chapter 3.4.2, so that the pump and Stokes field enhancements, taking place at the particle, were still taken into account. Since the contribution of the glass-oil interface, represents an offset that does not depend on the particle, initially for simplicity we considered a NP placed in a homogeneous material from the third-order non linearity point of view. To do this, for the borosilicate glass coverslip we set both the third order susceptibility $\chi_{\text{B}}^{(3)}$ and the induced CARS polarizability $\mathbf{P}_{\text{CARS,B}}$ equal to the ones had in oil, i.e.:

$$\begin{cases} \chi_{\text{B}}^{(3)} & = \chi_{\text{oil}}^{(3)} \\ \mathbf{P}_{\text{CARS,B}} & = \mathbf{P}_{\text{CARS,oil}} \end{cases} \quad (5.6.2)$$

Figure 5.26 shows the resulting source current \mathbf{J}_{CARS} (contour plot) and local CARS field \mathbf{E}_{CARS} amplitude (false colours) obtained when:

- left: $\chi_{\text{oil}}^{(3)} \neq 0$ and $\chi_{\text{Au}}^{(3)} = \chi_{\text{shell}}^{(3)} = 0$
- center: $\chi_{\text{Au}}^{(3)} \neq 0$ and $\chi_{\text{oil}}^{(3)} = \chi_{\text{shell}}^{(3)} = 0$
- right: $\chi_{\text{shell}}^{(3)} \neq 0$ and $\chi_{\text{oil}}^{(3)} = \chi_{\text{Au}}^{(3)} = 0$

selecting a NR, modeled as in Chapter 3.4, characterized by $D=25$ nm, $R_{\text{tip}}=D/(2.5)$, $t_{\text{shell}}=10$ nm and $AR=2$ (which results in a LSPR around 660 nm) and using λ_P and λ_S equal to 820 nm and 1076 nm respectively, to drive the molecular vibration at $\Omega_{\text{vib}}=2904$ cm⁻¹, with the consequent CARS emission at $\lambda_{\text{CARS}}=660$ nm. In all three cases the source current \mathbf{J}_{CARS} is different from zero only where the $\chi^{(3)}$ of the material is different from zero. The actual maximum value obtained for \mathbf{J}_{CARS} in the case of having just the gold third order contribution turns out to be one order of magnitude higher than the case of having only the oil third order contribution and about 20× higher than the case of having just the shell third order contribution. These results are qualitatively explained by the different strengths of the $\chi^{(3)}$ associated with the different materials. In fact $\chi_{\text{Au}}^{(3)} > \chi_{\text{oil}}^{(3)} > \chi_{\text{shell}}^{(3)}$. Another important

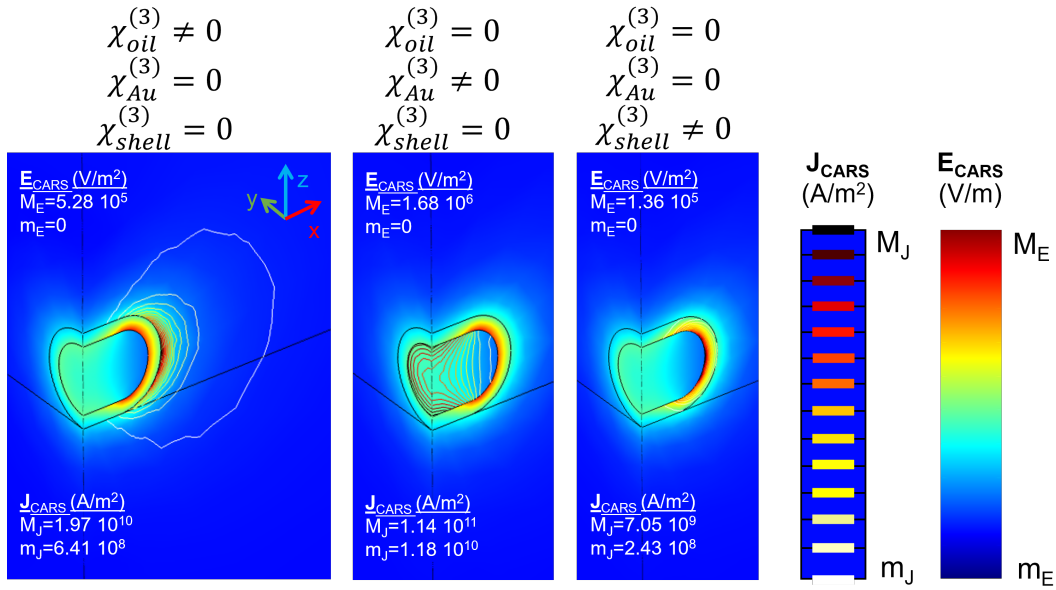


Figure 5.26: Nonlinear source current \mathbf{J}_{CARS} (contour plot) and local CARS field \mathbf{E}_{CARS} amplitude (false colours) obtained considering a SiAuNR (with $D=25$ nm, $AR=2$, $R_{\text{tip}}=D/(2.5)$, $t_{\text{shell}}=5$ nm) placed onto a glass substrate and surrounded by silicone oil, setting the NP to be in a homogeneous third order nonlinear and resonant medium ($\chi_{\text{B}}^{(3)} = \chi_{\text{oil}}^{(3)}$). Left: \mathbf{J}_{CARS} and \mathbf{E}_{CARS} obtained when only the oil has a third order nonlinear contribution. Center: \mathbf{J}_{CARS} and \mathbf{E}_{CARS} obtained when only the NP gold core has a third order nonlinear contribution. Right: \mathbf{J}_{CARS} and \mathbf{E}_{CARS} obtained when only the NP silica shell has a third order nonlinear contribution.

aspect to be taken into account is the position of the *third order active* material with respect to the region where pump and Stokes are more enhanced (see Fig.3.27). When $\chi_{\text{oil}}^{(3)} \neq 0$ (see Fig.5.26-left), \mathbf{J}_{CARS} reaches its maximum value at the NR tip within the resonant material: in this case \mathbf{J}_{CARS} can be generated only in oil and its value at the rod tip is maximum because this is the region where the pump and Stokes beams are more enhanced by the linear properties of the rod. When $\chi_{\text{Au}}^{(3)} \neq 0$, the \mathbf{J}_{CARS} maximum values are instead obtained at NR gold core more confined in the middle of the NR, where it can flow compared to the tip, and strongest near the surface, as expected due to field screening inside the metal. As for \mathbf{E}_{CARS} , in all three cases, we see that the generated local CARS field reaches its maximum value at the tip of the NR gold core, within the silica shell. This is the result of the CARS field enhancement taking place thanks to the linear properties of the NR. In fact, the CARS signal can be seen as an input field generated from the current source, and it got enhanced thanks to the linear properties of the nanorod, as in the case of pump and Stokes.

The magnitude of the enhancement provided to each beam is related to the particle involved in the process. Once the NP material and general geometrical characteristics are set, the value of the enhancement depends on the relative position between the field wavelength and the LSPR position. The latter, for a rod-like particle is mainly determined by the value of the NR aspect ratio. Additionally, the particle size is crucial because it defines the amount of each material present in the simulation volume. For this reason, while investigating the different contributions given by the different materials involved in the CARS generation process, it is also important to take into account the aspect ratio and the volume of the NR involved. Figure 5.27 shows how the extinction cross-section spectrum (left) and the characteristic LSPR position (right) vary considering a particle modeled as described in Chapter 3.4.2 with (a) $D=25$ nm, $R_{\text{tip}}=D/(2.5)$, $t_{\text{shell}}=5$ nm and (b) $D=50$ nm, $R_{\text{tip}}=D/(2.5)$, $t_{\text{shell}}=10$ nm, and changing the AR in steps of 0.2. The simulated extinction spectrum red-shifts for larger AR with the LSPR varying from 560 nm to 810 nm in the first case (Fig.5.27(a)) and from 580 nm to 820 nm in the second case (Fig.5.27(b)). The extinction peak turns out to be higher increasing the AR , due to the stronger scattering contribution for larger particle volumes involved.

In order to understand, via the COMSOL simulations, how the different materials contribute to the actual signal detected in the experiments, we need to take into account that we detect the interference between the CARS far field with the reference beam. Starting from the simulated CARS near field, we can compute the corresponding far field, using Eq.3.4.7, and then mimic the heterodyne detection via Eq.3.4.21, obtaining the simulated eH-CARS signal. Figure 5.28 shows the eH-CARS amplitude powers, computed as $\text{Abs}(\text{eH-CARS}) = \sqrt{\Re(\text{eH-CARS})^2 + \Im(\text{eH-CARS})^2}$, obtained when the only *third order active* material is the NP gold core (black, indicated with $\chi_{\text{Au}}^{(3)}$), is the oil (red, indicated with $\chi_{\text{oil}}^{(3)}$) and is the NP silica shell (blue, indicated with $\chi_{\text{shell}}^{(3)}$), and varying the LSPR position, i.e for different particle size. More precisely, in Fig.5.28 (a) the NRs giving the different LSPR positions are the same of Fig.5.27(a), while Fig.5.28 (b) has been obtained using the NRs of Fig.5.27(b). Figure 5.28 also shows how the different contributions are affected by driving the molecular oscillation at $\Omega_{\text{vib}}=2860$ cm^{-1} (left), at $\Omega_{\text{vib}}=2904$ cm^{-1} (center) and at $\Omega_{\text{vib}}=2960$ cm^{-1} (right), changing λ_S . Looking at the results for $\chi_{\text{Au}}^{(3)} \neq 0$ and $\chi_{\text{shell}}^{(3)} \neq 0$ we can see how their value is independent of the Ω_{vib} selected, as their contribution does not come from a resonant process but from a FWM one,

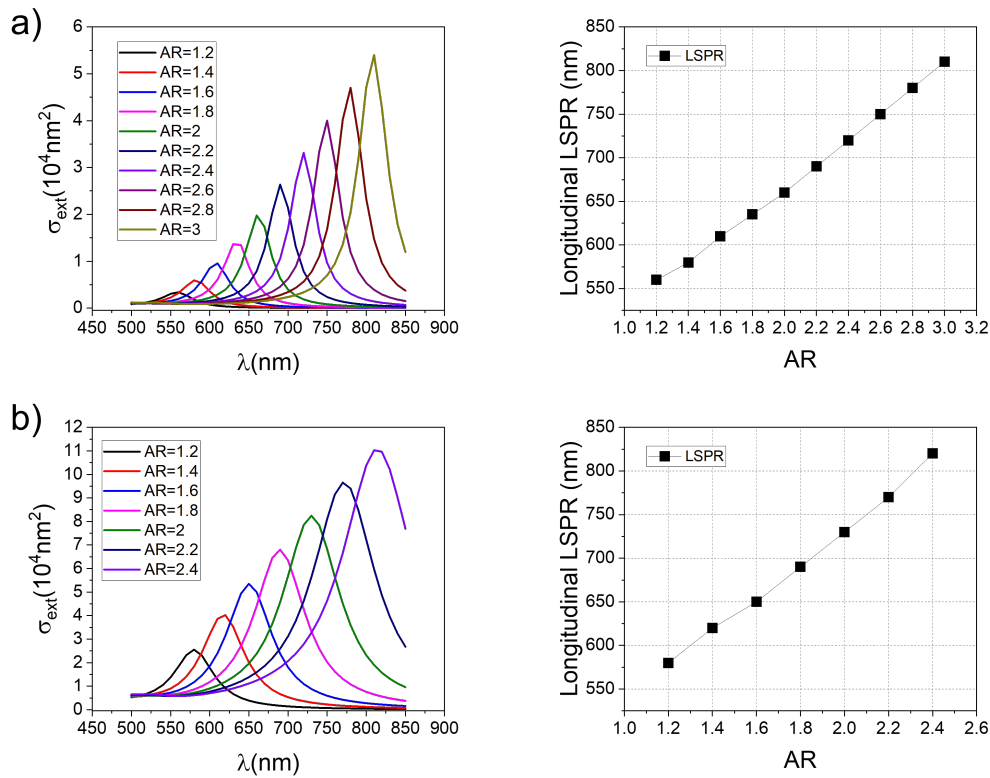


Figure 5.27: Simulated extinction cross-section spectra (left) and (right) consequent LSPR position in wavelength, obtained varying the NR aspect ratio AR , keeping constant all the other geometrical characteristics. (a) $D=25$ nm, $R_{\text{tip}}=D/(2.5)$ and $t_{\text{shell}}=5$ nm. (b) $D=50$ nm, $R_{\text{tip}}=D/(2.5)$ and $t_{\text{shell}}=10$ nm

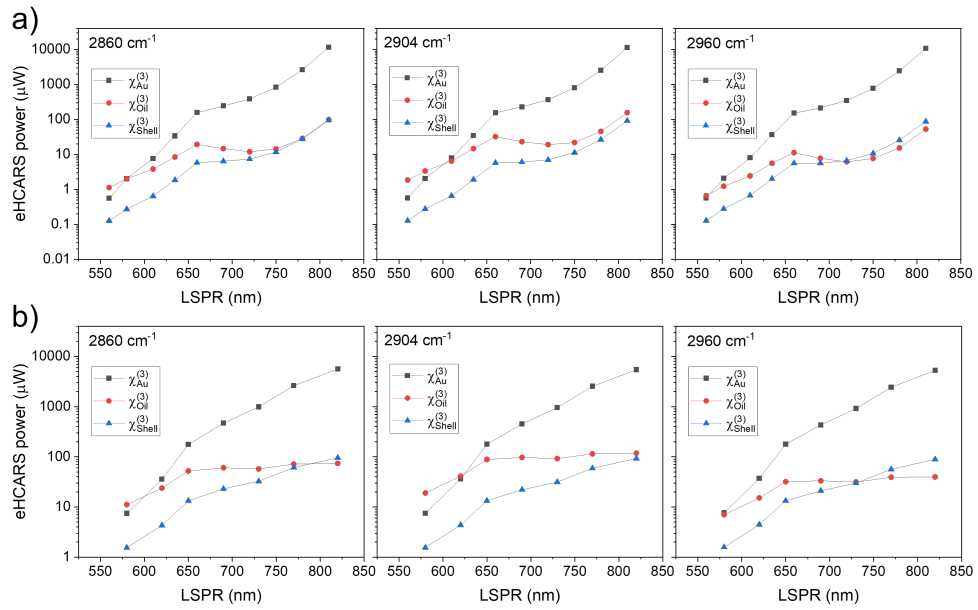


Figure 5.28: Study of the third order nonlinear contribution in the simulated-detected eH-CARS amplitude (Eq.3.4.21) obtained separately investigating the NP gold core (black, indicated with $\chi_{Au}^{(3)}$), the oil (red, indicated with $\chi_{oil}^{(3)}$) and the NP silica shell (blue, indicated with $\chi_{shell}^{(3)}$) third order contributions (see text) for a SiAuNRs surrounded by silicone oil and placed onto a glass substrate (index matched with the bulk material). The NP is considered as placed in a homogeneous material from the third-order non linearity point of view (see Eqs.5.6.2). Each LSPR corresponds to a different NP with (a) $D=25$ nm, $R_{tip}=D/(2.5)$, $t_{shell}=5$ nm and (b) $D=50$ nm, $AR=2$, $R_{tip}=D/(2.5)$, $t_{shell}=10$ nm, for which the AR has been varied. The results for three driven molecular vibration are shown: (Left) $\Omega_{vib}=2860$ cm^{-1} , (Center) $\Omega_{vib}=2904$ cm^{-1} , to whom corresponds the oil CARS resonance, and (Right) $\Omega_{vib}=2860$ cm^{-1} .

not involving vibrational states. On the contrary, in the case of $\chi_{\text{oil}}^{(3)} \neq 0$ the resonant behaviour is confirmed by an higher signal for $\Omega_{\text{vib}}=2904 \text{ cm}^{-1}$.

As already mentioned, once the $\chi^{(3)}$ is set, the dependence of the simulated results on the LSPR are determined by the combination of three aspects:

- the enhancement of the input pump and Stokes,
- the enhancement of the generated CARS,
- the quantity of material contributing to the third order nonlinear effect.

The first and second aspect are related to the particle geometry as the enhancement is determined both by the LSPR position with respect to the λ of the considered field and by the overall particle volume. As shown in Chapter 4.1.2, a particle characterized by a fixed AR gives a lower enhancement for an overall larger volume due to a higher radiative damping (Ref.[117]). The third aspect depends again on the particle volume as, for example, for a larger NP, more gold and shell materials are present in the foci of the exciting beams, with a consequent reduction of oil. In general, looking individually to the results for each excited molecular oscillation, for all three cases in which we have a different third order contribution, we can notice two different trends of the signal behaviour as a function of the LSPR. Let's focus our attention in particular on Fig.5.28 (a)-center obtained with the NPs of Fig.5.27. When the NP has an associate LSPR very blue-shifted compared to the pump field wavelength $\lambda_{\text{P}}=820 \text{ nm}$, we can assume that the enhancement of the latter is basically negligible. This is confirmed by looking at the $\sigma_{\text{ext}}(\lambda_{\text{P}})$ of the particles characterized by an AR between 1.2 and 2 (see Fig.5.27(a)-left). So, for this group of NRs the eH-CARS amplitudes, are mainly determined by the actual value of the $\chi^{(3)}$ contributing to the CARS generation, by the amount of excited material and by the distance in wavelength between their LSPR with respect to the λ_{CARS} . The combination of the aspects gives an increased detected signal for $\text{LSPR} \rightarrow \lambda_{\text{CARS}}$. It is interesting to notice that when the NP is very small (as for $AR=1.2$ and $AR=1.4$), thanks to the larger amount of oil excited, the contribution given from the latter is higher than the contribution given by the gold material despite $\chi_{\text{Au}}^{(3)} > \chi_{\text{oil}}^{(3)}$. Once $\text{LSPR} > \lambda_{\text{CARS}}$ the direct enhancement at λ_{CARS} starts to decrease while the enhancement at the pump wavelength becomes higher and more predominant. This results in a change of trend of the detected CARS field dependence as a function of the LSPR. Here we can see that, apart from having different actual values due to the associated $\chi^{(3)}$, the contribution of the signal given by the gold and the shell have the same trend. This is because when increasing the NR aspect ratio, both the shell volume and the gold core volume increase. On the contrary, in the case of the oil, the trend of the detected eH-CARS signal is the result of a competitive interplay between the pump enhancement, increasing for $\text{LSPR} \rightarrow \lambda_{\text{P}}$, and the decreased amount of oil generating the signal for larger NR. Notably, for all the cases, the predominant effect is the increase of the generated and detected CARS for $\text{LSPR} \rightarrow \lambda_{\text{P}}$ because of the two pump photons involved in the CARS process. These comments are in general valid also for the other excited Ω_{vib} and for the cases of larger NP with $D=50 \text{ nm}$ (Fig.5.28(b)) The main difference between Fig.5.28(a) and Fig.5.28(b) is a less pronounced resonant behavior at $\text{LSPR}=\lambda_{\text{CARS}}$. This can be explained by the broader extinction cross-section obtained with the larger particles (due to their stronger radiative damping) and as consequence both the pump enhancement for

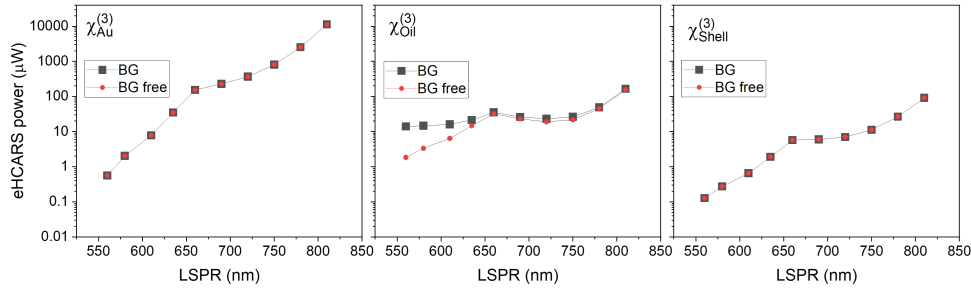


Figure 5.29: Study of the third order nonlinear contribution in simulated-detected eH-CARS amplitude (Eq.3.4.21), for $\Omega_{\text{vib}}=2904 \text{ cm}^{-1}$, obtained separately investigating the NP gold core (left, indicated with $\chi_{\text{Au}}^{(3)}$), the oil (center, indicated with $\chi_{\text{oil}}^{(3)}$) and the NP silica shell (right, indicated with $\chi_{\text{shell}}^{(3)}$) third order contributions (see text) for a SiAuNRs surrounded by silicone oil and placed (red, BG) in an homogeneous third order nonlinear material and (black, BG) onto a glass substrate (index matched with the bulk material) with $\chi_{\text{B}}^{(3)}=0$. Each LSPR corresponds to a different NP with $D=25 \text{ nm}$, $R_{\text{tip}}=D/(2.5)$, $t_{\text{shell}}=5 \text{ nm}$ for which the AR has been varied.

$\text{LSPR} < \lambda_{\text{CARS}}$ and the CARS field enhancement for $\text{LSPR} \rightarrow \lambda_{\text{p}}$ have to be taken into account.

In Fig.5.28 we did not take into account the additional step in $\chi^{(3)}$ due to the glass substrate. To include such step contribution, during the analysis of the third order contribution coming from the gold, the silica shell and the oil, the third order susceptibility of the glass substrate was set to zero ($\chi_{\text{B}}^{(3)}=0$) independently from $\chi_{\text{oil}}^{(3)}$. In this discussion we keep $\chi_{\text{B}}^{(3)}$ different from its actual value ($7.8 \times 10^{-23} \text{ m}^2/\text{V}^2$) to keep evaluating the contribution of oil, shell and gold separately, while all the other $\chi^{(3)}$ contribution are off. Figure 5.29 shows how the NR gold core (left), silica shell (right) and oil (center) individual contribution are affected by the introduction of $\chi_{\text{B}}^{(3)}=0$, compared with the case of Eqs.5.6.2 (here in red, indicated as BG free) and

$$\begin{cases} \chi_{\text{B}}^{(3)} & = 0 \\ \mathbf{P}_{\text{CARS,B}} & \neq \mathbf{P}_{\text{CARS,oil}} \end{cases} \quad (5.6.3)$$

in the exemplary situation of driven molecular vibration at $\Omega_{\text{vib}}=2904 \text{ cm}^{-1}$. As it is clear from the comparison, the gold and shell contribution (Fig.5.29 left and right respectively) are not affected by the glass substrate, because as far as $\chi_{\text{oil}}^{(3)} = \chi_{\text{B}}^{(3)}=0$ the particle is still like placed in an third order homogeneous material. When $\chi_{\text{oil}}^{(3)} \neq 0$ and $\chi_{\text{B}}^{(3)}=0$, the eH-CARS signal generated in oil is affected by the glass-oil interface when the considered particles has a LSPR blue-shifted compare to both λ_{CARS} and $< \lambda_{\text{p}}$. This is explained considering that for smaller AR the glass-oil interface within the focus is larger to the extend that it affects the signal given by the oil. As the AR increases the glass-oil contribution gets lower and negligible compared to the one of the oil only.

5.7 CARS local field enhancement

The R factor introduced in Sec.5.2 quantifies the enhancement measured in the far field, via the comparison of the eH-CARS signal detected at the NR PSF and

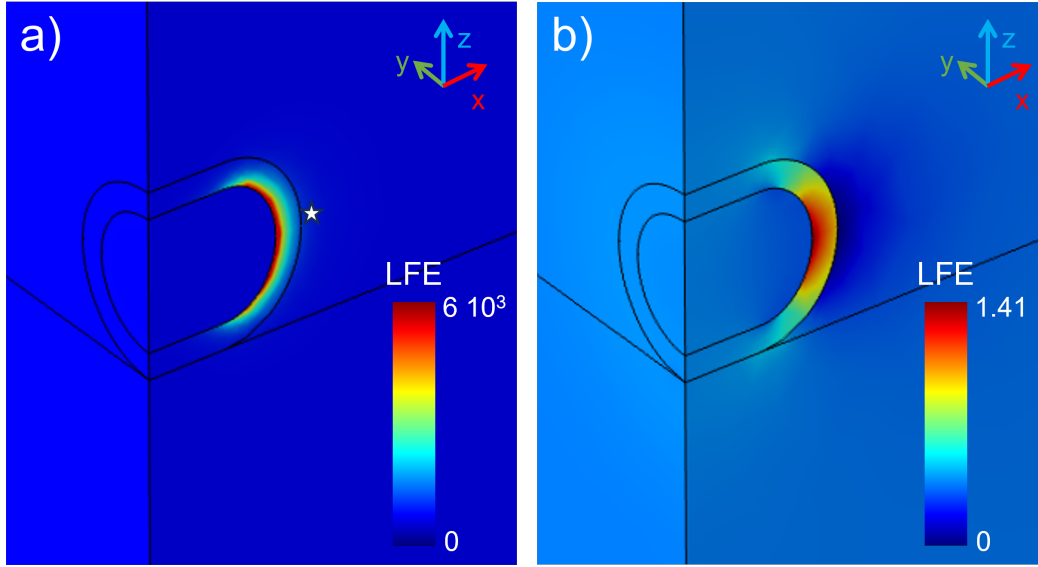


Figure 5.30: Local field enhancement (LFE) of the CARS signal, considering the CARS process taking place at a silica coated NR (with $D=25$ nm, $AR=2$, $R_{\text{tip}}=D/(2.5)$, $t_{\text{shell}}=5$ nm) in the case of (a) plasmonic gold core (ϵ_{Au} as in Chapter 4.1.3.1) and (b) dielectric core ($n=1.52$).

the one at the glass-oil interface away from the NR. In this section, exploiting the LFE eH-CARS COMSOL model (see Chapter 3.4.2), we aim at the estimation of the LFE obtained in the proximity of a NR. The LFE is defined and computed from the COMSOL simulations as:

$$\text{LFE} = \frac{|E_{\text{P}}^{\text{tot}}|^2 |E_{\text{S}}^{\text{tot}}| |E_{\text{CARS}}^{\text{tot}}|}{|E_{\text{P}}^{\text{back}}|^2 |E_{\text{S}}^{\text{back}}| |E_{\text{CARS}}^{\text{back}}|} \quad (5.7.1)$$

where E_{P} , E_{S} and E_{CARS} refer to the pump (at 820 nm), the Stokes (at 1076 nm) and CARS (at 662 nm) field respectively. For all of them $E^{\text{tot}}=E^{\text{sca}}+E^{\text{back}}$ are obtained as explained in Chapter 3.4.1 with E^{back} simulated as a beam characterized by Gaussian field profile at BFP of the objective (thus, same excitation condition of the CARS process). The results presented in this section are obtained considering a NR characterized by $D=25$ nm, $AR=2$, $R_{\text{tip}}=D/(2.5)$, $t_{\text{shell}}=5$ nm. To investigate the fields enhancement provided by the plasmonic properties of the particle, we considered a NP gold core characterized by a permittivity ϵ_{Au} , obtained as explained in Chapter 4.1.3.1. Additionally, to prove the importance of the plasmonic properties, we simulated the LFE eH-CARS process when the nanoparticle involved is dielectric. To simulate the absence of the plasmonic effect, we attributed to the NR core a fixed refractive index matched with the glass substrate refractive index ($n=1.52$). All the other linear aspect of the model are kept equal as what mentioned in Chapter 3.4.1. Regarding the third order materials properties, we set $\chi_{\text{B}}^{(3)} = 7.8 \times 10^{-23} \text{m}^2/\text{V}^2$ for the borosilicate glass coverslip, $\chi_{\text{Au}}^{(3)} = 2 \times 10^{-19} \text{m}^2/\text{V}^2$ for the NR gold core, $\chi_{\text{shell}}^{(3)} = 0.6\chi_{\text{B}}^{(3)}$ for the silica shell and $\chi_{\text{oil}}^{(3)}(2904 \text{cm}^{-1}) = \frac{1}{2} \bar{\chi}(2904 \text{cm}^{-1}) \chi_{\text{B}}^{(3)}$, with $\bar{\chi}(2904 \text{cm}^{-1})$ from data set of Fig.3.28, for the silicone oil.

Figure 5.30 reports the spatial LFE obtained in the CARS process with (a) a plasmonic NR and (b) a dielectric NR. The overall LFE obtained thanks to the NR plasmonic properties is $\sim 6 \times 10^3$. This plot suggest that, while from the experimental

point of view the shell is fundamental to avoid particle damage, on the other hands it represents a drawback because the highest field enhancement is obtained within its thickness. At the NR tip, i.e. at the shell-oil interface (star symbol in Fig.5.30(a)), the LFE is $\sim 5 \times 10^2$. The non-plasmonic enhancement displayed within the silica shell (Fig.5.30(b)) derives from the smaller refractive index of the shell ($n=1.458$) compared to the one used in the NR core and in oil ($n=1.52$). In fact, the field normal component to the shell surface, obeys to boundary condition, so the amplitude of each field will be higher of a factor $(n_B/n_{\text{shell}})^2$ within the shell. Considering all the fields together, this leads to an overall enhancement of $\sim (n_B/n_{\text{shell}})^8$.

5.8 R factor wavenumber dependence behaviour

This Section aims to study the wavenumber dependent behaviour of the measured far field enhancement, namely the R factor (see Sec.5.2). Additionally, this will be compared with the simulated results, using this comparison as a confirmation of the developed COMSOL model in reproducing the experimental results. As explained in Sec.3.3.2, in our eH-CARS experiments, in order to drive molecular oscillation at different wavenumber, we vary the selected IFD. To vary the selected IFD, we first tune the OPO to then change the delay time between pump and Stokes. λ_S and λ_{CARS} change only when the OPO is tuned. In this case, the resonance condition changes between the NR LSPR and Stokes and CARS field, thus changing also their enhancement. Conversely, the enhancement of pump is not modified, as its wavelength is never varied. For this study we selected six different IFD around the main silicone oil peak (at 2904 cm^{-1}), starting from 2840 cm^{-1} to 2940 cm^{-1} , with steps of 20 cm^{-1} . Precisely, to archive such IFDs, both the OPO and the pump-Stokes delay were tuned as follows:

- OPO tuned to have IFD= 2950 cm^{-1} , pump-Stokes delay to vary the IFD from 2900 cm^{-1} to 2940 cm^{-1} ;
- OPO tuned to have IFD= 2900 cm^{-1} , pump-Stokes delay to vary the IFD from 2840 cm^{-1} to 2880 cm^{-1} .

All the experimental results shown in this Section refer to measurements performed on the NR whose measured extinction spectrum is reported in Fig.4.16. We took this exemplar particle as the optical sizing conducted on it turns out to be crucial while simulating the eH-CARS signal for different IFD, to compare the simulated and experimental R factor. Looking at the extinction spectrum of this particle we can see that its LSPR is around 625 nm . In first approximation, the enhancement variation of the Stokes field, while selecting different IFD, can be neglected as λ_S turns out to be always well red-shifted than the LSPR. Conversely, the CARS field enhancement variation will affect the R factor evaluation. In fact, the λ_{CARS} blue shift, occurring for larger IFD, improves the ability to couple the field with the NR LSPR under study.

Figure 5.31 (top) shows the measured eH-CARS amplitude both at the NR (black) and at the glass-oil interface away from the NR (red), for the IFD selected, obtained inserting the $\lambda/4$ wave plate in the beams path and computing then the projection of the detected signal along and across the NR main axis. The bottom part of the figure reports the corresponding R factors computed as explained in Sec.5.2. Both eH-CARS amplitudes presents a main peak at IFD= 2904 cm^{-1} in accordance with the $\chi_{\text{oil}}^{(3)}$ wavenumber dependence (see Fig.3.28). Instead, the R factor

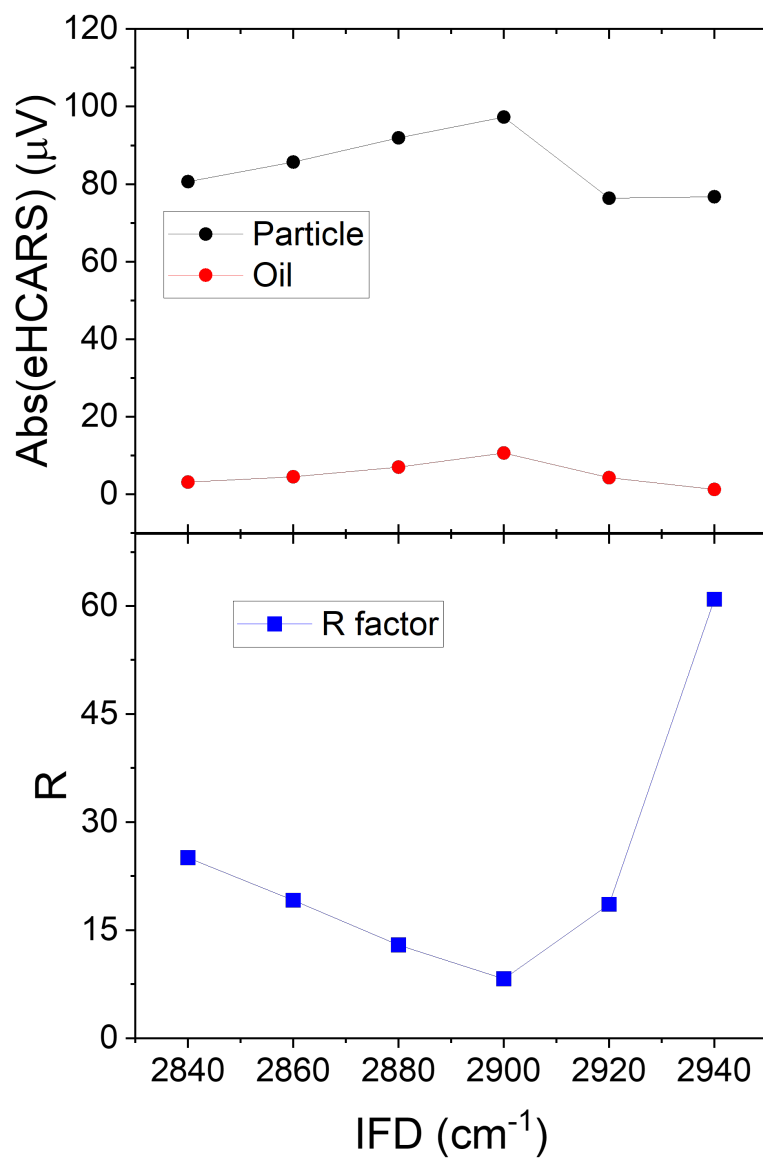


Figure 5.31: Top: eH-CARS amplitude as a function of the IFD, experimentally measured at the oil-glass interface away from the NR(red) and at the NR (black). Bottom: R factors wavenumber dependence.

presents a less intuitive wavenumber dependant behaviour. We find a minimum for $\text{IFD} = 2904 \text{ cm}^{-1}$, with increasing values moving away from the oil resonance. This result and the actual R factor values come from a competitive interplay between different contributions. Referring to Eq.5.2.4 which gives the definition of the R factor, we can notice that the numerator depends on the sum of the enhanced oil, enhanced shell, and enhanced gold contributions as well as on the unenhanced signal from the silicone oil, which is subtracted. Moving away from the resonance the enhanced gold and enhanced shell contributions remain unvaried, deriving from a nonresonant phenomenon. On the contrary, the signal from the silicone oil and the enhanced silicone oil decreased, giving a positive and negative contribution respectively to the evaluation of the R factor numerator. The denominator of Eq.5.2.4 simply decreases for $\text{IFD} \neq 2904 \text{ cm}^{-1}$ and when the IFD selected is considerably out from the oil resonance, as in the case of 2940 cm^{-1} , the CARS signal from oil is very small, so that the normalization can be significantly affected by noise.

For the comparison between the experimental data and the ones given by the developed COMSOL model, we simulated and computed the eH-CARS amplitude with the resulting R factor for different excited vibration Ω , varying from 2840 cm^{-1} to 2960 cm^{-1} with 5 cm^{-1} steps. For quantitative comparison of a wavenumber dependent behaviour, the simulation's results have to take into account the spectral resolution we have experimentally when exiting a vibrational mode. This spectral resolution is given by the full width at half maximum (FWHM) of the Fourier-limit of the temporal envelope of the chirped pump and Stokes pulses that in our setup is around 20 cm^{-1} (Ref.[102]). To include the spectral resolution in the simulation we convoluted the real and imaginary components of the simulated eH-CARS, as a function of the Ω , with a normalized Gaussian function, i.e.

$$g(x) = e^{-\frac{(x-\mu)^2}{2\sigma^2}} \quad (5.8.1)$$

where μ is the mean value and σ represents the standard deviation given by

$$\sigma = \frac{\text{FWHM}}{\sqrt{8\ln(2)}}. \quad (5.8.2)$$

The choice of σ controls the width of the Gaussian, which in turn determines the level of spectral smoothing. We performed the convolution operation by sliding the Gaussian function, evaluated in the same Ω interval as the eH-CARS, across the eH-CARS dataset. More precisely, we swept its mean value μ exactly as we did for the Ω . Thus, both the eH-CARS(Ω) and $g(\Omega)$ are not continuous functions, as they are evaluated in the Ω interval $[2840, 2960] \text{ cm}^{-1}$ in steps of 5 cm^{-1} . For this reason, the convolution translates, for each chosen μ value, in computing the sum of the weighted eH-CARS(Ω) values, where the weighting dataset is given by $g(\Omega)$ centered at a given μ (indicated in the following by $g_\mu(\Omega)$). Therefore, for each μ , the eH-CARS convoluted signal is obtained computing

$$N = \sum_{\Omega=2840\text{cm}^{-1}}^{2960\text{cm}^{-1}} \text{eH-CARS}(\Omega) \cdot g_\mu(\Omega) \quad (5.8.3)$$

and

$$D = \sum_{\Omega=2840\text{cm}^{-1}}^{2960\text{cm}^{-1}} g_\mu(\Omega) \quad (5.8.4)$$

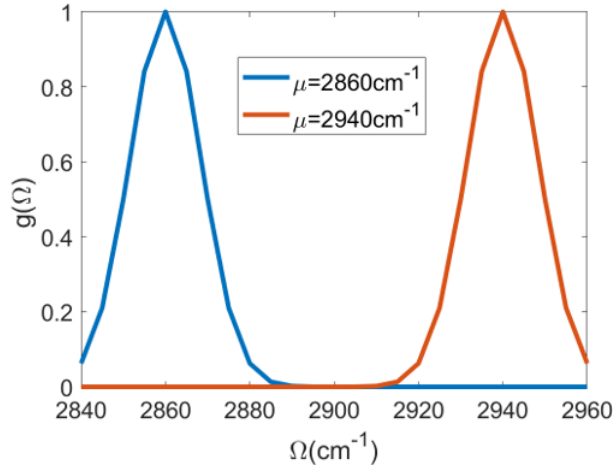


Figure 5.32: Gaussian function ($\sigma=8.48 \text{ cm}^{-1}$) used in the convolution onto the simulated eH-CARS signals to take into account the spectral resolution characterizing the real experiments. μ is translated in the convolution from 2840 cm^{-1} to 2960 cm^{-1} in steps of 5 cm^{-1} and here two examples are given for $\mu=2860 \text{ cm}^{-1}$ (blue) and $\mu=2860 \text{ cm}^{-1}$ (red).

so that

$$\text{eH-CARS}_{\text{conv}}(\mu) = \frac{N}{D}. \quad (5.8.5)$$

The division by the factor D ensures that the results are scaled appropriately.

Figure 5.32 shows the Gaussian function $g(\Omega)$ exploited for the convolution, when its mean value is shifted at 2860 cm^{-1} (blue) and 2940 cm^{-1} (red). For each mean position μ , we calculated the normalized weighted sum of the eH-CARS data points. This is effectively applying the Gaussian blur to the data. Figure 5.33 and Figure 5.34 report the comparison between the simulated eH-CARS data (solid line) and the data resulting from the convolution (dashed line). In particular, Fig.5.33 illustrates both real (red) and imaginary (blue) eH-CARS signals components. The top-left corner (a) refers to the case of absence of NR, while the other results are obtained by placing the NR in the simulation volume. Since the uncertainty on the actual value of the $\chi_{\text{Au}}^{(3)}$, we took advantage of this study to additionally investigate how different order of magnitude of $\chi_{\text{Au}}^{(3)}$ affects the detected eH-CARS and the R factor. For this reason we assigned to the gold third order susceptibility the following values: $\chi_{\text{Au}}^{(3)}=0 \text{ m}^2/\text{V}^2$ (b), $\chi_{\text{Au}}^{(3)}=3 \times 10^{-19} \text{ m}^2/\text{V}^2$ (c) and $\chi_{\text{Au}}^{(3)}=1 \times 10^{-18} \text{ m}^2/\text{V}^2$ (d). The NR geometry and parameters used in the simulation were set to be equal to the outcomes of the optical sizing (Chapter 4.1.3), i.e. $D=55 \text{ nm}$, $AR=1.37$, $g=0.75$ $R_{\text{tip}}=D/3$ and $t_{\text{shell}}=10 \text{ nm}$. In all four cases we notice that, as expected, the inclusion of the spectral resolution acts as a smoothing and blurring effect. Figure 5.34 shows on the top the eH-CARS amplitude obtained when in absence of the NR (red) and when it is placed in the simulation volume (black) and characterized by $\chi_{\text{Au}}^{(3)}=3 \times 10^{-19} \text{ m}^2/\text{V}^2$. On the bottom, it is possible to find the consequent computed R factors.

Once the $\text{eH-CARS}_{\text{conv}}(\Omega)$ signal has been computed, we can compare it with the experimental data measured at the six mentioned IFD (2840 cm^{-1} , 2860^{-1} , ..., 2940^{-1}). Figure 5.35 (top) shows a qualitative comparison of the simulated (black-lines) and experimental (red-symbols) eH-CARS amplitudes. Both the signal obtained at the NR (solid lines / square symbols) and in oil (dashed lines/circle sym-

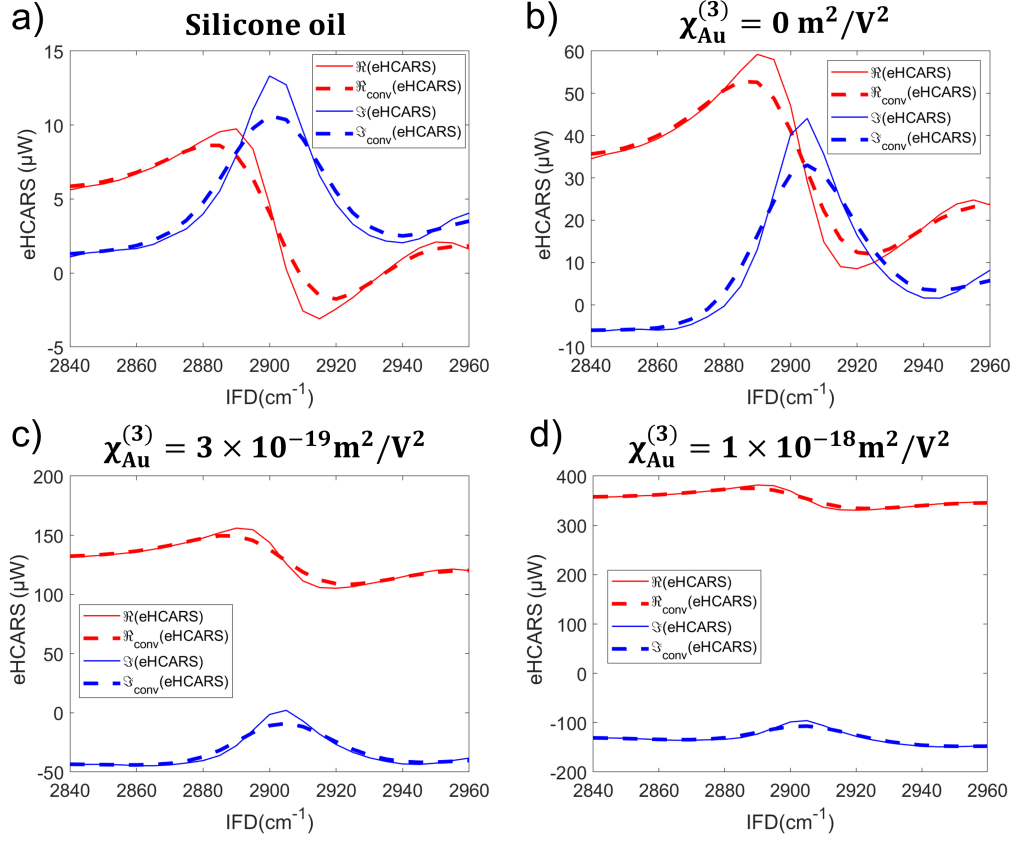


Figure 5.33: Comparison between simulated eH-CARS signal, as a function of Ω , obtained neglecting (solid lines) and taking into account (dashed line) the spectral resolution that affects the experiment (see text). Both real (red) and imaginary (blue) components of the eH-CARS are displayed. The simulation was performed for four different cases: (a) in the absence of the NR at the oil-glass interface, (b) with the NR and $\chi_{\text{Au}}^{(3)}=0 \text{ m}^2/\text{V}^2$, (c) with the NR and $\chi_{\text{Au}}^{(3)}=3 \times 10^{-19} \text{ m}^2/\text{V}^2$ and (d) with the NR and $\chi_{\text{Au}}^{(3)}=1 \times 10^{-18} \text{ m}^2/\text{V}^2$. Where the NR is present is has been modeled with $D=56 \text{ nm}$, $AR=1.37$, $g=0.75$ $R_{\text{tip}}=D/3$ and $t_{\text{shell}}=10 \text{ nm}$. The following third order materials properties have been used: $\chi_{\text{B}}^{(3)} = 7.8 \times 10^{-23} \text{ m}^2/\text{V}^2$ for the borosilicate glass coverslip, $\chi_{\text{Au}}^{(3)} = 3 \times 10^{-19} \text{ m}^2/\text{V}^2$ for the NR gold core, $\chi_{\text{shell}}^{(3)} = 0.6\chi_{\text{B}}^{(3)}$ for the silica shell.

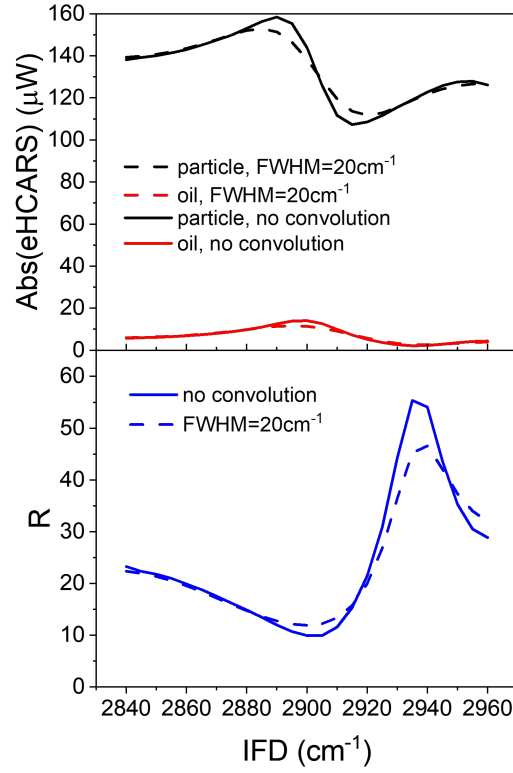


Figure 5.34: Top: Simulated eH-CARS amplitudes, as function of the IFD, obtained in presence (black) and absence (red) of the NR, neglecting (solid lines) and taking into account (dashed line) the spectral resolution that affects the real experiments. Bottom: Comparison for the computed R factor neglecting (solid lines) and taking into account (dashed line) the spectral resolution that affects the real experiments. The simulation were performed considering a NR with $D=55$ nm, $AR=1.37$, $g=0.75$ $R_{\text{tip}}=D/3$ and $t_{\text{shell}}=10$ nm. The following third order materials properties have been used: $\chi_{\text{B}}^{(3)} = 7.8 \times 10^{-23} \text{m}^2/\text{V}^2$ for the borosilicate glass coverslip, $\chi_{\text{Au}}^{(3)} = 3 \times 10^{-19} \text{m}^2/\text{V}^2$ for the NR gold core, $\chi_{\text{shell}}^{(3)} = 0.6\chi_{\text{B}}^{(3)}$ for the silica shell.

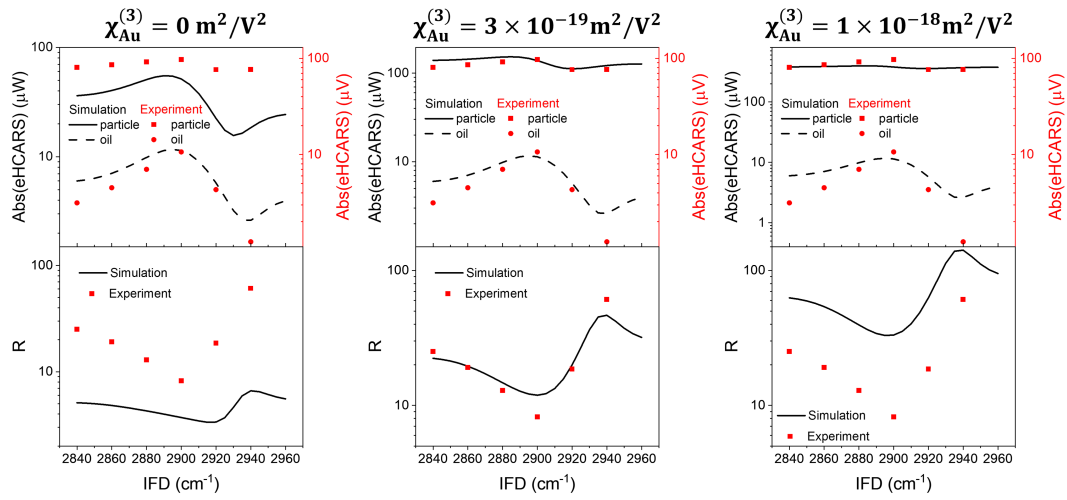


Figure 5.35: Top: eH-CARS amplitude as a function of the IFD, experimentally measured at the glass-oil interface (circle red symbols) and at the NR PSF (square red symbol) and simulated from the glass-oil interface only (dashed black line) and from the NR (solid black line). The log scale was adjusted to improve the qualitative comparison between the signals related to the glass-oil interface. Bottom: Quantitative comparison between the R factors resulting from the experimental (red symbols) and simulated (black solid line) eH-CARS dataset. The $\chi_{\text{Au}}^{(3)}$ employed in the simulation performed in presence of the NR has been set to $0\text{m}^2/\text{V}^2$ (left), $3 \times 10^{-19}\text{m}^2/\text{V}^2$ (center) and $1 \times 10^{-18}\text{m}^2/\text{V}^2$ (right).

bols) are displayed on a log scale. The simulated signal from the NR has been calculated setting $\chi_{\text{Au}}^{(3)}=0\text{m}^2/\text{V}^2$ (left), $\chi_{\text{Au}}^{(3)}=3\times 10^{-19}\text{m}^2/\text{V}^2$ (center) and $\chi_{\text{Au}}^{(3)}=1\times 10^{-18}\text{m}^2/\text{V}^2$ (right). A quantitative direct comparison between the amplitude factor is not possible as the simulated eH-CARS, computed via Eq.3.4.21, expresses the pulse peak power so that it is in units of watt, while the detected experimental one is in units of volt. In order to convert the simulated watt in volts, we should multiply them by the transimpedance ($\sim 10^5\text{V/A}$) that we have at the detectors, by the $\sim 70\%$ quantum efficiency of the photodetector (around 0.2 A/W, considering also the losses) and by the duty cycle of the source ($R_{\text{pulse}}T_{\text{pulse}} \sim 10^{-4}$), as in the experiment we measure the average signal powers instead of the peak powers. Additionally, the exact power at the sample has to be known while we estimate it from the average power measured at the entrance of the microscope and considering that 50% of it is lost due to the optics placed in between the microscope entrance and the sample. To have a qualitative comparison of the experimental and simulated eH-CARS spectral dependence, we plotted the two value sets on a logarithmic scale which overlaps the signal related to the silicone oil. The main discrepancy in the amplitude comparison for both the oil and NR case is an experimental faster reduction trend of the signal moving away from the resonance, toward lower IFD. A possible explanation for this trend can be found considering that in practice to change the IFD we apply a different delay on the pump beam. This affects the pump-Stokes time overlap which determines the excitation strength. Thus, this trend is the result of the weaker excitation strength due to the reduced pump-Stokes overlap. A higher value for $\chi_{\text{Au}}^{(3)}$ leads to a higher eH-CARS signal from the NR with a reduced spectral dependence. In fact, the non resonant gold third-order contribution becomes more and more predominant over the resonant one. Figure 5.35 (bottom) shows the quantitative comparison between the simulated and experimental R factor. The quantitative comparison is possible in this case thanks to the definition of the R factor, which is a normalized quantity hence unitless. We see that in the case of $\chi_{\text{Au}}^{(3)}=0\text{m}^2/\text{V}^2$ (Fig.5.35 bottom-left), the R factor obtained is one order of magnitude lower than the experimental one and with a different spectral dependence. When $\chi_{\text{Au}}^{(3)}=1\times 10^{-18}\text{m}^2/\text{V}^2$ we have the opposite discrepancy (Fig.5.35 bottom-right) as the R factor assumes values much higher than the experimental one. A good agreement both in terms of actual values and spectral behaviour is obtained for $\chi_{\text{Au}}^{(3)}=3\times 10^{-19}\text{m}^2/\text{V}^2$ (Fig.5.35 bottom-center), which is close to the value stated in the literature for four wave mixing and with pulses duration very close to our experimental condition (Ref.[110]).

5.9 R factor comparison

In this Section, we report a representative comparison between the R factor power dependence behaviour found for the three types of silica-coated gold nanorods experimentally investigated within this project (see Fig.5.36). It is important to re-emphasize that particles belonging to the same nominal group were characterized by significantly different optical properties, hence sizes. For this investigation, we decided to compare particles, belonging to the different nominal group, whose longitudinal LSPR turned out to be as much as possible close to 660 nm, i.e. the typical CARS wavelength (see Fig.5.37-left). The eH-CARS measurements have been performed as explained in Sec.5.4, employing circular polarized pump and Stokes beams and considering the projection of the detected eH-CARS signal (as measured, lock-in

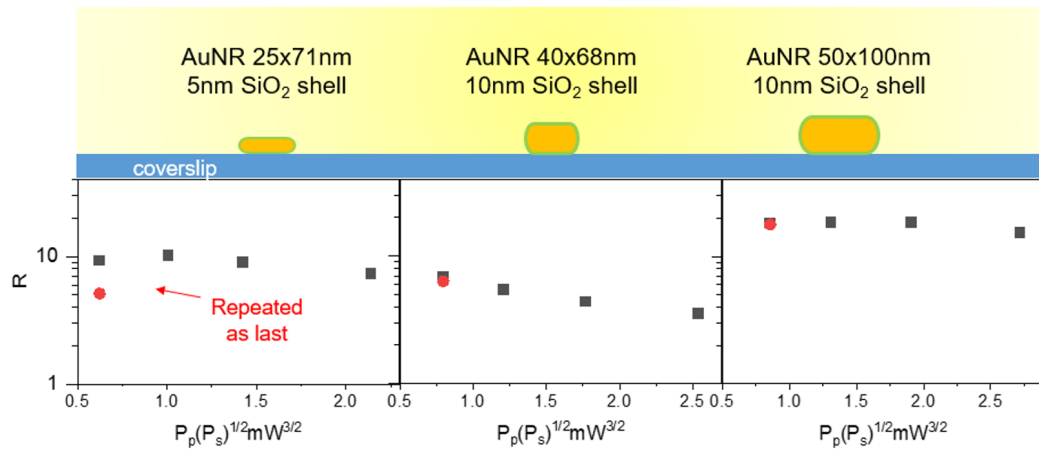


Figure 5.36: R factor versus power of incident fields from polarization resolved eH-CARS. Left: Nominal 25×71 nm NR with 5 nm of SiO_2 shell; Selected silicone oil resonance is 2904 cm^{-1} ; Circular polarization excitation and R factor computed considering the projection of the detected eHCARS signal along(co-) the longitudinal axis of the NR. Middle: Nominal 40×68 nm NR with 10 nm of SiO_2 shell; Selected silicone oil resonance is 2904 cm^{-1} ; Circular polarization excitation and R factor computed considering the projection of the detected eH-CARS signal along(co-) the longitudinal axis of the NR. Right: Nominal 50×100 nm NR with 10 nm of SiO_2 shell; Selected silicone oil resonance is 2904 cm^{-1} ; Circular polarization excitation and R factor computed considering the projection of the detected eH-CARS signal along(co-) the longitudinal axis of the NR.

offset corrected) along the longitudinal axis of the NR to compute the R factor (see Sec.5.2). Additionally, as a further confirmation of the instability versus saturation effect affecting the R factor value for pump and Stokes high powers, a last scan has been performed setting the powers at the lowest values of the sequence. Figure 5.37 shows the measured extinction spectra of the three representative particles under study within this Section, acquired before and after the eH-CARS power dependence measurements. The resistance of a NR against the reshaping mainly depends on the thickness of its silica shell. The nominal $25 \text{ nm} \times 71 \text{ nm}$ -SiAuNR with 5 nm silica shell turned out to be more subjected to particle reshape/destruction. This is clear looking at the extinction spectrum variation measured before and after the laser exposure (Fig.5.37-top) and from the comparison of R factor obtained in the first and last scan repetition performed at low powers (Fig 5.36, red symbol). Instead, both the nominal $40 \text{ nm} \times 68 \text{ nm}$ -SiAuNR and the nominal $50 \text{ nm} \times 100 \text{ nm}$ -SiAuNR, characterized by a 10 nm silica shell, results to be more resistant as confirmed by the measured extinction cross-sections (Fig.5.37-middle and bottom) and by the last scan at low powers, giving R factors values very close to the initial one. Eventually, the stability of such NR enabled us to discover the presence of the CARS saturation effect taking place for high applied laser powers (see Sec.5.4.1).

For completeness, we investigated the R-factor values resulting from the LFE eH-CARS simulations with SiAuNRs placed at the glass-oil interface, with λ_P and λ_S equal to 820 nm and 1076 nm respectively, to drive the molecular vibration at $\Omega_{\text{vib}} = 2904 \text{ cm}^{-1}$, with the consequent CARS emission at $\lambda_{\text{CARS}} = 660 \text{ nm}$. The NR characteristics have been varied to simulate NR characterized by diameter and shell thickness equal to the nominal ones of the particles employed in the experiments.

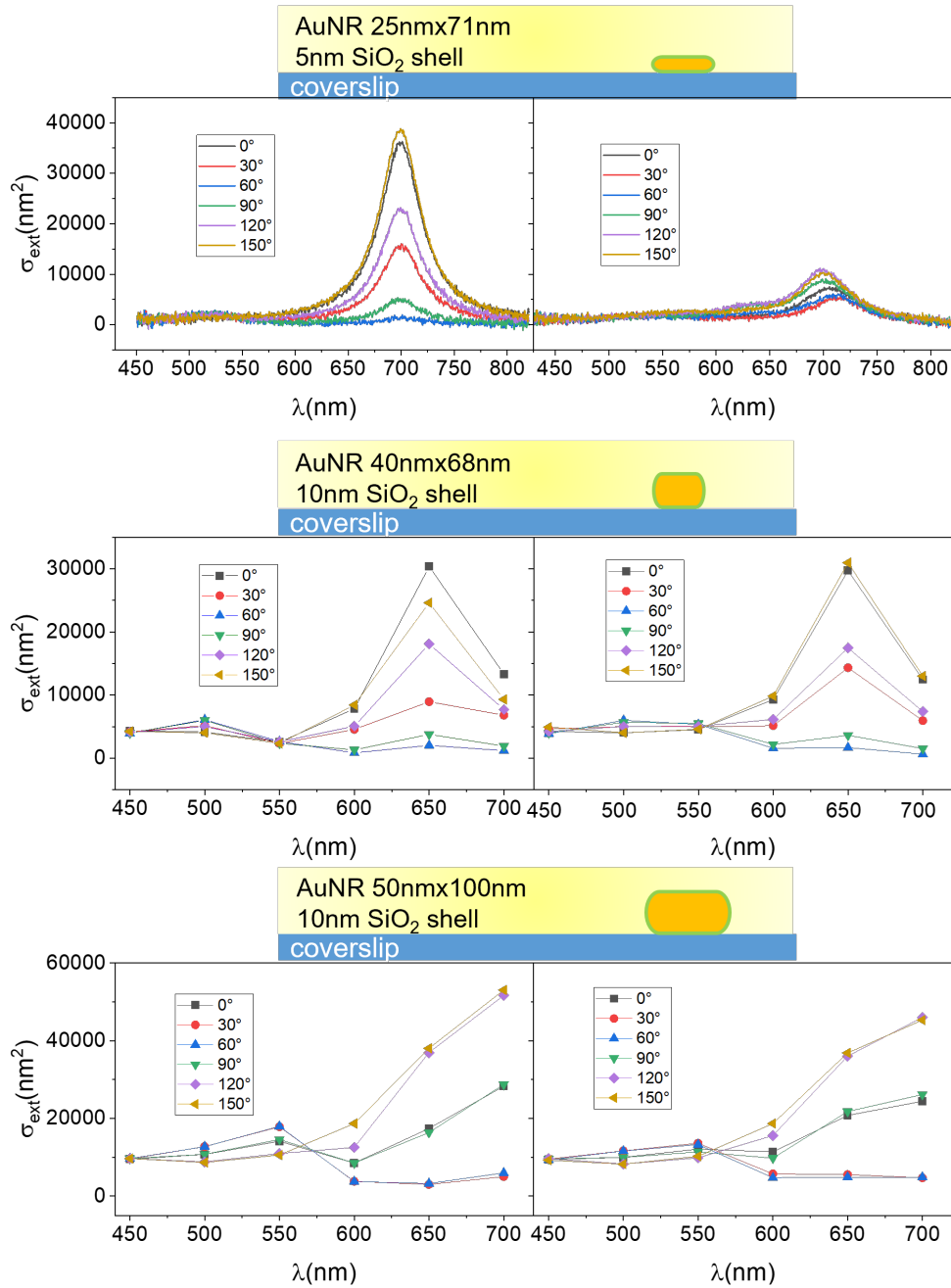


Figure 5.37: Polarization resolved single particle extinction spectra σ_{ext} measured before and after the LFE eH-CARS set of measurements reported in Fig.5.36. Each row refers to the particle whose size and silica shell thickness are reported in the corresponding sketch. For details about the acquisition procedure of the extinction measurement see Chapter3.3.1.

Instead, the aspect ratio was varied in order to shift the corresponding longitudinal LSPR around 560 nm, 660 nm, and 720 nm. In Fig.5.38-left, the simulated longitudinal extinction cross-section spectra for all the nine simulated NR are shown. Each row and color corresponds to a given value of diameter (D) and shell thickness (t_{shell}), as indicated. Different symbols are used to indicate different AR. Specifically, the triangles have been used to indicate an aspect ratio (AR) such that the consequent LSPR is at ~ 720 nm, the squares for LSPR at ~ 660 nm, and the circle for LSPR at ~ 560 nm. In Fig.5.38-right the simulated R factor LSPR dependent behaviour is reported. In Fig.5.38-left the same color-symbols legend is used. When discussing the findings presented here, it's crucial to consider that the resulting R factor is influenced both by CARS field enhancement provided by the NR and by the quantity of nonresonant material (NR gold core and silica shell) involved in the process, which gives the FWM field contribution. The NRs with LSPR ~ 560 nm are characterized by an extinction spectrum nearly at zero at the pump wavelength, so that the pump enhancement can be neglected in all three cases. The higher R factor is obtained for $D=50$ nm ($R=1.15$) followed by the one obtained for $D=40$ nm ($R=0.41$) and $D=25$ nm ($R=0.27$). Such results are reasonable considering that the NR with $D=50$ nm, different from the NRs with D equal to 25 nm and 40 nm, has the spectral width of the extinction peak such that $\sigma_{\text{ext}}(\lambda_{\text{CARS}})$ is not as close to zero compared to the other, thus providing a higher enhancement to the CARS signal by the oil surrounding the NR. Additionally, the largest is the overall particle volume the largest is the FWM contribution from the NR gold core and silica shell. When LSPR is ~ 660 nm, all the NR under study can effectively provide an enhancement to the CARS signal from silicone oil. Again the overall volume determines the amount of FWM contributions. Taking into account these two aspects one could think that the largest NR would provide the highest R factor. Notably, this is not the case as the highest R factor is obtained for $D=40$ nm. This can be explained by considering that the radiative damping affecting the particle, which decreases the field enhancement obtained, is proportional to the particle volume. As a consequence, the radiative damping obtained for $D=50$ nm is strong enough to make the consequent R factor lower than the one obtained for $D=40$ nm. The more the LSPR approaches the λ_{p} the more the pump enhancement becomes dominant compared to the other effects taking place. The log scale used in this graph does not allow us to appreciate that the R factor obtained in the three cases are actually slightly different, i.e. $R=269.6$ for $D=25$ nm, $R=268.5$ for $D=40$ nm, and $R=272.3$ for $D=50$ nm. Such R factors are determined mainly by the FWM contribution given by the NRs gold core (see Section 5.6). Interestingly, here is evident how the strength of the contribution from gold is highly dependent on the vicinity of the LSPR to λ_{p} rather than the overall gold volume. The LSPR obtained for $D=25$ nm and $AR=2.8$ is at 780 nm, thus closer to 820 nm than the LSPR (at 770 nm) obtained with $D=40$ nm or $D=50$ nm and $AR=2.4$ and $AR=2.2$ respectively.

5.10 Conclusions

In this Chapter, our primary objective was to establish a proof of principle for the LFE eH-CARS technique.

We aimed to explore how nanorods behave when subjected to different excitation methods, specifically comparing circular and linear polarization. In the latter case, we additionally examined the behavior of the LFE eH-CARS signal concerning

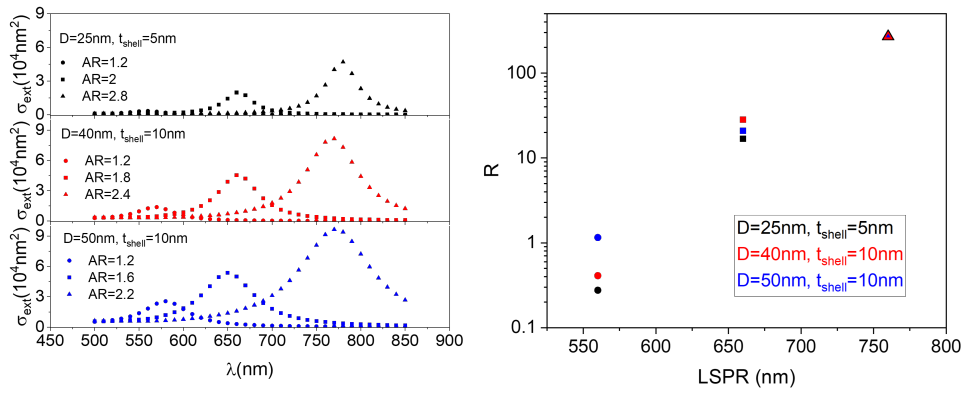


Figure 5.38: Left: Simulated extinction cross-section spectra σ_{ext} of silica coated gold NR, placed at a glass substrate and surrounded by index matching silicone oil ($n=1.52$), with diameter D equal to 25 nm (top, black), 40 nm (middle, red) and 50 nm (bottom, blue), and silica shell thickness t_{shell} set to 5 nm, 10 nm and 10 nm respectively. The aspect ratio (AR) of each NR was varied, as indicated, to shift the corresponding LSPR as about 560 nm (circle), 660 nm (square) and 760 nm (triangles). Right: Computed R factor as a function of the LSPR position of silica-coated gold NRs with $D=25$ nm $t_{\text{shell}}=5$ nm (black), $D=40$ nm $t_{\text{shell}}=10$ nm (red) and $D=50$ nm $t_{\text{shell}}=10$ nm (blue). The different symbols refers to the legend in (Right) to indicate the AR value used to obtain a given LSPR position.

changes in linear polarization rotation. Our analysis leads to the conclusion that each exciting polarization method has its own set of advantages and disadvantages. Circular polarization offers the advantage of independent excitation regardless of the particle's in-plane orientation. However, it reduces overall excitation power due to amplitude reduction of the exciting field when passing through a $\lambda/4$ wave plate and results in worse signal-to-noise ratio as the signal is split between co-circular and cross-circular detection channels. In contrast, linear polarization eliminates these two disadvantages but requires the laser exposure of the particle prior to perform an actual measurements, as in-plane particle orientation is not known in advance. In general, the preferred approach is to use circular polarization during excitation and, in post-processing, calculate signal projections along and across the nanorod. This results in an improved signal-to-noise ratio and reduces the number of times the rod undergoes laser exposure.

We quantified the CARS enhancement (named R factor) for different AuNR sizes and silica shell thickness, using silicone oil (known Raman spectrum) as material surrounding the antenna for proof-of-principle. Additionally, we characterized the dependence of such enhancement on the power of the incident beams, and we tested the particle stability under laser power exposure. Finally, we investigated the enhancement behavior upon wavenumber detuning between the CARS driving fields and the vibrational resonance under study. The nominal 25 nm \times 71 nm AuNRs with 5 nm silica shell provide a good R factor but statistically not always are really stable (damages occur more simply because of the less thick shell). The nominal 40 nm \times 68 nm AuNRs with 10 nm silica shell provide a comparable R factor but are more stable. Last, The nominal 50 nm \times 100 nm AuNRs with 10 nm silica shell provide a R factor higher with respect to all the others and are definitely well stable. The stability of the mentioned SiAuNRs was also tested using the condition of real

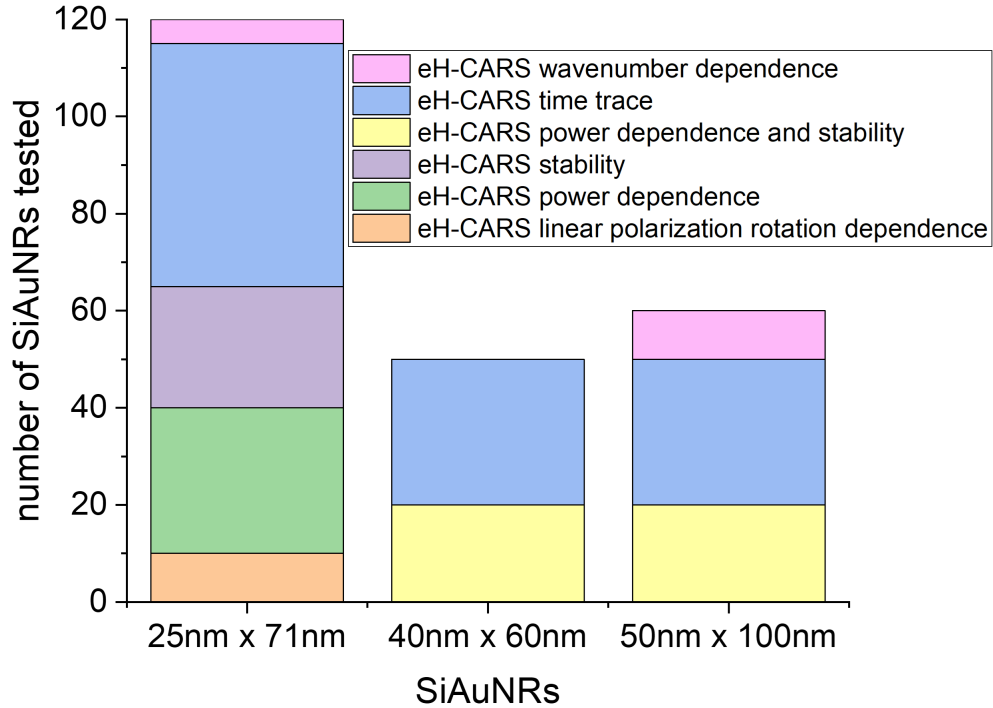


Figure 5.39: Bar plot providing a visual representation of the number of particles investigated during the various characterizations. Distinct particle groups are shown on the x-axis, with the height of each colored box within the columns representing the number of particles characterized with the corresponding measurement. Each color denotes a specific characterization method, providing a visual overview of the distribution of analyses across different particle groups. Example: Among the nominal 50nm×100nm SiAuNRs group, a total of 60 rods underwent characterization. Specifically, 10 of these rods were specifically utilized for the eH-CARS wavenumber dependence characterization.

sensing measurements, where the laser beams remained for a certain amount of time on the SiAuNRs. Similar considerations about the different particles stability were drawn.

The results presented in this Chapter were obtained from measurements on individual particles, which represent on average the particle behavior. Figure 5.39 reports an overview of the number of particles, for each group, used for the different characterizations, and that gave results in agreement with the ones shown. Distinct particle groups are shown on the x-axis, with the height of each colored box within the columns representing the number of particles characterized by the corresponding measurement. Each color denotes a specific characterization method, providing a visual overview of the distribution of analyses across different particle groups. Via COMSOL modeling, we studied the various $\chi^{(3)}$ contributions from both the resonant and non resonant material present in the focal volume, i.e. the NP gold core, the silica shell, and the resonant oil. Additionally, we compared simulated and experimental LFE eH-CARS wavenumber dependence. From this comparison, we were able to infer the value of the third order susceptibility of gold. In fact, in the

literature, the reported values of the third-order susceptibility of gold span over several orders of magnitudes. This is due to the various techniques utilized to measure the gold third order nonlinearity, which employed different laser pulses durations, thus probing different contributions to the gold nonlinear response over various time scales. Overall, this work demonstrated that LFE eH-CARS can be achieved with SiAuNRs, and simulations showed local enhancement factors in the order of 1000 at the nanorod tips.

Chapter 6

LFE eH-CARS, TPF, SHG with AuNBs

Cell membranes are laterally heterogeneous systems at the submicrometer scale. The nanoscale spatial arrangement and diffusion patterns of membrane lipids and protein components contribute to organize functionalities within the bilayer. These functionalities are related to processes like transmembrane signaling, intracellular trafficking, and cell adhesion (Ref.[142]). The lipid nanodomains (or rafts) hypothesis, first formulated by Simons and Ikonen in 1997 (Ref.[143]), emerged as a way of explaining the lateral membrane inhomogeneity. The operational definition of lipid rafts proposed the presence of dynamic clusters of sphingolipids and cholesterol, occurring over a wide range of timescale (Ref.[144]) in terms of both lateral mobility and association-dissociation. Upon specific interactions, they organize themselves forming functionally important and relatively ordered membrane regions, recruiting other lipids and proteins (Ref.[145],[146],[147]). The dimensions of such membrane regions are thought to be below the optical diffraction limit (10 nm-200 nm). Obviously, the detailed properties (size, lifetime, stability) and compositions of domains are intrinsically context-dependent and reflect the specifics of the membrane in which they arise (Ref.[148]). Nowadays, the evidence of lipid raft formation was confirmed for example via Förster resonance energy transfer (Ref.[149]), interferometric scattering microscopy (Ref.[150]) and atomic force microscopy (Ref.[151]) by studying model membranes, like giant unilamellar vesicles (GUVs). They are essentially large, single-layered lipid vesicles with diameters typically ranging from a few micrometers to tens of micrometers. Although GUVs can be prepared to contain proteins within their lipid bilayers, they results in oversimplified systems compared to biological cell membranes. Fluorescence microscopy, employing a variety of fluorophore-labeled lipids, also enables the visualization of domains within lipid membranes (Ref.[152]). Moreover, fluorescence correlation spectroscopy has been exploited to detect nanodomains in living cell membranes (Ref.[153]). However, there are significant drawbacks to this approach, notably photobleaching and the potential disruption of the natural lipid behavior due to the introduction of fluorescent markers. For instance, it has been observed that several lipids with a preference for specific membrane domains, such as sphingolipids and sterols, which stems from their molecular structure, fail to segregate into ordered phases when labeled with fluorescent markers, in contrast to their unaltered counterparts (Ref.[154]).

Numerous studies have indicated that lipid rafts serve as domains within the cell membrane where specific signaling molecules, including receptors, have a propensity

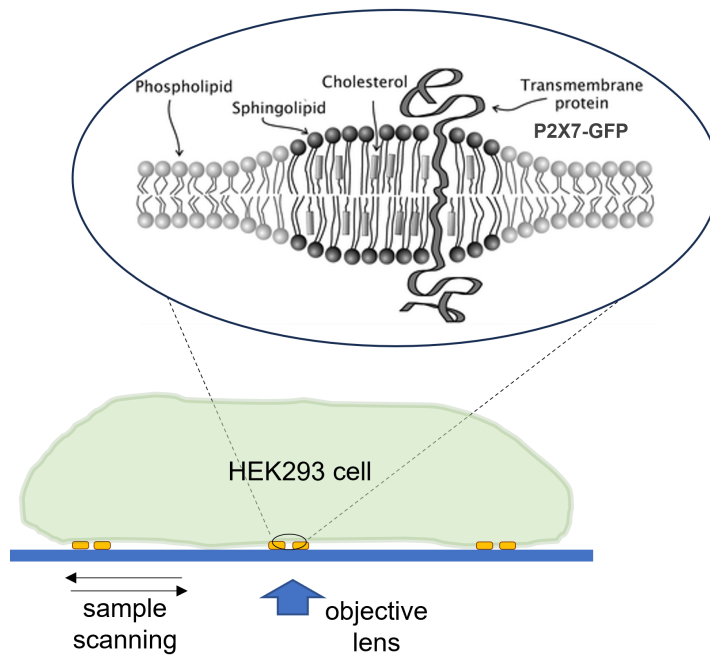


Figure 6.1: Sketch of the sample used in Chapter 6.4.2. HEK293 cells expressing C-terminally GFP-His-tagged rat P2X7 receptors are seeded onto a microscopic coverslip containing multiple AuNB nanoantennas. The inset (adapted from Ref.[1]) shows P2X7 associated with a membrane region that is enriched in sphingolipids and cholesterol (liquid ordered phase).

to aggregate (Ref.[155]). For instance, research has demonstrated the association of P2X7 receptors with lipid rafts enriched in cholesterol. The P2X7 receptor possesses a unique structural configuration linked to a mechanism of action that remains incompletely understood, facilitating the permeability of large ionic molecules either through the receptor itself or neighboring membrane proteins (Ref.[156]). Presently, this receptor is the subject of extensive research as a potential therapeutic target due to its involvement in numerous disorders related to inflammation, immunity, and cell death. P2X7, like its family members, employs adenosine triphosphate (ATP) as a ligand. Intriguingly, P2X7, to become activated, necessitates high levels of ATP, which are typically absent under physiological conditions, to become activated and play a role in cellular damage signaling (Ref.[157]). P2X7 is predominantly described as a receptor situated on the cell's surface, implying its integration into the outermost layer of the cell membrane. The precise location of this receptor within the plasma membrane is of significant importance, particularly concerning other proteins involved in ATP transport and metabolism. Notably, the receptor has been reported to exist in various regions within the cell membrane, encompassing lipid rafts, the apical and basolateral membranes, and even within intracellular compartments. Although P2X7 has an ambiguous mechanism of action, there is a general consensus that the receptor is consistently associated with inflammation (Ref.[158]). In addition, it has more recently been related to thrombosis, fibrosis, tumor progression and neuronal disorders (Ref.[159],[160]). After demonstrating the capability of our AuNBs to identify moving entities in the nanostructure proximity (see Section 6.3), Section 6.4 introduces preliminary findings about an alternative approach for detecting the association of P2X7 receptors with lipid rafts in the membranes of

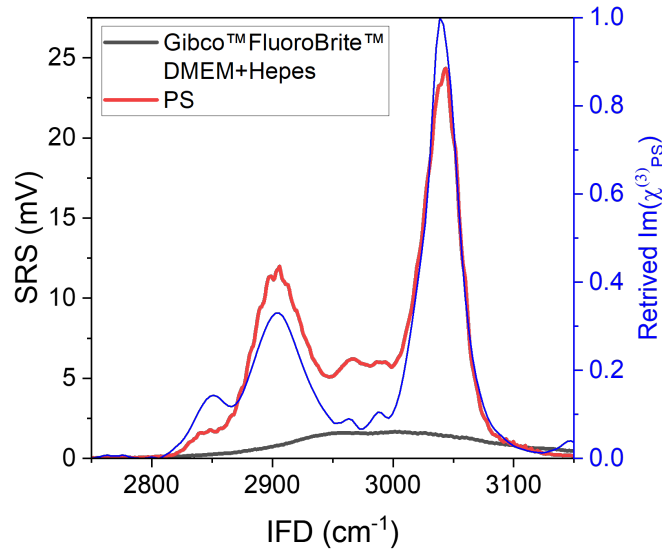


Figure 6.2: Measured SRS spectra of polystyrene (PS) and Gibco™ FluoroBrite™ DMEM. Spectra acquired tuning the OPO to have $\text{IFD}_c = 2950 \text{ cm}^{-1}$ and scanning the pump-Stokes delay over 500 ps. As the relative peaks intensities observed are affected by the pump-Stokes overlap from the spectral focusing method and temporal ordering for $\text{IFD} > 2950 \text{ cm}^{-1}$, we also plotted here for comparison the retrieved, normalized $\Im(\chi_P^{(3)} S)$ adapted from Ref.[161].

living cells.

6.1 Time trace measurements procedure

The multimodal microscope introduced in Chapter 3.3 allows us to measure the extinction cross-section and to acquire simultaneously eH-CARS or SRS with fluorescence, and SHG signals, simply by changing the illumination and detection path. More precisely we have two fluorescence channels with different detection filter ranges, the first detecting green wavelength (indicated in the following with TPF) and the second detected more red shifted wavelength (indicated in the following with RED). Thus the setup provides a convenient switch from the extinction cross-section measurements to correlative time trace measurements, without having to remount the sample. In fact, the excitation can be switched from a white-light to laser source and the detection from the sCMOS camera (used for wide-field extinction) to the dual-polarization balanced PDs (used for eH-CARS) or to a PD (used for SRS) together with the lock-in amplifier, as well as PMTs (used for fluorescence). As mentioned in Chapter 3.2, when using the AuNBs, a $\sim 3 \mu\text{l}$ PS drop is placed next to the nanostructures area. This is needed for the spatio-temporal alignment of pump, Stokes and reference beams, used for SRS and eHCARS. As shown in Fig.6.2 the polystyrene material is characterized by a first Raman peak at $\text{IFD} = 3050 \text{ cm}^{-1}$ and a second one at $\text{IFD} = 2904 \text{ cm}^{-1}$. Additionally, it is shown the comparison with the Gibco™ FluoroBrite™ DMEM SRS spectrum, used as media in the experiment with cells, which is not characterized by any evident sharp Raman peak. Still, it has an SRS contribution probably due to water with a resonant tail and some organic

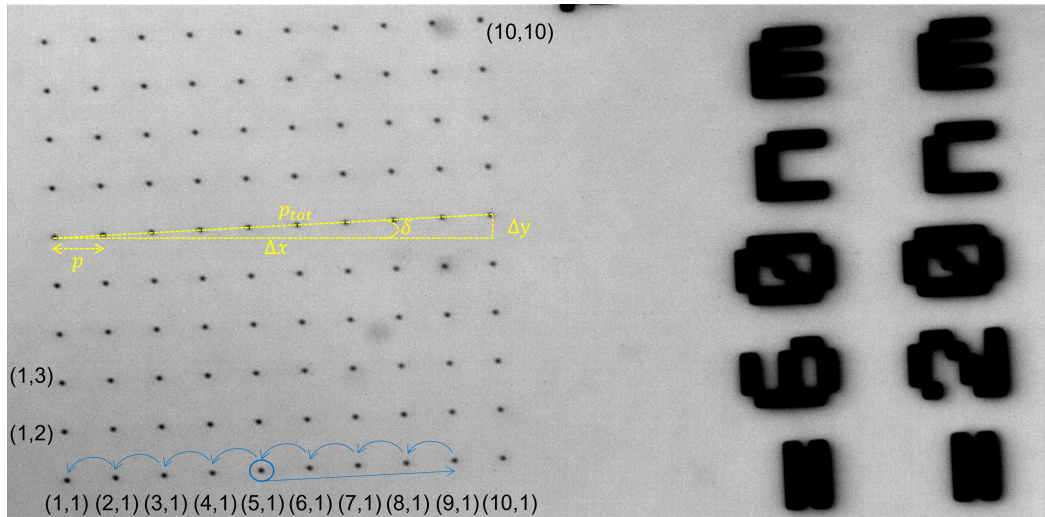


Figure 6.3: Transmission wide-field image of an AuNBs array with indication about how the periodicity and orientation are determined (yellow) and the order followed to successively and automatically measure nine nanoantennas in a row (blue).

component in the medium. The PS SRS spectrum has been acquired by tuning the OPO to have $\text{IFD}_c=2950 \text{ cm}^{-1}$ and scanning the pump-Stokes delay over 500 ps. As the relative peaks intensities observed are affected by the pump-Stokes overlap from the spectral focusing method and temporal ordering for $\text{IFD}>2950 \text{ cm}^{-1}$, we also plotted here for comparison the retrieved, normalized $\Im(\chi_P^{(3)}S)$ adapted from Ref.[161].

The SRS and eH-CARS measurements presented in the following sections were performed by selecting one of these two mentioned IFD. At the beginning of each session of measurements, the calibration of the IFD, in SRS modality, and of the epi-CARS signal versus reference delay in eH-CARS modality were carried out (see calibration in Chapter 3.3.2). Each IFD was selected by both tuning the IFD_c addressed by the OPO idler, used as Stokes beam and tuning the pump-Stokes overlap with the spectral focusing method. Table 6.1 reports the pump wavelength, the IFD_c and the consequent Stokes and CARS wavelengths used for each IFD. After

IFD (cm^{-1})	Pump (nm)	IFD_c (cm^{-1})	Stokes (nm)	CARS (nm)
2904	820	2950	1080	660
3050	820	3100	1099	653

Table 6.1: IFD (cm^{-1}), pump wavelength (nm), IFD_c (cm^{-1}), Stokes wavelength (nm), CARS wavelength (nm) used within this Chapter.

the setup calibration on the PS drop, the sample nanostage is moved to the nanoantennas area and the exact array periodicity and orientation were determined (see Fig.6.3, yellow indication). This allows us to measure successively and automatically all the nanoantennas in a row. In live-mode transmission and looking at one row in the array, the nanostage is moved to determine the distance between PSF center point of the edge antennas. More specifically, we determined the Δx and Δy shifts separating such antennas, to then compute the orientation δ of the array as mounted in the microscope sample holder. Ideally, this angle should be zero, but in

practice, it turns out to be challenging to reach such value due to the mounting by hand of the coverslip onto the microscope slide. Once determined Δx and Δy , δ is computed as

$$\delta = \arctg\left(\frac{\Delta y}{\Delta x}\right) \quad (6.1.1)$$

and consequently the distance between the two edge antennas (p_{tot}) and the exact array periodicity in the x direction (p) can be found as

$$p_{\text{tot}} = \frac{\Delta x}{\cos(\delta)} \quad (6.1.2)$$

and

$$p = \frac{p_{\text{tot}}}{n - 1} \quad (6.1.3)$$

where n is the number of the AuNBs in the row (i.e. 10). Within the same array, every particle is labeled with a unique identifier depending on its position in the array with the bottom left particle being (1,1) and the top right being (10, 10) (see Fig.6.3 for some examples). After this setup calibration procedure, the session of measurements starts following the steps described below.

1. Prior to any laser exposure, a wide-field extinction measurement is performed on the AuNBs array understudy (as described in Chapter 4.2), to extract the extinction cross-section of each AuNB.
2. A 3D eH-CARS centering measurement is carried out by scanning $2 \mu\text{m}$ in x-, y-, and z-direction around the central nanoantenna of the selected row (for example nominal (5,1), circled in blue in Fig.6.3). Based on this acquisition the nanostage is moved to bring the antenna in the laser focus and in the central position on the xy-plane, such that the LFE eH-CARS signal can be optimized. From this point to the end of the acquisition on the selected row, the nanostage is programmed to move sequentially, according to the calculated AuNB positions..
3. A 2D eH-CARS image ($2 \mu\text{m} \times 2 \mu\text{m}$) is successively acquired for all the AuNBs in the row, following the order indicated with the blue arrows in Fig.6.3.
4. 20s-long time traces are recorded successively at the nanoantenna sites, using 0.1 ms sample period which was later downsampled for the analysis.
5. Again a 2D eH-CARS image ($2 \mu\text{m} \times 2 \mu\text{m}$) is acquired for all the AuNBs in the row. This repeated passage is needed to check whether the presence of slow mechanical drifts might have affected the LFE eH-CARS signal recorded in the time traces.
6. The procedure from point 2 involving the laser is repeated for the next nanoantennas rows.
7. Finally a wide-field extinction measurement is performed for extinction cross-section comparison before and after the laser exposure.

The measurements involving the laser beams were carried out employing a linearly polarized excitation aligned along the longitudinal axis of the AuNBs. Thus, prior to starting the measurements, the optimized rotation of the $\lambda/2$ wave plate was found and the signal provided by each AuNB was detected in the nominal eH-CARS horizontal channel.

6.2 Control sample

Prior to testing the ability of the designed AuNBs to sense sub-micron objects moving in their proximity, the nanostructured coverslip was placed in an imaging gasket filled with Gibco™ FluoroBrite™ DMEM with 25 mM HEPES. This sample is needed to have an understanding of the background fluorescence and eH-CARS signal provided by the nanoantennas.

We performed fluctuation correlation analysis between LFE eH-CARS, nominal SHG, and fluorescence. Fluorescence was measured at two wavelength detection ranges, namely the green 500 nm-560 nm range indicated with "TPF", and a red-shifted 560 nm-620 nm range indicated with "RED". The latter was detected by exploiting the F-CARS detection channel in Fig.3.18, substituting the original filter with a different one which allows the detection of wavelengths longer than 540 nm. Importantly, such filter blocks the OPO reference used for eH-CARS at around 660 nm (see Chapter 3.3.3).

Figure 6.4 gives a representative correlative time trace acquired onto this control sample, selecting $\text{IFD}=2904\text{ cm}^{-1}$, and exciting power at the sample $P_P=0.86\text{ mW}$ and $P_S=1.84\text{ mW}$. Within this sample, measurements were sequentially carried out on 100 antennas.

Especially because of the complexity of the experiment, when measuring a correlative time trace on a nanoantenna it is essential to define criteria that help to assess the reliability of the measurements. The 2D LFE eH-CARS images and the extinction cross-section spectra acquired before and after the correlative time traces, as mentioned in Sec.6.1, are needed to better understand the signal recorded in the time traces. Before attributing any variations in these signals to the presence of an object near the antenna, it is essential to verify that the signal changes are not a result of potential damage to the antenna during laser exposure or antenna displacement caused by mechanical drifts in the experimental setup. Moreover, when measuring the eH-CARS two additional aspects have to be taken into account:

- The epi-CARS generated signal is measured via heterodyne detection, employing the interference with the reference beam and the balanced photodiodes. Therefore, it is necessary to check that the photocurrents remained balanced during the measurement.
- The setup is typically used in sample-scanning modality, i.e. the nanostage is moved while maintaining the laser in a fixed position. The laser-scanning modality can be used to perform SRS, F-CARS, and fluorescence measurements, thanks to galvo mirrors moving the beams in x- and y- directions. Such mirrors are placed before the entrance of the microscope. However, the laser-scanning modality cannot be applied for eH-CARS measurements within our setup, as varying the direction of the pump and Stokes beams changes the spatial overlap between the epi-CARS signal and the reference beam, significantly affecting their interference and in turn the eH-CARS detection. Thus, once the optimized alignment of the galvo mirrors is found to maximize such interference, they should not be moved. Due to electrical instabilities of the setup, it turned out that in some sessions of measurements, the galvo mirror moving the beam in the x-direction was subjected to unwanted fluctuations of its position during the time trace. This resulted in drops of the consequent eH-CARS detected signal. For this reason, the data recorded while galvo mirrors instabilities were taking place have to be considered unreliable. The galvo

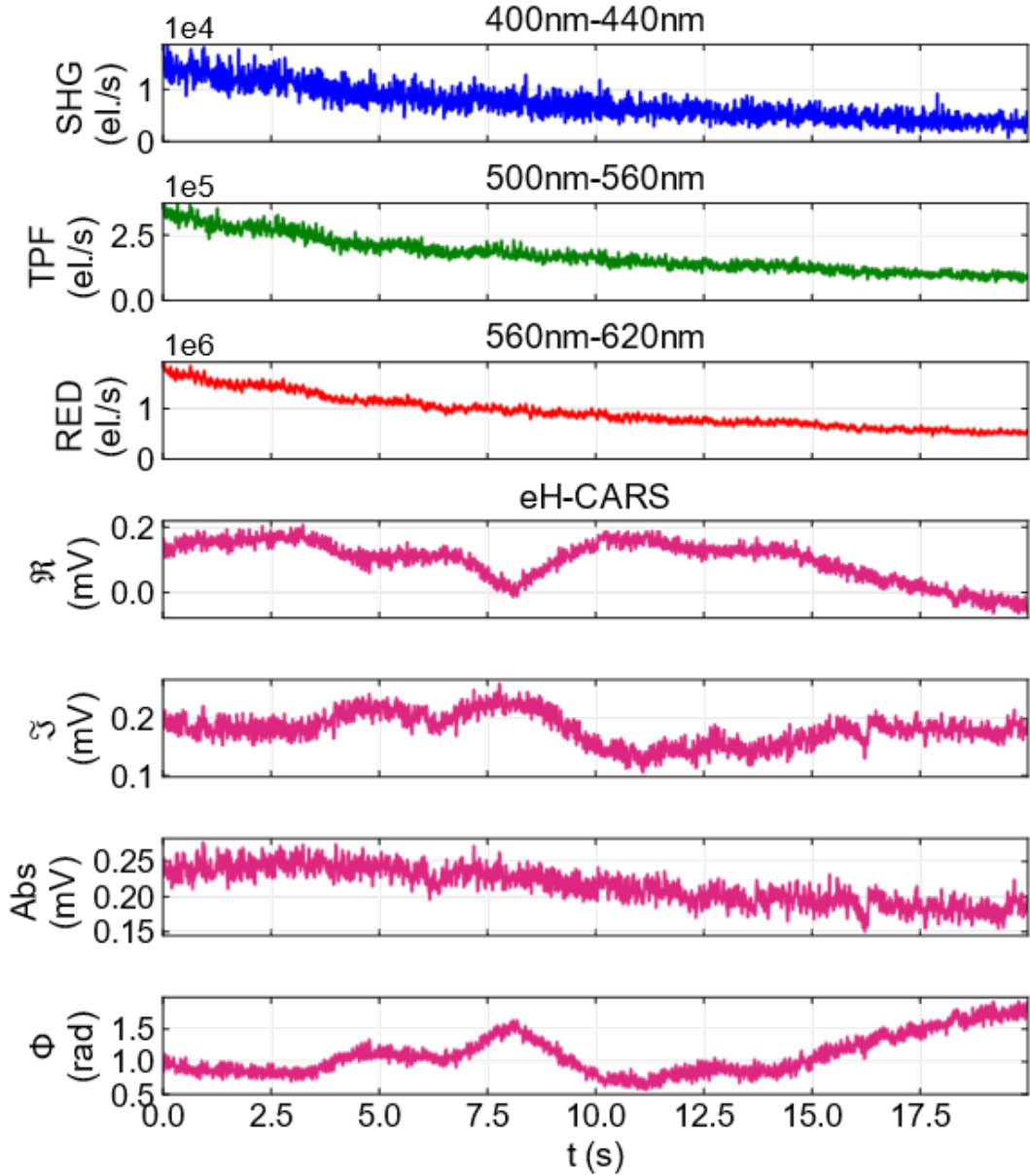


Figure 6.4: Representative fluctuation correlation time traces between (from top to bottom rows) nominal SHG-, TPF-, and eH-CARS signal (real component (\Re), imaginary component (\Im), amplitude (Abs) and phase (Φ)). Sample: AuNBs surrounded by Gibco™ FluoroBrite™ DMEM with 25mM HEPES. Time traces of 20 s (as indicated) were recorded with 0.1 ms sample period at the antenna's site and downsampled to 10 ms. IFD=2904 cm^{-1} . Exciting power at the sample: $P_P=0.86$ mW and $P_S=1.84$ mW. For the PMTs channels, we reported an indication of the detected bandwidth for clarity. See reliability check in Fig.6.5.

mirrors employed in the setup (Galvo scanner H6210 from Cambridge Technology (CTI)) have sensors that provide their position, enabling to check if instabilities have occurred. Positions are digitally recorded by the software only if the galvo is moved, therefore a very small shift of pump and Stokes beams was set enabling recording during the scan, without affecting the detected eH-CARS. This shift was around 10 nm in steps of 3 nm.

Furthermore, similarly to the discussion in Chapter 5.5, a quantitative analysis of the eH-CARS signal needs compensation for the reference beam fluctuations. Thus, the complex eH-CARS signals are corrected by the summed absolute BPD currents:

$$S = S_d \frac{\langle i_\Sigma \rangle}{i_\Sigma} \quad (6.2.1)$$

where $S_d(S)$ here represents the detected (corrected) either $\Re(\text{eH-CARS})$ or $\Im(\text{eH-CARS})$, $i_\Sigma = \sum_{n=1}^4 i_n$ and $\langle i_\Sigma \rangle$ is the average value of i_Σ .

Figure 6.4 is organized so that from the first to the third row, the nominal SHG-, TPF-, RED- channels are displayed. At the bottom, we find the eH-CARS related channels. More precisely we reported both the real (\Re) and imaginary (\Im) components, corrected for the reference fluctuations (Eq.6.2.1) and the corresponding field amplitude (Abs) and phase (Φ). We chose to plot the real and imaginary components of the eH-CARS signal as they are the quantities that we directly detect hence they have a well-defined noise.

Figure 6.5 illustrates the four criteria that have been established to determine the reliability of the measurement associated with the data presented in Fig.6.4. Panel (a) in Fig.6.5 shows the previously described 2D eH-CARS images acquired before and after the time traces. These data indicate whether the nanoantenna did or did not significantly drift in position during the measurement and whether the maximal signal amplitude had changed significantly, possibly indicating that the nanoantenna was damaged during the laser exposure. Also, the single-particle extinction cross-section spectra in panel (b) indicate possible structural changes in the nanoantenna modifying its spectral line shape. Panel (c) reports the recorded position of the galvo mirrors during the time trace so that any fluctuation from the nominal position can be clearly visible. Finally, panel (d) shows both the individual currents (i_0, i_1, i_2, i_3) of the four balanced photodetectors (left scale) and $\bar{i} = \frac{i_\Sigma}{\langle i_\Sigma \rangle}$ (right scale) used to correct the eH-CARS signals for reference fluctuations. The currents being symmetric around 0 indicates that they are indeed balanced. The sum of the absolute currents indicates any fluctuation originating from the excitation lasers and allows us to tell them apart from relevant fluctuations caused by the environment around the nanoantennas.

For all the correlative time traces, acquired at antenna's site and shown within this work, the four criteria have been checked and the results of such controls are reported in Appendix A.

The nominal SHG-, TPF-, and RED- channels of Figure 6.4 are affected by a background which was slowly decreasing over time. Such background was generally present in all the measurements performed on different antennas. It can be related to the thermal emission in the visible from the hot electron gas associated with the nanoantennas. In fact, the effective thermal electronic temperature can vary from 2000 K to 4000 K (Ref.[162]) upon ps pulsed-laser excitation. The value of the background depends on the specific characteristics of each antenna, which can differ from others due to fabrication defects. A similar behaviour is seen in the

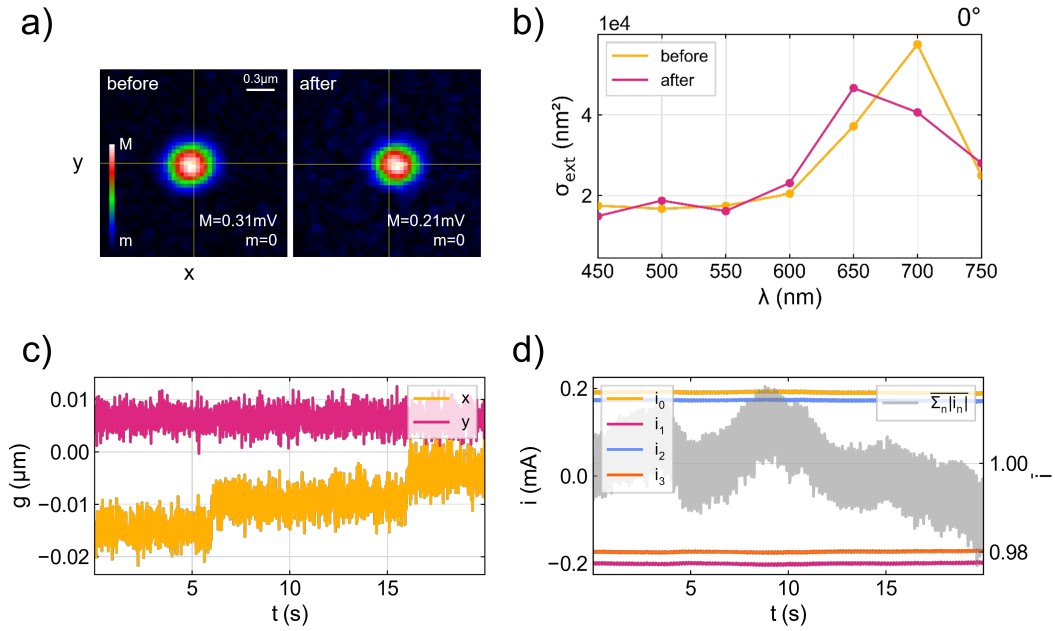


Figure 6.5: Four criteria to be checked to consider the correlative time trace recorded (shown in Fig.6.16) at the antenna as reliable. (a) A 2D eH-CARS amplitude image ($2\mu\text{m} \times 2\mu\text{m}$) measured at the AuNB focus, before and after the correlative measurement, shows that the antenna remained reasonably centered (yellow cross) during the time trace. Rainbow scales from m (black) to M (white) as indicated. Exciting power at the sample: $P_P=1.2\text{mW}$ (pump) and $P_S=4\text{mW}$ (Stokes). (b) Single particle extinction cross-sections, measured before and after the laser exposure, show that the antenna was not affected by significant structural changes during the laser exposure. (c) Galvo mirrors positions (along x and y directions) recorded during the time traces, to visualize possible instabilities affecting the recorded signal. (d) Four BPD currents (i_0, i_1, i_2, i_3) recorded during the time trace measurement were balanced (symmetric around the x -axis). Additionally, the $\bar{i} = \frac{i_\Sigma}{\langle i_\Sigma \rangle}$ used to correct the recorded time trace eH-CARS is shown.

eH-CARS amplitude over time, where we recorded a decrease of the initial signal value of the 40%. The phase displays slow fluctuations caused by the mechanical drift taking place, with a final value different from the initial one, explained by the occurred LSPR shift (see Fig.6.5(b)). The slow decreasing trend present in all the fluorescent and eH-CARS amplitude channels can be explained considering both the mechanical drifts that always affect the measurements, making worse the focusing condition (see Fig.6.5(a)), and possibly by the rounding up of the triangular structure forming the antennas, due to the laser exposure, which causes typically a blue shift of the extinction spectrum (see Fig.6.5(b)).

In the Appendix A.2, we present two reliability checks that lead us to exclude the corresponding time traces due to either conspicuous mechanical drifts (Fig.A.2) or significant particle damage (Fig.A.3).

6.3 PS beads

We first tested the ability to use the designed AuNBs for chemical sensing via LFE eH-CARS of sub-micron objects, namely PS beads, moving in their proximity with the samples described in Chapter 3.2.2.

6.3.1 Fluctuation correlation analysis: SRS vs SHG, and fluorescence

Prior to measure on the antennas, we performed fluctuations correlation analysis between SRS signal and nominal SHG, TPF, and RED fluorescence. Pump and Stokes beams were focused in a region of the coverslip away from the nanoantennas and within the sample bulk volume, as none of the mentioned signals was detected in the epi-direction. These measurements were fundamental to understand if the prepared samples could allow us to detect well separated spikes related to single beads entering the laser foci. With the 200 nm PS beads, we prepared two kinds of samples exchanging the diluting solution from a 50% glycerol/water (v/v) to a fully DI water, to vary the diffusion time (see Chapter 3.2.2) of the PS beads in the probed area. Both samples have been tested and the results are reported in Fig.6.6 and Fig.6.10 respectively. In each figure, two representative 20 s time traces are shown. They were obtained by recording simultaneously the four detection channels, exciting vibrational resonances (IFD) at 2904 cm^{-1} and at 3050 cm^{-1} , as indicated. Relatively high pump and Stokes powers (reported in the legends) were employed to ensure the SRS detection. The sample period used for the acquisition was 0.1 ms, applying then a 10 ms binning for a better S/N. These figures, as the ones that follow in this Subsection, are organized so that from the first to the fourth row, the nominal SHG, TPF, RED fluorescence, and SRS channels are displayed. For the PMTs channels, we indicate the detected bandwidth for clarity. The event of beads encountering the laser focus is clearly visible by looking at the TPF and RED channels. The dynamics recorded in these channels are consistent with fluorophore excitation, emission, and photobleaching events. The TPF and RED fluorescence intensity ratio is consistent with the manufacturer's specifications. For the ratio estimation, we integrated the emission spectra curve provided by the manufacturer within the wavelength range selected by the two filters and we divided the resulting integrals obtaining ~ 6 which is of the same order of magnitude of the experimental one (~ 3 , see Fig.6.7). When the diluting solution is given by 50% glycerol/water

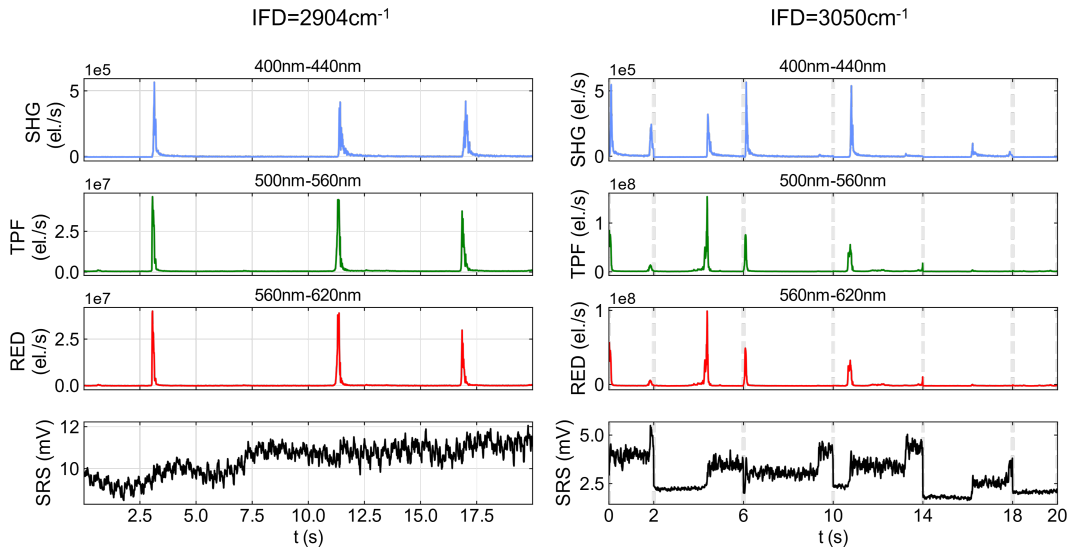


Figure 6.6: Representative fluctuation correlation time traces between (from top to bottom row) nominal SHG, TPF, RED fluorescence, and SRS signals. Sample: 200 nm diameter YG fluorescent PS bead in a 50% glycerol/water (v/v) solution. Time traces of 20 s were recorded simultaneously in the mentioned channels with 0.1 ms sample period, downsampled to 10 ms. Powers employed at the sample: $P_P=4.7$ mW and $P_S=12.29$ mW. (Left) $\text{IFD}=2904\text{ cm}^{-1}$, (Right) $\text{IFD}=3050\text{ cm}^{-1}$. For the PMTs channels, we reported an indication of the detected bandwidth for clarity.

(v/v) (Fig.6.6) and the IFD selected is at 2904 cm^{-1} (Fig.6.6-left), no correlation between the SRS signal and all the other channels is found. Additionally in this case the SRS background (due to the bulk material) is higher than the one obtained with the IFD at 3050 cm^{-1} (Fig.6.6-right). This is explained considering that at $\sim 2904\text{ cm}^{-1}$ the glycerol, in the diluting solution, presents a Raman peak (see Fig.6.8). Therefore, the SRS contrast between glycerol and polystyrene is sufficiently low to hide the detection of beads entering the focus in the SRS channel. Conversely, when a fully DI water diluting solution is used, the higher SRS contrast between the PS bead and the bulk material enables the detection of a well evident change of the signal when a bead enters the laser focus. Additionally, the SRS time-trace reveals that an optical trapping is taking place, so that for each spike recorded in the first three channels, a step in the SRS channel is found. Optical trapping is a physical phenomenon that occurs when a particle, the PS bead in our case, enters the path of the tightly focused laser beam and experiences a trapping force (\mathbf{F}_T). A detailed explanation of this phenomenon is beyond the scope of this work and can be found in Ref. [164],[165],[166]. Briefly, when the bead radius is much smaller than the wavelength of the laser beams involved, the bead itself can be treated as an electric dipole interacting with the external field. The optical force experienced by the bead is given by (neglecting a weak spin-curl force in fields of inhomogeneous polarization):

$$\mathbf{F}_T = \frac{1}{4} \Re(\alpha) \nabla |E_i|^2 + k \Im(\alpha) \frac{n}{c} \mathbf{S}_i \quad (6.3.1)$$

where \mathbf{E}_i is the input electric field, \mathbf{S}_i is the associated Poynting vector, k is the wavevector in the medium ($k = 2\pi/\lambda$) and α the bead polarizability. \mathbf{F}_T is therefore given by two contributions: the first term is called *gradient force* (\mathbf{F}_G) and the

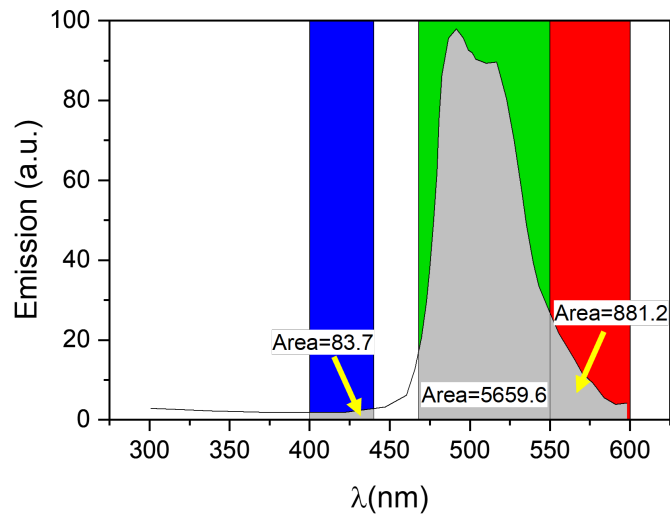


Figure 6.7: Specification emission spectra of YG Fluorescent Microspheres (adapted from Ref.[2]) where the bandwidth of the detection of SHG-, TPF-, and RED-channels are highlighted with the corresponding representative colors (blue, green, and red). The resulting integrals of the emission curve in the different regions are reported.

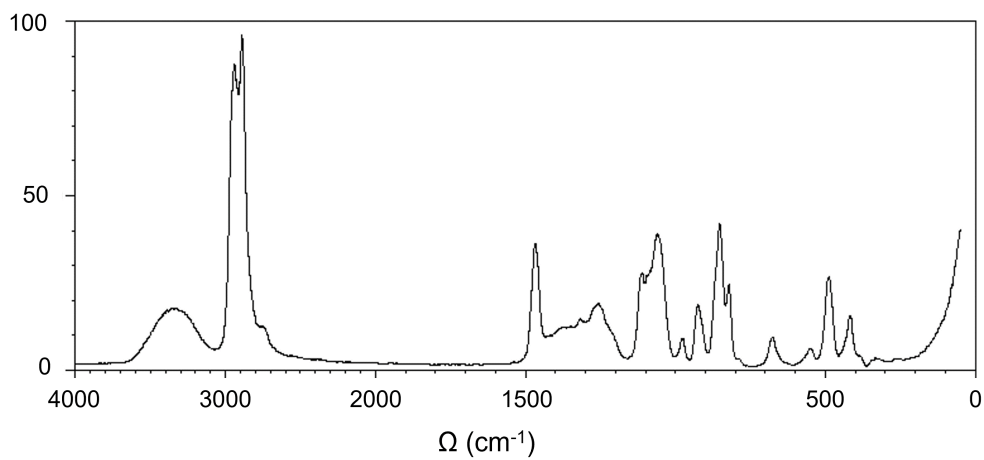


Figure 6.8: Raman spectrum of glycerol adapted from Ref.[163].

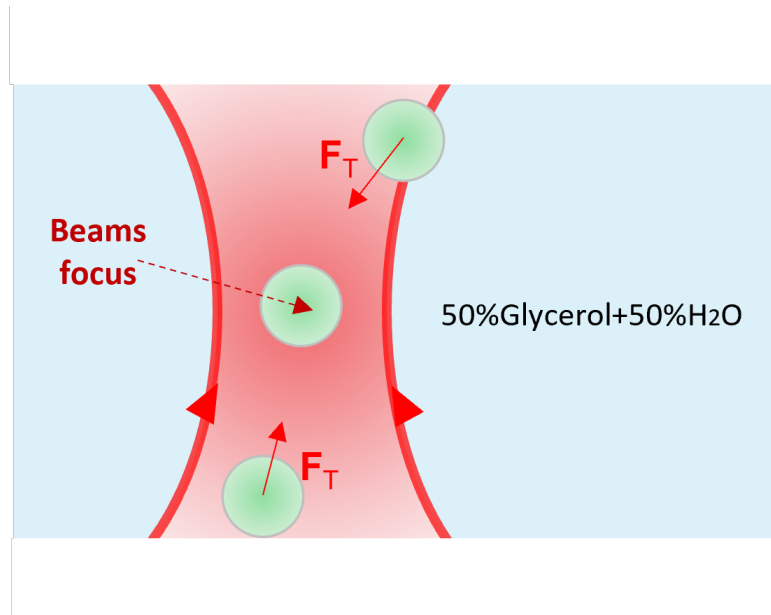


Figure 6.9: Illustration of the optical trapping taking place in a sample given by PS beads moving in a bulk medium and encountering a tightly focused beam.

second term is called *scattered force* (\mathbf{F}_S). The optical trapping is caused by \mathbf{F}_G , which is a conservative force as it arises from the potential energy of the dipole in the electric field. As the intensity of the field I_i is proportional to $|E_i|^2$, we can write

$$\mathbf{F}_G \propto \Re(\alpha)\nabla I_i \quad (6.3.2)$$

The PS beads in our experiment have a positive polarizability, thanks to their refractive index $n_{PS}=1.59$ higher than the bulk medium refractive index ($n_b \simeq (n_{H_2O} + n_{Gly})/2=1.4$), hence they are attracted towards the high-intensity region of the optical field (see Fig.6.9). \mathbf{F}_G is strong for high power and for laser beam tightly focused. Conversely, \mathbf{F}_S is not conservative as it arises from the transfer of momentum from the field to the particle, as a result of the scattering and absorption processes. It points in the direction of propagation of the incident light and is proportional to the field intensity (as the magnitude of the Poynting vector represents the intensity of the electromagnetic wave). A bead results efficiently trapped when $|\mathbf{F}_S| < |\mathbf{F}_G|$. In our measurements, the beads are affected by both pump- and Stokes-related \mathbf{F}_G . We can consider in first approximation that their contributions are similar as the pump is characterized by a lower power than the Stokes beam in our experiment, but thanks to its shorter wavelength, is more strongly focused. When one bead is trapped, it occupies space within the focal volume. To facilitate the trapping and detection of additional beads, the focal volume needs to be emptied from beads already trapped. For this reason, we performed the measurements with a different approach, namely the focal point of the beams was rapidly shifted in the x direction, of about $10 \mu\text{m}$, and, after a measurement period, returned back, using the galvo mirror. The gray grids displayed in Fig.6.6-right coincide with time at which the beam shift is applied. A slightly different SRS background level is found for the two galvo positions as the change in beam position and direction slightly affects the collection geometry. From Fig.6.6-right the following conclusions can be drawn:

- If no beads are present in the focal volume, when working with $P_P=4.7 \text{ mW}$

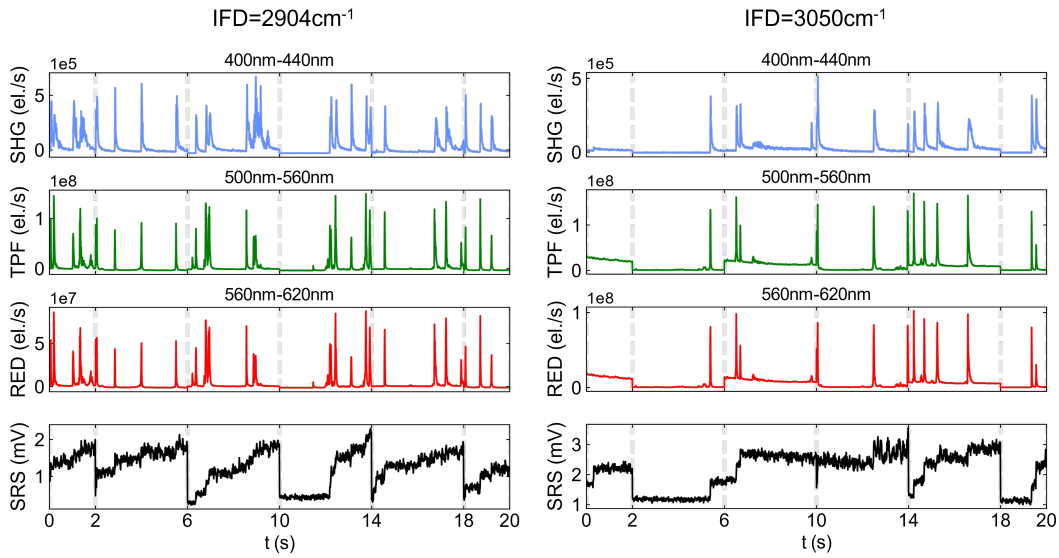


Figure 6.10: Representative fluctuation correlation time traces between (from top to bottom row) nominal SHG-, TPF-, RED- fluorescence and SRS- signals. Sample: 200 nm diameter YG fluorescent PS beads in fully DI water solution. Time traces of 20 s were recorded simultaneously (with 0.1 ms sample period) and downsampled to 10 ms. Powers employed: $P_P=4.7$ mW and $P_S=12.29$ mW. (Left) $\text{IFD}=2904\text{ cm}^{-1}$, (Right) $\text{IFD}=3050\text{ cm}^{-1}$. For the PMTs channels, we reported an indication of the detected bandwidth for clarity.

and $P_S=12.29$ mW, the typical SRS background level is around 2 mV;

- Once a bead is trapped, the SRS signal increases by about 1 mV;
- It is possible to trap two beads in the focal volume resulting in an SRS signal of about 4 mV.
- In some cases the step recorded in the SRS can be correlated to a spike (typically weak) in the SHG channel but no spikes in the other channels meaning that the fluorophore attached to the bead already went through photobleaching.

When using fully DI water (results in Fig.6.10 and Fig.6.11), it is clear looking at all the channels that we are able to detect a higher number of beads in a 20 s time trace, thanks to their faster diffusion speed. In this condition, both IFD selected allow the detection of the beads in the SRS channel as the glycerol, used in the previous case, is not present. The SRS signal from water (i.e. in the absence of a bead) is slightly higher for $\text{IFD}=3050\text{ cm}^{-1}$ which is closer to the water Raman resonance. The difference between Fig.6.10 and Fig.6.11 is in the pump and Stokes power employed. For $P_P=5.1$ mW and $P_S=11.73$ mW (Fig.6.10), it is possible to see how the trapping works for more than 2 beads (see time interval 2 s-6 s in Fig.6.10-left and time interval 14 s-18 s in Fig.6.10-right suggesting that 4 beads are trapped). This means that the laser beams are able to organize the position of the beads in the focal volume so that several are trapped. However, more beads appear to be passing near the focus, as it can be seen from the number of fluorescence spikes. When pump and Stokes powers are halved ($P_P=2.45$ mW and $P_S=5.96$ mW, Fig.6.11) the following considerations can be drawn:

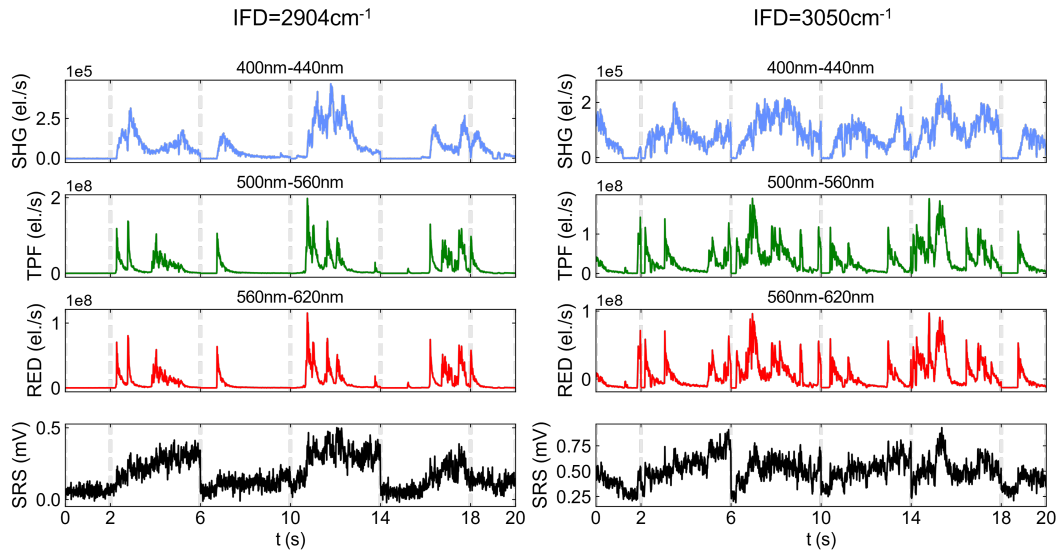


Figure 6.11: Representative fluctuation correlation time traces between (from top to bottom row) nominal SHG, TPF, RED fluorescence and SRS signals. Sample: 200 nm diameter YG fluorescent PS bead in fully DI water solution. Time traces of 20 s (as indicated) were recorded simultaneously with 0.1 ms sample period and downsampled to 10 ms. Powers employed: $P_P=2.45$ mW and $P_S=5.96$ mW. (Left) $\text{IFD}=2904\text{ cm}^{-1}$, (Right) $\text{IFD}=3050\text{ cm}^{-1}$. For the PMTs channels, we reported an indication of the detected bandwidth for clarity.

- As expected, the SRS signal from the PS beads as well as the SRS background signal from the bulk medium are reduced compared to the previous measurements. The latter remains still higher for $\text{IFD}=3050\text{ cm}^{-1}$ due to the water Raman resonance.
- The trapping is not as strong as before. The beams are not able to trap more than two to three beads, as can be seen in Fig.6.11-left. In the time interval 2 s-6 s, the first two beads entering the focus are well trapped and cannot escape from it. Instead, the third bead shows well-visible fluctuation in the photobleaching dynamics (see TPF and RED channels), suggesting it did not find an equilibrium position within the focal volume. Additionally in Fig.6.11-right, we find an example of SRS signal well correlated in its dynamics with the TPF and RED channels (see $t\sim 6$ s or $t\sim 15$ s). Related to these cases we may suppose the beads stayed in the focal volume only for an amount of time such that the photobleaching dynamics could start, but it escaped before completed.

Figure 6.12 reports two zoom-in of Fig.6.11-left and Fig.6.11-right respectively. In the following, Fig.6.12-left is used to derive important considerations about the physical origin of the signal recorded in the nominal SHG channel. The detection of an actual SHG signal can take place only when a non-centrosymmetric object interacts with the laser beam. Polystyrene is a centrosymmetric material hence PS beads should not provide SHG field if completely within the focal volume. However a bead could provide SHG signal if it finds an equilibrium position, possibly due to other beads already occupying the focal volume, such that only a part of the structure is within the focal volume, introducing a symmetry breaking (see Fig.6.13).

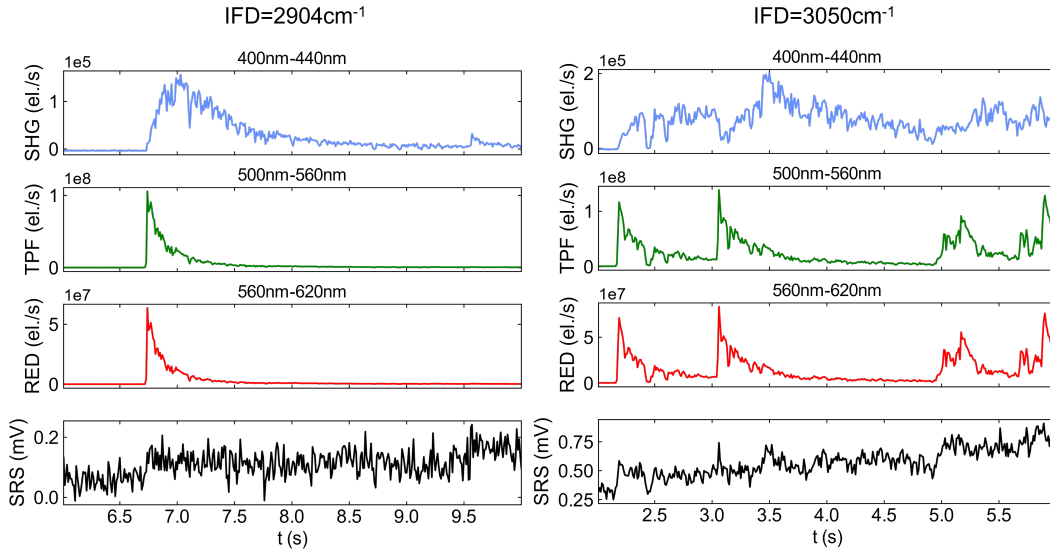


Figure 6.12: Zoom in into two intervals (indicated in the horizontal axis) of the representative fluctuation correlation time traces of Fig.6.11-left (left) and Fig.6.11-right (right)

The fluorescence and SRS channels in the time interval of Fig.6.12-left show that only one particle entered within the focal volume, in fact just one spike is detected in the fluorescence channels and a corresponding step in the SRS channel. The latter suggests also that the bead is well-trapped. This evidence therefore does not support the hypothesis of SHG signal coming from the interface of the bead. Alternatively, the signal recorded in the nominal SHG channel can be due to fluorescence, blue-shifted compared to the emission spectrum of the YG dye, as a consequence of the dye undergoing a photo-reaction which changes its structure (Ref.[167]). Generally, fluorescent dyes are made by conjugated systems. i.e. molecules that have alternated single and double bonds. The longer the conjugated length of the system, the longer the wavelength at which the dye absorbs and emits. A reduction of the conjugated length thus results in a blue-shift of the dye absorption and emission spectra. Comparing the signal detected simultaneously in the TPF and nominal SHG channels, we observe that they exhibit dynamics which are related to each other, namely the decay time of the green fluorescence channel appears equal to the rise time of the SHG. To better quantify this behavior we have described the TPF dynamics as an exponential decay (see Fig.6.14) of the form:

$$f_{\text{TPF}}(t) = A_{\text{TPF}} e^{-\gamma_1(t-t_0)} \quad (6.3.3)$$

where A_{TPF} is an amplitude factor, and t_0 is the time in which the decay starts ($t_0 \simeq 6.76$ s). The decay rate constant ($\gamma_1 \text{ s}^{-1} \simeq 5.8 \text{ s}^{-1}$) well describes the exponential growth recorded in the SHG channel. In the following interval of time, the blue-shifted fluorescence decays indicating that a subsequent photobleaching phenomenon takes place. Thus, the overall dynamics in the nominal SHG channel can be well described by the combination of an exponential decay and an exponential growth, i.e.:

$$f_{\text{SHG}}(t) = A_{\text{SHG}}(1 - e^{-\gamma_1(t-t_0)})e^{-\gamma_2(t-t_0)} \quad (6.3.4)$$

where A_{SHG} is the amplitude factor and $\gamma_2 (\simeq 2.4 \text{ s}^{-1})$ is the decay rate constant characterizing the second part of the dynamics. Interestingly, we see that around

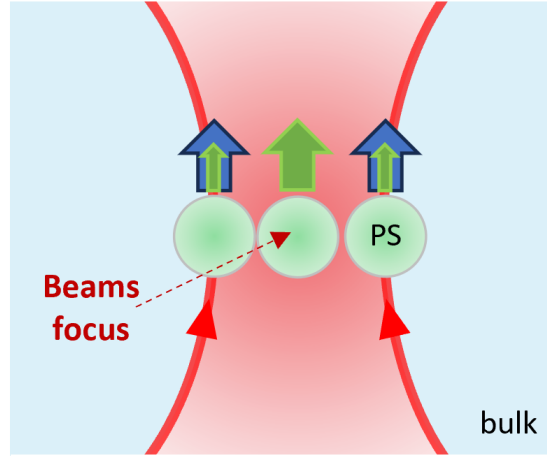


Figure 6.13: Illustration of a possible configuration where PS beads, moving in a bulk medium, encounters a tightly focused beam, emitting SHG signal (represented with the blue bold arrows) compared to the TPF signal (represented with the green bold arrows), which is anyway emitted by the bead. The TPF field reaches its maximum when the bead is at the center of the focal volume, i.e. where the pump beam intensity is maximum.

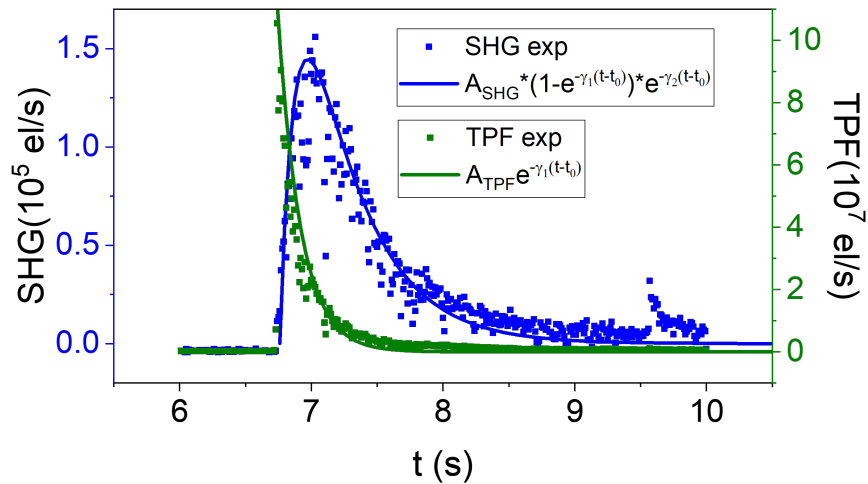


Figure 6.14: Nominal SHG- and TPF- channels of Fig.6.12-left fitted with Eq.6.3.4 and Eq.6.3.3 respectively. Parameters: $A_{\text{TPF}} \simeq 1 \times 10^8$ el/s, $A_{\text{SHG}} \simeq 1.5 \times 10^5$ el/s, $\gamma_1 \simeq 5.8 \text{ s}^{-1}$, $\gamma_2 \simeq 2.4 \text{ s}^{-1}$, $t_0 \simeq 6.76 \text{ s}$.

$t \simeq 9.6$ s, another weak peak appears in the SHG channel, followed again by an exponential decay. As this is not associated with any peaks in the TPF and RED channels, while we do see a step in the SRS one, we can attribute this peak to a PS bead, already photobleached, which enters the focal volume hence breaking the symmetry and generating 'true' SHG. In light of this discussion, the behaviour displayed in Fig.6.12-right can also be understood. Here, the first two beads entering the focal volume, at $t \sim 2.1$ s and $t \sim 3.1$ s, undergo photobleaching, which affects their emission in the TPF and RED channels. As in the previous case, the first photobleaching phenomenon changes the dye to emit in the blue-shifted channel and a rise in the SHG channel is observed with a rate equal to the decay in the TPF channel. Due to the short delay between the two beads, the fluorescence decay of the first bead in the SHG channel is not well visible, while for the second bead, the reduction of signal in time is clear. Additionally, in this zoom-in, we can see how, at these applied powers ($P_P=2.45$ mW and $P_S=5.96$ mW), the beams provide a weak trap. The fluctuation recorded in the fluorescence channels and a not well defined step in the SRS when the second bead arrives suggests that only one bead is trapped, i.e. the second bead has replaced the first in the focal volume. A third bead enters the focal volume at about $t \simeq 5$ s at which point a step in the SRS signal is observed, suggesting that two beads are now trapped. However, the third bead does not suddenly photobleach as the others. Also, the SHG behaviour is different from the previous cases. A possible explanation is that the position of the bead in the trap is unstable and the bead continues to move in and out of the focal volume, giving a TPF and RED fluorescence varying with its relative position with respect to the focal point and actual SHG signal from its interface when it is not completely within the focal volume. The SRS-fluorescence measurements reported in Fig.6.15, were taken using 100 nm PS beads diluted in a 50% glycerol/water (v/v) solution. Considering the smaller size of these beads, we tested them by selecting the IFD at 3050 cm^{-1} to have the strongest resonant peak of the polystyrene. While the fluorescence emission by the bead encountering the focal volume is strong enough to be detected, despite the high power used, the SRS signal is not strong enough to reveal the presence of the bead in the foci (the apparent SRS steps in Fig.6.15 left are attributed to the SRS background from water which is detected in a slightly different way due to the step-movements in galvo position, as explained previously).

6.3.2 Fluctuation correlation analysis: LFE eH-CARS vs SHG, and fluorescence

In this Section, we present the fluctuation correlation analysis between the signal recorded in the detection channels of LFE eH-CARS and SHG, TPF, and RED fluorescence when the laser beams are focused at AuNBs. The presented representative time traces show how using AuNBs allowed us to detect the presence of moving objects in their proximity. Both 200 nm and 100 nm PS fluorescent beads in 50% glycerol/water (v/v) solution were separately used with the AuNBs samples. Figure 6.16, Figure 6.17 and Figure 6.18 are organized as described for Section 6.2. The IFD and laser powers selected to perform the measurements are specified in the caption of each figure. Let us start with the sample prepared with 200 nm PS beads in 50% glycerol/water (v/v) solution. Figure 6.16 and Figure 6.17 display a representative time traces obtained setting $\text{IFD}=2904 \text{ cm}^{-1}$ and $\text{IFD}=3050 \text{ cm}^{-1}$ respectively. The corresponding reliability checks are reported in Appendix A.3. In both Fig.6.16 and

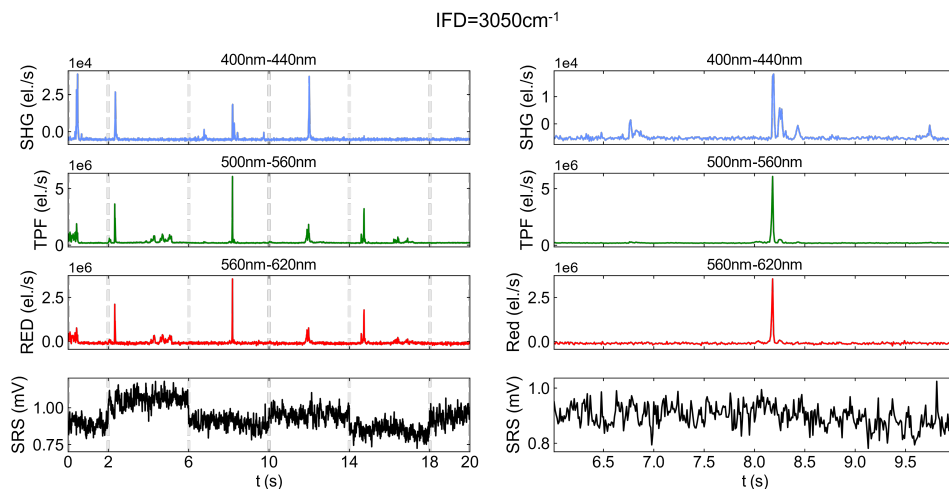


Figure 6.15: Representative fluctuation correlation time traces between (from top to bottom row) nominal SHG-, TPF-, RED- fluorescence and SRS- signals. Sample: 100 nm diameter YG fluorescent PS bead in a 50% glycerol/water (v/v) solution. Time traces of 20 s were recorded simultaneously with 0.1 ms sample period and downsampled to 10 ms. Powers employed: $P_P=5.12$ mW and $P_S=10.2$ mW. (Left) $\text{IFD}=2904$ cm^{-1} , (Right) $\text{IFD}=3050$ cm^{-1} . For the PMTs channels, we reported an indication of the detected bandwidth for clarity.

Fig.6.17, the background signal recorded in the SHG-, TPF-, and RED- channels can be related to the thermal emission in the visible from the hot electron gas associated with the specific nanoantennas. For example, we can notice that the AuNB in Fig.6.17 strongly emits in the TPF channel, giving less contrast when a bead passes by. However, the event of a bead moving around the antennas remains visible, independently from the selected IFD. The values of the signals recorded in the SHG, TPF, and RED channels associated with the beads are lower than the typical values seen in Sec.6.3.1, due to the lower laser power employed at the sample (Left: $P_P=0.76$ mW and $P_S=1.74$ mW, Right: $P_P=0.67$ mW and $P_S=1.21$ mW) to avoid damaging the antenna. Comparing the TPF and RED channels, we observe that the longitudinal surface plasmon resonance of the antennas, centered around 660 nm (see Fig.A.4 (b)), significantly enhances the red-shifted fluorescent emission of the bead, since the fluorescence intensity detected in the RED channel is higher than the intensity in the TPF channel, contrary to the manufacturer specifications (see Fig.3.10). Additionally, due to the several seconds spent by the beads at the antenna site, we can also hypothesize they get weakly trapped at the antenna. The signal recorded in the nominal SHG channel could be again attributed to the dye photobleaching dynamics. In fact, during the time interval 7.6s-9s of Fig.6.16 we can see that the SHG signal gradually increases until the bead escapes from the trapping. Alternatively, the signal recorded in the SHG channel could be attributed to the 'blue' tail of the fluorescence emitted by the bead, which can be enhanced by the transversal LSPR which characterizes all the antennas (see Chapter 4.2).

The exact dynamics of a bead entering the focal volume are not straightforward to explain. In fact, the presence of the antenna complicates the overall picture as different antenna-bead relative positions are likely to give different features to the

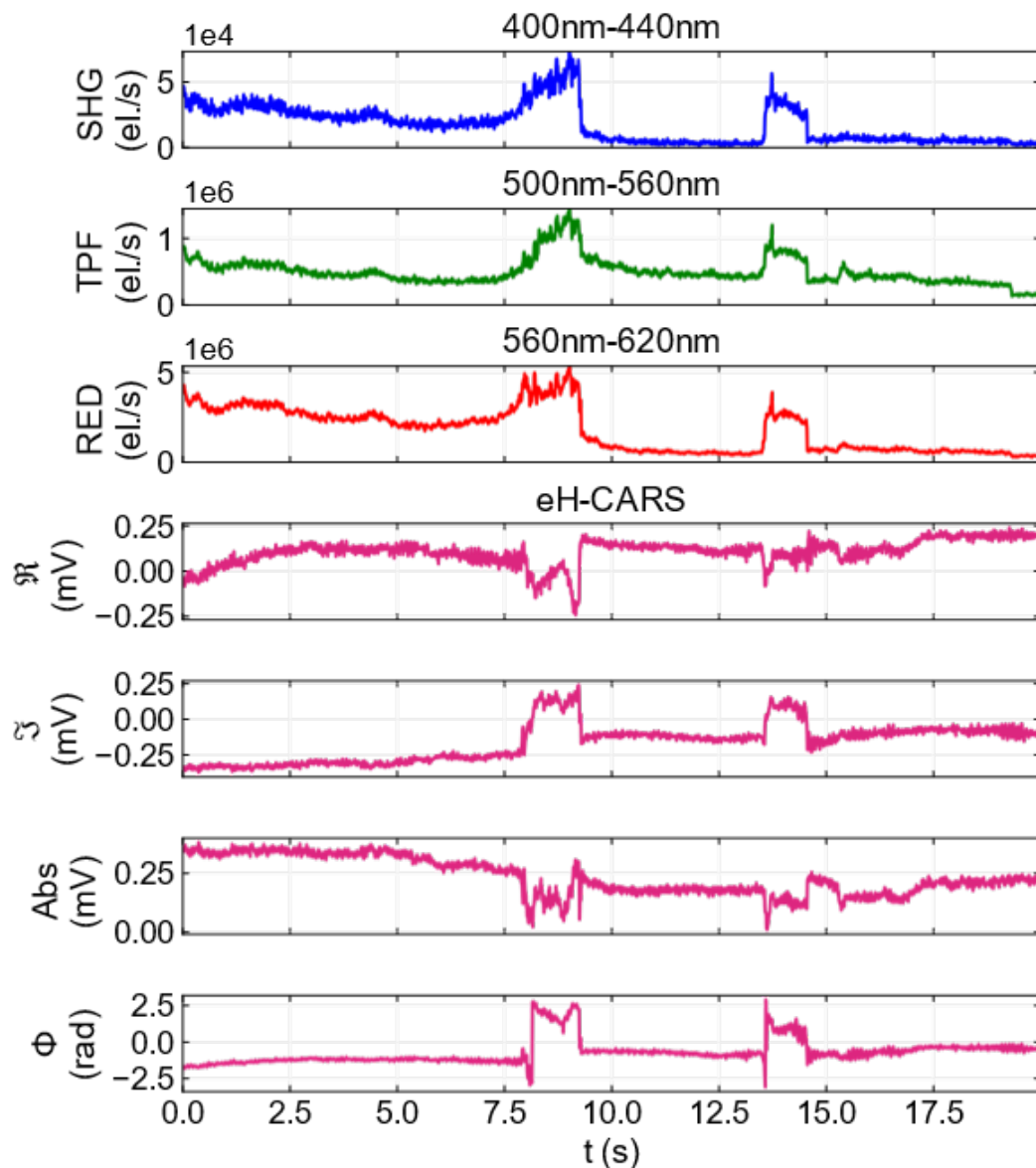


Figure 6.16: Representative fluctuation correlation time traces between (from top to bottom rows) nominal SHG-, TPF-, RED fluorescence and eH-CARS signal (real component (\Re), imaginary component (\Im), amplitude (Abs) and phase (Φ)). Sample: AuNBs sample with 200 nm diameter YG fluorescent PS bead in 50% glycerol/water (v/v) solution (see Chapter 3.2). Time traces of 20 s were recorded with 0.1 ms sample period at the antenna's site and downsampled to 10 ms. IFD=2904 cm^{-1} ; Exciting power at the sample: $P_P=0.76$ mW and $P_S=1.74$ mW. For the PMTs channels, we reported an indication of the detected bandwidth for clarity. See reliability check in Fig.A.4.

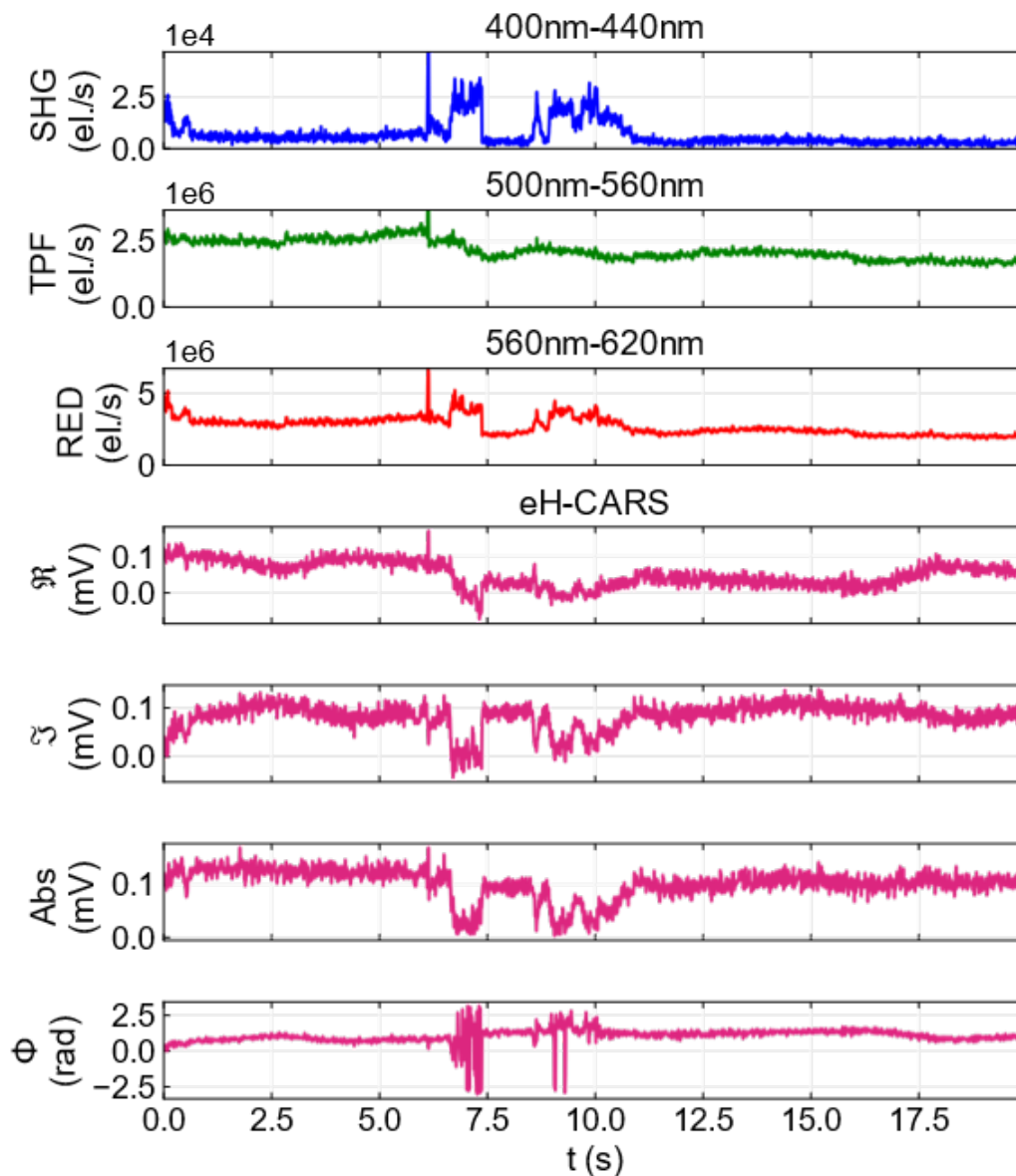


Figure 6.17: Representative fluctuation correlation time traces between (from top to bottom rows) nominal SHG-, TPF-, RED fluorescence and eH-CARS signal (real component (\Re), imaginary component (\Im), amplitude (Abs) and phase (Φ)). Sample: AuNBs sample with 200 nm diameter YG fluorescent PS bead in 50% glycerol/water (v/v) solution (see Chapter 3.2). Time traces of 20 s (as indicated) were recorded with 0.1 ms sample period at the antenna's site and downsampled to 10 ms. IFD=3050 cm^{-1} ; Exciting power at the sample: $P_P=0.67$ mW and $P_S=1.21$ mW. For the PMTs channels, we reported an indication of the detected bandwidth for clarity. See reliability check in Fig.A.5.

detected signal. Importantly, the variations of the signal in the first three channels are always correlated with fluctuations recorded in the eH-CARS channels. As in the case of the nanorods (see Chapter.5.6) due to the high $\chi^{(3)}$ associated with the gold material, the nanostructure emits itself a non-resonant FWM signal at λ_{CARS} . Thus, if no PS beads are passing by the antenna, at the AuNB we record FWM background signal stable in both amplitude and phase. This has been verified by measuring time traces onto a control sample where the antennas were surrounded only by Gibco™ FluoroBrite™ DMEM with 25mM HEPES, as shown in Section6.2(see e.g. Fig.6.5). The actual phase and amplitude values are strictly dependent on the specific antenna optical properties and independent of the IFD selected, as the signal arises from a non-resonant phenomenon. The measured eH-CARS field fluctuations correlated to variation in the fluorescence channels, experimentally shows that this signal originates from the bead CARS field. Notably, the measured eH-CARS field is an interference between the PS bead CARS and the antenna FWM field. The vibrationally-resonant CARS from the beads is characterized by a well-defined phase shift relative to the driving fields, which is different from the AuNB FWM field non-resonantly excited. Additionally, the interference between these fields depends on the bead-antenna relative position, which affects the relative phase, leading to either constructive or destructive interference.

We point out that the LFE eH-CARS signal measured at a AuNB allows us to detect a bead in the Raman-related channel also when the IFD selected is at 2904 cm^{-1} , contrary to the case of Fig.6.6-left. This is due to:

- the epi-detection employed, which allows us to be sensitive to interfaces rather than to the bulk material (dominantly emitting CARS in the forward direction) within which the beads are moving. In this way, the signal detected is strongly related to the interaction between the bead and the antenna and less affected by the Raman resonance of glycerol;
- pump, Stokes and CARS field enhancement at the antenna, which improves the detection of CARS field from the bead. In fact, the only epi-detection is not sufficient to enable the transient beads detection in the eH-CARS channel in the absence of the antenna. Such inability can be seen in Appendix A.4, where we show correlative time traces between SHG-, TPF-, and RED-channels and the eH-CARS channels, acquired focusing at the bulk-glass coverslip interface, in the absence of a AuNB, selecting IFD= 3050 cm^{-1} . The minimum pump and Stokes powers needed to detect spikes in the SHG-, TPF-, and RED- channels were approximately 1.4 mW and 2.5 mW, respectively (Fig.A.7). However, this level of power was insufficient to produce correlated spikes or fluctuations in the eH-CARS signal. Subsequently, we increased the powers to 5 mW and 11.5 mW, (Fig.A.8) but the eH-CARS signal still exhibited no discernible correlation with the other channels.
- the different resulting interferences between the antenna FWM field and the CARS field arising from the bulk medium versus the PS bead.

Similar consideration can be drawn for the results obtained with the AuNBs sample prepared with the 100 nm diameter PS beads in 50% glycerol/water (v/v) solution (Fig.6.18). The correlative time traces were acquired with IFD= 3050 cm^{-1} and actual powers at the sample focus equal to $P_{\text{P}}=0.63\text{ mW}$ and $P_{\text{S}}=1.35\text{ mW}$. During this 20s correlative time trace, we can see potentially 5 beads moving in the proximity of the antenna. The dynamics recorded in the fluorescence channels are again

challenging to interpret. As a bead gets trapped it starts to fluctuate in the antenna proximity and different dynamics can be recorded depending on the exact position of the bead. Contrary to the case in Fig.6.15, the epi-detection and the presence of the antenna again enable us to detect in the Raman-related channels the presence of the object close to the antenna. In the Appendix A.5 we reported additional measurements performed on AuNBs samples prepared with 200 nm diameter PS beads in a fully DI water solution, for both IFD=2904 cm⁻¹ and IFD=3050 cm⁻¹. These measurements underscore the importance of having the bead located in close proximity to the antenna in order to capture correlated signals in the eH-CARS channels. Fig.A.10 in the appendix shows a case where bead-related signals appear in the fluorescence channels, however these are not correlated with the eH-CARS readout which exhibits a nearly constant time-trace dominated by the FWM contribution from the antenna. This suggests that the beads were not in the antenna near-field, but traveled within the larger beam focal volume above the antenna, thus generating fluorescence signals but no LFE eH-CARS.

6.4 Cells

A similar methodology compared to the one employed with the PS fluorescence beads, was applied to investigate HEK293 cells expressing C-terminally GFP-His-tagged rat P2X7 receptors. The cells were placed onto the AuNBs array (see sample preparation in Chapter 3.2.3) as schematically represented in Fig.6.1. In this way, the antennas could probe the cell membrane and detect the presence of the P2X7 associated with lipid components. In the cell related study, we measured correlative time traces between SHG-, TPF- and LFE eH-CARS channels. We followed the procedure described in Section 6.1 acquiring data at ~ 100 antenna sites for each sample. The 20s correlative time traces were acquired with 0.1 ms sample period, downsampled to 10 ms in the analysis. The IFD selected was at 2904 cm⁻¹, to match the C-H stretch vibrational transitions strongly present in lipids such as cholesterol and sphingolipids (Ref.[168]). The time trace figures of the following subsections are organized so that the nominal SHG- and TPF- channels are respectively displayed from the top. At the bottom, we find the eH-CARS related channels, i.e. its real (\Re) and imaginary (\Im) components (corrected for the reference fluctuations via Eq.6.2.1) and the consequent field amplitude (Abs) and phase (Φ).

6.4.1 Control sample P2X7

In the course of this study, we conducted measurements on an additional control sample to establish a baseline for our experimental data analysis. This is given by HEK293 wild-type living cells (in GibcoTM FluoroBriteTM DMEM with 25 mM HEPES) onto the nanostructured coverslip (see sample preparation in Chapter 3.2.3). The latter provides insights into the appearance of fluorescence and its correlation with eH-CARS when the studied cell lacks GFP-His-tagged rat P2X7 receptors. While measuring the correlative time traces in the control sample, we observed that the results were affected by unwanted galvo mirror fluctuations in random time intervals (see reliability check in Fig.A.13). To directly illustrate where the acquired SHG, TPF, and eH-CARS signals can be considered reliable, we displayed in the first row the recorded galvo mirrors position in time and colored in gray the time intervals that must not be taken into account.

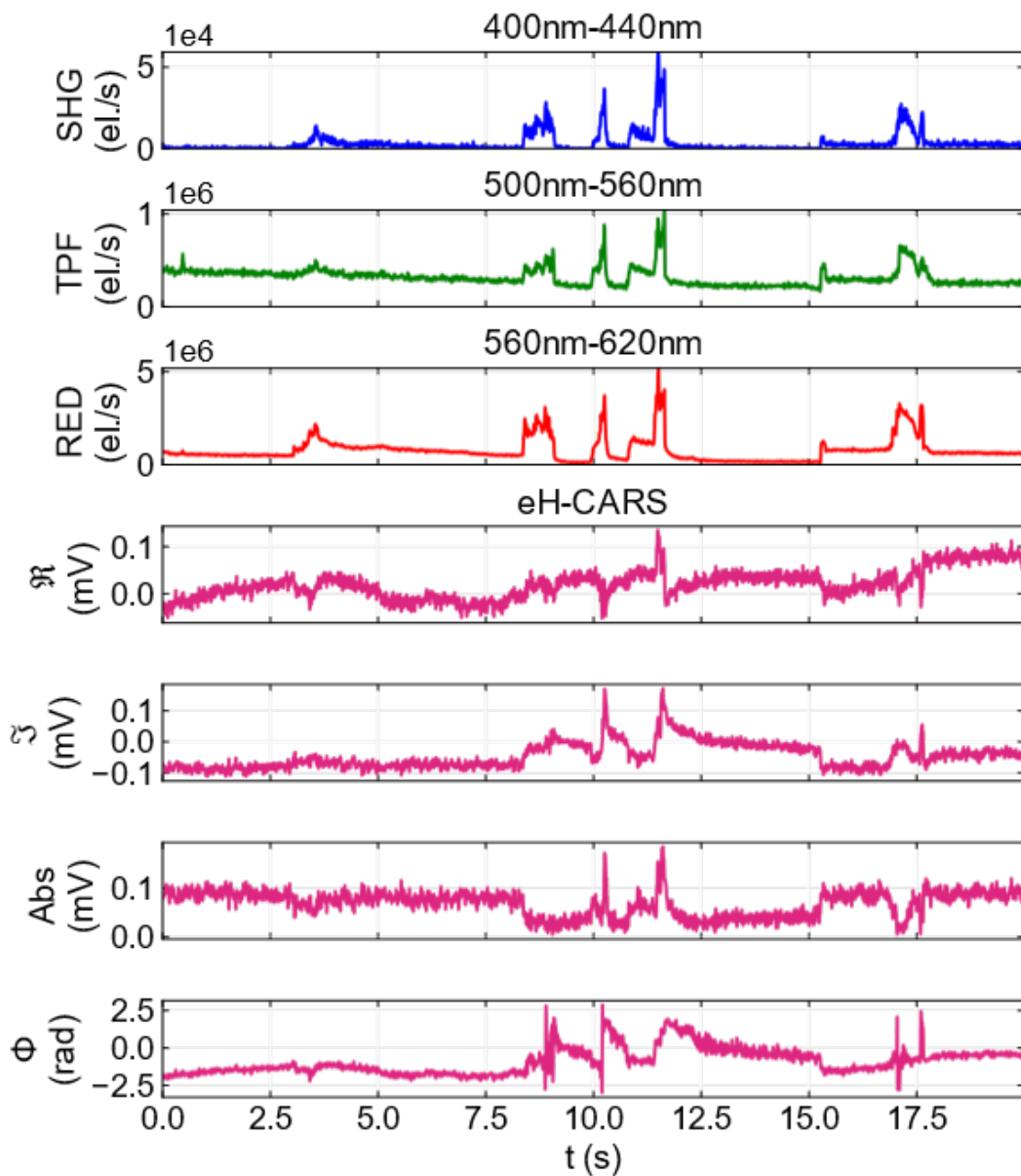


Figure 6.18: Representative fluctuation correlation time traces between (from top to bottom rows) nominal SHG-, TPF-, RED fluorescence and eH-CARS signal (real component (\Re), imaginary component (\Im), amplitude (Abs) and phase (Φ)). Sample: AuNBs sample with 100 nm diameter YG fluorescent PS bead in 50% glycerol/water (v/v) solution (see Chapter 3.2). Time traces of 20 s were recorded with 0.1 ms sample period at the antenna's site and downsampled to 10 ms. IFD=3050 cm^{-1} . Exciting power at the sample: $P_P=0.63$ mW and $P_S=1.35$ mW. For the PMTs channels, we reported an indication of the detected bandwidth for clarity. See reliability check in Fig.A.6.

Figure 6.19 shows a representative correlative time trace acquired using this control sample. When HEK293 wild-type living cells are placed on top of the antenna we would expect an increase of the background fluorescence, associated with autofluorescence from the cell membrane components. Due to the higher background fluorescence provided by the antennas, the cells related one, seems to not affect the recorded signal. Regarding the eH-CARS related channels and considering the overall reliable data set acquired, transient events distinguishable from the overall constant behaviour of the antenna, as the one taking place at $t \sim 13$ s, have been documented in 20% of the total recorded time. Thanks to the jump both in amplitude and in phase we can assume that the transient entity is resonant at $\text{IFD} = 2904 \text{ cm}^{-1}$.

6.4.2 P2X7-GFP-His

In this last section, we show representative correlative time traces acquired at HEK293 cells expressing C-terminally GFP-His-tagged rat P2X7 receptors onto AuNBs. The presence of the GFP tag allows us to check if transient events associated with the diffusion of P2X7 receptors passing near the nanoantenna correlate with eH-CARS fluctuations that can be potentially attributed to lipid nanodomains. Figure 6.20 and Figure 6.21 show two examples of the correlative time traces. The reliability checks (see Appendix A.6) confirm that the variations recorded in the traces are directly attributed to the cell sample itself, rather than to antenna reshaping or setup instabilities. In this session of measurements, the galvo mirrors did not show evident malfunctioning, so we did not plot their positions in time during the traces.

In Figure 6.20 we see a first $\text{Abs}(\text{eH-CARS})$ well defined variation in the time interval ~ 2 s-11 s associated with a weak fluorescence signal fluctuation (see horizontal violet arrow). At $t \sim 5$ s-6 s (see bold violet arrow) additional fluctuations, on top of the longer one, are displayed in all the channels. At $t \sim 11$ s (see bold red arrow) a further jump is detected in all the channels. This suggests the presence of entities, emitting both fluorescence and eH-CARS. Compared with the control results, it is plausible to attribute the variation of the fluorescence signal to the GFP label on the P2X7 receptor. The correlation with the eH-CARS signal fluctuation could be explained by a cluster of lipids, driven at $\text{IFD} = 2904 \text{ cm}^{-1}$ supporting the hypothesis that P2X7 associates with lipid rafts. After the transient fluctuations, we can see the overall eH-CARS coming back nearly to the initial value, thus suggesting that this value is the sole contribution by the AuNB.

An analogous situation is found in Figure 6.21 at $t \sim 2$ s. We see a clear and fast rise in both the SHG, TPF and $\text{Abs}(\text{eH-CARS})$ channels. Conversely, the jump in the eH-CARS phase is less evident. At $t \sim 11.5$ s, another statistically relevant feature of the measured results can be found. Here, we see a fluctuation of the SHG, TPF signals, and eH-CARS phase, but not correlated to any significant change of the eH-CARS amplitude. Considering the complex mix between the eH-CARS field and the FWM field from the antenna, it is not surprising that transient events might manifest as an amplitude change or as a phase change of the detected signal, albeit a detailed understanding of this behavior requires further future studies.

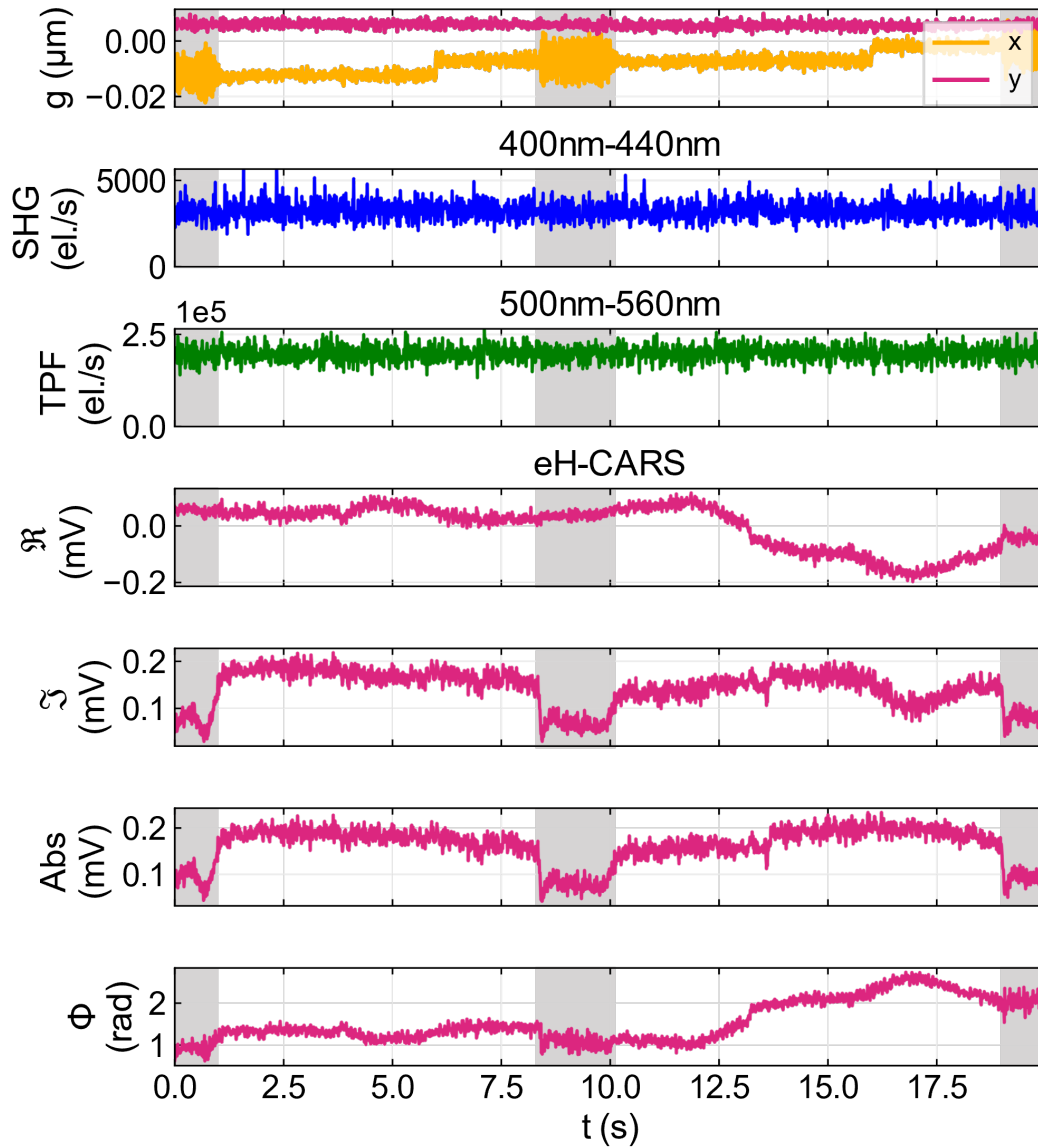


Figure 6.19: Representative fluctuation correlation time traces between (from top to bottom rows) galvo mirrors position, nominal SHG-, TPF-, and eH-CARS signals (real component (\Re), imaginary component (\Im), amplitude (Abs) and phase (Φ)). Sample: HEK293 wild-type living cells onto AuNBs. Time traces of 20 s (as indicated) were recorded with 0.1 ms sample period at the antenna's site and downsampled to 10 ms. IFD= 2904 cm^{-1} . Exciting power at the sample: $P_P=0.86\text{ mW}$ and $P_S=1.79\text{ mW}$. For the PMTs channels, we reported an indication of the detected bandwidth for clarity. See reliability check in Fig.A.13.

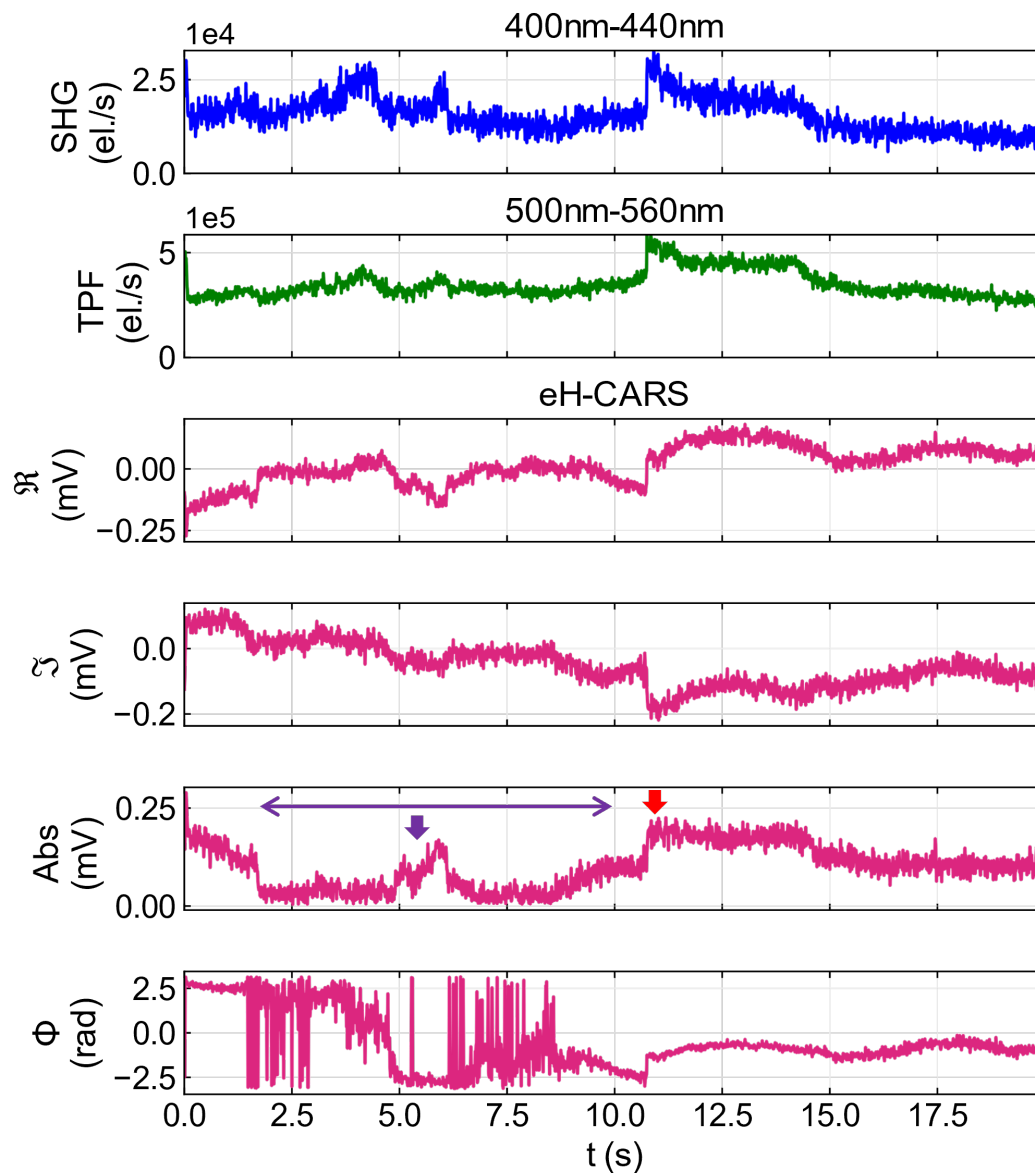


Figure 6.20: Representative fluctuation correlation time traces between (from top to bottom rows) nominal SHG-, TPF-, and eH-CARS signal (real component (\Re), imaginary component (\Im), amplitude (Abs) and phase (Φ)). Sample: HEK293 cells expressing C-terminally GFP-His-tagged rat P2X7 receptors onto AuNBs. Time traces of 20 s (as indicated) were recorded with 0.1 ms sample period at the antenna's site and downsampled to 10 ms. IFD=2904 cm^{-1} . Exciting power at the sample: $P_P=0.9$ mW and $P_S=2$ mW. For the PMTs channels, we reported an indication of the detected bandwidth for clarity. See reliability check in Fig.A.14.

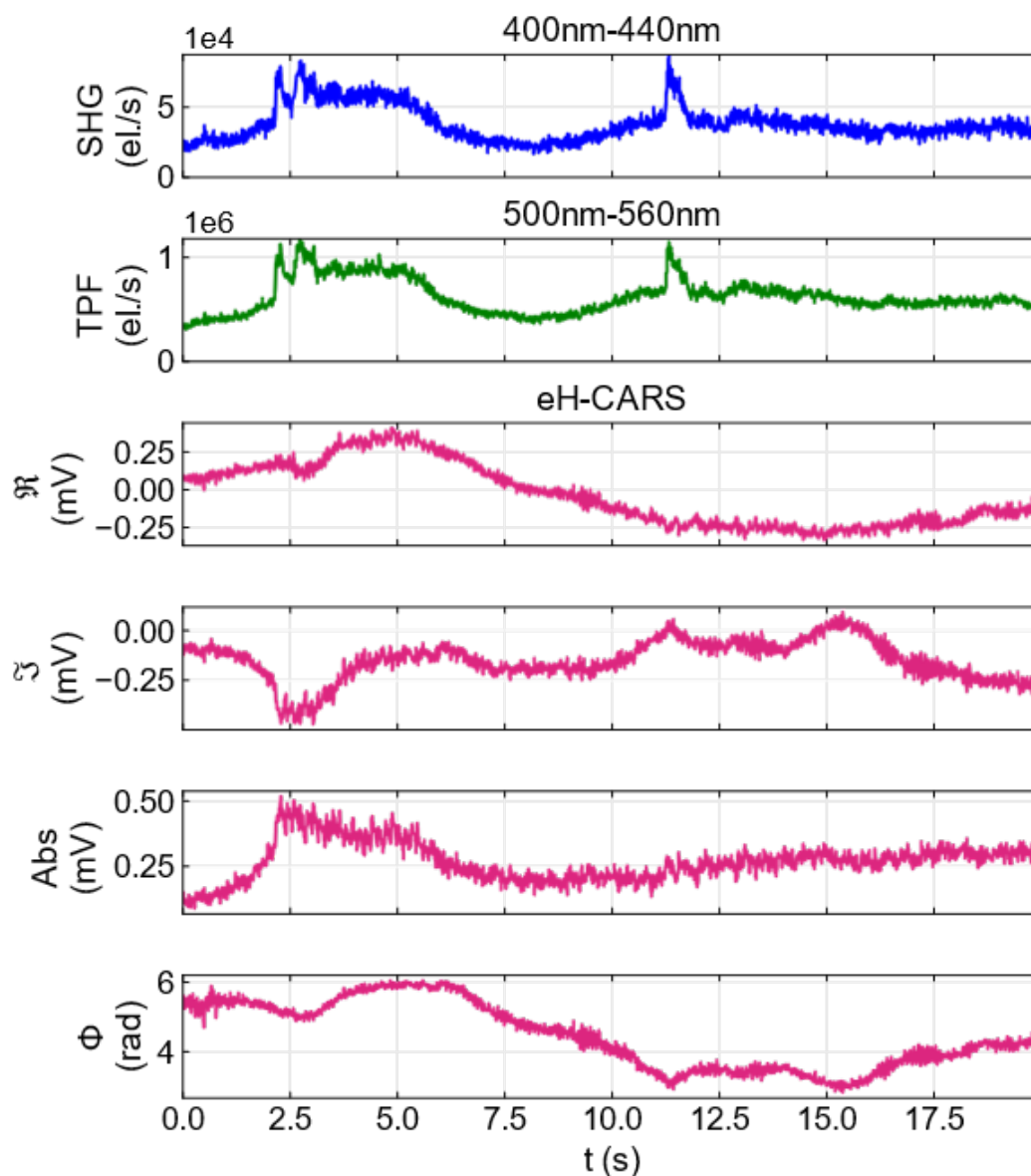


Figure 6.21: Representative fluctuation correlation time traces between (from top to bottom rows) nominal SHG-, TPF-, and eH-CARS signal (real component (\Re), imaginary component (\Im), amplitude (Abs) and phase (Φ)). Sample: HEK293 cells expressing C-terminally GFP-His-tagged rat P2X7 receptors onto AuNBs. Time traces of 20 s (as indicated) were recorded with 0.1 ms sample period at the antenna's site and downsampled to 10 ms. $\text{IFD}=2904\text{ cm}^{-1}$. Exciting power at the sample: $P_P=0.9\text{ mW}$ and $P_S=2\text{ mW}$. For the PMTs channels, we reported an indication of the detected bandwidth for clarity. See reliability check in Fig.A.15.

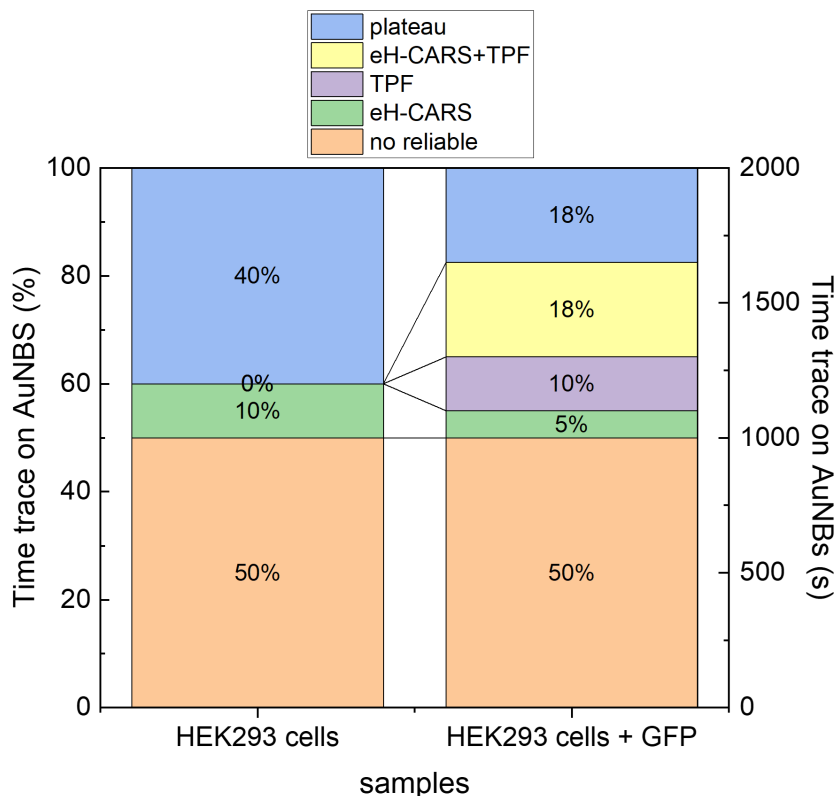


Figure 6.22: Bar chart plot providing a visual representation of the main categories of events observed during our experimental study with cells.

6.4.3 Conclusion and Outlook

The progress made so far has addressed numerous challenges regarding the viability of the experiment, which entails a high degree of complexity as it combines nanofabrication, correlative nonlinear optics, and live cell sensing. Protocols to attach the HEK293 cells on top of the nanoantennas and keep them alive sufficiently long to acquire data on ~ 100 nanoantennas were successfully established. We demonstrated through the measurement of the extinction cross-section that the nanoantennas are unaffected by the biological environment, whereas the laser excitation during the correlative measurements induces often reshaping of the nanoantennas. In Figure 6.22, we present a bar chart plot that provides a visual representation of the main categories of events observed during our experimental study with cells. The plot is designed to offer a comprehensive and concise overview, presenting the events in terms of both their percentage distribution and the total time they appeared. Precisely, the left y-axis of the plot indicates the percentage distribution of each event category, providing insights into the relative occurrence frequencies. This information is crucial for understanding the prevalence of different event types within the dataset. On the right y-axis, we present the overall time associated with these events. The two distinct columns represent the different cell samples investigated within our study, i.e. HEK293 wild-type living cells (left), which was our control

sample, and HEK293 living cells expressing C-terminally GFP-His-tagged rat P2X7 receptors (right). By visually comparing these columns, it is possible to gain insights into the variation and consistency of event occurrences across samples. The main categories of events shown are:

- *eH-CARS*: fluctuations in the eH-CARS channel that do not correlate with other recorded signals
- *TPF*: fluctuations in the TPF channel that do not correlate with other recorded signals
- *eH-CARS + TPF*: correlated events in TPF and eH-CARS channels
- *plateau*: time in which both the TPF channel and the eH-CARS one presented signal attributable to antenna emission
- *no reliable*: recorded time excluded from the evaluation because the correspondent measurements did not pass the reliability check

On each prepared sample we acquired 20 seconds sequences on approximately 100 antennas, resulting in 2000 seconds of data per each kind of sample; however, 50% of the acquired time sequences were excluded due to reliability issues caused by mechanical drift and antenna damage. When measuring HEK293 wild-type living cells, relevant fluctuations in fluorescence were not observed, likely due to the antenna's background fluorescence masking the cell's autofluorescence. Additionally, only 10% of the acquired time exhibited variations in the eH-CARS signal, without correlation with the TPF channel. The remaining signal in both fluorescence and eH-CARS channels was attributed to the antenna, displaying a plateau-like pattern. On the other hand, when measuring HEK293 living cells expressing C-terminally GFP-His-tagged rat P2X7 receptors, we observed significant fluctuations in the TPF channel (10% of the recorded time) that did not correlate with eH-CARS signals, while 5% of the acquired time showed variations in the eH-CARS signal independent of changes in fluorescence. Correlated fluctuations between TPF and eH-CARS signals were observed during 18% of the overall recorded time, leaving the rest of the recorded time without any noticeable fluctuations in either the eH-CARS or fluorescence channel. Overall, we found evidence of LFE eH-CARS correlatively with TPF fluorescence. A possible interpretation of the observed eH-CARS and TPF signals dynamics is that they originate by lipid raft components close to a GFP-tagged P2X7. Lipid rafts are ordered and thicker membrane domains with a high packing density of lipid molecules, hence exhibiting stronger CARS signals compared to the disordered counterpart, as shown in e.g. lipid membrane model systems. However, from this study, robust conclusions cannot be drawn due to the limited number of measurements made, primarily because of the unavailability of additional nanostructures and cells within the project's timeline. In addition to confirm the reliability of the recorded dynamics, by repeating the measurements onto several samples prepared in the same way, further investigation could be made about the chemical composition of the detected lipid domains. In the current implementation, the eH-CARS is excited and detected at a single vibrational resonance, hence with limited specificity. A way to verify the presence of cholesterol within the entity transiting at the antenna could be the depletion of the current cholesterol from the HEK293 cell membranes and its replacement by deuterated cholesterol (work in

progress within Dr. Mark Young's group). In fact, the deuterated vibrational resonance ($\sim 2150\text{ cm}^{-1}$), is significantly shifted compared to the nondeuterated lipid CH stretch vibration providing a molecularly specific vibrational tag.

Chapter 7

Conclusion

In this work we demonstrated LFE CARS, exploiting a scheme, presented in Chapter 3.3.2, where CARS is detected interferometrically in epi-geometry, with the local field enhancement of the CARS field provided by a single plasmonic nanostructure used as nanoantenna. Importantly, incoherent processes such as photoluminescence from the metal nanoparticles are suppressed by the interferometric heterodyne detection employed in our setup.

We aimed to work with nanostructures whose geometrical characteristics (i.e. size and shape) were capable of yielding a LSPR around 660 nm. This requirement was driven by the necessity to achieve a resonance condition between the LSPR of the particle and the CARS wavelength generated within our experimental setup, by the molecules of interest, specifically lipids. Two types of gold nanoantennas were explored, i.e. SiAuNRs and AuNBs. As indicated in the literature and confirmed by our experimental extinction measurements reported in Chapter 4.1.1, both the nanorod and the nanobowtie structures are characterized by a transversal and a longitudinal LSPR, corresponding to the oscillation of the electrons across and along the structure's main axis. The transversal LSPR wavelength position is primarily determined by the material constituting the nanostructure (i.e. gold, chosen for its known biocompatibility), while the longitudinal LSPR is mainly determined by the aspect ratio characterizing the nanoantennas.

SiAuNRs were purchased from Nanopartz. For this project, three different sizes of nanorods were selected: 25 nm × 71 nm, 40 nm × 68 nm, and 50 nm × 100 nm (nominal width × length sizes). Silica coating was introduced to prevent the reshaping of the gold nanorods upon laser excitation, which is a known issue with these nanoparticles. The smallest SiAuNRs had a silica shell thickness of 5 nm, while the others had a silica shell thickness of 10 nm. We successfully developed a protocol, described in Chapter 3.1, for the covalent binding of silica-coated NPs to glass, which was essential to avoid particle movement during laser exposure. Initially, we examined the optical characteristics of each NR group through single-particle optical extinction microscopy measurements (see Chapter 4.1). We experimentally obtained the evidence indicating significant variations in optical properties and, consequently geometric characteristics, among particles within the same nominal size group. We attributed such heterogeneity to the nanoparticles colloidal synthesis process, which is known to produce a range of sizes centered around an average value. However, a precise knowledge about the size and shape of the nanoparticles turns out to be a requirement due to significant consequences in the LFE CARS process. Information regarding the shape was obtained through statistical analysis of nanoparticles

ensembles using TEM measurements. As shown in Chapter 4.1.3, to quantify the size of a single SiAuNR measured, we developed an *optical sizing* tool, which relies on the comparison between measured and simulated extinction cross-sections. The latter were obtained via an elaborate model developed with the commercial software COMSOL Multiphysics, reproducing the experimental extinction measurements (see Chapter 3.4 and sub-Section 3.4.1).

Conversely, AuNBs have been designed and fabricated within the project, as shown in Chapter 3.2, in collaboration with the Single Molecule Biophotonics group based at the Institute of Photonic Science (ICFO, Barcelona, Spain). The extinction measurements shown in Chapter 4.2 played a pivotal role in guiding the choice for the optimized nominal geometrical parameters for nanofabrication. The parameters available for optimization were essentially the nanoantenna length l and apex-angle α , being others parameters constrained by fabrication requirements. For each length and the apex angle combination, an array of 100 antennas was fabricated and measured via widefield extinction technique. The latter technique is advantageous in terms of measurement speed because it allows all the structures of the assembly to be measured simultaneously and individually. It turns out that the optimized combination was given by 60 nm length and 90° apex angle which results in a longitudinal LSPR centered at 665 nm.

SiAuNRs have been used to carry out LFE eH-CARS proof of principle, as reported in Chapter 5. We quantified experimentally the CARS enhancement, measurable in the far field and referred to as the R factor, for the selected SiAuNRs. For this study, silicone oil (known Raman spectrum) was chosen as bulk material surrounding the antenna. We explored how nanorods behave when subjected to different excitation methods, specifically comparing circular and linear polarization. Given the sample preparation adopted and the consequent unknown knowledge of the particle in-plane orientation, the recommended measurement method involves circular polarization during excitation and a subsequent analysis of the detected signal projections along and across the nanorod. This approach enhances the signal-to-noise ratio by a factor $\sqrt{2}$ and minimizes the laser exposure experienced by the rod. We characterized the dependence of the quantified CARS enhancement on the exciting beams power, additionally studying their resistance against reshaping due to the laser exposure, and on the wavenumber detuning between the CARS driving fields and the vibrational resonance under study. The nominal $25\text{ nm} \times 71\text{ nm}$ AuNRs with 5 nm silica shell provide a good R factor (~ 10) but statistically they are not resistant (reshaping was observed on most particles, suggesting that the 5 nm thin shell is not sufficient to prevent this effect). The nominal $40\text{ nm} \times 68\text{ nm}$ AuNRs with 10 nm silica shell provide a comparable R factor and they are more resistant. Last, the nominal $50\text{ nm} \times 100\text{ nm}$ AuNRs with 10 nm silica shell provide a R factor higher (~ 15) with respect to all the others and are stable.

Via the COMSOL model presented in Chapter 3.4.2, we compared simulated and experimental LFE eH-CARS. The geometry of the SiAuNRs was modeled based on acquired TEM images (Fig.3.1). Using the model, we explained the experimentally observed decrease of the measured R factor for high laser powers, attributing it to a saturation effect of the CARS phenomenon itself. Indeed, the simulations enabled us to estimate the pump and Stokes peak power at the laser focus and to verify its close proximity to the threshold stated in the literature for saturation. Such peak powers are essential quantities that cannot be determined from measurements due to the lack of direct knowledge of the effective near-field enhancement provided by

the nanostructure. Exploiting eH-CARS COMSOL simulations, we studied the various third-order contributions from the resonant and nonresonant material within the focal volume, i.e. the NP gold core, the silica shell, and the resonant oil. Notably, the gold antenna itself considerably contributes to the measured CARS signal through a non-resonant emission (due to electronic four-wave mixing) at the CARS wavelength. By comparing our experimental R factor values with the ones obtained from different choices of the gold third-order susceptibility, we were able to infer a third-order susceptibility value for gold, reshaping was observed on most particles, suggesting that the 5nm thin shell is not sufficient to prevent this effect the value stated in the literature for similar experimental conditions. In fact, in the literature, the reported values of the third-order susceptibility of gold span over several orders of magnitudes. This is due to the various techniques utilized to measure the gold third-order nonlinearity, which employed different laser pulse durations, thus probing different contributions to the gold nonlinear response over various time scales. Overall, the work presented in Chapter 5 demonstrated that LFE eH-CARS can be achieved with AuNRs, and simulations showed local enhancement factors in the order of 10^3 at the nanorod tips.

After the proof-of-principle demonstration, in Chapter 6 we employed the AuNBs in the developed LFE eH-CARS technique. The AuNBs were exploited as antennas to identify moving entities in the nanostructure proximity, performing correlative fluorescence and LFE-eHCARS sensing measurements with the involved laser beams focused at a single AuNB. Similarly to the SiAuNRs, the AuNBs resistance against reshaping due to laser exposure was tested. We considered a sensing configuration experiment, as shown in Chapter 6.2. Here, the laser beams were kept focused at the antennas for tens of seconds, resulting in time trace measurements. The surrounding media was given by Gibco™ FluoroBrite™ DMEM with 25 mM HEPES, as later this was employed when working with cells to reduce the fluorescence background. Thanks to this choice, it was possible also to measure and characterize the antennas-related background fluorescence, deriving from thermal emission, and LFE eH-CARS signal, arising from gold non-resonant contribution, provided by the nanoantennas. Both signals slowly decreased versus time due to the worsening of the focusing conditions from slow mechanical drifts and were not characterized by fast fluctuations. In general, the AuNBs resistance against shape changing does not seem to be statistically robust. In fact, 50% of the measured antennas turned out to be damaged at the end of the time trace acquisition, pointing out the necessity for a redesign of the protective layer. Up to this point, an Al_2O_3 passivation layer, 3 nm thick, has been applied to coat the nanoantennas, aiming to improve thermal stability. Especially because of the complexity of the experiment, we defined criteria helping to assess the reliability of each correlative time trace performed on the nanoantennas, so that measurements affected by antennas damages, mechanical drifts and instabilities, or/and unwanted electrical fluctuation could be discarded from the evaluation. Additionally, a detailed protocol for carrying out the experiment has been established in order to minimize the duration of the overall measurement session when working with cells (see Chapter 6.1). The optimized measurement conditions involve keeping the cells inside an incubator to maintain the proper environment, including temperature and humidity. However, this would have introduced additional variables into the results, such as temperature fluctuations, which could not be investigated within the project's timeline. Preliminary investigations estimated that the cell could survive outside the incubator for approximately

2 hours on average. To keep the overall measurement duration under 2 hours, we took advantage of the fact that the antennas were fabricated in arrays. This ensures that the distance between the antennas is well-defined, allowing for automated measurements to minimize the overall acquisition duration. Later, we moved to dynamic sensing experiments (see Chapter 6.3). First, we investigated two proof of principle samples given by fluorescent PS beads characterized by 100 nm and 200 nm diameter. In both cases, the fluorescent PS beads were moving in either a water or glycerol/water solution. We aimed to understand the benefits of introducing antennas by comparing the results of correlative measurements between fluorescence and either SRS and LFE eH-CARS. The correlative measurements involving SRS were performed in bulk media, away from the nanostructure, while those involving LFE eH-CARS were performed at the antennas. The fluorescent signal related to the passage of beads was always detectable, whether in the focal volume of the beams for SRS or in proximity to the antenna for LFE eH-CARS. In contrast, we observed SRS signals correlating with fluorescence only when using relatively high applied powers at the sample ($P_P \sim 4$ mW and $P_S \sim 10$ mW) and larger diameter beads. Interestingly, at this applied power, particle trapping phenomena occurred. This evidence was also significant in interpreting the behavior of the recorded fluorescence. The trapping caused the particles to remain within the laser focal volume, leading to a shift of the fluorescence towards more blue-shifted wavelengths, which can be explained by the bleaching of the fluorescent dye. Moreover, we found clear evidence of LFE eH-CARS correlating with fluorescence measuring both PS diameters and employing lower laser powers at the sample ($P_P \sim 0.5$ mW and $P_S \sim 1$ mW). Effective sensing of the PS beads with LFE eH-CARS is possible thanks to the combination of several factors: the use of epi-detection, which is sensitive to interfaces rather than bulk material; the enhancement of the pump, Stokes, and CARS fields at the antenna, which improves the detection of the CARS signal from the bead; and the different feature of the antenna's FWM field interfering with the CARS field from the bulk medium and the PS bead. However, the exact dynamics of a PS bead entering the focal volume in proximity of the antenna are not straightforward to be explained. In fact, the presence of the antenna complicates the overall picture, as different antenna-bead relative positions are likely to give different features in the detected signal. We point out here that the overall detected LFE eH-CARS signal is given by the interference between the enhanced eHCARS signal from the PS beads near the antenna and the FWM signal from the antenna itself. A more in-depth exploration of the dynamics of the PS beads is currently in progress. From the experimental point of view, the collected data can be used for an analysis akin to Fluorescence Correlation Spectroscopy (FCS) to examine the correlations between the fluorescence and the LFE eH-CARS signals. From a simulating point of view, the COMSOL model presented in Chapter 3.4.2, can be adapted to the case of a PS bead close to a single AuNB, allowing for studying the dependence of the detected signal on the antenna-PS bead relative position. Given the limited availability of nanostructure arrays within our project timeline, we were able to prepare samples using only the specified PS beads. Exploring the performance of the designed nanostructures with smaller beads, down to tens of nanometers, would be advantageous. Furthermore, it would be worthwhile to investigate different bulk media where these beads can exhibit fluctuation, thereby varying the viscosity. As demonstrated, there exists a diffusion speed threshold for the PS beads, beyond which higher speeds hinder sufficient interaction between the antennas and the PS bead signal for detection.

The study involving fluorescent PS beads was followed by correlative fluorescence and LFE-eHCARS sensing measurements at the AuNBs with either HEK293 wild-type living cells, as a control sample, and HEK293 living cells over-expressing a GFP-tagged P2X7, which is a membrane receptor thought to partition in lipid nanodomains, rich in cholesterol and saturated lipids (see Chapter 6). In collaboration with Dr. Mark Young's group based at Cardiff University, protocols, presented in Chapter 3.2.3, were successfully established to deposit the HEK293 cells on top of the nanoantennas and keep them alive sufficiently long to perform the sensing measurement. When measuring HEK293 wild-type living cells, relevant fluctuations in fluorescence were not observed, likely due to the antenna's background fluorescence masking the cell's autofluorescence. Additionally, only 10% of the acquired time exhibited variations in the eH-CARS signal, without correlation with the TPF channel. The remaining signal in both fluorescence and eH-CARS channels was attributed to the antenna, displaying a plateau-like pattern. Conversely, while measuring the HEK293 living cells over-expressing a GFP-tagged P2X7, we found evidence of LFE eH-CARS correlatively with TPF fluorescence, suggesting the presence of lipid rafts, exhibiting stronger CARS signals compared to lipid disordered counterparts, close to a GFP-tagged P2X7. Although the reliability of the detected time traces was confirmed by the established criteria, the repeatability of the results should be deeply verified by conducting measurements on multiple samples prepared in the same manner. Additionally, further investigation could be made about the chemical composition of the detected lipid domains.

In the current implementation, the eH-CARS is excited and detected at a single vibrational resonance, hence with limited specificity. A way to verify the presence of cholesterol within the entity transiting at the antenna could be the depletion of the current cholesterol from the HEK293 cell membranes and its replacement by deuterated cholesterol (work in progress within Dr. Mark Young's group). In fact, the deuterated vibrational resonance ($\sim 2150\text{ cm}^{-1}$), is significantly shifted compared to the nondeuterated lipid CH stretch vibration providing a molecularly specific vibrational tag.

The developed LFE eH-CARS technique and the initial experimental evidence hold significant promises, opening avenues for direct studies in living cells regarding the existence of lipid rafts and their influence on the organization of key membrane receptors within the cellular membrane. A considerable limitation of the available setup is that eH-CARS spectra can be acquired only sequentially, i.e. one wavenumber at a time, with a consequent reduction in acquisition speed and chemical specificity on living samples. As an outlook, going forward it would be very useful to implement a spectrally-resolved broadband eH-CARS, to interrogate and detect multiple vibrational modes in one spectral acquisition simultaneously. An important aspect in implementing this configuration is related to the need to tailor, both temporally and spectrally, the pump, Stokes, and reference fields such that multiple vibrations can be excited simultaneously and distinguished spectrally. This could be implemented using an appropriate choice of spectral bandwidth (hence femtosecond pulses) and chirp combinations. A broadband eH-CARS implementation would bring a significant advantage of distinguishing between the enhanced CARS signal from the biological molecules and the signal coming from the electronic FWM process in the antenna, as the latter would not exhibit a vibrational resonance and could thus be separated as a spectrally constant contribution. An additional improvement going forward would be the design and fabrication of optimal plasmonic nanoantennas,

in terms of shape stability, enhancement factors, and ability to enhance multiple vibrational resonances.

As a long term vision, LFE eH-CARS using single plasmonic nanoparticles (e.g. nanorods) sufficiently small to be internalised by living cells without disrupting endogenous pathways opens the way to nanoscale label-free chemical sensing directly inside living cells with unprecedented spatio-temporal capabilities.

Appendix A

Appendix

A.1 Lock-in offset correction

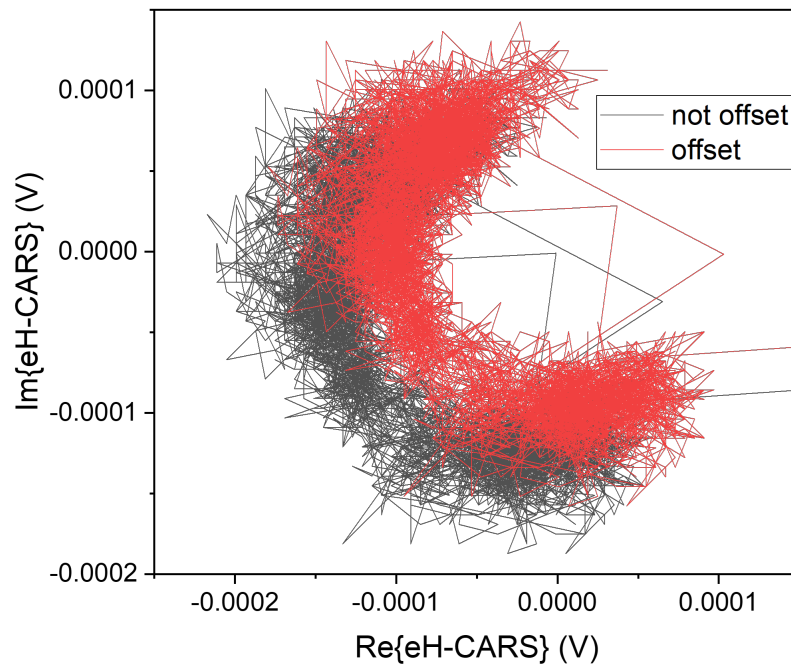


Figure A.1: Example of the lock-in offset correction for a eH-CARS signal applied to the real and imaginary parts of the measured eH-CARS signal.

A.2 Example of reliability checks with negative outcome

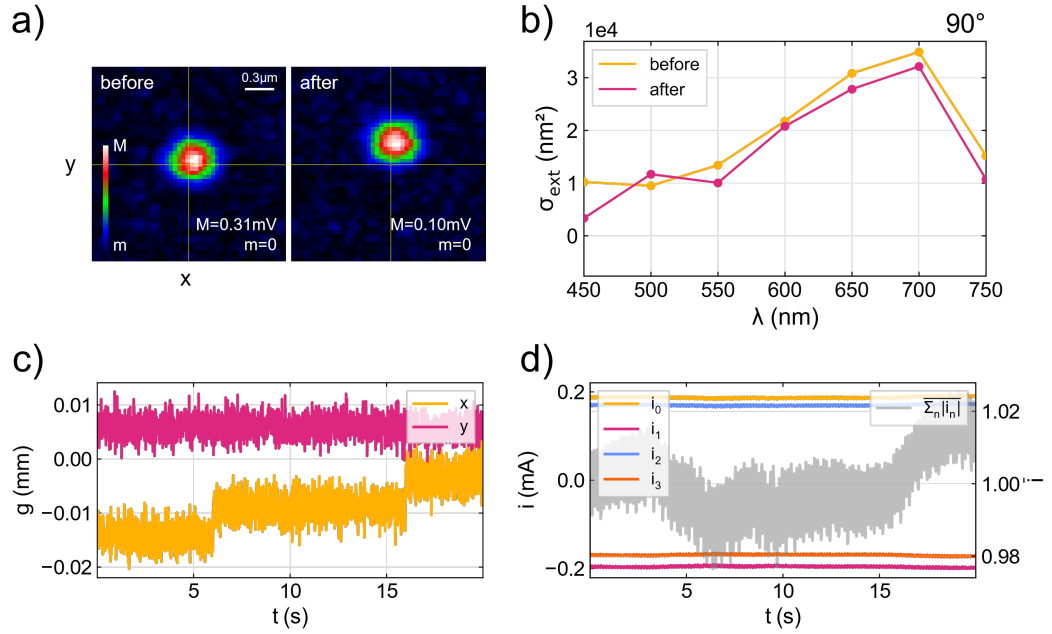


Figure A.2: Example of reliability checks with negative outcome due to mechanical drifts. (a) A 2D eH-CARS amplitude scan ($2 \mu\text{m} \times 2 \mu\text{m}$) measured at the AuNB focus, before and after the correlative measurement. Rainbow scales from m (black) to M (white). (b) Single particle extinction cross-sections, measured before and after the laser exposure. (c) Galvo mirror positions (along x and y directions) recorded during the time traces. (d) Four BPD currents (i_0, i_1, i_2, i_3) recorded during the time trace measurement were balanced (symmetric around the x-axis). Additionally, the $\bar{i} = \frac{i_\Sigma}{\langle i_\Sigma \rangle}$ used to correct the recorded time trace eH-CARS is shown as well.

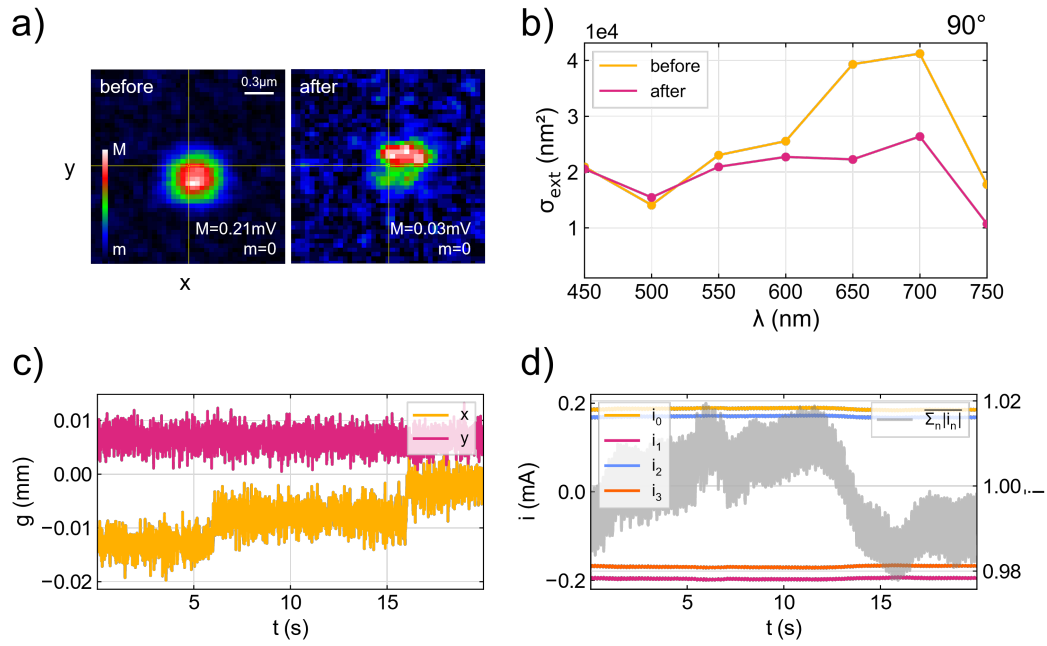


Figure A.3: Example of reliability checks with negative outcome due to particle damage. (a) A 2D eH-CARS amplitude scan ($2\mu\text{m} \times 2\mu\text{m}$) measured at the AuNB focus, before and after the correlative measurement. Rainbow scales from m (black) to M (white). (b) Single particle extinction cross-sections, measured before and after the laser exposure. (c) Galvo mirror positions (along x and y directions) recorded during the time traces. (d) Four BPD currents (i_0, i_1, i_2, i_3) recorded during the time trace measurement were balanced (symmetric around the x-axis). Additionally, the $\bar{i} = \frac{i_\Sigma}{\langle i_\Sigma \rangle}$ used to correct the recorded time trace eH-CARS is shown as well.

A.3 Selection criteria for correlative time traces measurements of Chapter 6.3.2

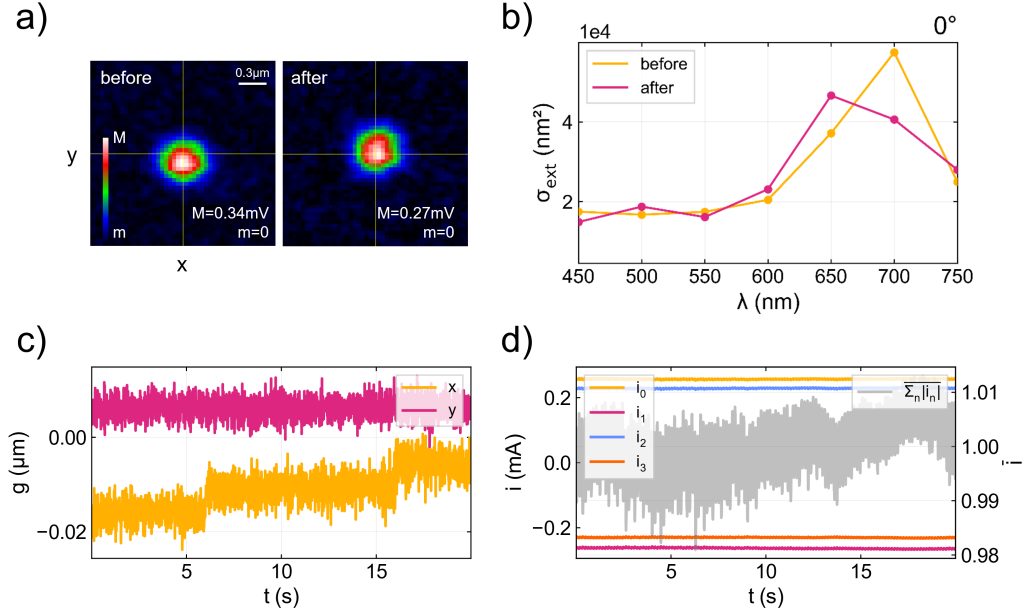


Figure A.4: Four criteria to be checked to consider the correlative time trace recorded at the antenna (shown in Fig.6.16) as reliable. (a) A 2D eH-CARS amplitude scan ($2\mu\text{m} \times 2\mu\text{m}$) measured at the AuNB focus, before and after the correlative measurement, shows that the antenna remained reasonably centered (yellow cross) during the time trace. Rainbow scales from m (black) to M (white). (b) Single particle extinction cross-sections, measured before and after the laser exposure, show that no significant structural changes affected the antenna during the laser exposure. (c) Galvo mirror positions (along x and y directions) recorded during the time traces to visualize possible instabilities affecting the recorded signal. (d) Four BPD currents (i_0, i_1, i_2, i_3) recorded during the time trace measurement were balanced (symmetric around the x -axis). Additionally, the $\bar{i} = \frac{i_{\Sigma}}{\langle i_{\Sigma} \rangle}$ used to correct the recorded time trace eH-CARS is shown as well.

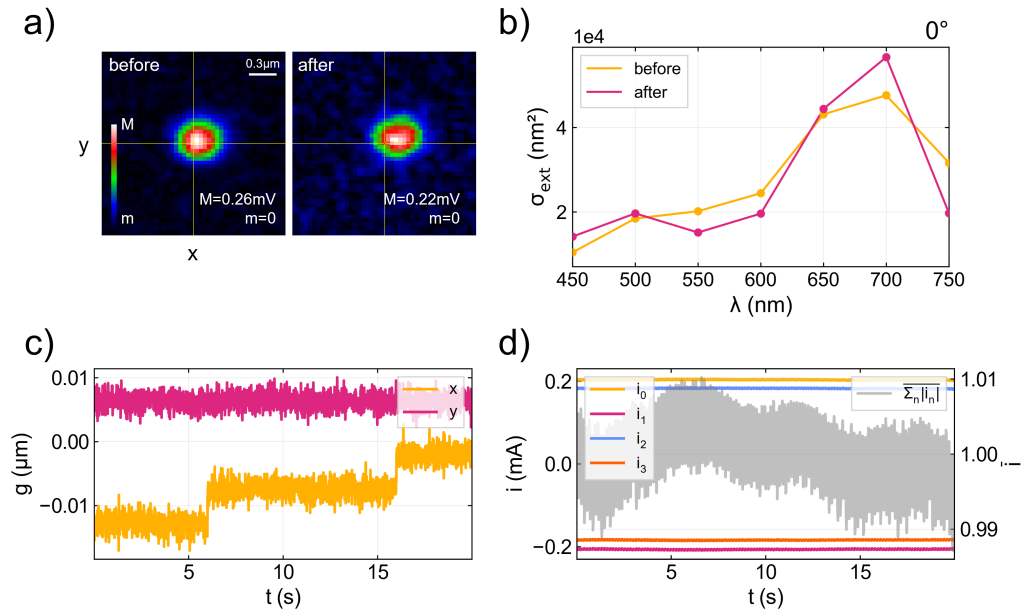


Figure A.5: Four criteria to be checked to consider the correlative time trace recorded at the antenna (shown in Fig.6.17) as reliable. (a) A 2D eH-CARS amplitude scan ($2\mu\text{m} \times 2\mu\text{m}$) measured at the AuNB focus, before and after the correlative measurement, shows that the antenna remained reasonably centered (yellow cross) during the time trace. Rainbow scales from m (black) to M (white). (b) Single particle extinction cross-sections, measured before and after the laser exposure, show that no significant structural changes affected the antenna during the laser exposure. (c) Galvo mirror positions (along x and y directions) recorded during the time traces to visualize possible instabilities affecting the recorded signal. (d) Four BPD currents (i_0, i_1, i_2, i_3) recorded during the time trace measurement were balanced (symmetric around the x -axis). Additionally, the $\bar{i} = \frac{i_{\Sigma}}{\langle i_{\Sigma} \rangle}$ used to correct the recorded time trace eH-CARS is shown as well.

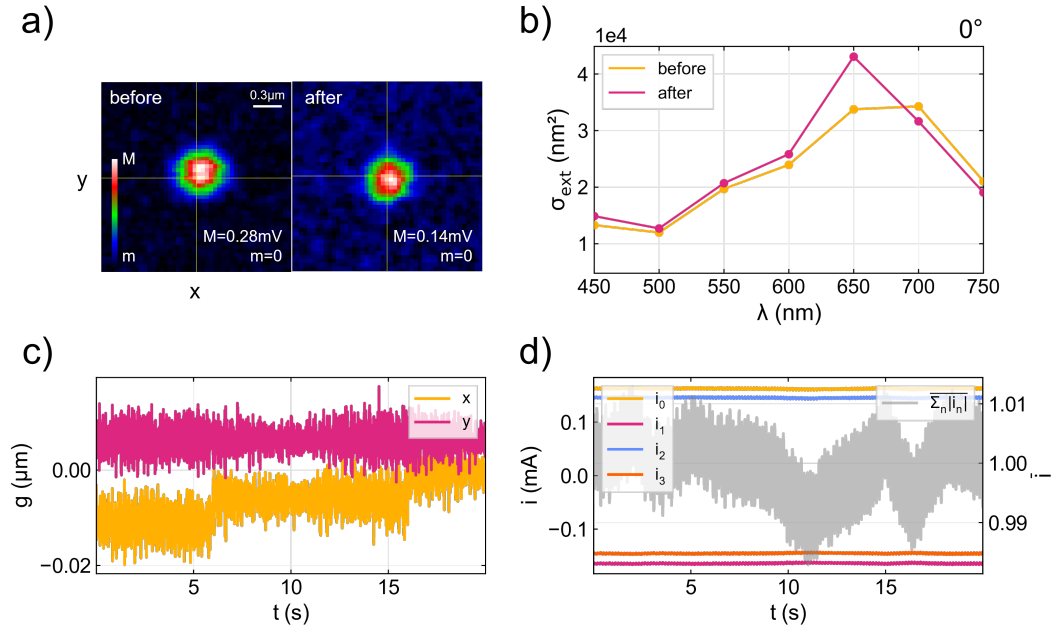


Figure A.6: Four criteria to be checked to consider the correlative time trace recorded at the antenna (shown in Fig.6.18) as reliable. (a) A 2D eH-CARS amplitude scan ($2\mu\text{m} \times 2\mu\text{m}$) measured at the AuNB focus, before and after the correlative measurement, shows that the antenna remained reasonably centered (yellow cross) during the time trace. Rainbow scales from m (black) to M (white). (b) Single particle extinction cross-sections, measured before and after the laser exposure, show that no significant structural changes affected the antenna during the laser exposure. (c) Galvo mirror positions (along x and y directions) recorded during the time traces to visualize possible instabilities affecting the recorded signal. (d) Four BPD currents (i_0, i_1, i_2, i_3) recorded during the time trace measurement were balanced (symmetric around the x-axis). Additionally, the $\bar{i} = \frac{i_\Sigma}{\langle i_\Sigma \rangle}$ used to correct the recorded time trace eH-CARS is shown as well.

A.4 Correlative time traces measurements performed at bulk-glass coverslip interface of a sample prepared with 200nm PS beads in 50% glycerol/water (v/v) solution

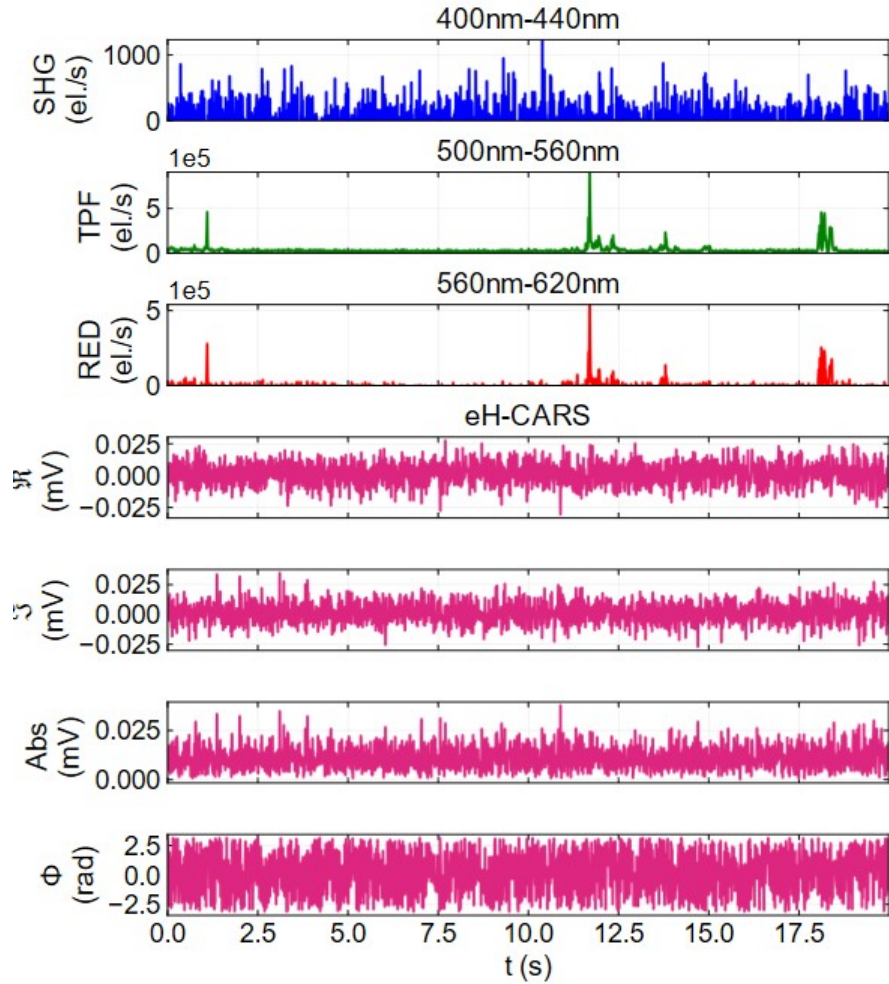


Figure A.7: Representative fluctuation correlation plot between (from top to bottom rows) nominal SHG-, TPF-, RED fluorescence and eH-CARS signal (real component (\Re), imaginary component (\Im), amplitude (Abs) and phase (Φ)). Sample: 200nm diameter YG fluorescent PS beads in 50% glycerol/water (v/v) solution (see Chapter 3.2). Time traces of 20s (as indicated) were recorded with 0.1 ms sample period at the antenna's site and downsampled to 10ms. IFD=3050cm⁻¹. Exciting power at the sample: $P_P=1.4$ mW and $P_S=2.5$ mW. For the PMTs channels, we reported an indication of the detected bandwidth for clarity.

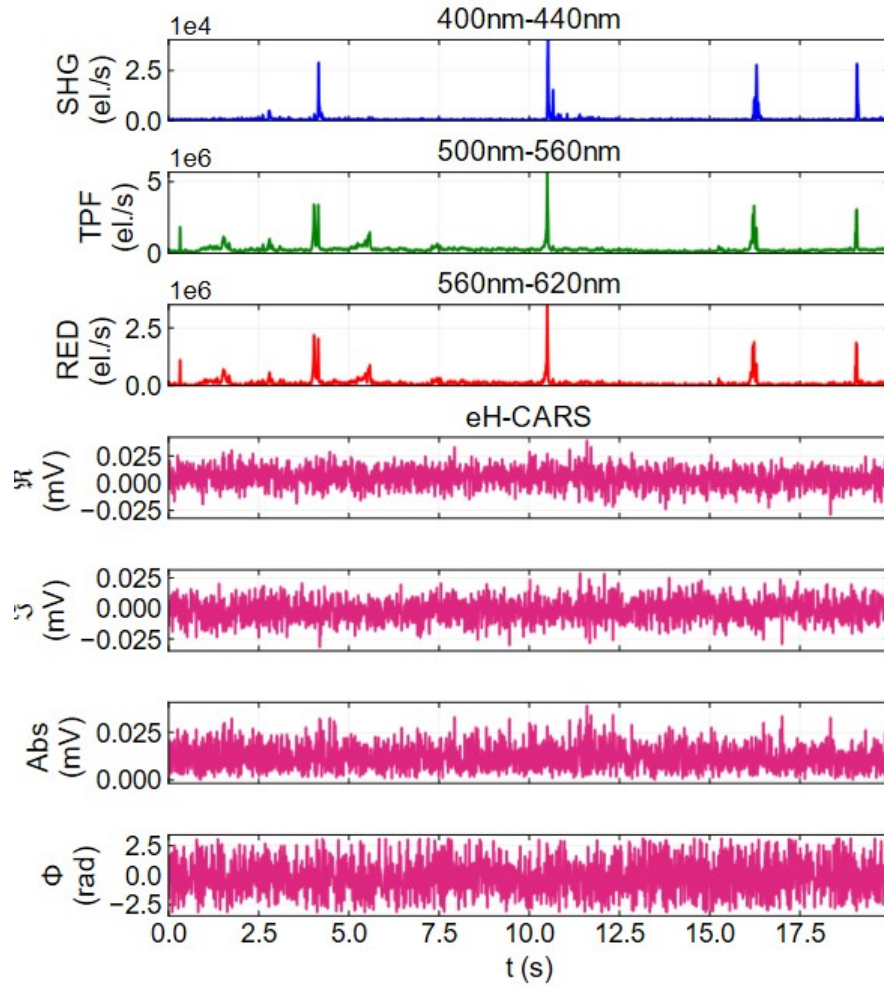


Figure A.8: Representative fluctuation correlation plot between (from top to bottom rows) nominal SHG-, TPF-, RED fluorescence and eH-CARS signal (real component (\Re), imaginary component (\Im), amplitude (Abs) and phase (Φ)). Sample: 200nm diameter YG fluorescent PS beads in 50% glycerol/water (v/v) solution (see Chapter 3.2). Time traces of 20s (as indicated) were recorded with 0.1ms sample period at the antenna's site and downsampled to 10ms. $\text{IFD}=3050\text{cm}^{-1}$. Exciting power at the sample: $P_P=5\text{mW}$ and $P_S=11.5\text{mW}$. For the PMTs channels, we reported an indication of the detected bandwidth for clarity.

A.5 Correlative time traces measurements and selection criteria performed on AuNBs sample prepared with the 200nm PS beads in fully DI water solution

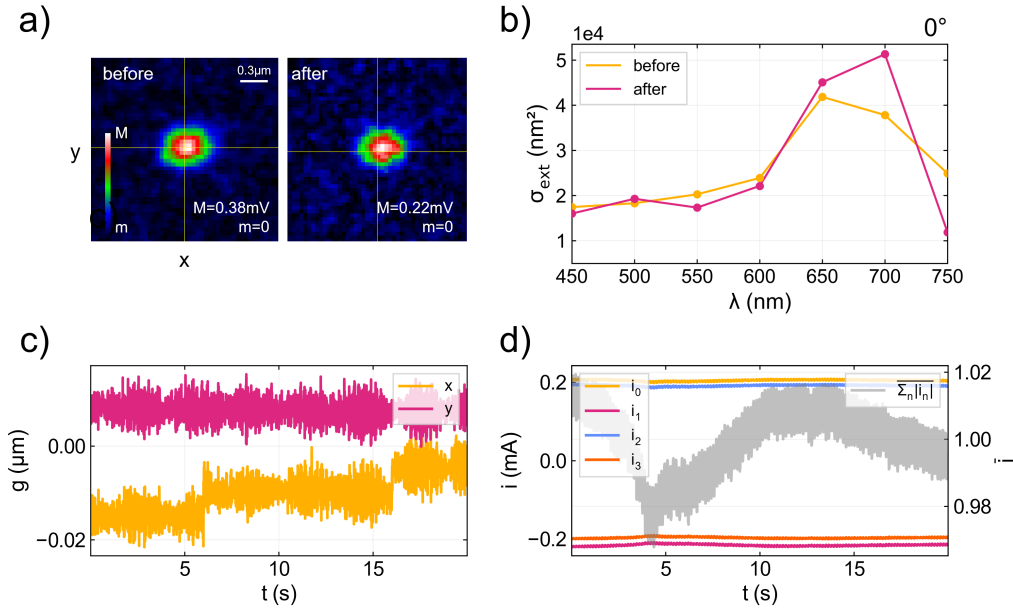


Figure A.9: Four criteria to be checked to consider the correlative time trace recorded (shown in Fig.A.10) at the antenna as reliable. (a) A 2D eH-CARS amplitude scan ($2\mu\text{m} \times 2\mu\text{m}$) measured at the AuNB focus, before and after the correlative measurement, shows that the antenna remained reasonably centered (yellow cross) during the time trace. Rainbow scales from m (black) to M (white). (b) Single particle extinction cross-sections, measured before and after the laser exposure, show that not significant structural changes affected the antenna during the laser exposure. (c) Galvo mirror positions (along x and y directions) recorded during the time traces to visualize possible instabilities affecting the recorded signal. (d) Four BPD currents (i_0, i_1, i_2, i_3) recorded during the time trace measurement were balanced (symmetric around the x -axis). Additionally, the $\bar{i} = \frac{i_{\Sigma}}{\langle i_{\Sigma} \rangle}$ used to correct the recorded time trace eH-CARS is shown as well.

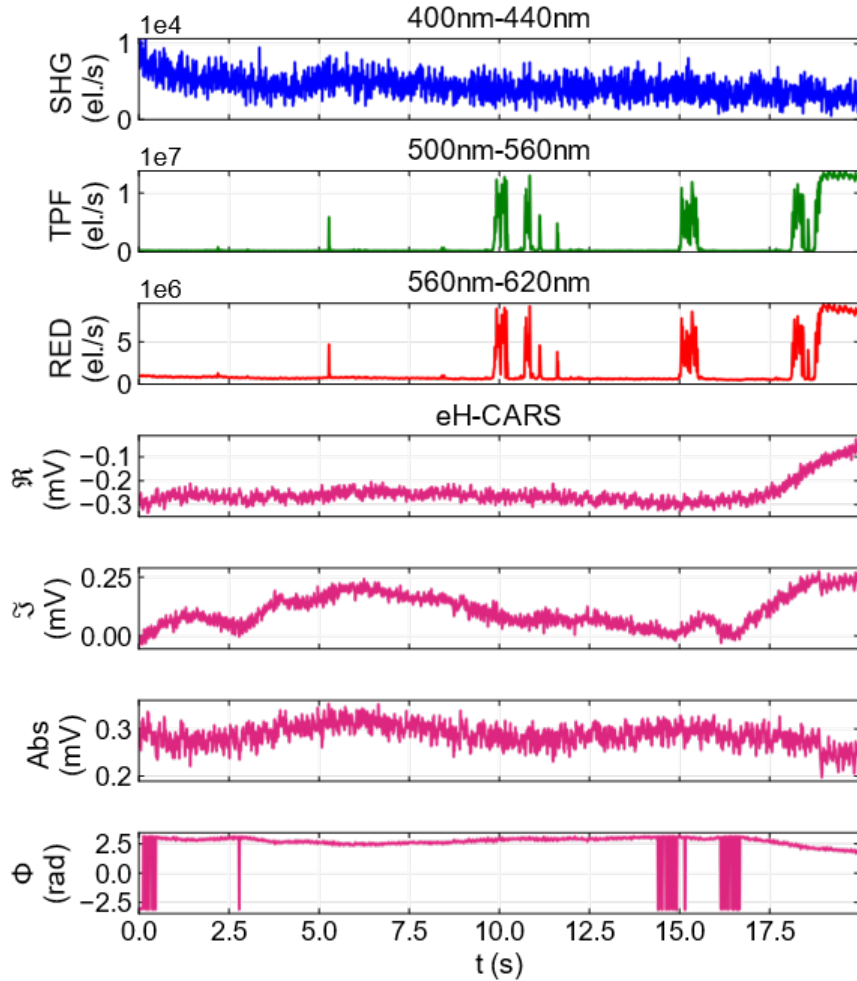


Figure A.10: Representative fluctuation correlation plot between (from top to bottom rows) nominal SHG-, TPF-, RED fluorescence and eH-CARS signal (real component (\Re), imaginary component (\Im), amplitude (Abs) and phase (Φ)). Sample: AuNBs sample with 200nm diameter YG fluorescent PS bead in fully DI water (see Chapter 3.2). Time traces of 20s (as indicated) were recorded with 0.1ms sample period at the antenna's site and downsampled to 10ms. IFD= 2904cm^{-1} . Exciting power at the sample: $P_P=0.68\text{mW}$ and $P_S=1.56\text{mW}$. For the PMTs channels, we reported an indication of the detected bandwidth for clarity.

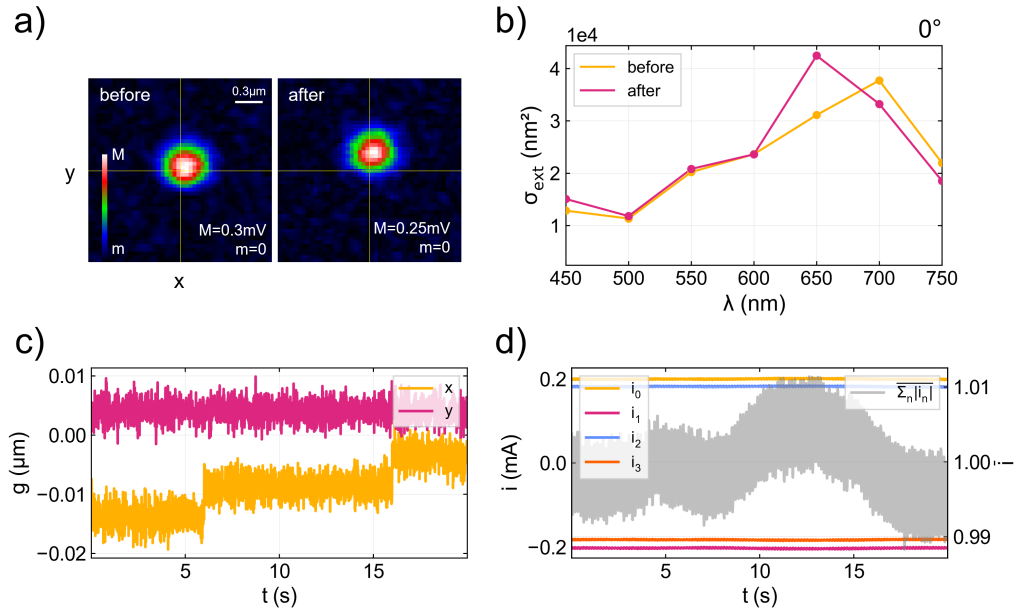


Figure A.11: Four criteria to be checked to consider the correlative time trace recorded at the antenna (shown in Fig.A.12) as reliable. (a) A 2D eH-CARS amplitude scan ($2\mu\text{m} \times 2\mu\text{m}$) measured at the AuNB focus, before and after the correlative measurement, shows that the antenna remained reasonably centered (yellow cross) during the time trace. Rainbow scales from m (black) to M (white). (b) Single particle extinction cross-sections, measured before and after the laser exposure, show that not significant structural changes affected the antenna during the laser exposure. (c) Galvo mirror positions (along x and y directions) recorded during the time traces to visualize possible instabilities affecting the recorded signal. (d) Four BPD currents (i_0, i_1, i_2, i_3) recorded during the time trace measurement were balanced (symmetric around the x -axis). Additionally, the $\bar{i} = \frac{i_\Sigma}{\langle i_\Sigma \rangle}$ used to correct the recorded time trace eH-CARS is shown as well.

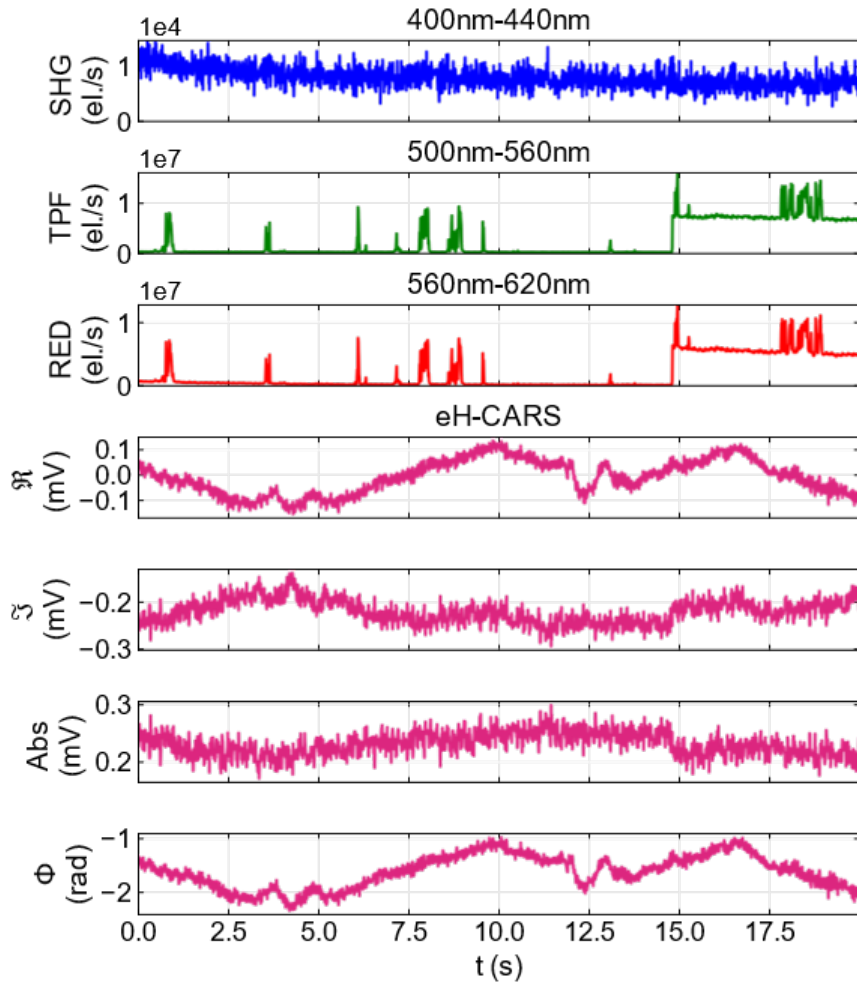


Figure A.12: Representative fluctuation correlation plot between (from top to bottom rows) nominal SHG-, TPF-, RED fluorescence and eH-CARS signal (real component (\Re), imaginary component (\Im), amplitude (Abs) and phase (Φ)). Sample: AuNBs sample with 200nm diameter YG fluorescent PS bead in fully DI water (see Chapter 3.2). Time traces of 20s (as indicated) were recorded with 0.1ms sample period at the antenna's site and downsampled to 10ms. IFD= 3050cm^{-1} . Exciting power at the sample: $P_P=0.68\text{mW}$ and $P_S=1.56\text{mW}$. For the PMTs channels, we reported an indication of the detected bandwidth for clarity.

A.6 Selection criteria for correlative time traces measurements of Chapter 6.4

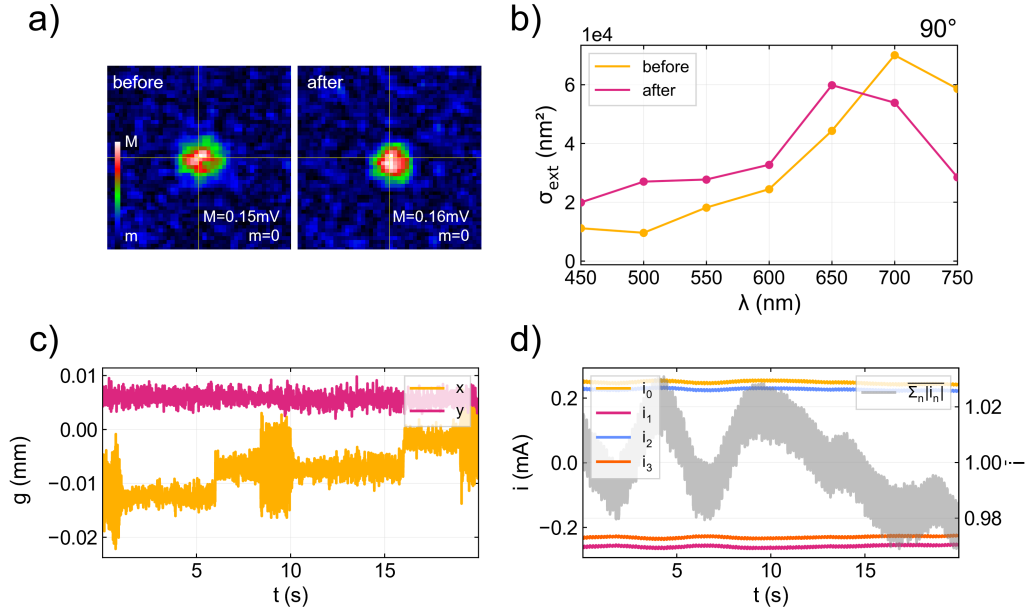


Figure A.13: Four criteria to be checked to consider the correlative time trace recorded (shown in Fig.6.19) at the antenna as reliable. (a) A 2D eH-CARS amplitude scan ($2\mu\text{m} \times 2\mu\text{m}$) measured at the AuNB focus, before and after the correlative measurement, shows that the antenna remained reasonably centered (yellow cross) during the time trace. Rainbow scales from m (black) to M (white). (b) Single particle extinction cross-sections, measured before and after the laser exposure, show that no significant structural changes affected the antenna during the laser exposure. (c) Galvo mirror positions (along x and y directions) were recorded during the time traces to visualize possible instabilities affecting the recorded signal. (d) Four BPD currents (i_0 , i_1 , i_2 , i_3) recorded during the time trace measurement were balanced (symmetric around the x -axis). Additionally, the $\bar{i} = \frac{i_\Sigma}{\langle i_\Sigma \rangle}$ used to correct the recorded time trace eH-CARS is shown as well.

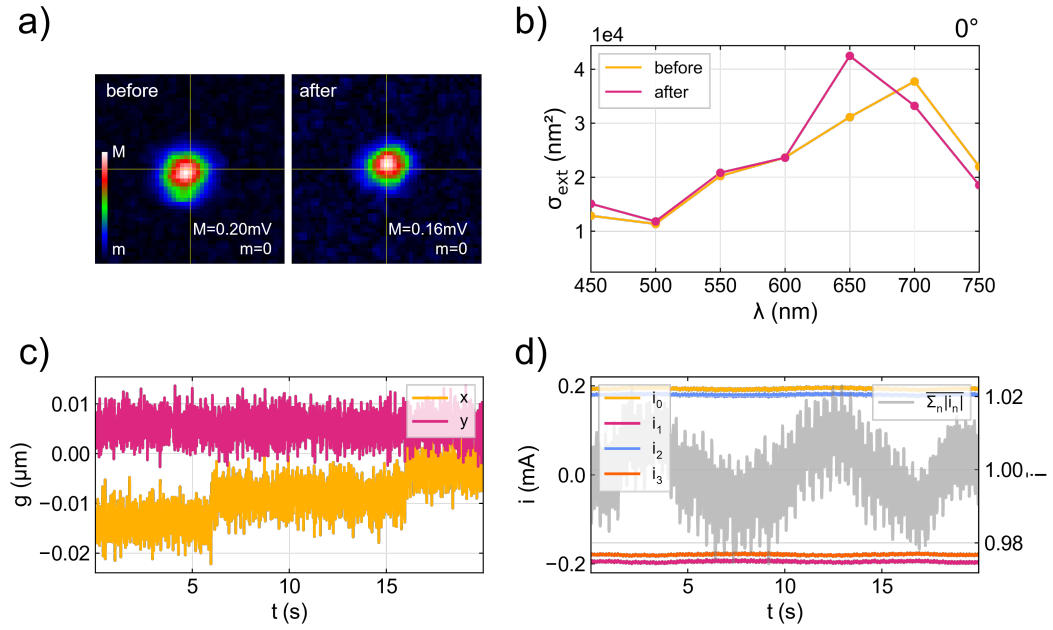


Figure A.14: Four criteria to be checked to consider the correlative time trace recorded (shown in Fig.6.20) at the antenna as reliable. (a) A 2D eH-CARS amplitude scan ($2\mu\text{m} \times 2\mu\text{m}$) measured at the AuNB focus, before and after the correlative measurement, shows that the antenna remained reasonably centered (yellow cross) during the time trace. Rainbow scales from m (black) to M (white). (b) Single particle extinction cross-sections, measured before and after the laser exposure, show that no significant structural changes affected the antenna during the laser exposure. (c) Galvo mirror positions (along x and y directions) were recorded during the time traces to visualize possible instabilities affecting the recorded signal. (d) Four BPD currents (i_0 , i_1 , i_2 , i_3) recorded during the time trace measurement were balanced (symmetric around the x -axis). Additionally, the $\bar{i} = \frac{\sum_n |i_n|}{\langle i_\Sigma \rangle}$ used to correct the recorded time trace eH-CARS is shown as well.

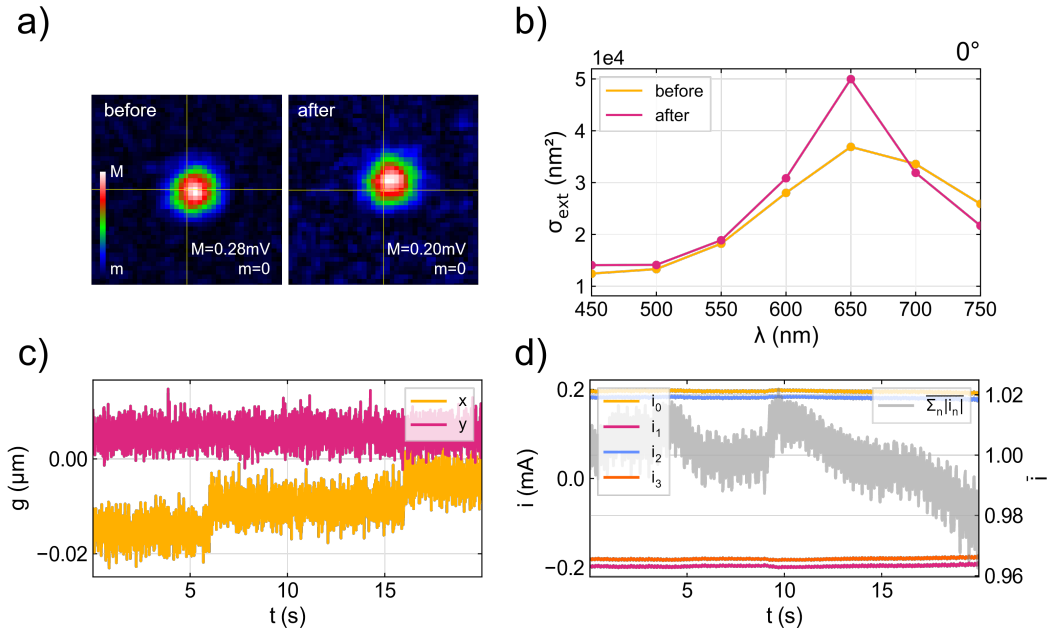


Figure A.15: Four criteria to be checked to consider the correlative time trace recorded (shown in Fig.6.21) at the antenna as reliable. (a) A 2D eH-CARS amplitude scan ($2\mu\text{m} \times 2\mu\text{m}$) measured at the AuNB focus, before and after the correlative measurement, shows that the antenna remained reasonably centered (yellow cross) during the time trace. Rainbow scales from m (black) to M (white). (b) Single particle extinction cross-sections, measured before and after the laser exposure, show that no significant structural changes affected the antenna during the laser exposure. (c) Galvo mirror positions (along x and y directions) were recorded during the time traces to visualize possible instabilities affecting the recorded signal. (d) Four BPD currents (i_0 , i_1 , i_2 , i_3) recorded during the time trace measurement were balanced (symmetric around the x -axis). Additionally, the $\bar{i} = \frac{i_\Sigma}{\langle i_\Sigma \rangle}$ used to correct the recorded time trace eH-CARS is shown as well.

Bibliography

- [1] Stefan Semrau and Thomas Schmidt. Membrane heterogeneity—from lipid domains to curvature effects. *Soft Matter*, 5(17):3174–3186, 2009.
- [2] Fluorophore reference listing. https://www.polysciences.com/german/awfile/index/attach/file/SS_PSI_Fluorophore_Ref_Listing.pdf/. Accessed: 2023-06-31.
- [3] Michael E Dailey, Erik Manders, David R Soll, and Mark Terasaki. Confocal microscopy of living cells. *Handbook of biological confocal microscopy*, pages 381–403, 2006.
- [4] Winnok H De Vos, Didier Beghuin, Christian J Schwarz, David B Jones, Jack JWA van Loon, Juergen Bereiter-Hahn, and Ernst HK Stelzer. Invited review article: Advanced light microscopy for biological space research. *Review of Scientific Instruments*, 85(10), 2014.
- [5] Walter Lang et al. *Nomarski differential interference-contrast microscopy*. Carl Zeiss Oberkochen, 1982.
- [6] Roger Y Tsien. The green fluorescent protein. *Annual review of biochemistry*, 67(1):509–544, 1998.
- [7] Marcel Bruchez Jr, Mario Moronne, Peter Gin, Shimon Weiss, and A Paul Alivisatos. Semiconductor nanocrystals as fluorescent biological labels. *science*, 281(5385):2013–2016, 1998.
- [8] Jose Requejo-Isidro. Fluorescence nanoscopy. methods and applications. *Journal of chemical biology*, 6:97–120, 2013.
- [9] Stefan W Hell. Toward fluorescence nanoscopy. *Nature biotechnology*, 21(11):1347–1355, 2003.
- [10] Michael Hofmann, Christian Eggeling, Stefan Jakobs, and Stefan W Hell. Breaking the diffraction barrier in fluorescence microscopy at low light intensities by using reversibly photoswitchable proteins. *Proceedings of the National Academy of Sciences*, 102(49):17565–17569, 2005.
- [11] Stefan W Hell and Jan Wichmann. Breaking the diffraction resolution limit by stimulated emission: stimulated-emission-depletion fluorescence microscopy. *Optics letters*, 19(11):780–782, 1994.
- [12] Stefan W Hell and Matthias Kroug. Ground-state-depletion fluorescence microscopy: A concept for breaking the diffraction resolution limit. *Applied Physics B*, 60:495–497, 1995.

-
- [13] Eric Betzig, George H Patterson, Rachid Sougrat, O Wolf Lindwasser, Scott Olenych, Juan S Bonifacino, Michael W Davidson, Jennifer Lippincott-Schwartz, and Harald F Hess. Imaging intracellular fluorescent proteins at nanometer resolution. *science*, 313(5793):1642–1645, 2006.
- [14] Michael J Rust, Mark Bates, and Xiaowei Zhuang. Sub-diffraction-limit imaging by stochastic optical reconstruction microscopy (storm). *Nature methods*, 3(10):793–796, 2006.
- [15] Rohit Bhargava. Infrared spectroscopic imaging: the next generation. *Applied spectroscopy*, 66(10):1091–1120, 2012.
- [16] Brynmor J Davis, P Scott Carney, and Rohit Bhargava. Theory of mid-infrared absorption microspectroscopy: II. heterogeneous samples. *Analytical chemistry*, 82(9):3487–3499, 2010.
- [17] Jiaze Yin, Meng Zhang, Yuying Tan, Zhongyue Guo, Hongjian He, Lu Lan, and Ji-Xin Cheng. Video-rate mid-infrared photothermal imaging by single-pulse photothermal detection per pixel. *Science Advances*, 9(24):eadg8814, 2023.
- [18] GJ Puppels, FFM De Mul, Cornelis Otto, J Greve, M Robert-Nicoud, DJ Arndt-Jovin, and TM Jovin. Studying single living cells and chromosomes by confocal raman microspectroscopy. *Nature*, 347(6290):301–303, 1990.
- [19] Mahmoud Ghomi. *Applications of Raman spectroscopy to biology: from basic studies to disease diagnosis*, volume 5. IOS press, 2012.
- [20] George Turrell and Jacques Corset. *Raman microscopy: developments and applications*. Academic Press, 1996.
- [21] Renzo Vanna, Alejandro De la Cadena, Benedetta Talone, Cristian Manzoni, Marco Marangoni, Dario Polli, and Giulio Cerullo. Vibrational imaging for label-free cancer diagnosis and classification. *La Rivista del Nuovo Cimento*, 45(2):107–187, 2022.
- [22] Alba Alfonso-García, Simon G Pfisterer, Howard Riezman, Elina Ikonen, and Eric O Potma. D38-cholesterol as a raman active probe for imaging intracellular cholesterol storage. *Journal of biomedical optics*, 21(6):061003–061003, 2016.
- [23] Ji-Xin Cheng and Xiaoliang Sunney Xie. *Coherent Raman scattering microscopy*. CRC press, 2016.
- [24] Yanping Li, Binglin Shen, Shaowei Li, Yihua Zhao, Junle Qu, and Liwei Liu. Review of stimulated raman scattering microscopy techniques and applications in the biosciences. *Advanced Biology*, 5(1):2000184, 2021.
- [25] Andreas Zumbusch, Gary R Holtom, and X Sunney Xie. Three-dimensional vibrational imaging by coherent anti-stokes raman scattering. *Physical review letters*, 82(20):4142, 1999.
- [26] Michael D Duncan, J Reintjes, and TJ Manuccia. Scanning coherent anti-stokes raman microscope. *Optics letters*, 7(8):350–352, 1982.
-

- [27] Conor L Evans, Eric O Potma, Mehron Puoris' haag, Daniel Côté, Charles P Lin, and X Sunney Xie. Chemical imaging of tissue in vivo with video-rate coherent anti-stokes raman scattering microscopy. *Proceedings of the national academy of sciences*, 102(46):16807–16812, 2005.
- [28] Dario Polli, Vikas Kumar, Carlo M Valensise, Marco Marangoni, and Giulio Cerullo. Broadband coherent raman scattering microscopy. *Laser & Photonics Reviews*, 12(9):1800020, 2018.
- [29] Francesco Masia, Wolfgang Langbein, and Paola Borri. Measurement of the dynamics of plasmons inside individual gold nanoparticles using a femtosecond phase-resolved microscope. *Physical Review B*, 85(23):235403, 2012.
- [30] Hideaki Kano and Hiro-o Hamaguchi. Ultrabroadband ($> 2500\text{cm}^{-1}$) multiplex coherent anti-stokes raman scattering microspectroscopy using a supercontinuum generated from a photonic crystal fiber. *Applied Physics Letters*, 86(12), 2005.
- [31] Ji-Xin Cheng and X Sunney Xie. Coherent anti-stokes raman scattering microscopy: instrumentation, theory, and applications. *The Journal of Physical Chemistry B*, 108(3):827–840, 2004.
- [32] Dmitry Pestov, Robert K Murawski, Gombojav O Ariunbold, Xi Wang, Miaochan Zhi, Alexei V Sokolov, Vladimir A Sautenkov, Yuri V Rostovtsev, Arthur Dogariu, Yu Huang, et al. Optimizing the laser-pulse configuration for coherent raman spectroscopy. *science*, 316(5822):265–268, 2007.
- [33] Fake Lu, Wei Zheng, and Zhiwei Huang. Elliptically polarized coherent anti-stokes raman scattering microscopy. *Optics letters*, 33(23):2842–2844, 2008.
- [34] Feruz Ganikhanov, Conor L Evans, Brian G Saar, and X Sunney Xie. High-sensitivity vibrational imaging with frequency modulation coherent anti-stokes raman scattering (fm cars) microscopy. *Optics letters*, 31(12):1872–1874, 2006.
- [35] Israel Rocha-Mendoza, Paola Borri, and Wolfgang Langbein. Quadruplex cars micro-spectroscopy. *Journal of Raman Spectroscopy*, 44(2):255–261, 2013.
- [36] Israel Rocha-Mendoza, Wolfgang Langbein, Peter Watson, and Paola Borri. Differential coherent anti-stokes raman scattering microscopy with linearly chirped femtosecond laser pulses. *Optics letters*, 34(15):2258–2260, 2009.
- [37] Ji-Xin Cheng, Andreas Volkmer, and X Sunney Xie. Theoretical and experimental characterization of coherent anti-stokes raman scattering microscopy. *JOSA B*, 19(6):1363–1375, 2002.
- [38] Ji-xin Cheng, Andreas Volkmer, Lewis D Book, and X Sunney Xie. An epi-detected coherent anti-stokes raman scattering (e-cars) microscope with high spectral resolution and high sensitivity. *The Journal of Physical Chemistry B*, 105(7):1277–1280, 2001.
- [39] Eric O Potma and X Sunney Xie. Detection of single lipid bilayers with coherent anti-stokes raman scattering (cars) microscopy. *Journal of Raman spectroscopy*, 34(9):642–650, 2003.

-
- [40] Erik T Garbacik, Jeroen P Korterik, Cees Otto, Jennifer L Herek, and Herman L Offerhaus. Epi-detection of vibrational phase contrast coherent anti-stokes raman scattering. *Optics letters*, 39(20):5814–5817, 2014.
- [41] Andreas Volkmer, Ji-Xin Cheng, and X Sunney Xie. Vibrational imaging with high sensitivity via epidetected coherent anti-stokes raman scattering microscopy. *Physical Review Letters*, 87(2):023901, 2001.
- [42] Conor L Evans, Eric O Potma, and X Sunney Xie. Coherent anti-stokes raman scattering spectral interferometry: determination of the real and imaginary components of nonlinear susceptibility χ (3) for vibrational microscopy. *Optics letters*, 29(24):2923–2925, 2004.
- [43] Eric O Potma, Conor L Evans, and X Sunney Xie. Heterodyne coherent anti-stokes raman scattering (cars) imaging. *Optics letters*, 31(2):241–243, 2006.
- [44] Jurna Martin, Jeroen P Korterik, Cornelis Otto, Jennifer Lynn Herek, and Herman L Offerhaus. Vibrational phase contrast microscopy by use of coherent anti-stokes raman scattering. *Physical review letters*, 103(4):043905, 2009.
- [45] Wolfgang Langbein, David Regan, Iestyn Pope, and Paola Borri. Invited article: Heterodyne dual-polarization epi-detected cars microscopy for chemical and topographic imaging of interfaces. *APL Photonics*, 3(9), 2018.
- [46] Wolfgang Langbein, Dafydd Sion Harlow, David Regan, Iestyn Pope, and Paola Borri. Heterodyne dual-polarization epi-detected cars microscopy for chemical and topographic imaging of interfaces. In *Label-free Biomedical Imaging and Sensing (LBIS) 2019*, volume 10890, page 1089003. SPIE, 2019.
- [47] Lu Wei, Zhixing Chen, Lixue Shi, Rong Long, Andrew V Anzalone, Luyuan Zhang, Fanghao Hu, Rafael Yuste, Virginia W Cornish, and Wei Min. Supermultiplex vibrational imaging. *Nature*, 544(7651):465–470, 2017.
- [48] H Chew, D-S Wang, and Milton Kerker. Surface enhancement of coherent anti-stokes raman scattering by colloidal spheres. *JOSA B*, 1(1):56–66, 1984.
- [49] EJ Liang, A Weippert, J-M Funk, A Materny, and W Kiefer. Experimental observation of surface-enhanced coherent anti-stokes raman scattering. *Chemical physics letters*, 227(1-2):115–120, 1994.
- [50] V Namboodiri, M Namboodiri, GI Cava Diaz, M Oppermann, G Flachenecker, and A Materny. Surface-enhanced femtosecond cars spectroscopy (se-cars) on pyridine. *Vibrational Spectroscopy*, 56(1):9–12, 2011.
- [51] Taro Ichimura, Norihiko Hayazawa, Mamoru Hashimoto, Yasushi Inouye, and Satoshi Kawata. Local enhancement of coherent anti-stokes raman scattering by isolated gold nanoparticles. *Journal of Raman Spectroscopy*, 34(9):651–654, 2003.
- [52] Norihiko Hayazawa, Taro Ichimura, Mamoru Hashimoto, Yasushi Inouye, and Satoshi Kawata. Amplification of coherent anti-stokes raman scattering by a metallic nanostructure for a high resolution vibration microscopy. *Journal of applied physics*, 95(5):2676–2681, 2004.
-

- [53] Taro Ichimura, Norihiko Hayazawa, Mamoru Hashimoto, Yasushi Inouye, and Satoshi Kawata. Tip-enhanced coherent anti-stokes raman scattering for vibrational nanoimaging. *Physical review letters*, 92(22):220801, 2004.
- [54] Steven Yampolsky, Dmitry A Fishman, Shirshendu Dey, Eero Hulkko, Mayukh Banik, Eric O Potma, and Vartkess A Apkarian. Seeing a single molecule vibrate through time-resolved coherent anti-stokes raman scattering. *Nature Photonics*, 8(8):650–656, 2014.
- [55] Yu Zhang, Yu-Rong Zhen, Oara Neumann, Jared K Day, Peter Nordlander, and Naomi J Halas. Coherent anti-stokes raman scattering with single-molecule sensitivity using a plasmonic fano resonance. *Nature communications*, 5(1):4424, 2014.
- [56] Sebastian Schlucker, Mohammad Salehi, Gero Bergner, Max Schutz, Philipp Strobel, Alexander Marx, Iver Petersen, Benjamin Dietzek, and Jurgen Popp. Immuno-surface-enhanced coherent anti-stokes raman scattering microscopy: immunohistochemistry with target-specific metallic nanoprobe and nonlinear raman microscopy. *Analytical chemistry*, 83(18):7081–7085, 2011.
- [57] Moon Sung Kang, So Yun Lee, Ki Su Kim, and Dong-Wook Han. State of the art biocompatible gold nanoparticles for cancer theragnosis. *Pharmaceutics*, 12(8):701, 2020.
- [58] Małgorzata Kus-Liśkiewicz, Patrick Fickers, and Imen Ben Tahar. Biocompatibility and cytotoxicity of gold nanoparticles: recent advances in methodologies and regulations. *International journal of molecular sciences*, 22(20):10952, 2021.
- [59] Guillermo González-Rubio, Andrés Guerrero-Martínez, and Luis M Liz-Marzán. Reshaping, fragmentation, and assembly of gold nanoparticles assisted by pulse lasers. *Accounts of chemical research*, 49(4):678–686, 2016.
- [60] Robert W Boyd. Quantum-mechanical theory of the nonlinear optical susceptibility. *Nonlinear optics*, pages 129–187, 2003.
- [61] Robert W Boyd, Zhimin Shi, and Israel De Leon. The third-order nonlinear optical susceptibility of gold. *Optics Communications*, 326:74–79, 2014.
- [62] Chandrasekhara Venkata Raman and Kariamanikkam Srinivasa Krishnan. A new type of secondary radiation. *Nature*, 121(3048):501–502, 1928.
- [63] Katrin Kneipp and Harald Kneipp. Single molecule raman scattering. *applied spectroscopy*, 60(12):322A–334A, 2006.
- [64] Gisela Eckhardt, Robert W Hellwarth, Fred J McClung, Steven E Schwarz, Daniel Weiner, and EJ Woodbury. Stimulated raman scattering from organic liquids. *Physical Review Letters*, 9(11):455, 1962.
- [65] N Bloembergen and YR Shen. Coupling between vibrations and light waves in raman laser media. *Physical Review Letters*, 12(18):504, 1964.
- [66] R. W. Hellwarth. Theory of stimulated raman scattering. *Phys. Rev.*, 130:1850–1852, Jun 1963.

-
- [67] RW Terhune, PD Maker, and CM Savage. Measurements of nonlinear light scattering. *Physical Review Letters*, 14(17):681, 1965.
- [68] Georg Placzek. Rayleigh-streuung und raman-effekt. (*No Title*), 1934.
- [69] E Garmire, F Pandarese, and CH Townes. Coherently driven molecular vibrations and light modulation. *Physical Review Letters*, 11(4):160, 1963.
- [70] David W McCamant, Philipp Kukura, Sangwoon Yoon, and Richard A Mathies. Femtosecond broadband stimulated raman spectroscopy: Apparatus and methods. *Review of scientific instruments*, 75(11):4971–4980, 2004.
- [71] VP Gupta. *Molecular and laser spectroscopy: advances and applications*. 2017.
- [72] Chien-Sheng Liao and Ji-Xin Cheng. In situ and in vivo molecular analysis by coherent raman scattering microscopy. *Annual review of analytical chemistry*, 9:69–93, 2016.
- [73] Richard C Prince, Renee R Frontiera, and Eric O Potma. Stimulated raman scattering: from bulk to nano. *Chemical reviews*, 117(7):5070–5094, 2017.
- [74] eg PA Franken, Alan E Hill, CW Peters, and Gabriel Weinreich. Generation of optical harmonics. *Physical review letters*, 7(4):118, 1961.
- [75] Robert W Boyd. *Nonlinear optics*. Academic press, 2020.
- [76] Maria Göppert-Mayer. Über elementarakte mit zwei quantensprüngen. *Annalen der Physik*, 401(3):273–294, 1931.
- [77] Winifried Denk, James H Strickler, and Watt W Webb. Two-photon laser scanning fluorescence microscopy. *Science*, 248(4951):73–76, 1990.
- [78] Patrik R Callis. Two-photon-induced fluorescence. *Annual Review of Physical Chemistry*, 48(1):271–297, 1997.
- [79] Richard KP Benninger and David W Piston. Two-photon excitation microscopy for the study of living cells and tissues. *Current protocols in cell biology*, 59(1):4–11, 2013.
- [80] Min Gu and CJR Sheppard. Comparison of three-dimensional imaging properties between two-photon and single-photon fluorescence microscopy. *Journal of microscopy*, 177(2):128–137, 1995.
- [81] K Lance Kelly, Eduardo Coronado, Lin Lin Zhao, and George C Schatz. The optical properties of metal nanoparticles: the influence of size, shape, and dielectric environment, 2003.
- [82] Cecilia Noguez. Optical properties of isolated and supported metal nanoparticles. *Optical Materials*, 27(7):1204–1211, 2005.
- [83] Jana Olson, Sergio Dominguez-Medina, Anneli Hoggard, Lin-Yung Wang, Wei-Shun Chang, and Stephan Link. Optical characterization of single plasmonic nanoparticles. *Chemical Society Reviews*, 44(1):40–57, 2015.
- [84] Gregory V Hartland. Optical studies of dynamics in noble metal nanostructures. *Chemical reviews*, 111(6):3858–3887, 2011.
-

- [85] Craig F Bohren and Donald R Huffman. *Absorption and scattering of light by small particles*. John Wiley & Sons, 2008.
- [86] Salem Marhaba. Effect of size, shape and environment on the optical response of metallic nanoparticles. *Noble and precious metals-Properties, nanoscale effects and applications*, 2018.
- [87] Peter B Johnson and R-WJPrB Christy. Optical constants of the noble metals. *Physical review B*, 6(12):4370, 1972.
- [88] Milton Kerker, D-S Wang, and H Chew. Surface enhanced raman scattering (sers) by molecules adsorbed at spherical particles. *Applied optics*, 19(19):3373–3388, 1980.
- [89] Greg T Hermanson. *Bioconjugate techniques*. Academic press, 2013.
- [90] Scott Boyd and Hiroshi Yamazaki. Tosyl chloride activation of a rayon/polyester cloth for protein immobilization. *Biotechnology techniques*, 7:277–282, 1993.
- [91] Y Tabata, SV Lonikar, F Horii, and Y Ikada. Immobilization of collagen onto polymer surfaces having hydroxyl groups. *Biomaterials*, 7(3):234–238, 1986.
- [92] Gelon Albrecht, Monika Ubl, Stefan Kaiser, Harald Giessen, and Mario Hentschel. Comprehensive study of plasmonic materials in the visible and near-infrared: linear, refractory, and nonlinear optical properties. *Acs Photonics*, 5(3):1058–1067, 2018.
- [93] Gelon Albrecht, Stefan Kaiser, Harald Giessen, and Mario Hentschel. Refractory plasmonics without refractory materials. *Nano letters*, 17(10):6402–6408, 2017.
- [94] Stephen A Lee and Stephan Link. Chemical interface damping of surface plasmon resonances. *Accounts of Chemical Research*, 54(8):1950–1960, 2021.
- [95] Donald R Herriott and George R Brewer. Electron-beam lithography machines. *Electron-Beam Technology in Microelectronic Fabrication*, pages 141–216, 1980.
- [96] Christophe Vieu, F Carcenac, A Pepin, Y Chen, M Mejias, A Lebib, L Manin-Ferlazzo, L Couraud, and H Launois. Electron beam lithography: resolution limits and applications. *Applied surface science*, 164(1-4):111–117, 2000.
- [97] Lukas M Payne, Wolfgang Langbein, and Paola Borri. Polarization-resolved extinction and scattering cross-sections of individual gold nanoparticles measured by wide-field microscopy on a large ensemble. *Applied Physics Letters*, 102(13):131107, 2013.
- [98] Lukas M Payne, Wolfgang Langbein, and Paola Borri. Wide-field imaging of single-nanoparticle extinction with sub-nm² sensitivity. *Physical Review Applied*, 9(3):034006, 2018.
- [99] Lukas M Payne, Wiebke Albrecht, Wolfgang Langbein, and Paola Borri. The optical nanosizer—quantitative size and shape analysis of individual nanoparticles by high-throughput widefield extinction microscopy. *Nanoscale*, 12(30):16215–16228, 2020.

-
- [100] Israel Rocha-Mendoza, Wolfgang Langbein, and Paola Borri. Coherent anti-stokes raman microspectroscopy using spectral focusing with glass dispersion. *Applied Physics Letters*, 93(20):201103, 2008.
- [101] Werner Österle, A Giovannozzi, Thomas Gradt, Ines Häusler, A Rossi, B Wetzel, G Zhang, and AI Dmitriev. Exploring the potential of raman spectroscopy for the identification of silicone oil residue and wear scar characterization for the assessment of tribofilm functionality. *Tribology International*, 90:481–490, 2015.
- [102] Wolfgang Langbein, Israel Rocha-Mendoza, and Paola Borri. Coherent anti-stokes raman micro-spectroscopy using spectral focusing: theory and experiment. *Journal of Raman Spectroscopy: An International Journal for Original Work in all Aspects of Raman Spectroscopy, Including Higher Order Processes, and also Brillouin and Rayleigh Scattering*, 40(7):800–808, 2009.
- [103] Attilio Zilli. *Measuring and modelling the absolute optical cross-sections of individual nano-objects*. PhD thesis, Cardiff University, 2018.
- [104] Jian-Ming Jin. *The finite element method in electromagnetics*. John Wiley & Sons, 2015.
- [105] Julius Adams Stratton and LJ Chu. Diffraction theory of electromagnetic waves. *Physical Review*, 56(1):99, 1939.
- [106] Jiang He, Wei Liu, and Yao-Xiong Huang. Simultaneous determination of glass transition temperatures of several polymers. *PLoS One*, 11(3):e0151454, 2016.
- [107] Ian H Malitson. Interspecimen comparison of the refractive index of fused silica. *Josa*, 55(10):1205–1209, 1965.
- [108] Robert L Olmon, Brian Slovick, Timothy W Johnson, David Shelton, Sang-Hyun Oh, Glenn D Boreman, and Markus B Raschke. Optical dielectric function of gold. *Physical Review B*, 86(23):235147, 2012.
- [109] Robert Adair, LL Chase, and Stephen A Payne. Nonlinear refractive-index measurements of glasses using three-wave frequency mixing. *JOSA B*, 4(6):875–881, 1987.
- [110] Jan Renger, Romain Quidant, Niek Van Hulst, and Lukas Novotny. Surface-enhanced nonlinear four-wave mixing. *Physical review letters*, 104(4):046803, 2010.
- [111] Arnica Karuna, Francesco Masia, Paola Borri, and Wolfgang Langbein. Hyper-spectral volumetric coherent anti-stokes raman scattering microscopy: quantitative volume determination and nacl as non-resonant standard. *Journal of Raman Spectroscopy*, 47(9):1167–1173, 2016.
- [112] George C Papavassiliou. Optical properties of small inorganic and organic metal particles. *Progress in Solid State Chemistry*, 12(3-4):185–271, 1979.
- [113] Stephan Link and Mostafa A El-Sayed. Shape and size dependence of radiative, non-radiative and photothermal properties of gold nanocrystals. *International reviews in physical chemistry*, 19(3):409–453, 2000.
-

- [114] Yu-Ying Yu, Ser-Sing Chang, Chien-Liang Lee, and CR Chris Wang. Gold nanorods: electrochemical synthesis and optical properties. *The Journal of Physical Chemistry B*, 101(34):6661–6664, 1997.
- [115] Mona B Mohamed, Kamal Z Ismail, Stephan Link, and Mostafa A El-Sayed. Thermal reshaping of gold nanorods in micelles. *The Journal of Physical Chemistry B*, 102(47):9370–9374, 1998.
- [116] Otto L Muskens, Guillaume Bachelier, Natalia Del Fatti, Fabrice Vallee, Arnaud Brioude, Xuchuan Jiang, and Marie-Paule Pileni. Quantitative absorption spectroscopy of a single gold nanorod. *The Journal of Physical Chemistry C*, 112(24):8917–8921, 2008.
- [117] Claire Deeb, Xuan Zhou, Jeeroome Plain, Gary P Wiederrecht, Renaud Bachelot, Milo Russell, and Prashant K Jain. Size dependence of the plasmonic near-field measured via single-nanoparticle photoimaging. *The Journal of Physical Chemistry C*, 117(20):10669–10676, 2013.
- [118] Krystyna Kolwas and Anastasiya Derkachova. Impact of the interband transitions in gold and silver on the dynamics of propagating and localized surface plasmons. *Nanomaterials*, 10(7):1411, 2020.
- [119] Marcos M Alvarez, Joseph T Khoury, T Gregory Schaaff, Marat N Shafigullin, Igor Vezmar, and Robert L Whetten. Optical absorption spectra of nanocrystal gold molecules. *The Journal of Physical Chemistry B*, 101(19):3706–3712, 1997.
- [120] Nicolas I Grigorchuk. Radiative damping of surface plasmon resonance in spheroidal metallic nanoparticle embedded in a dielectric medium. *JOSA B*, 29(12):3404–3411, 2012.
- [121] Yisu Wang, Zoltan Sztranyovszky, Attilio Zilli, Wiebke Albrecht, Sara Bals, Paola Borri, and Wolfgang Langbein. Quantitatively linking morphology and optical response of individual silver nanohedra. *Nanoscale*, 14(30):11028–11037, 2022.
- [122] N. W. Ashcroft and N. D. Mermin. *Solid State Physics*. Holt-Saunders, 1976.
- [123] OL Muskens, P Billaud, M Broyer, N Del Fatti, and F Vallée. *Physical Review B*, 78(20):205410, 2008.
- [124] Attilio Zilli, Wolfgang Langbein, and Paola Borri. Quantitative measurement of the optical cross sections of single nano-objects by correlative transmission and scattering microspectroscopy. *ACS photonics*, 6(8):2149–2160, 2019.
- [125] Wei Ding, Renaud Bachelot, Sergei Kostcheev, Pascal Royer, and Roch Espiau de Lamaestre. Surface plasmon resonances in silver bowtie nanoantennas with varied bow angles. *Journal of Applied Physics*, 108(12):124314, 2010.
- [126] Vahid Khoshdel and Mehrdad Shokooch-Saremi. Plasmonic nano bow-tie arrays with enhanced lspr refractive index sensing. *Micro & Nano Letters*, 14(5):566–571, 2019.
- [127] Anthony Gerrard and James M Burch. *Introduction to matrix methods in optics*. Courier Corporation, 1994.

-
- [128] Michael Ware and Justin Peatross. *Physics of Light and Optics (Black & White)*. Lulu. com, 2015.
- [129] Xuxing Lu, Deep Punj, and Michel Orrit. Two-photon-excited single-molecule fluorescence enhanced by gold nanorod dimers. *Nano Letters*, 22(10):4215–4222, 2022.
- [130] Anke Horneber, Kai Braun, Jan Rogalski, Paul Leiderer, Alfred J Meixner, and Dai Zhang. Nonlinear optical imaging of single plasmonic nanoparticles with 30 nm resolution. *Physical Chemistry Chemical Physics*, 17(33):21288–21293, 2015.
- [131] Tian Zhao, Jeremy W Jarrett, Jeffrey S Johnson, Kyoungweon Park, Richard A Vaia, and Kenneth L Knappenberger Jr. Plasmon dephasing in gold nanorods studied using single-nanoparticle interferometric nonlinear optical microscopy. *The Journal of Physical Chemistry C*, 120(7):4071–4079, 2016.
- [132] Céline Molinaro, Yara El Harfouch, Etienne Palleau, Fabien Eloi, Sylvie Marguet, Ludovic Douillard, Fabrice Charra, and Céline Fiorini-Debuisschert. Two-photon luminescence of single colloidal gold nanorods: revealing the origin of plasmon relaxation in small nanocrystals. *The Journal of Physical Chemistry C*, 120(40):23136–23143, 2016.
- [133] Max Born and Emil Wolf. *Principles of optics: electromagnetic theory of propagation, interference and diffraction of light*. CUP Archive, 2000.
- [134] Li Jiang, Iwan W Schie, Jun Qian, Sailing He, and Thomas Huser. Coherent anti-stokes emission from gold nanorods and its potential for imaging applications. *ChemPhysChem*, 14(9):1951–1955, 2013.
- [135] Matthieu Loumaigne, Clyde Midelet, Tristan Doussineau, Philippe Dugourd, Rodolphe Antoine, Meriem Stamboul, Anne Débarre, and Martinus HV Werts. Optical extinction and scattering cross sections of plasmonic nanoparticle dimers in aqueous suspension. *Nanoscale*, 8(12):6555–6570, 2016.
- [136] William M Tolles, Joseph W Nibler, JR McDonald, and Albert B Harvey. A review of the theory and application of coherent anti-stokes raman spectroscopy (cars). *Applied Spectroscopy*, 31(4):253–271, 1977.
- [137] Yasuo Yonemaru, Almar F Palonpon, Shogo Kawano, Nicholas I Smith, Satoshi Kawata, and Katsumasa Fujita. Super-spatial-and-spectral-resolution in vibrational imaging via saturated coherent anti-stokes raman scattering. *Physical Review Applied*, 4(1):014010, 2015.
- [138] MD Duncan, P Oesterun, F König, and Robert L Byer. Observation of saturation broadening of the coherent anti-stokes raman spectrum (cars) of acetylene in a pulsed molecular beam. *Chemical Physics Letters*, 80(2):253–256, 1981.
- [139] Li Gong, Wei Zheng, Ying Ma, and Zhiwei Huang. Saturated stimulated-raman-scattering microscopy for far-field superresolution vibrational imaging. *Physical Review Applied*, 11(3):034041, 2019.
-

- [140] Leonid G Kazovsky. Optical heterodyning versus optical homodyning: A comparison. *Journal of optical communications*, 6(1):18–24, 1985.
- [141] HR Carleton and WT Maloney. A balanced optical heterodyne detector. *Applied optics*, 7(6):1241–1243, 1968.
- [142] Alex J Laude and Ian A Prior. Plasma membrane microdomains: organization, function and trafficking. *Molecular membrane biology*, 21(3):193–205, 2004.
- [143] Kai Simons and Elina Ikonen. Functional rafts in cell membranes. *nature*, 387(6633):569–572, 1997.
- [144] Charles A Day and Anne K Kenworthy. Tracking microdomain dynamics in cell membranes. *Biochimica et Biophysica Acta (BBA)-Biomembranes*, 1788(1):245–253, 2009.
- [145] Erdinc Sezgin, Ilya Levental, Satyajit Mayor, and Christian Eggeling. The mystery of membrane organization: composition, regulation and roles of lipid rafts. *Nature reviews Molecular cell biology*, 18(6):361–374, 2017.
- [146] Marek Cebecauer, Mariana Amaro, Piotr Jurkiewicz, Maria João Sarmiento, Radek Sachl, Lukasz Cwiklik, and Martin Hof. Membrane lipid nanodomains. *Chemical reviews*, 118(23):11259–11297, 2018.
- [147] Daniel Lingwood and Kai Simons. Lipid rafts as a membrane-organizing principle. *science*, 327(5961):46–50, 2010.
- [148] Frederick A Heberle. With lipid rafts, context is everything. *Biophysical Journal*, 117(9):1549–1551, 2019.
- [149] Alena Koukalová, Mariana Amaro, Gokcan Aydogan, Gerhard Gröbner, Philip TF Williamson, Ilya Mikhalyov, Martin Hof, and Radek Šachl. Lipid driven nanodomains in giant lipid vesicles are fluid and disordered. *Scientific Reports*, 7(1):5460, 2017.
- [150] J Ortega Arroyo, J Andrecka, KM Spillane, N Billington, Y Takagi, JR Sellers, and P Kukura. Label-free, all-optical detection, imaging, and tracking of a single protein. *Nano letters*, 14(4):2065–2070, 2014.
- [151] Fuyuki Tokumasu, Albert J Jin, Gerald W Feigenson, and James A Dvorak. Nanoscopic lipid domain dynamics revealed by atomic force microscopy. *Biophysical journal*, 84(4):2609–2618, 2003.
- [152] Radek Šachl, Jan Bergstrand, Jerker Widengren, and Martin Hof. Fluorescence correlation spectroscopy diffusion laws in the presence of moving nanodomains. *Journal of Physics D: Applied Physics*, 49(11):114002, 2016.
- [153] Hai-Tao He and Didier Marguet. Detecting nanodomains in living cell membrane by fluorescence correlation spectroscopy. *Annual review of physical chemistry*, 62:417–436, 2011.
- [154] Erdinc Sezgin, Ilya Levantal, Guenter Schwarzmann, Veronika Mueller, Alf Honigmann, Vladimir Belov, Christian Eggeling, Unal Coskun, Kai Simons, and Petra Schwille. Partitioning, diffusion, and ligand binding of raft lipid analogs in model and cellular plasma membranes. *Biophysical Journal*, 102(3):296a–297a, 2012.

-
- [155] Mikel Garcia-Marcos, Jean-Paul Dehaye, and Aida Marino. Membrane compartments and purinergic signalling: the role of plasma membrane microdomains in the modulation of p2xr-mediated signalling. *The FEBS journal*, 276(2):330–340, 2009.
- [156] A Surprenant, F Rassendren, E Kawashima, RA North, and G Buell. The cytolytic p2z receptor for extracellular atp identified as a p2x receptor (p2x7). *Science*, 272(5262):735–738, 1996.
- [157] Wolfgang G Junger. Immune cell regulation by autocrine purinergic signalling. *Nature Reviews Immunology*, 11(3):201–212, 2011.
- [158] Geoffrey Burnstock and Vera Ralevic. Purinergic signaling and blood vessels in health and disease. *Pharmacological reviews*, 66(1):102–192, 2014.
- [159] Geoffrey Burnstock and Gillian E Knight. The potential of p2x7 receptors as a therapeutic target, including inflammation and tumour progression. *Purinergic signalling*, 14(1):1–18, 2018.
- [160] Tatiana Novitskaya, Elena Chepurko, Roman Covarrubias, Sergey Novitskiy, Sergey V Ryzhov, Igor Feoktistov, and Richard J Gumina. Extracellular nucleotide regulation and signaling in cardiac fibrosis. *Journal of molecular and cellular cardiology*, 93:47–56, 2016.
- [161] Francesco Masia, Adam Glen, Phil Stephens, Paola Borri, and Wolfgang Langbein. Quantitative chemical imaging and unsupervised analysis using hyperspectral coherent anti-stokes raman scattering microscopy. *Analytical Chemistry*, 85(22):10820–10828, 2013.
- [162] Lukas Roloff, Philippe Klemm, Imke Gronwald, Rupert Huber, John M Lupton, and Sebastian Bange. Light emission from gold nanoparticles under ultrafast near-infrared excitation: Thermal radiation, inelastic light scattering, or multiphoton luminescence? *Nano letters*, 17(12):7914–7919, 2017.
- [163] Glycerol(56-81-5) raman. https://www.chemicalbook.com/SpectrumEN_56-81-5_Raman.htm. Accessed: 2023-06-20.
- [164] Philip H Jones, Onofrio M Maragò, and Giovanni Volpe. *Optical tweezers: Principles and applications*. Cambridge University Press, 2015.
- [165] Keir C Neuman and Steven M Block. Optical trapping. *Review of scientific instruments*, 75(9):2787–2809, 2004.
- [166] Alexander Rohrbach and Ernst HK Stelzer. Trapping forces, force constants, and potential depths for dielectric spheres in the presence of spherical aberrations. *Applied optics*, 41(13):2494–2507, 2002.
- [167] Alexander P Demchenko. Photobleaching of organic fluorophores: quantitative characterization, mechanisms, protection. *Methods and applications in fluorescence*, 8(2):022001, 2020.
- [168] Jun Ando, Masanao Kinoshita, Jin Cui, Hiroyuki Yamakoshi, Kosuke Dodo, Katsumasa Fujita, Michio Murata, and Mikiko Sodeoka. Sphingomyelin distribution in lipid rafts of artificial monolayer membranes visualized by raman microscopy. *Proceedings of the National Academy of Sciences*, 112(15):4558–4563, 2015.
-